

University of Southampton Research Repository ePrints Soton

Copyright © and Moral Rights for this thesis are retained by the author and/or other copyright owners. A copy can be downloaded for personal non-commercial research or study, without prior permission or charge. This thesis cannot be reproduced or quoted extensively from without first obtaining permission in writing from the copyright holder/s. The content must not be changed in any way or sold commercially in any format or medium without the formal permission of the copyright holders.

When referring to this work, full bibliographic details including the author, title, awarding institution and date of the thesis must be given e.g.

AUTHOR (year of submission) "Full thesis title", University of Southampton, name of the University School or Department, PhD Thesis, pagination



Faculty of Engineering and the Environment
School of Engineering Sciences

Micromagnetic simulations of three dimensional core-shell nanostructures

Andreas Knittel

Thesis for the title
Doctor of Philosophy

June 2011

UNIVERSITY OF SOUTHAMPTON

ABSTRACT

FACULTY OF ENGINEERING AND THE ENVIRONMENT
SCHOOL OF ENGINEERING SCIENCES

Doctor of Philosophy

Simulation of three-dimensional magnetic nanostructures

Andreas Knittel

In the last 20 years, computer simulations, based on the micromagnetic model, have become an important tool for the characterisation of ferromagnetic structures. This work mainly uses the finite-element (FE) based micromagnetic solver Nmag to analyse the magnetic properties of ferromagnetic shell structures of different shapes and with dimensions below one micrometre. As the magnetic properties of structures in this size regime depend crucially on their shape, they have a potential towards engineering by shape manipulation. The finite-element method (FEM) discretises the micromagnetic equations on an unstructured mesh and, thus, is suited to model structures of arbitrary shape. The standard way to compute the magnetostatic potential within FE based micromagnetics is to use the hybrid finite element method / boundary element method (FEM/BEM), which, however, becomes computationally expensive for structures with a large surface. This work increases the efficiency of the hybrid FEM/BEM by using a data-sparse matrix type (hierarchical matrices) in order to extend the range of structures accessible by micromagnetic simulations. It is shown that this approximation leads only to negligible errors. The performed micromagnetic simulations include the finding of (meta-)stable micromagnetic states and the analysis of the magnetic reversal behaviour along certain spatial directions at different structure sizes and shell thicknesses. In the case of pyramidal shell structures a phase diagram is delineated which specifies the micromagnetic ground state as a function of structure size and shell thickness. An additional study demonstrates that a simple micromagnetic model can be used to qualitatively understand the magnetic reversal of a triangular platelet-shaped core-shell structure, which exhibits specific magnetic properties, as its core material becomes superconducting below a certain critical field H_{crit} .

Contents

1. Introduction	3
1.1. Research on ferromagnetic Materials	3
1.2. The Growth of magnetic structures	4
1.3. Computational micromagnetism	5
1.4. Structure of the thesis	6
2. Theoretical fundamentals	9
2.1. Basic micromagnetics	9
2.1.1. Magnetisation	9
2.1.2. The micromagnetic model	10
2.1.3. Brown's equation	14
2.1.4. The Landau-Lifshitz-Gilbert equation	15
2.2. Hybrid FEM/BEM	16
2.2.1. The Fredkin-Koehler approach	17
2.2.2. The García-Cervera-Roma approach	19
2.2.3. Discretisation of the integral equation	20
2.2.4. The Lindholm-formula	22
2.2.5. Summary	24
2.3. Hierarchical matrices	25
2.3.1. Structure of \mathcal{H} -matrices	25
2.3.2. Creating low rank approximations using interpolation	29
2.3.3. Algorithms for low-rank approximation	34
2.3.4. \mathcal{H} -matrix assembly in HLib	36
3. Compression of the boundary element matrix	39
3.1. Introduction	39
3.1.1. The studied system	41
3.1.2. Error analysis	42
3.1.3. Determination of parameter sets	42
3.2. Efficiency of \mathcal{H} -matrix assembly algorithms	44
3.2.1. B_{ij} by Gaussian quadrature	44
3.2.2. B_{ij} by analytical formula	48
3.2.3. Summary	55

3.3.	Discussion of Numerical Errors	56
3.3.1.	FE discretisation in square platelets	57
3.3.2.	Hierarchical matrices in FE simulation of thin platelets	65
3.4.	Summary and outlook	76
4.	Micromagnetic studies of pyramidal-shaped shell structures	79
4.1.	Experimental growth of Nickel structures	80
4.2.	Methodology	82
4.2.1.	The investigated system	82
4.2.2.	The micromagnetic method	83
4.2.3.	Exploring the parameter space	85
4.3.	Numerical results	86
4.3.1.	Energetic ground states at $H_{\text{ext}} = 0$	86
4.3.2.	Hysteresis	99
4.3.3.	Pyramidal shells with rounded edges and corners	111
4.4.	Conclusions	112
5.	Stray field investigations on core-shell-structures	115
5.1.	Experimental background	115
5.2.	Simulation results	120
5.2.1.	Superconducting regions in triangular Pb/Ni core shell structures	122
5.2.2.	Magnetic reversal in cuboidal Nickel shells	140
6.	Summary and outlook	145
6.1.	Hierarchical matrices in FE-based micromagnetic simulations.	145
6.2.	Micromagnetic studies of pyramidal-shaped shell structures.	147
6.3.	Stray field investigations on core-shell-structures	148
A.	Notes on potential theory	151
A.1.	Some definitions	151
A.2.	Derivation	152
B.	Determining HLib parameters	157
C.	Analytical expression for the stray field in a rectangular prism	167
C.1.	Derivation of the formula	167
C.2.	Testing the formula	173
D.	Accuracy of the finite element discretisation	179
D.1.	Tests on the accuracy of micromagnetic simulations on pyramidal shells.	179

D.2. Numerical tests on the computation of the superconducting volume	188
---	-----

List of Figures

2.1. Introduction of variables used in the Lindholm formula.	23
2.2. Creation of a cluster tree through bisection.	27
2.3. Two-dimensional illustration of two clusters and their bounding boxes for explanation of admissibility criterion.	28
2.4. Illustration of how cluster trees are combined to hierarchical structure of \mathcal{H} -matrix.	30
2.5. Approximation of a matrix block by an R_k -matrix.	31
2.6. Graph showing 4-th order Lagrange polynomials.	32
3.1. A square, thin platelets with a side length L and a thickness t	41
3.2. Finite-element discretisation error of demagnetisation factor D_z	43
3.3. Hierarchical matrix approximation error of demagnetising fac- tor D_z (elements $B_{i,j}$ by numerical quadrature).	45
3.4. Memory footprint of \mathcal{H} -matrix approximations (elements $B_{i,j}$ by numerical quadrature).	46
3.5. Assembly times of full BE matrix and \mathcal{H} -matrix approximations (elements $B_{i,j}$ by numerical quadrature).	47
3.6. Hierarchical matrix approximation error of demagnetising fac- tor D_z (elements $B_{i,j}$ by analytical formula).	49
3.7. Dependence of hierarchical matrix approximation error on method of computing matrix elements B_{ij}	50
3.8. Memory footprint of \mathcal{H} -matrix approximations (elements $B_{i,j}$ by analytical formula).	51
3.9. Dependence of \mathcal{H} -matrix memory footprint on method of com- puting matrix elements B_{ij}	52
3.10. Assembly times of full BE matrix and \mathcal{H} -matrix approximations (elements $B_{i,j}$ by analytical formula).	53
3.11. Dependence of \mathcal{H} -matrix assembly time on method of comput- ing matrix elements B_{ij}	54
3.12. Analytical and FE-based computation of the demagnetisation field within a thin, square platelet.	58
3.13. Onion state in a thin, square platelet.	64

3.14. FD and FE-based simulation results of the magnetic reversal within a thin square platelet (along a near in-plane direction).	66
3.15. FD and FE-based simulation results of the magnetic reversal within a thin square platelet (along an out-of-plane direction).	67
3.16. Deviations of the demagnetisation field within a thin, square platelet due to hierarchical matrix approximations.	71
3.17. Equipotential surfaces of the magnetic scalar potential in a homogeneously magnetised platelet.	72
3.18. Effect of hierarchical matrices on magnetic reversal simulations in thin, square platelet (along near in-plane direction).	74
3.19. Effect of hierarchical matrices on magnetic reversal simulations in thin, square platelet (along out-of-plane direction).	75
4.1. Left: atomic force microscope image of a pyramidal core-shell (Ag-Ni) structure. Right: graph of its magnetic reversal.	80
4.2. Introduction of the pyramidal shell geometry.	82
4.3. Left: face-centred cubic unit cell of nickel crystal. Right: (0,1,1) crystal planes.	83
4.4. Polar plot of the shape anisotropy of a pyramidal shell.	87
4.5. Observed single domain states within pyramidal shells.	88
4.6. Observed vortex states within pyramidal shells.	91
4.7. Cross-sectional view of the symmetric and the asymmetric vortex state.	92
4.8. Equipotential surfaces of the exchange energy density exhibiting the core of an asymmetric vortex state.	93
4.9. Phase diagram of the energetic ground states in pyramidal shell structures.	94
4.10. Comparison of the total micromagnetic energies of different states.	95
4.11. Magnetisation, demagnetisation field and demagnetisation energy of a symmetric and an asymmetric vortex state.	96
4.12. Cross-section of a pyramidal shell illustrating the creation of surface charges.	97
4.13. Magnetic reversal of a pyramidal shell ($a = 100$ nm and $t_{\text{rel}} = 10\%$) along the z -direction.	100
4.14. Magnetic reversal of a pyramidal shell ($a = 250$ nm and $t_{\text{rel}} = 10\%$) along the z -direction.	101
4.15. The magnetic reversal along the x -direction for different geometry sizes and shell thicknesses.	102
4.16. Magnetic reversal of a pyramidal shell ($a = 250$ nm and $t_{\text{rel}} = 50\%$) along the x -direction.	103
4.17. Figure defining parameters to describe blunt, pyramidal shells.	106

4.18. Introduction of the pyramidal shell geometry with rounded corners.	107
4.19. Magnetic reversal along the z -direction for pyramidal shells ($a = 100$ nm, $t_{\text{rel}} = 10\%$) with different degrees of rounding at the corners.	108
4.20. Magnetic reversal along the x -direction for pyramidal shells ($a = 100$ nm, $t_{\text{rel}} = 10\%$) with different degrees of rounding at the corners.	109
4.21. Magnetic reversal along the x -direction for pyramidal shells ($a = 250$ nm, $t_{\text{rel}} = 10\%$) with different degrees of rounding at the corners.	110
5.1. Atomic force microscope images of a triangular Pb-Ni platelet and a Sn-Ni rectangular prism.	116
5.2. Atomic force microscope image of the cross-section through a triangular Pb-Ni platelet.	116
5.3. Experimental setup for measuring the stray field of core-shell structures.	117
5.4. Experimentally measured magnetic reversal of a Pb/Ni core-shell structure.	118
5.5. Geometry of investigated core-shell structures (triangular platelet and rectangular prism).	121
5.6. Micromagnetic states of a triangular platelet-shaped Ni shell at different external fields.	125
5.7. Micromagnetic states of triangular platelet-shaped Ni shells with different shell thicknesses at $ \vec{H}_{\text{ext}} = 1000$ Oe.	126
5.8. Superconducting fraction within the core of a triangular platelet-shaped Pb-Ni core-shell structure at different pinning fields. . .	127
5.9. Superconducting fraction within the core of triangular platelet-shaped Pb-Ni core-shell structures with different shell thicknesses.	128
5.10. Superconducting fraction within the core of a triangular platelet-shaped Pb/Ni core-shell structure. 3D visualisations are given at marked field strengths.	129
5.11. 3D visualisations corresponding to data points (b)-(d) of Figure 5.10.	130
5.12. 3D visualisations corresponding to data points (e)-(g) of Figure 5.10.	131
5.13. Stray field within the core of a triangular platelet-shaped Pb/Ni core-shell structure.	132
5.14. Spatially resolved stray field at a Hall element positioned below a triangular platelet-shaped core-shell structure.	133

5.15. Magnetisation reversal along the z -direction of a rectangular prism-shaped Ni shell ($h = 122.5$ nm, $l = 1043.0$ nm, $w = 143.5$ nm, $t = 21$ nm).	137
5.16. Magnetic configurations at $ H_{\text{ext},z} = 32$ Oe and $ H_{\text{ext},z} = 29$ Oe (see Figure 5.15).	138
5.17. Magnetisation reversal along the z -direction of a rectangular prism-shaped Ni shell ($h = 220.5$ nm, $l = 2044.0$ nm, $w = 241.5$ nm, $t = 21$ nm).	139
A.1. Mathematical problem solved by the boundary element method.	152
A.2. Approach to evaluate equation A.5 at a point on the boundary ∂R .	153
B.1. Dependency of the accuracy and the time of the \mathcal{H} -matrix assembly by interpolation on the polynomial order.	159
B.2. Dependency of the accuracy and the time of the \mathcal{H} -matrix assembly by ACA on the parameter ϵ_{aca} .	160
B.3. Dependency of the accuracy and the time of the \mathcal{H} -matrix assembly by ACA+ on the parameter ϵ_{aca} .	161
B.4. Dependency of the accuracy and the time of the \mathcal{H} -matrix assembly by HCA I on the polynomial order and the parameter ϵ_{aca} .	162
B.5. Dependency of the accuracy and the time of the \mathcal{H} -matrix assembly by HCA II on the polynomial order and the parameter ϵ_{aca} .	163
B.6. Dependency of the accuracy and the time of the \mathcal{H} -matrix assembly by HCA II (with $\epsilon_{\text{aca}} = 10^{-7}$) on the polynomial order.	164
B.7. Dependence of the accuracy, time and memory footprint of the \mathcal{H} -matrix assembly by HCA II on the re-compression parameter ϵ .	165
B.8. Dependence of the accuracy and time of the \mathcal{H} -matrix assembly by HCA II on the quadrature order q .	166
C.1. Rectangular prism with surface charges stemming from the homogeneous magnetisation.	167
C.2. Visualisation of solutions of the integral (C.4).	168
C.3. Asymptotic behaviour of the derived formula for the demagnetisation field.	175
C.4. Rectangular prism with marked lines, along which the demagnetisation field is computed.	176
C.5. Demagnetisation field in a homogeneously magnetised rectangular prism along a line parallel to the x -direction (see Figure C.4).	177

C.6. Demagnetisation field in a homogeneously magnetised rectangular prism along a line parallel to the y -direction (see Figure C.4).	177
C.7. Demagnetisation field in a homogeneously magnetised rectangular prism along a line parallel to the z -direction (see Figure C.4).	178
D.1. Edge length distribution within the mesh of a pyramidal shell .	180
D.2. Splitting of a tetrahedron via an h-type refinement.	180
D.3. Averaged magnetisation of a flower and a vortex state within a pyramidal shell ($a = 120$ nm, $t_{\text{rel}} = 80$ %) as a function of the mesh shell resolution.	182
D.4. Micromagnetic energy densities of a flower and a vortex state (within a pyramidal shell with $a = 120$ nm and $t_{\text{rel}} = 80$ %) as a function of the shell mesh resolution.	183
D.5. Average magnetisation of a flower and a vortex state within a pyramidal shell ($a = 50$ nm, $t_{\text{rel}} = 10$ %) as a function of the shell mesh resolution.	184
D.6. Total energy density of a flower and a vortex state (within a pyramidal shell with $a = 50$ nm and $t_{\text{rel}} = 10$ %) as a function of the mesh resolution.	185
D.7. Dependence of the superconducting fraction within the core of a triangular platelet-shaped Pb/Ni core-shell structure on the core mesh resolution.	189

List of Tables

3.1. Parameter values for \mathcal{H} -matrix assembly algorithms.	44
3.2. Demagnetising field computation in a thin, square platelet: comparing the rms error of the FFT and hybrid FEM/BEM.	60
3.3. Relaxing a homogeneous in-plane configuration in a thin, square platelet: comparison between Nmag and OOMMF.	62
3.4. Relaxing a homogeneous out-of-plane configuration in a thin, square platelet: comparison between Nmag and OOMMF.	63
3.5. Rms error of the demagnetisation field due to hierarchical matrix approximations assembled by different algorithms.	68
3.6. Convergence of the algorithms ACA+ and HCA II with respect to their algorithm-specific parameters.	68
3.7. Relaxing a homogeneous (near) in-plane configuration in a thin, square platelet: effect of hierarchical matrix approximations.	69
3.8. Relaxing a homogeneous out-of-plane configuration in a thin, square platelet: effect of hierarchical matrix approximations.	70
4.1. Remanent states for pyramidal shell geometries.	99
C.1. Rms error of the demagnetising field computation with OOMMF.	176
D.1. Effect of an h-type refinement on the average and maximal edge length of tetrahedral meshes with different resolutions.	181
D.2. Properties of pyramidal shell meshes with different resolutions: average and maximal edge length, number of tetrahedron layers resolving shell.	181
D.3. Dependence of the stray field rms error within the core of a triangular-shaped Pb/Ni core-shell structure on M_S^{Vac}	191

Declaration of Authorship

I, Andreas Knittel, declare that the thesis entitled *Micromagnetic simulations of three dimensional core-shell nanostructures* and the work presented in it are both my own, and have been generated by me as the result of my own original research. I confirm that

- this work was done wholly or mainly while in candidature for a research degree at this University;
- where any part of this thesis has previously been submitted for a degree or any other qualification at this University or any other institution, this has been clearly stated;
- where I have consulted the published work of others, this is always clearly attributed;
- where I have quoted from the work of others, the source is always given. With the exception of such quotation, this thesis is entirely my own work;
- I have acknowledged all main sources of help;
- where the thesis is based on work done by myself jointly with others, I have made clear exactly what was done by others and what I have contributed myself. Experimental co-workers have provided the Figures 4.1, 5.1 and 5.2. Figure 5.3 is virtually a copy of Figure 2 in [1].
- parts of this work have been published as:
 - **A. Knittel**, M. Franchin, G. Bordignon, T. Fischbacher, S. J. Bending and H. Fangohr, Compression of Boundary Element Matrix in Micromagnetic Simulations, *Journal of Applied Physics*, 105:07D542, 2009
 - **A. Knittel**, M. Franchin, T. Fischbacher, F. Nasirpour, S. J. Bending and H. Fangohr, Micromagnetic studies of three-dimensional pyramidal shell structures, *New Journal of Physics*, 12(11):113048, 2010

- A. Müller, S. E. C. Dale, M. A. Engbarth, S. J. Bending, L. M. Peter, **A. Knittel** and H. Fangohr
Field-Tuneable Diamagnetism in Ferromagnetic-Superconducting CoreShell Structures, *Advanced Functional Materials*, 21(10), 2011
- F. Nasirpouri, M. A. Engbarth, S. J. Bending, L. M. Peter, **A. Knittel**, H. Fangohr and M. V. Milosevic
Three-dimensional ferromagnetic architectures with multiple metastable states, *Applied Physics Letters*, 98:22, 2011

Signed: _____

Date: _____

Acknowledgments

First and foremost, I would like to thank Prof. Dr. Hans Fangohr for being such an encouraging supervisor. He was always approachable and gave me very good advice during the ups and downs of my PhD. Without him I could not have completed the thesis in this form.

I also would like to thank Dr. Thomas Fischbacher, who was my second supervisor. Nmag, the tool I have been using throughout my PhD, is his brainchild. He gave me very good support, especially when I was working on the inclusion of the hierarchical matrix methodology into Nmag.

Matteo Franchin was a fellow PhD and, later, a Post-Doc in Hans Fangohr's group. With his vast knowledge on Nmag and Linux-based systems in general, he provided me with invaluable advice on countless occasions. Therefore, I am deeply indebted to him.

I would also like to thank Giuliano Bordinon, who, at the beginning of my PhD, often gave me advice, especially on computer-related issues. He was the one, who set up my first computer at Southampton.

André Müller, Dr. Farzad Nasirpouri and Prof. Dr. Simon Bending have performed very interesting experiments, whose analysis was one of my key tasks during the PhD. I appreciated our fruitful exchange on physical issues very much, and would like to thank them for our very good collaboration.

I also want to thank the University of Southampton for providing such a pleasant working atmosphere. It was also very pleasant because of the nice colleagues in building 25. These were Matteo, Giuliano, Jörn, Hani, Stephan, Jun, Lindsay, Massoud, Raoul, Ernesto, Dmitri and Max.

I like to thank Phil Myles for proofreading my thesis and providing valuable corrections.

The funding for my PhD was provided by the Engineering and Physical Sciences Research Council (EPSRC) UK (EP/E040063/1, EP/E039944/1).

Finally, I am mostly indebted to my family, especially to my parents. Without their support my academic achievements would not have been possible.

1. Introduction

In modern computers, logic operations are performed on integrated circuits, i.e. electronic circuits which are imprinted on a thin silicon wafer. The fundamental building blocks of these circuits are semiconductor transistors, which function as switches of electronic signals. The performance of an integrated circuit can be increased by increasing the number of transistors it accommodates. In 1965, Gordon E. Moore stated that the number of transistors on an integrated circuit (IC) could be doubled every year [2], corresponding to an increase from 64 transistors per chip in 1965 to 65,000 transistors per chip in 1975. After 1975, Moore envisaged a doubling of the number of components per chip every 18 months. Due to the uncanny accuracy of his predictions this exponential growth became known as Moore's law. A similar performance increase has also been achieved for other components of modern computers, such as the hard disks and the random access memories (RAM) [3]. This advancement in the capabilities of modern computers has in turn spawned a new branch of theoretical physics, namely computational physics, which also forms the backdrop of the present work. It is concerned with the numerical analysis of ferromagnetic, mesoscopic structures on the basis of the micromagnetic model. In the mesoscopic regime dimensions from a few nanometres to a few micrometres are examined [4]. The following introduction discusses why the research on ferromagnetic materials is very promising and how the present work fits into this broader framework. Finally, the structure of this thesis is outlined.

1.1. Research on ferromagnetic Materials

Ferromagnetism is a form of collective magnetism, i.e. the microscopic magnetic moments are coupled through the so-called exchange interaction, so that ferromagnetic materials, such as nickel, iron, cobalt and different alloys (e.g. permalloy), exhibit strong magnetic properties even in the absence of an external magnetic field. This makes the materials so attractive with respect to applications in modern technological devices. An important field of research is the development of magnetic sensors, such as anisotropic magnetoresistors

1. Introduction

(AMR), which are used for the contactless measurement of electrical currents, measurements of movements and rotational speed in machinery, earth field sensing and navigation systems [5]. Furthermore, the discovery of giant magnetoresistance (GMR) [6, 7], which was also awarded the Nobel prize in physics in 2007, has led to the development of Giant Magneto Resistance (GMR) sensors, which are now used in the read heads of modern hard drives, enhancing their capabilities significantly [8]. In the long run, GMR sensors are likely to replace AMR sensors in other fields [8]. Another important research direction is the development of non-volatile magnetic random access memory devices, for which different approaches, such as MRAM [9], the racetrack memory [10] and VRAM [11] have been proposed. Unlike DRAM devices, these memory devices store data without the supply of power, thus realising an instant-boot-up computer. Research into ultra-strong permanent magnets allows for the construction of more efficient and more compact motors [12]. Another promising research direction is the development of magnetic quantum dot cellular automata, which can be used to perform logic operations on systems of magnetic nanodots, and may lead to future generations of processors [13, 14]. Finally, much work has been devoted to the growth of patterned arrays of magnetic elements, which may allow for the development of novel hard drives with enhanced storage capabilities [15]. This list of potential applications is far from complete, but already demonstrates the potential of the field of ferromagnetic materials, especially in the nanometre regime.

1.2. The Growth of magnetic structures

The magnetocrystalline anisotropy of bulk magnetic material governs its magnetic behaviour and is therefore key to its technological applicability. It is an intrinsic property of the material and, generally, cannot readily be tailored [16], although recent progress in ion irradiation appears to be promising in that respect [17]. In contrast, the magnetic behaviour of a nanomagnet is also largely influenced by the interaction of the magnetisation with its shape. This dependency provides the possibility of fine-tuning magnetic properties through shape-manipulation, which in turn requires very precise growth techniques. Lithographic methods have been widely used to produce ordered arrays of nanoelements [18]. The basic idea is to deposit a thin resist layer onto a substrate, parts of which are then chemically altered by exposing them to radiation. Finally, different techniques are used in order to transfer the generated pattern into an array of nanoelements. However, these nanoelements are usually not very well defined along the direction perpendicular to the original resist layer, and the grown structures tend to be platelets. In contrast,

chemical methods are based on what is often referred to as the ‘bottom up’ approach, i.e. the nanoparticles develop from smaller units. The challenge of fabricating nanoparticles of non-spherical geometry is therefore to obtain a suitably anisotropic growth. Corresponding research on magnetic nanoparticles has led to the growth of Co spheres and rods [19] and a wide variety of shapes for hard magnetic iron compounds [20, 21]. Electrodeposition is a wet-chemical method [22, 23, 1]. It can be used in conjunction with lithographic methods in order to create arrays of electrodeposited structures, providing a cheap method of fabricating the patterned media of complex geometries [18]. A large part of the thesis is concerned with modelling the properties of three-dimensional (3D) nickel structures, which can be grown by electrodeposition.

1.3. Computational micromagnetism

The micromagnetic model was introduced by Brown [24] and is often used to compute stable magnetic configurations and magnetic dynamics within ferromagnetic systems. Due to their non-linearity, analytical approaches to solving the micromagnetic equations are only feasible for highly symmetric geometries, and, even in those cases, cannot address certain phenomena like metastability. With the aforementioned development of modern computers, numerical methods can be employed. The disadvantage of numerical results is that they generally give less physical insight than corresponding analytical solutions. On the other hand, micromagnetic simulations not only yield the magnetisation, but other important scalar and vector fields as well, such as energy densities and effective magnetic fields corresponding to the different energetic contributions. A careful examination of these fields can reveal a lot about the underlying physical mechanisms.

In micromagnetics, there are two standard methods to solve the micromagnetic equations numerically. These are the finite difference method (FDM) and the finite element method (FEM) [25]. FDM discretises the micromagnetic equations on a cubic grid, and is a very efficient method of studying the magnetic properties of ferromagnetic structures of cuboidal shape. For such structures, the FD based solver OOMMF [26] is used in the present work. With respect to more general shapes, standard FDM generally leads to significant deviations [27, 28], which may be mitigated through modified approaches [27, 28, 29]. FEM discretises the micromagnetic equations on an unstructured mesh and thus can account for, in principle, arbitrary geometries. Due to this flexibility the FE based solver Nmag [30], which uses a tetrahedral mesh for the discretisation, will mostly be employed. There are certain efficiency issues, that arise when Nmag is used to simulate relatively large structures

1. Introduction

(dimensions of several hundred nanometres) and structures with a large surface to volume ratio. The reason is that the computation of the magnetostatic potential ϕ via a hybrid finite element method / boundary element method (FEM/BEM) involves the assembly and storage of a dense boundary element method.

Therefore a part of this work will deal with the optimisation of Nmag through the external library HLib [31], so that the range of computationally tractable structures is enhanced. The underlying idea is to use hierarchical matrices, which are data-sparse, hierarchically structured matrices, to approximate the above-mentioned boundary element matrix. Micromagnetic studies of fundamental geometries have been mostly carried out for planar structures, such as square [32, 33, 34, 35] and circular [36, 37, 35] platelets, and ferromagnetic cubes [38, 39]. Due to the above-mentioned limitations of standard growth techniques, more complex three dimensional nanoelements have been subject to far less research. In the literature, one can find micromagnetic investigations on cones [40, 41], pyramids [40], partially spherical structures [42, 43], prolate spheroids [44], tetrahedrons and octahedrons [45], and hexagonally shaped islands [46]. Energetic ground states of spherical core-shell structures have been studied analytically by deriving expressions for the micromagnetic energy contributions [47].

1.4. Structure of the thesis

This thesis is structured as follows: chapter 2 provides a short introduction to the micromagnetic model (Section 2.1). This chapter also alludes to the hybrid finite element method / boundary element method (FEM/BEM) (Section 2.2), which is the standard way to compute the long-range, magnetostatic interaction in finite-element micromagnetism. The efficiency of the hybrid FEM/BEM can be increased by using hierarchical matrices, which are introduced in the final section (2.3) of the chapter. Chapter 3 presents a study on how the efficiency of the finite-element solver Nmag can be increased by coupling it with the HLib library, an implementation of the hierarchical matrix methodology. The efficiency of the hierarchical matrices is discussed with respect to the error they introduce. Chapter 4 presents a micromagnetic study on the magnetic properties of pyramidal-shaped nickel shells. The focus of this investigation lies in the micromagnetic states, that occur within shells of different shapes and sizes, and on the magnetic reversal along certain spatial directions. Chapter 5 presents experimental results by co-workers at the University in Bath on hybrid Pb/Ni and Sn/Ni systems (Section 5.1). These structures contain a triangular platelet-shaped lead (Pb) core, which is cov-

ered by a nickel (Ni) layer. Since the Pb core becomes superconducting below a critical temperature $T_{\text{crit}} = 7.2\text{ K}$ and because the Ni shell is ferromagnetic, this hybrid system exhibits specific properties during magnetic reversal at temperatures $T < T_{\text{crit}}$. Sub-section 5.2.1 shows that we can qualitatively understand these properties on the basis of a relatively simple model. Finally, magnetic reversal of rectangular prism-shaped nickel shells is investigated with the standard micromagnetic model (Section 5.2.2). The main part of the thesis is concluded by a short chapter, which summarises the main findings and gives an outlook on future research (Chapter 6). Supplementary information to main part of the thesis is given in the Appendices A, B, C and D. All formulas are given in SI units.

2. Theoretical fundamentals

This chapter presents a brief introduction to micromagnetics (Section 2.1), especially focussing on hybrid FEM/BEM, a method commonly used to compute the magnetostatic interaction in FE-based micromagnetic codes (Section 2.2), but also in FD based codes [48]. Finally, hierarchical matrices will be introduced, which can be used to increase the efficiency of hybrid FEM/BEM (Section 2.3).

2.1. Basic micromagnetics

Micromagnetics (also known as micromagnetism) is a phenomenological theory of ferromagnetic materials. While a relatively simple theory, it correctly describes a wide range of phenomena occurring in ferromagnetic materials. For example, it allows for the numerical computation of the properties of hysteresis and realistic domain structures of, in principle, arbitrary ferromagnetic structures. The increasing capabilities of modern computers also enhance its range of applications (e.g. larger structures can be investigated), so that a growth in the popularity of the model can still be expected. As only a brief overview of the theory of micromagnetics is possible, the reader is referred to the corresponding literature for a more detailed account (see for example [24, 49, 50]).

2.1.1. Magnetisation

We approach magnetism on a mesoscopic level, i.e. instead of looking at the magnetic moments μ_i of each atom i , we introduce the magnetisation \vec{M} by taking a spatial average over the atomic moments:

$$\vec{M}(\vec{r}) = \frac{\sum_{i \in V} \mu_i}{V}. \quad (2.1)$$

The sum over i runs over all atoms of a certain volume V . The volume V has to be large in comparison with atomic dimensions, so that atomic effects (for example thermal fluctuations and the quantisation of magnetic moments) can be

2. Theoretical fundamentals

neglected. Atomic length scales lie in the range of 1 \AA , so that $V \gg 1 \text{ \AA}^3$ should hold. On the other hand, an averaging, as in equation (2.1), also leads to a reduction in the number of degrees of freedom of the system, so that the physics will be influenced by a too large value for V . In micromagnetics, different material-dependent length scales exist, which yield the dimension of the system's smallest occurring features [51]. Typically these length scales lie in the range of several nanometres, so that we can estimate the upper bound of V by $V \lesssim 1 \text{ nm}^3$. At the relevant micromagnetic length scales ($\gtrsim 10 \text{ nm}$), it is then pertinent to consider the magnetisation as a continuous, three-dimensional vector field (as in equation (2.1)), which is defined in each point in space. The magnetisation defines the magnetic state of a structure. Therefore, it is the aim of many theoretical studies to compute the magnetisation, and thus find the magnetic state for different magnetic systems (ferromagnetic systems, ferrimagnetic systems and anti-ferromagnetic systems). Those computations are often based on the micromagnetic model, that will be introduced in the next chapter.

2.1.2. The micromagnetic model

The micromagnetic model was established by Brown [24]. It introduces different energetic contributions, which act as a torque upon $\vec{M}(\vec{r})$. These energetic contributions are typically from magnetocrystalline anisotropy, exchange interaction, magnetostatic interaction and an externally applied magnetic field. We will introduce these contributions as follows and give corresponding energetic expressions. If required, the model can be extended by adding further contributions, such as magnetoelastic and thermal energies (see for example [50]).

Exchange energy

The exchange interaction is a quantum mechanical effect, which arises from the wave character of electrons. It leads to an additional term in the energy (exchange energy), which does not have any classical equivalent. The continuum expression for the exchange energy was derived by Landau and Lifshitz [52]. It reads:

$$E_{\text{ex}} = \int_V \frac{A}{M_S^2} ((\nabla M_x)^2 + (\nabla M_y)^2 + (\nabla M_z)^2) dV. \quad (2.2)$$

The exchange constant A and the saturation magnetisation M_S are material dependent parameters. Since A is positive-definite, the exchange term always

tries to minimise the spatial variation of the magnetisation vector $\vec{M}(\vec{r})$, i.e. it aligns the magnetisation homogeneously. Thus, the exchange term acts as a glue, which leads to a spatial coupling of the magnetisation. The magnetism in exchange-coupled systems (ferromagnetic, ferrimagnetic and anti-ferromagnetic systems) is usually much stronger than in systems where the exchange coupling is absent (dia and paramagnetic systems).

Magnetocrystalline anisotropy energy

Magnetocrystalline anisotropy is an intrinsic property of a magnetic material. Its origin lies in quantum mechanical spin-orbit interaction, which defines a coupling between the orbital angular momentum and the spin of an electron in the atomic shell. As a consequence, the electronic spins couple to the electronic structure of the lattice. Since an electronic angular momentum produces an equivalent magnetic moment, this leads to magnetic anisotropy. The calculation of magnetocrystalline anisotropy from first principles has not led to a satisfactory agreement with experimental data [53, 54], so that the effect is not yet fully understood. The symmetry of magnetocrystalline anisotropy reflects the symmetry of the crystal. That is to say that crystals with a cubic lattice (e.g. Iron and Nickel) exhibit cubic magnetic anisotropy and crystals with a hexagonal lattice (e.g. Cobalt) uni-axial magnetic anisotropy. In the case of uni-axial anisotropy, the following phenomenological expression for anisotropy energy is often used, which follows from a simple Taylor expansion, where higher order terms are neglected:

$$E_{\text{anis}} = \int_V \frac{K}{M_S^2} (\vec{M} \cdot \vec{e})^2 dV. \quad (2.3)$$

Here, K is the first magnetocrystalline anisotropy constant. In the case of $K < 0$, equation (2.3) energetically favours an alignment of the magnetisation vector \vec{M} along the the unit vector \vec{e} , which is therefore also called the direction of the easy axis. Conversely, for a positive value of K the anisotropy energy is minimised when the magnetisation lies in the plane, whose normal vector \hat{n} is given by \vec{e} . So, instead of an easy axis, the magnetocrystalline anisotropy defines an easy plane.

Magnetostatic energy

We introduce the demagnetisation field \vec{H}_{demag} , which is generated by the magnetisation $\vec{M}(\vec{r})$. In this sub-section, it is assumed that this is the only contribution to the total magnetic field \vec{H}_{tot} . Then, from basic electrodynamics, we know the relation between the magnetisation \vec{M} , the demagnetization

2. Theoretical fundamentals

field \vec{H}_{demag} and the magnetic flux density \vec{B} :

$$\vec{B} = \mu_0(\vec{H}_{\text{demag}} + \vec{M}). \quad (2.4)$$

We infer from Gauss' law of magnetism:

$$\nabla \cdot \vec{B} = 0 \implies \nabla \cdot \vec{H}_{\text{demag}} = -\nabla \cdot \vec{M}. \quad (2.5)$$

Furthermore, we assume that there are no free currents ($\vec{j} = 0$) and the electric displacement field \vec{D} does not change over time, so that Ampère's circuital law reads

$$\nabla \times \vec{H}_{\text{demag}} = 0. \quad (2.6)$$

Therefore, a magnetic scalar potential $\phi(\vec{r})$ can be introduced by:

$$\vec{H}_{\text{demag}} = -\nabla\phi. \quad (2.7)$$

ϕ is the solution of Poisson's equation:

$$\nabla^2\phi = -\rho_M, \quad (2.8)$$

the effective magnetic charge density ρ_M being:

$$\rho_M = -\nabla \cdot \vec{M}. \quad (2.9)$$

Let the finite region \mathcal{R}_m describe the extent of a ferromagnetic material, that contains a magnetisation with a constant magnitude $|\vec{M}| = M_S$. Outside of \mathcal{R}_m , the magnetisation vanishes, i.e. $|\vec{M}| = 0$. We will refer to the latter region as the vacuum region \mathcal{R}_v . Due to the finiteness of \mathcal{R}_m , the demagnetisation field will approach zero when $|\vec{r}| \rightarrow \infty$, i.e.

$$\lim_{|\vec{r}| \in \mathcal{R}_v \rightarrow \infty} |\vec{H}_{\text{demag}}| = 0.$$

Thus, the potential ϕ has to be constant at $|\vec{r}| \rightarrow \infty$. One usually chooses

$$\lim_{|\vec{r}| \in \mathcal{R}_v \rightarrow \infty} \phi = 0, \quad (2.10)$$

which defines an open boundary condition for ϕ , i.e. a boundary condition at $|\vec{r}| \rightarrow \infty$. Furthermore, using equation 2.5 and the divergence theorem of vector calculus we find a jump in the normal derivative of ϕ at ∂R :

$$\lim_{\vec{r} \in \mathcal{R}_v \rightarrow \partial R} \frac{\partial \phi}{\partial \hat{n}} - \lim_{\vec{r} \in \mathcal{R}_m \rightarrow \partial R} \frac{\partial \phi}{\partial \hat{n}} = -\hat{n} \cdot \vec{M}, \quad (2.11)$$

with \hat{n} being the local normal vector of the boundary ∂R . By employing Stokes' theorem and equation (2.6), one can readily show that:

$$\begin{aligned}\hat{t} \cdot \nabla \phi &= \hat{t} \cdot \vec{H}_{\text{demag}} \quad \text{for } \vec{r} \in \mathcal{R}_m \rightarrow \partial R \\ &= \hat{t} \cdot \vec{H}_{\text{demag}} \quad \text{for } \vec{r} \in \mathcal{R}_v \rightarrow \partial R,\end{aligned}\tag{2.12}$$

where \hat{t} is a unit vector in the local tangent plane of ∂R , i.e. $\hat{n} \perp \hat{t}$. Therefore, we find that on the sub-space ∂R :

$$\lim_{\vec{r} \in \mathcal{R}_m \rightarrow \partial R} \phi = \lim_{\vec{r} \in \mathcal{R}_v \rightarrow \partial R} \phi + C$$

holds. One usually sets C to zero, so that ϕ is continuous over ∂R . Using these boundary conditions and Green's second identity (equation (A.4) in Appendix A), the following expression for ϕ is readily derived [55]:

$$\phi(\vec{r}) = \frac{1}{4\pi} \int_{\mathcal{R}_m} \frac{\nabla \cdot \vec{M}(\vec{R})}{|\vec{r} - \vec{R}|} d^3 R + \frac{1}{4\pi} \oint_{\partial R} \frac{\hat{n}(\vec{R}) \cdot \vec{M}(\vec{R})}{|\vec{r} - \vec{R}|} d^2 R.\tag{2.13}$$

So beside a term due to the effective magnetic-charge density, one obtains another term arising from an effective magnetic surface-charge density:

$$\sigma_M = \hat{n} \cdot \vec{M}.\tag{2.14}$$

Note that a surface charge term does not occur in Coulomb's law of electrostatics. This is due to the fact that, unlike equation (2.9), the charge density cannot be written as the divergence of a vector field. The energy of the magnetisation in its own demagnetisation field is given by:

$$E_{\text{demag}} = -\frac{1}{2} \int_{\mathcal{R}_m} \vec{M}(\vec{r}) \cdot \vec{H}_{\text{demag}}(\vec{r}) d^3 r.\tag{2.15}$$

Here the factor $1/2$ avoids a double-counting of the magnetostatic energy contribution between two points, \vec{r} and \vec{R} within \mathcal{R}_m .

Zeeman energy

When applying an external magnetic field \vec{H}_{ext} , the total Zeeman energy of the magnetisation $\vec{M}(\vec{r})$ is given by:

$$E_H = - \int_{\mathcal{R}_m} \vec{H}_{\text{ext}}(\vec{r}) \cdot \vec{M}(\vec{r}) d^3 r.\tag{2.16}$$

2. Theoretical fundamentals

2.1.3. Brown's equation

Adding all energy contributions of the micromagnetic model together, an expression for the functional of free energy is obtained:

$$\begin{aligned}
F[\vec{M}(\vec{r})] = \int_{\mathcal{R}_m} & \left(\frac{A}{M_S^2} ((\nabla M_x)^2 + (\nabla M_y)^2 + (\nabla M_z)^2) \right. \\
& + \frac{K}{M_S^2} (\vec{M}(\vec{r}) \cdot \vec{e})^2 \\
& + \frac{1}{2} \vec{M}(\vec{r}) \cdot \vec{H}_{\text{demag}}(\vec{r}) \\
& \left. + \vec{H}_{\text{ext}}(\vec{r}) \cdot \vec{M}(\vec{r}) \right) d^3r.
\end{aligned} \tag{2.17}$$

If using $\vec{M}(\vec{r}) = M_S \vec{m}(\vec{r})$ (with $|\vec{m}(\vec{r})| = 1$), varying the free energy F with respect to $\vec{m}(\vec{r})$ and set the result equal to zero, Brown's equations [56] are obtained:

$$\begin{aligned}
\vec{m}(\vec{r}) \times (2A\Delta\vec{m}(\vec{r}) + 2K(\vec{m}(\vec{r}) \cdot \vec{e})\vec{e} + M_S\vec{H}_{\text{ext}} + M_S\vec{H}_{\text{demag}}) &= 0 \\
\left. \frac{\partial \vec{m}}{\partial \hat{n}} \times \vec{m} \right|_{\partial R} &= 0.
\end{aligned} \tag{2.18}$$

We define the effective field \vec{H}_{eff} as:

$$\vec{H}_{\text{eff}} = \underbrace{\frac{2A}{M_S} \Delta\vec{m}(\vec{r})}_{\vec{H}_{\text{exch}}} + \underbrace{\frac{2K}{M_S} (\vec{m}(\vec{r}) \cdot \vec{e})\vec{e}}_{\vec{H}_{\text{anis}}} + \vec{H}_{\text{ext}} + \vec{H}_{\text{demag}}. \tag{2.19}$$

Furthermore, one can readily show that the vectors \vec{m} and $\frac{\partial \vec{m}}{\partial \hat{n}}$ are orthogonal, so that Brown's equations (2.18) read:

$$\begin{aligned}
\vec{m}(\vec{r}) \times \vec{H}_{\text{eff}} &= 0 \\
\left. \frac{\partial \vec{m}}{\partial \hat{n}} \right|_{\partial R} &= 0.
\end{aligned} \tag{2.20}$$

The first equation states that the system is in an equilibrium state when the torque, exerted by the effective field $\vec{H}_{\text{eff}}(\vec{r})$ on $\vec{M}(\vec{r})$, disappears. Equivalently, one could say that an equilibrium is reached when the magnetisation aligns with the local effective field. The second equation specifies the boundary conditions on ∂R .

2.1.4. The Landau-Lifshitz-Gilbert equation

In the last section the Brown equation was introduced (2.18). Physically this equation states that, in order to reach thermodynamic equilibrium, $\vec{M}(\vec{r})$ has to be relaxed, such that, for each \vec{r} , it is parallel to the effective magnetic field $\vec{H}_{\text{eff}}(\vec{r})$, introduced in equation (2.19). To relax the magnetisation (or magnetic moment) in an external magnetic field, the Landau-Lifshitz equation, which was derived in 1935 [52], can be used. However, this equation is said to be unphysical, in the sense that it was tailored just for the sake of reaching the correct final state [57, 58, 59]. A physically more realistic approach is to use Gilbert's equation [57]:

$$\frac{d\vec{M}(\vec{r})}{dt} = -\gamma\vec{M}(\vec{r}) \times \vec{H}(\vec{r}) + \frac{\alpha}{M_S}\vec{M}(\vec{r}) \times \frac{d\vec{M}(\vec{r})}{dt}. \quad (2.21)$$

The first term on its right-hand side describes the precession of the magnetisation around the magnetic field \vec{H} . The gyromagnetic ratio γ is a microscopic constant, which determines the ratio between the magnetic moment and the angular momentum of an electron. The second term reflects the damping towards thermodynamic equilibrium. Here, the parameter α is the phenomenological Gilbert damping constant. It has to be derived from experiments. One can easily reformulate the Gilbert equation into a form equivalent to the Landau-Lifshitz equation:

$$\frac{d\vec{M}(\vec{r})}{dt} = -\frac{\gamma}{1+\alpha^2}\vec{M}(\vec{r}) \times \vec{H}(\vec{r}) - \frac{\alpha\gamma}{M_S(1+\alpha^2)}\vec{M}(\vec{r}) \times (\vec{M}(\vec{r}) \times \vec{H}(\vec{r})). \quad (2.22)$$

This equation is usually called the Landau-Lifshitz-Gilbert equation. Compared to the Gilbert equation (2.21), it is numerically more convenient to handle, since the time-derivative of the magnetisation appears just on the left-hand side of the equation. By replacing \vec{H} with the effective magnetic field \vec{H}_{eff} of equation (2.19), a partial differential equation is obtained, which has to be solved within the micromagnetic model. The numerical solution requires a discretisation in space and time. Different approaches for spatial discretisation have to be undertaken when using the finite difference method (FDM) (see for example [38, 60, 25]) or the finite element method (FEM): FDM is based on a cuboidal mesh and FEM on an unstructured (in most cases tetrahedral) mesh. This work mainly focusses on the latter method. As we do not address the technical details of FEM and time integration, the interested readers are referred to [61, 62, 59, 63, 64]. In the next section, a rather specific problem is discussed. It deals with the so called open boundary problem, which arises when computing the demagnetisation field \vec{H}_{demag} in FE based micromagnetics.

2.2. Hybrid FEM/BEM

The computation of the magnetic scalar potential ϕ of equation (2.13) is the numerically most challenging part of computational micromagnetics. A direct discretisation of the integral equation (2.13) is numerically expensive, since the operation scales quadratically with the number of discretisation nodes N . Instead, a start is made from the local formulation of the problem, which is given by Poisson's equation (see also equation (2.8)):

$$\nabla^2 \phi(\vec{r}) = \begin{cases} \nabla \cdot \vec{M}(\vec{r}) & \text{for } \vec{r} \in \mathcal{R}_m \\ 0 & \text{for } \vec{r} \in \mathcal{R}_v \end{cases}. \quad (2.23)$$

The scalar potential has to be continuous at the boundary ∂R between \mathcal{R}_m and \mathcal{R}_v , i.e. with $\vec{r}_m \in \mathcal{R}_m$, $\vec{r}_v \in \mathcal{R}_v$, and $\vec{r} \in \partial R$:

$$\Delta \phi(\vec{r}) = \lim_{\vec{r}_v \rightarrow \vec{r}} \phi(\vec{r}_v) - \lim_{\vec{r}_m \rightarrow \vec{r}} \phi(\vec{r}_m) = 0, \quad (2.24)$$

while its normal derivative is discontinuous:

$$\Delta \left(\frac{\partial \phi(\vec{r})}{\partial \hat{n}} \right) = \lim_{\vec{r}_v \rightarrow \vec{r}} \frac{\partial \phi(\vec{r}_v)}{\partial \hat{n}} - \lim_{\vec{r}_m \rightarrow \vec{r}} \frac{\partial \phi(\vec{r}_m)}{\partial \hat{n}} = -\hat{n} \cdot \vec{M}(\vec{r}). \quad (2.25)$$

Furthermore the potential needs to disappear at infinity, i.e.:

$$\phi(\vec{r}) \rightarrow 0 \quad \text{for } |\vec{r}| \rightarrow \infty. \quad (2.26)$$

Equations (2.23-2.26) define a mathematical problem with boundary conditions at infinity, the so called open boundary problem. For arbitrary ferromagnetic regions \mathcal{R}_m FEM is the best suited method for a numerical solution. However, the fact that the solution domain is infinite implies that one cannot solve the problem with conventional FEM, which is a finite-domain method. There are different techniques available that allow for tackling such an open boundary problem (for an overview see for example [65]). The simplest approach is to perform a truncation of the domain at a selectable outer boundary in the vacuum region. Provided that it is sufficiently far away, one can assume that the potential on the boundary is approximately zero, allowing for the use of a conventional finite element method on the reduced domain. In order to obtain decent numerical results, the dimension of the meshed region should exceed that of the magnetic region by a factor of about 5, with respect to any direction in space [65, 59]. Besides the fact that the corresponding discretisation matrix can become relatively large, this method also poses some technical problems concerning the meshing of the different regions (magnetic and vacuum region). The current standard approach for computing the magnetostatic

scalar potential is a hybrid finite element method / boundary element method (FEM/BEM), which was introduced by Fredkin and Koehler [66]. Its basic idea is to restructure the problem defined by equations (2.23-2.26), such that it decomposes into a Poisson equation in a finite domain (which corresponds to the ferromagnetic region \mathcal{R}_m), and a Laplace equation defined on the entire space. The former equation can then be solved by applying FEM, while BEM is used to solve the Laplace equation. Two different realisations of hybrid FEM/BEM exist. The first was proposed in the original paper [66], and is widely used in state-of-the-art micromagnetic finite element codes. The second realisation has recently been proposed by García-Cervera and Roma and is said to be numerically better behaved [48]. Both methods are discussed, starting with the original Fredkin and Koehler approach.

2.2.1. The Fredkin-Koehler approach

The idea is to split the magnetic potential ϕ as defined in equation (2.23) into two contributions, ϕ_1 and ϕ_2 :

$$\phi = \phi_1 + \phi_2. \quad (2.27)$$

ϕ_1 is assumed to be the solution of the inhomogeneous Neumann problem:

$$\Delta\phi_1 = \nabla\vec{M}(\vec{r}) \quad (2.28)$$

with

$$\frac{\partial\phi_1(\vec{r})}{\partial\hat{n}} = \hat{n} \cdot \vec{M}(\vec{r}) \quad (2.29)$$

on ∂R . Within the vacuum region \mathcal{R}_v one defines $\phi_1(\vec{r}) = 0$. In order to comply with equations (2.23-2.26), ϕ_2 has to be the solution of Laplace's equation:

$$\Delta\phi_2(\vec{r}) = 0. \quad (2.30)$$

At the boundary ∂R between the magnetic and vacuum domain, ϕ_2 has a discontinuity of:

$$\Delta\phi_2(\vec{r}) = \lim_{\vec{r}_v \rightarrow \vec{r}} \phi_2(\vec{r}_v) - \lim_{\vec{r}_m \rightarrow \vec{r}} \phi_2(\vec{r}_m) = \phi_1(\vec{r}), \quad (2.31)$$

and its normal-derivative is continuous. At infinity, $\phi_2(\vec{r})$ has to disappear, i.e.:

$$\phi_2(\vec{r}) \rightarrow 0 \quad \text{for} \quad |\vec{r}| \rightarrow \infty. \quad (2.32)$$

So, the open boundary problem is rewritten, such that there are two different mathematical problems to deal with. First, equations (2.28) and (2.29) define a

2. Theoretical fundamentals

Poisson equation in a finite domain, something which can be straight-forwardly solved with conventional FEM. The open boundary character of the problem is included in the set of equations (2.30-2.32). However, the crucial difference to our original problem is that we dispensed with inhomogeneity, i.e. we replaced the Poisson equation (2.23) by the Laplace equation (2.30). BEM is a standard technique to solve Laplace's equation, and, applying it to equations (2.30-2.26) yields the following integral equation (see Appendix A):

$$\phi_2(\vec{R}) = \frac{1}{4\pi} \int_{\partial R} \phi_1(\vec{r}) g(\vec{r}, \vec{R}) d^2r. \quad (2.33)$$

The part of the integrand that depends only on the integration variable is called the source of the integral. In this case, the source is the potential ϕ_1 , so that ϕ_2 can be retrieved from knowledge of ϕ_1 on the boundary ∂R between \mathcal{R}_m and \mathcal{R}_v . The kernel is the part of the integrand that depends on the integration variable \vec{r} and the variable \vec{R} in the solution space. It defines the correlation between the integration space and the solution space. Here, the kernel is the classical double layer potential:

$$g(\vec{r}, \vec{R}) = \frac{(\vec{R} - \vec{r}) \cdot \hat{n}(\vec{r})}{|\vec{R} - \vec{r}|^3}. \quad (2.34)$$

As before, the vector $\hat{n}(\vec{r})$ is the local normal vector on the surface ∂R . In micromagnetics we usually only need to compute the magnetic scalar potential ϕ within the ferromagnetic region \mathcal{R}_m . Therefore the solution domain of equation (2.33) corresponds to \mathcal{R}_m , while the integration domain is the interface ∂R . Assuming that we discretise the ferromagnetic region \mathcal{R}_m on a mesh with N volume nodes, the boundary ∂R will be discretised on a surface mesh of about $N_s \propto O(N^{2/3})$ surface nodes. The matrix resulting from our discretisation of equation (2.33) will therefore have $\propto O(N)$ rows and $\propto O(N^{2/3})$ columns, so that its size and therefore the general numerical complexity scales with $O(N^{5/3})$. Note that the FEM part of the hybrid FEM/BEM scales with $O(N)$, so that the BEM part turns out to be the limiting factor for the performance of the algorithm. However, the computational cost can be reduced by restricting the solution domain of the integral equation to the boundary ∂R . For this, the limit $\vec{R} \in \mathcal{R}_m \rightarrow \partial R$ of equation (2.33) needs to be taken from the side of the ferromagnetic region \mathcal{R}_m , turning the integral into (see also Appendix A):

$$\phi_2(\vec{R}) = \frac{1}{4\pi} \int_{\partial R} \phi_1(\vec{r}) \frac{(\vec{R} - \vec{r}) \cdot \hat{n}(\vec{r})}{|\vec{R} - \vec{r}|^3} d^2r + \left(\frac{\Omega(\vec{R})}{4\pi} - 1 \right) \phi_1(\vec{R}). \quad (2.35)$$

The appearance of the additional diagonal term in equation (2.35) is due to the discontinuity of the integral in equation (2.33) over the boundary ∂R . The integral needs to have this discontinuity property in order to comply with equation (2.31). The variable $\Omega(\vec{R})$ in (2.35) is defined as follows: let \vec{r} be a reference point within the ferromagnetic region \mathcal{R}_m , \vec{R} a point on the boundary ∂R and $\partial R(\vec{R})$ the local neighbourhood of ∂R around \vec{R} . Let us now take the limit $\vec{r} \rightarrow \vec{R}$. Then, $\Omega(\vec{R})$ is the solid angle covered by $\partial R(\vec{R})$ with respect to \vec{r} . As before, the complexity of the matrix-vector equation arising from the discretisation of (2.35) can be estimated and one finds that the matrix size scales with $O(N^{4/3})$ (N = number of volume nodes). From the discretisation, only values for the potential ϕ_2 on the boundary ∂R are obtained. However, one can use these values as Dirichlet boundary conditions in order to solve Laplace's equation (2.30) for ϕ_2 within the ferromagnetic region \mathcal{R}_m with FEM.

2.2.2. The García-Cervera-Roma approach

The method proposed by García-Cervera and Roma [48] is very similar to the approach presented in Sub-section 2.2.1. Therefore, we will not discuss all its details, but just stress the differences with the Fredkin-Koehler approach. The starting point is the open boundary problem, as defined in equations (2.23-2.26). As before, the magnetic scalar potential ϕ is split into the sum of two potential ϕ_a and ϕ_b . However, the definitions of ϕ_a and ϕ_b are different. ϕ_a is the solution of the inhomogeneous Dirichlet problem defined by:

$$\Delta \phi_a = \nabla \vec{M}(\vec{r}), \quad (2.36)$$

with

$$\phi_a(\vec{r}) = 0 \quad (2.37)$$

on ∂R . Within the vacuum domain \mathcal{R}_v $\phi_a(\vec{r})$ is set to 0. As in Sub-section 2.2.1, ϕ_a can be obtained by FEM. The second potential ϕ_b is then defined by Laplace's equation:

$$\Delta \phi_b(\vec{r}) = 0. \quad (2.38)$$

At the boundary ∂R between the magnetic and vacuum domain, the normal derivative of ϕ_b has a discontinuity of:

$$\Delta \left(\frac{\partial \phi_b(\vec{r})}{\partial \hat{n}} \right) = \lim_{\vec{r}_v \rightarrow \vec{r}} \phi_b(\vec{r}_v) - \lim_{\vec{r}_m \rightarrow \vec{r}} \phi_b(\vec{r}_m) = -\hat{n} \cdot \vec{M}(\vec{r}) + \frac{\partial \phi_a(\vec{r})}{\partial \hat{n}}, \quad (2.39)$$

2. Theoretical fundamentals

while the potential itself is continuous. At infinity $\phi_b(\vec{r})$ has to disappear, i.e.:

$$\phi_b(\vec{r}) \rightarrow 0 \quad \text{for} \quad |\vec{r}| \rightarrow \infty. \quad (2.40)$$

As discussed in the previous section, the problem posed by equations (2.38-2.40) can be solved with BEM. The following integral equation for ϕ_b can be obtained:

$$\phi_b(\vec{R}) = \frac{1}{4\pi} \int_{\partial R} \frac{q(\vec{r})}{|\vec{R} - \vec{r}|} d^2r, \quad (2.41)$$

with

$$q(\vec{r}) = -\hat{n} \cdot \vec{M}(\vec{r}) + \frac{\partial \phi_a(\vec{r})}{\partial \hat{n}}. \quad (2.42)$$

Due to the performance issues discussed in Sub-section 2.2.1, equation (2.41) is not used to compute the potential ϕ_b for the entire ferromagnetic region \mathcal{R}_m . Instead, it is only used to compute ϕ_b on ∂R , yielding the Dirichlet boundary conditions for solving the Laplace equation (2.38) within \mathcal{R}_m with FEM. Note that, due to the continuity of ϕ_b , there is no need to take a formal, mathematical limit as in Sub-section 2.2.1. In the literature, the kernel of equation (2.41) is:

$$g(\vec{R}, \vec{r}) = \frac{1}{|\vec{R} - \vec{r}|}, \quad (2.43)$$

referred to as the classical single layer potential.

2.2.3. Discretisation of the integral equation

In order to apply a hybrid FEM/BEM, it is necessary to discretise either equation (2.35) or (2.41) (see discussion in Section 2.2.1). For a demonstrative discussion of discretisation procedures, we consider equation (2.41):

$$\phi_b(\vec{R}) = \frac{1}{4\pi} \int_{\partial R} \frac{q(\vec{r})}{|\vec{R} - \vec{r}|} d^2r.$$

The integration space as well as the solution space of this integral equation correspond to the boundary ∂R . Therefore, one first creates a surface mesh (in most cases: a triangular surface mesh) on ∂R , which defines a set of nodal points $\{i\}$. Then we locally expand the source of the integral, i.e. $q(\vec{r})$, in terms of a set of basis functions $\psi_j(\vec{r})$, with local supports Ω_j around the nodal points:

$$q(\vec{r}) = \sum_j q(\vec{r}_j) \psi_j(\vec{r}). \quad (2.44)$$

The potential ϕ_b is evaluated at the nodal points \vec{R}_i , so that the integral equation turns into a system of equations:

$$\phi_b(\vec{R}_i) = \sum_j \frac{1}{4\pi} \int_{\Omega_j} \frac{\psi_j(\vec{r})}{|\vec{R}_i - \vec{r}|} d^2r \cdot q(\vec{r}_j). \quad (2.45)$$

For the triangular mesh the local support Ω_j of basis function $\psi_j(\vec{r})$ is the union of those triangles T_{jk} that contain the nodal point \vec{r}_j at one of their corners, i.e. $\Omega_j = \cup_k T_{jk}$. Suppose that the corners of the triangle T_{jk} are, besides \vec{r}_j itself, the neighbouring nodal points \vec{r}_{j+1} and \vec{r}_{j+2} , then a local linear function on T_{jk} can be defined as:

$$\varphi_{jk}(\vec{r}) = \begin{cases} \frac{\det(\vec{r}, \vec{r}_{j+1}, \vec{r}_{j+2})}{\det(\vec{r}_j, \vec{r}_{j+1}, \vec{r}_{j+2})}, & \text{if } \vec{r} \in T_{jk} \\ 0, & \text{else} \end{cases}. \quad (2.46)$$

This definition implies $\varphi_{jk}(\vec{r}_j) = 1$ and $\varphi_{jk}(\vec{r}_{j+1}) = \varphi_{jk}(\vec{r}_{j+2}) = 0$. The local basis functions $\psi_j(\vec{r})$ are then defined as the sum over all triangle functions:

$$\psi_j(\vec{r}) = \sum_k \varphi_{jk}(\vec{r}). \quad (2.47)$$

For a graphical visualisation of the functions $\psi_j(\vec{r})$ and $\varphi_{jk}(\vec{r})$ see for example page 20 of [62]. With the definition (2.47) equation (2.45) can be rewritten as:

$$\phi_b(\vec{R}_i) = \sum_{jk} \frac{1}{4\pi} \int_{T_{jk}} \frac{\varphi_{jk}(\vec{r})}{|\vec{R}_i - \vec{r}|} d^2r \cdot q(\vec{r}_j). \quad (2.48)$$

This equation can also be written as a vector equation:

$$\Phi_b = \mathbf{B} \cdot \mathbf{Q}. \quad (2.49)$$

The vectors Φ_b and \mathbf{Q} contain the corresponding potential values ϕ_b and q at the sites of the surface mesh. The elements B_{ij} of the boundary element matrix \mathbf{B} are defined as:

$$B_{ij} = \frac{1}{4\pi} \int_{\Omega_j} \frac{\psi_j(\vec{r})}{|\vec{R}_i - \vec{r}|} d^2r = \frac{1}{4\pi} \sum_k \int_{T_{jk}} \frac{\varphi_{jk}(\vec{r})}{|\vec{R}_i - \vec{r}|} d^2r. \quad (2.50)$$

Analogously one can define the vector equation for the double layer equation (2.35) within the Fredkin-Koehler approach:

$$\Phi_2 = \mathbf{B} \cdot \Phi_1, \quad (2.51)$$

2. Theoretical fundamentals

with

$$B_{ij} = \frac{1}{4\pi} \int_{\Omega_j} \psi_j(\vec{r}) \frac{(\vec{R}_i - \vec{r}) \cdot \hat{n}(\vec{r})}{|\vec{R}_i - \vec{r}|^3} d^2r + \left(\frac{\Omega(\vec{R}_i)}{4\pi} - 1 \right) \delta_{i,j} \quad (2.52)$$

$$= \frac{1}{4\pi} \sum_k \left(\int_{T_{jk}} \varphi_{jk} \frac{(\vec{R}_i - \vec{r}) \cdot \hat{n}(\vec{r})}{|\vec{R}_i - \vec{r}|^3} d^2r \right) + \left(\frac{\Omega(\vec{R}_i)}{4\pi} - 1 \right) \delta_{i,j} \quad (2.53)$$

The difficult part when calculating the elements B_{ij} of the boundary element matrix is the evaluation of the integrals of the triangles T_{jk} , especially for the case $i = j$, where the integral becomes singular. This integration can either be done numerically, or an analytical formula can be used. The latter is introduced in Sub-section 2.2.4. A general disadvantage of BEM, which also holds in our case, is that the boundary element matrix \mathbf{B} is dense and non-symmetric. As a result, we have to store a matrix that scales quadratically with the number of surface nodes N_s . Therefore, the hybrid FEM/BEM becomes numerically expensive for the study of structures with a large number of surface nodes.

2.2.4. The Lindholm-formula

When computing the elements of the boundary element matrix \mathbf{B} , integrals of the form:

$$(a) K_{T,k} = \int_T \frac{\varphi_{Tk}(\vec{r})}{|\vec{R} - \vec{r}|} d^2r \quad \text{or} \quad (b) L_{T,k} = \int_T \varphi_{Tk}(\vec{r}) \frac{(\vec{R} - \vec{r}) \cdot \hat{n}(\vec{r})}{|\vec{R} - \vec{r}|^3} d^2r,$$

need to be evaluated. The index T refers to the triangle over which the integral is computed, and the index k runs over the three vertices of T . The linear basis function $\varphi_{Tk}(\vec{r})$ is of the type defined in equation (2.46), i.e. it is 1 at the site of vertex k , and 0 at the other two vertex points. Based on preliminary work by van Herk [67], Lindholm derived analytical expressions for $L_{T,k}$ and $K_{T,k}$ [68]. Using his notation, the single layer potential $K_{T,k}$ can be written as:

$$K_{T,i} = \frac{\eta_{i+1}s_{i+1}}{8\pi A_T} \left(\zeta \Omega_T + \sum_{j=1}^3 \eta_j P_j \right) - \frac{s_{i+1}}{8\pi A_T} \sum_{j=1}^3 \gamma_{ij} ((\zeta^2 + \eta_j^2) P_j + s_j^2 Q_j), \quad (2.54)$$

and the double layer potential $L_{T,i}$ reads:

$$L_{T,i} = \frac{s_{i+1}}{8\pi A_T} \left(\eta_{i+1} \Omega_T - \zeta \sum_{j=1}^3 \gamma_{ij} P_j \right). \quad (2.55)$$

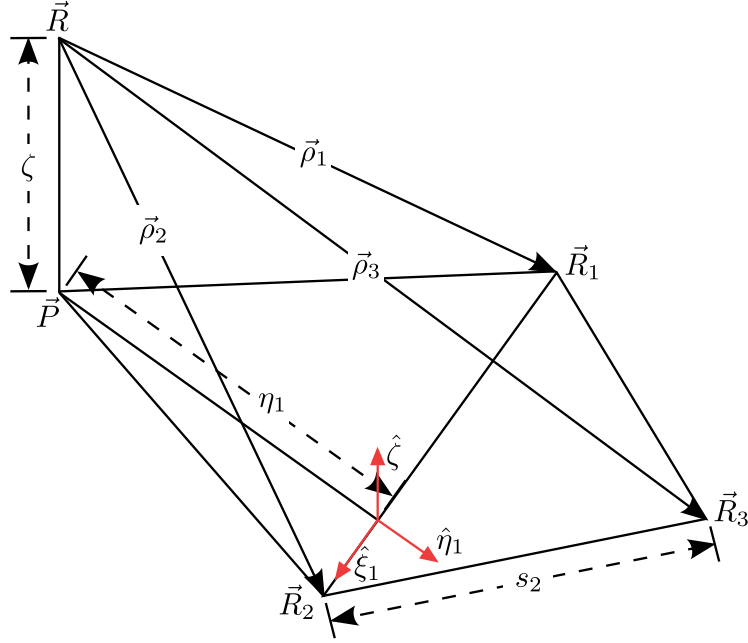


Figure 2.1.: Graphical illustration of variables used in the Lindholm formula: the triangle vertices are \vec{R}_1 , \vec{R}_2 , and \vec{R}_3 , the observation point is \vec{R} . For each side of the triangle, a local coordinate system $\hat{\xi}_i$, $\hat{\eta}_i$, ζ is defined (only illustrated for $i = 1$). The point \vec{P} is the projection of \vec{R} onto the triangle plane.

The symbols occurring in those equations are defined as follows: as shown in Figure 2.1 the unit vector $\hat{\zeta}$ is the normal vector of the triangle T . We also define a unit vector $\hat{\xi}_i$, which is parallel to a side i . We complete the local tripod for each side i by introducing a third unit vector $\hat{\eta}_i = \hat{\zeta} \times \hat{\xi}_i$. The vectors $\vec{\rho}_i$ are defined as $\vec{\rho}_j = \vec{R}_j - \vec{R}$, i.e. it is the difference vector between the position of the j th vertex of the triangle and the observation point \vec{R} . Furthermore we write the projections of $\vec{\rho}_j$ onto the unit vectors $\hat{\eta}_i$ and ζ as:

$$\begin{aligned} \eta_i &= \hat{\eta}_i \cdot \vec{\rho}_i \\ \zeta &= \hat{\zeta} \cdot \vec{\rho}_i, \quad \text{the same result for } i = 1, 2, 3. \end{aligned}$$

The length of a triangle side is given by:

$$s_j = |\vec{\rho}_{j+1} - \vec{\rho}_j| = |\vec{R}_{j+1} - \vec{R}_j|.$$

The solid angle Ω_T , which is covered by the triangle T with respect to the observation point \vec{R} , is computed by using:

$$\Omega_T = 2 \operatorname{sgn}(\zeta) \arccos \left(\frac{\rho_1 \rho_2 \rho_3 + \rho_1 \vec{\rho}_2 \cdot \vec{\rho}_3 + \rho_2 \vec{\rho}_3 \cdot \vec{\rho}_1 + \rho_3 \vec{\rho}_1 \cdot \vec{\rho}_2}{\sqrt{2(\rho_2 \rho_3 + \vec{\rho}_2 \cdot \vec{\rho}_3)(\rho_3 \rho_1 + \vec{\rho}_3 \cdot \vec{\rho}_1)(\rho_1 \rho_2 + \vec{\rho}_1 \cdot \vec{\rho}_2)}} \right).$$

2. Theoretical fundamentals

An alternative, more efficient formulation for the solid angle is proposed in [69]. Furthermore the following definitions are used:

$$\begin{aligned}\gamma_{ij} &= \hat{\xi}_{i+1} \cdot \hat{\xi}_j \\ P_j &= \ln \left(\frac{\rho_j + \rho_{j+1} + s_j}{\rho_j + \rho_{j+1} - s_j} \right) \\ Q_j &= [(\rho_j + \rho_{j+1})/2s_j][(\rho_j - \rho_{j+1})^2/s_j^2 + 1].\end{aligned}$$

2.2.5. Summary

To recapitulate the main conclusions on the hybrid FEM/BEM: the basic idea of the approach is to split the magnetic scalar potential ϕ into the sum of two potentials ϕ_1 and ϕ_2 (see equation (2.27)). ϕ_1 and ϕ_2 can then be computed within the ferromagnetic region \mathcal{R}_m by using a three-step approach.

1. For the computation of ϕ_1 within \mathcal{R}_m a Poisson equation with Neumann (Sub-section 2.2.1) or Dirichlet boundary conditions (Sub-section 2.2.2) is solved. This is usually done by applying the finite element method.
2. From the values of ϕ_1 or its normal derivative on the boundary ∂R , corresponding boundary values for ϕ_2 are derived by discretising the boundary integral equation (2.35) or (2.41), respectively. Having obtained the discretisation matrix, this step only involves the computation of a matrix-vector multiplication.
3. Finally, the finite element method can be used for computing ϕ_2 within \mathcal{R}_m , only needing to solve the Laplace equation (2.30) with those Dirichlet boundary values calculated in step 2.

The main advantage of this method is that only the magnetic region has to be meshed. This is especially useful in the case of simulations where one considers several magnetic bodies that move relative to each other [70, 71]. The maximal storage requirements of the method are due to the storage of the boundary element matrix B which is dense and non-symmetric. When N_s is the number of surface nodes, B has N_s^2 elements. For the study of large magnetic structures with many surface elements, this scaling behaviour still poses an unmanageable problem. In the next section, hierarchical matrices will be introduced. These can be used to improve the efficiency of the method.

2.3. Hierarchical matrices

This section provides brief account of hierarchical matrices. These can be used to approximate dense matrices occurring within the frameworks of the finite element method (FEM) and the boundary element method (BEM). As we use the library HLib [31], which is an implementation of the hierarchical matrix methodology, we will especially follow the corresponding lecture notes [72]. For a more detailed introduction, interested readers are referred to those lecture notes or alternatively to [73, 74, 75].

Hierarchical matrices (or \mathcal{H} -matrices) [74, 75] are data-sparse matrices, which can be used to enhance the efficiency of BEM and FEM by approximating dense matrices. Their application ranges from fields like elasticity [76] to electromagnetism [77, 78, 79] to micromagnetics [70, 80, 81, 82]. The term data-sparse refers to the fact that \mathcal{H} -matrices can be fully described by few matrix elements. This section provides a short introduction to \mathcal{H} -matrices on the basis of the boundary integral equations introduced in the last chapter (see equations (2.35) and (2.41-2.42)). The boundary integrals are of the form:

$$\int_{\partial R} q(\vec{r}) g(\vec{R}, \vec{r}) d^2 r, \quad (2.56)$$

where ∂R is the surface to be integrated over, $q(\vec{r})$ the source function, and $g(\vec{R}, \vec{r})$ the kernel function (see also discussion after equation (2.33)). The discretisation matrix B of this integral can now be approximated by a hierarchical matrix if the following condition is met:

The kernel function $g(\vec{r}, \vec{R})$ has a singularity in the case of $\vec{r} = \vec{R}$, but is well behaved and smooth when $|\vec{r} - \vec{R}|$ is large.

Since this is true for the double (2.35) and the single layer potential (2.41), one can use hierarchical matrices to optimise the Fredkin-Koehler (Sub-section 2.2.1) and the Garcia-Cervera-Roma (Sub-section 2.2.2) approach of hybrid FEM/BEM.

2.3.1. Structure of \mathcal{H} -matrices

Within the \mathcal{H} -matrix approach, a matrix is organised in a hierarchical quadtree. The matrix is split into sub-matrices, which are stored in the leaves of the tree. The following discusses how a hierarchical matrix is created. We start from our surface mesh, which was constructed at the interface between the magnetic region \mathcal{R}_m and the vacuum region \mathcal{R}_v . This mesh is used to discretise

2. Theoretical fundamentals

the integral with respect to the variables \vec{r} and \vec{R} . It is subdivided into clusters of nodes, which in turn are organised in a binary cluster tree. There are different clustering procedures to create such a cluster tree. These are summarised in [72]. Figure 2.2 illustrates the standard geometric clustering procedure. The whole mesh corresponds to the root of the cluster tree. As a first step a bounding box is constructed around the mesh, which is then split into two boxes along the direction of its largest extension. As outlined in Figure 2.2, a geometrical bisection is employed for the splitting process. The nodes within each small box constitute clusters, which are the sons of the root cluster. This process is repeated recursively as long as the number of nodes within the son clusters is larger than a parameter n_{\min} . Besides geometrical bisection, there are alternative techniques for the determination of the sons, e.g. cardinality-based or regular subdivision (see for example Section 2.1 in [72]). Another important aspect with respect to the creation of hierarchical matrices is admissibility. For its introduction, let us consider a cluster Ω_I in the integration space and a cluster Ω_S in the solution space. The mapping between these two clusters is defined by a boundary element matrix, which arises from the discretisation of integral (2.56) on the corresponding nodes and is a sub-matrix of the boundary element matrix arising from the discretisation of the entire mesh. We assume that this sub-matrix can be approximated by a data-sparse approximation, if the distance between the two clusters is sufficiently large and, thus, the kernel in the integral (2.56) is smooth. If this is the case, the two clusters Ω_I and Ω_S are said to be admissible. In order to establish the admissibility of the two clusters, different heuristic admissibility conditions have been introduced (see for example Sub-sections 2.2.2 and 2.2.3 in [72], or Section 3.2 in [75]). The standard admissibility condition reads (see also [73, 72, 75]):

$$\min(\text{diam}(Q_I), \text{diam}(Q_S)) \leq \eta \text{dist}(Q_I, Q_S). \quad (2.57)$$

The symbols $\text{diam}(Q_I)$ and $\text{diam}(Q_S)$ refer to the diameter of the bounding boxes constructed around the clusters Ω_I and Ω_S , respectively. $\text{dist}(Q_I, Q_S)$ refers to the distance between these bounding boxes. These quantities are also graphically illustrated in Figure 2.3. According to equation 2.57, the two clusters will be admissible, if the smaller of the two diagonals of the corresponding bounding boxes is smaller than the product of a heuristic parameter η and the distance between the two boxes. The hierarchical structures of a hierarchical matrix, also called a block cluster tree, is then created as follows: the root clusters are defined in the integration and the solution space (also referred to as column and row cluster, respectively). For hybrid FEM/BEM, these clusters will be the same and contain all nodes on the boundary between the

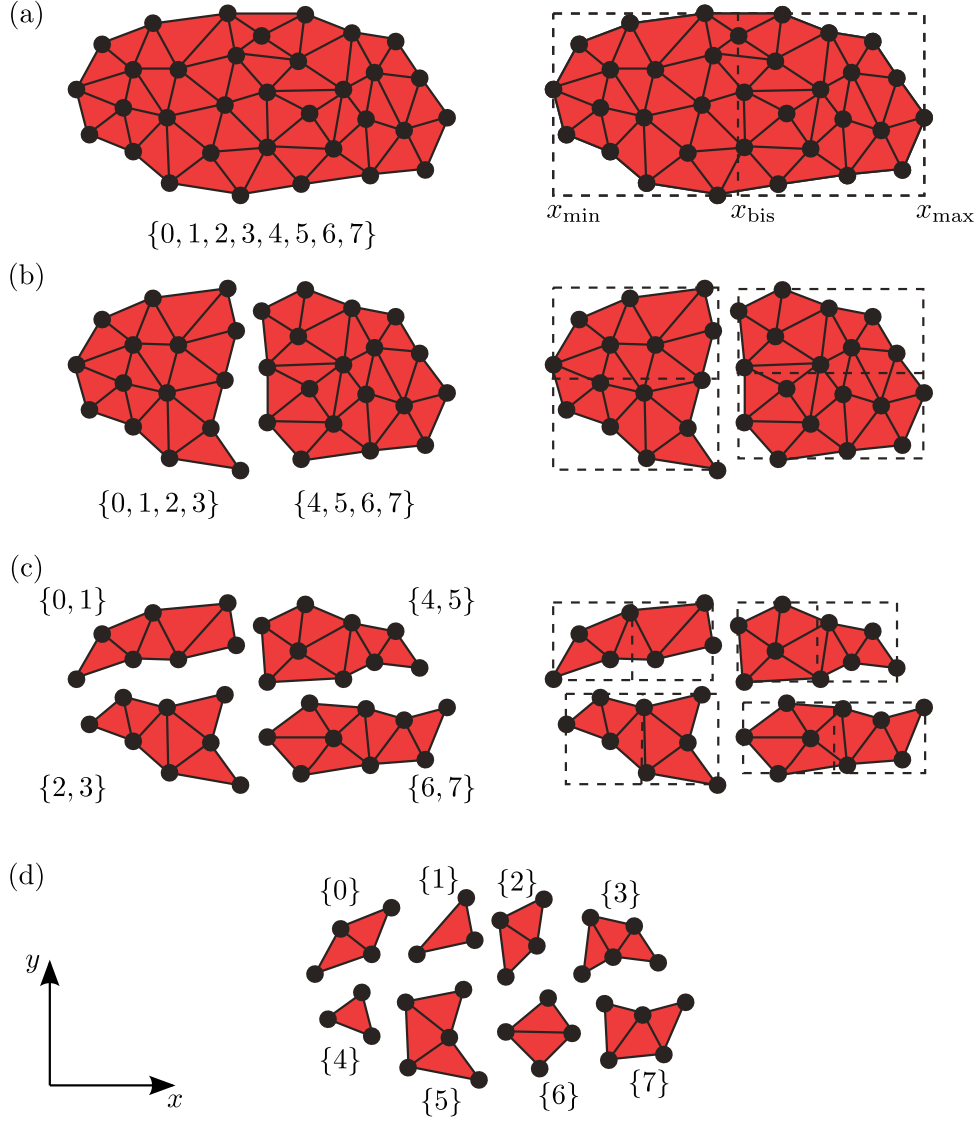


Figure 2.2.: 2-dimensional illustration of how a cluster tree is created. A geometrical bisection is used to subdivide the mesh into spatially separated clusters. (a) The full mesh corresponds to the root of the cluster tree. A bounding box is constructed around the mesh which is then bisected at $x_{\text{bis}} = (x_{\text{min}} + x_{\text{max}})/2$. The x -direction is chosen for the bisection, as the extension of the root cluster is largest along this direction. Each mesh node with $x < x_{\text{bis}}$ belongs to the first son $\{0, 1, 2, 3\}$ and each mesh node with $x > x_{\text{bis}}$ belongs to the second son $\{4, 5, 6, 7\}$. (b) The sons of the root cluster are split accordingly. Since the extension of the sons is largest along the y -direction the bisection is carried out along this direction. (c) The clusters of the next tree level are split again. (d) The parameter n_{min} has been set to 3 so that the clusters of this level are not split anymore and become leaves. Note, that triangular meshes of the clusters only serve as a visual aid.

2. Theoretical fundamentals

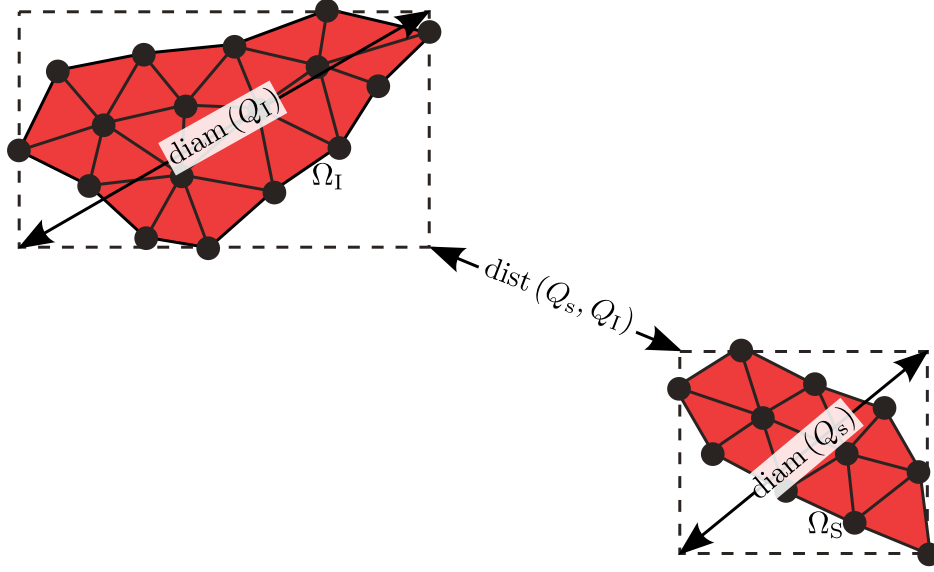


Figure 2.3.: Two dimensional illustration of two clusters Ω_I and Ω_S and their bounding boxes Q_I and Q_S . $\text{diam}(Q_I)$ and $\text{diam}(Q_S)$ denote the diagonal length of the corresponding bounding. $\text{dist}(Q_I, Q_S)$ is the distance between the two bounding boxes. The triangular meshes of the clusters only serve as a visual aid.

ferromagnetic and the vacuum region. The corresponding bounding boxes are created and it is checked as to whether the admissibility condition is fulfilled. For root clusters, this is not usually the case, so that the root of the block cluster tree is not a leaf but a node with sons. Then, one descends one level down in the cluster trees to the sons of the root cluster to test the admissibility for the four possible combinations of son clusters (four, since we only combine clusters belonging to different cluster trees). This procedure is repeated recursively until a combination of two clusters is admissible, or one of the nodes of the cluster tree becomes a leaf. In the former case, the sub-matrix correlating the two clusters, can be approximated by a data-sparse approximation. In the latter case, an inadmissible leaf is created and the corresponding sub-matrix is stored in full. The resulting structure is a level-consistent block cluster tree [72], i.e. the level of a node in the block cluster tree is equal to the level of the nodes in the cluster tree, from which it has been derived.

We also see the motivation for introducing a threshold parameter n_{\min} when constructing a cluster tree. It prevents the leaves of the block cluster tree / hierarchical matrix becoming very small. This, in turn, would lead to a significantly higher memory footprint for the hierarchical structure. The leaves of a hierarchical matrix are shown in Figure 2.4. The red blocks are inadmissible leaves. They typically lie close to the diagonal of the matrix. The green blocks denote admissible leaves. At the top of this figure, the corresponding cluster

trees are also shown. The combinations of clusters which make up leaves in the first two rows of the hierarchical matrix are specifically marked.

We have now discussed the structure of a hierarchical matrix and how it is created. This leaves the question as to how a data-sparse matrix within an admissible leaf is assembled. One way of doing it is to approximate the kernel of the integral (2.56) in terms of a degenerate expansion. This is shown in the next sub-section. The general structure of a data-sparse matrix approximation is given in Figure 2.5. The full sub-matrix (with N rows and N columns) is approximated by a matrix product between two low-rank matrices. A matrix with N rows and k columns is multiplied with a matrix with k rows and N columns, so that only $2kN_s$ elements have to be stored. With $k \ll N$, this ultimately leads to a substantial reduction in computational complexity (memory footprint, matrix assembly time and arithmetic operations), which can be achieved by the use of hierarchical matrices (see also [83, 72]). Since it is the product of two matrices of rank k , and thus its rank is k , the approximated matrix is also called an R_k -matrix.

2.3.2. Creating low rank approximations using interpolation

This sub-section shows how one can approximate a full boundary element matrix block, which correlates two spatially sufficiently separated clusters, by degenerate expansion. Generally, a degenerate expansion with $m + 1$ terms can be written as:

$$g(\vec{R}, \vec{r}) \approx \tilde{g}(\vec{R}, \vec{r}) = \sum_{k=0}^m u_k(\vec{R}) v_k(\vec{r}). \quad (2.58)$$

Then one can expand the boundary integral equation (2.56) as follows:

$$\begin{aligned} \phi(\vec{R}) &= \int_{\partial R} q(\vec{r}) g(\vec{R}, \vec{r}) d^2 r \\ &\approx \int_{\partial R} q(\vec{r}) \tilde{g}(\vec{R}, \vec{r}) d^2 r \\ &= \sum_{k=0}^m v_k(\vec{R}) \int_{\partial R} q(\vec{r}) u_k(\vec{r}) d^2 r. \end{aligned} \quad (2.59)$$

As in Sub-section 2.2.3, we discretise this equation on a triangular surface mesh. The term $q(\vec{r})$ is expanded in terms of local basis functions $\psi_j(\vec{r})$, with local supports Ω_j around the nodal points (see equation (2.44)). The potential

2. Theoretical fundamentals

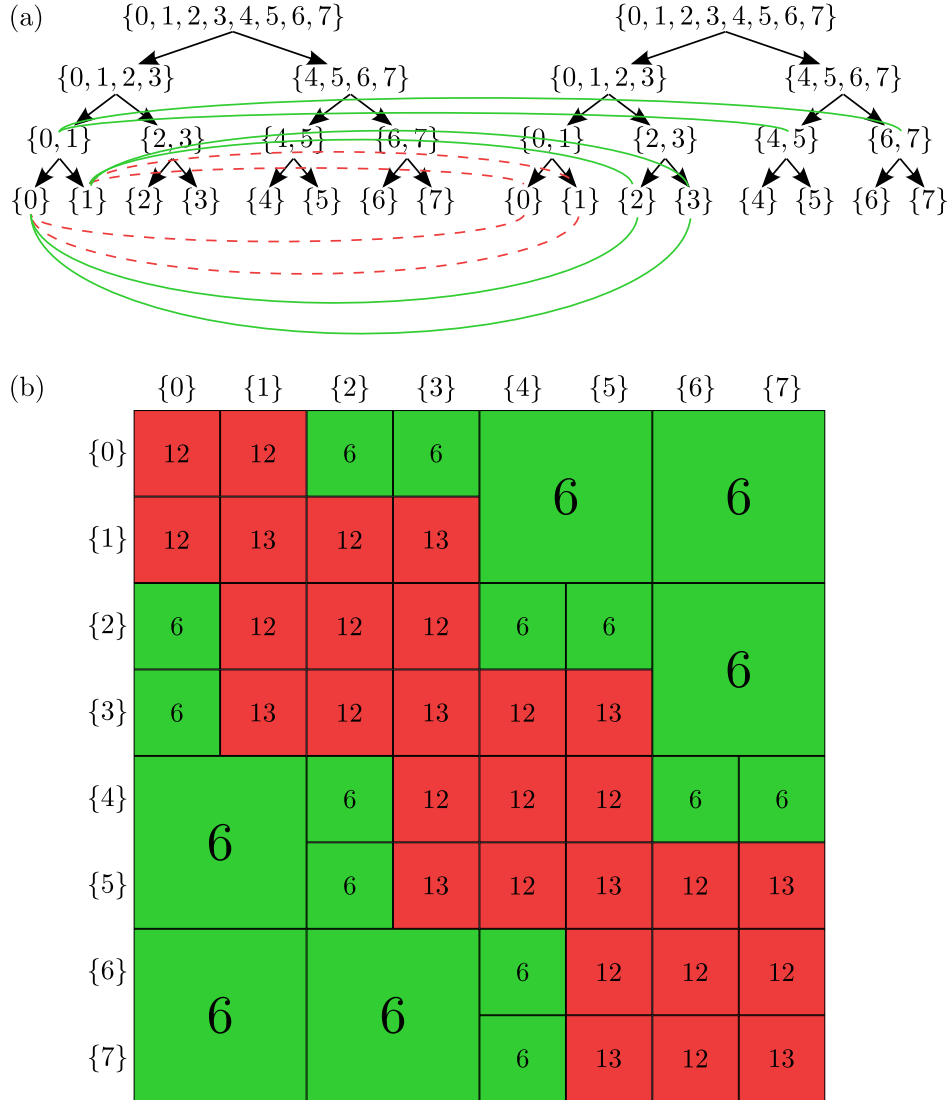


Figure 2.4.: (a) Two cluster trees are combined to form a block cluster tree, which determines the hierarchical structure of an \mathcal{H} -matrix. In this work the two cluster trees are equal, but generally this does not have to be the case. The lines combine those leaves/nodes of the cluster trees, which form leaves in the first two rows of the resulting \mathcal{H} -matrix (dotted, red lines correspond to inadmissible leaves; green, full lines correspond to admissible leaves). (b) Structure of an \mathcal{H} -matrix. The corresponding index sets of the row and column clusters are shown on the left and at the top, respectively. The red blocks refer to inadmissible leaves and the green blocks to admissible leaves. The number within each block corresponds to the rank of the matrix stored within the leaf. The ranks within the admissible leaves are considerably lower, causing the enhanced efficiency of hierarchical matrices with respect to conventional matrices.

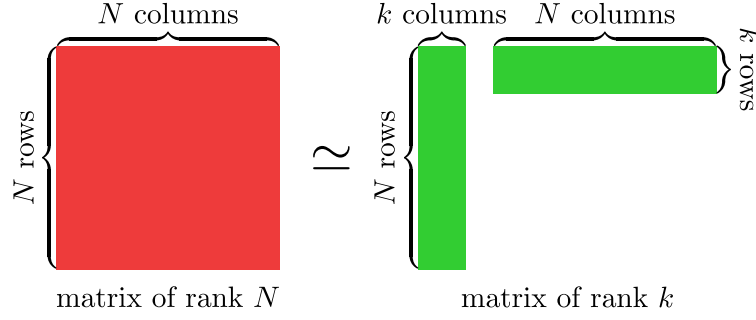


Figure 2.5.: Approximation of a matrix block by an R_k -matrix. The red box refers to an $N \times N$ matrix, which can be approximated by an R_k -matrix. An R_k -matrix is defined as the matrix product of an $N \times k$ with a $k \times N$ matrix.

$\phi(\vec{R})$ is evaluated at the mesh nodes. This yields:

$$\phi(\vec{R}_i) \approx \sum_{k=0}^m v_k(\vec{R}_i) \sum_{j=1}^{N_s} \int_{\partial R} u_k(\vec{r}) \psi_j(\vec{r}) d^2 r q(\vec{r}_j). \quad (2.60)$$

The discretisation leads to the following set of equations, which correspond to a matrix decomposition, as shown in Figure 2.5:

$$\Phi = S T \cdot \vec{q}. \quad (2.61)$$

The matrix S is defined as

$$S_{ij} = v_j(\vec{R}_i),$$

and has N_s rows and $m + 1$ columns. The matrix T is defined as

$$T_{ij} = \int_{\partial R} u_i(\vec{r}) \psi_j(\vec{r}) d^2 r$$

and has $m + 1$ rows and N_s columns. The vectors Φ and \vec{q} read

$$\Phi = (\phi(\vec{r}_1), \phi(\vec{r}_2), \dots, \phi(\vec{r}_{N_s}))$$

and

$$\vec{q} = (q(\vec{r}_1), q(\vec{r}_2), \dots, q(\vec{r}_{N_s})).$$

A prominent example of a degenerate expansion is a Taylor expansion. However, for a Taylor expansion, one would need to compute derivatives of the kernel $g(\vec{R}, \vec{r})$ in terms of \vec{r} or \vec{R} , making a general implementation of this method more difficult. HLib contains an implementation of another type of degenerate expansion, namely polynomial interpolation. The following seeks to introduce this method. We start by considering the one-dimensional case, i.e. we want to approximate the function $f(x)$ on the interval $[-1, 1]$. To

2. Theoretical fundamentals

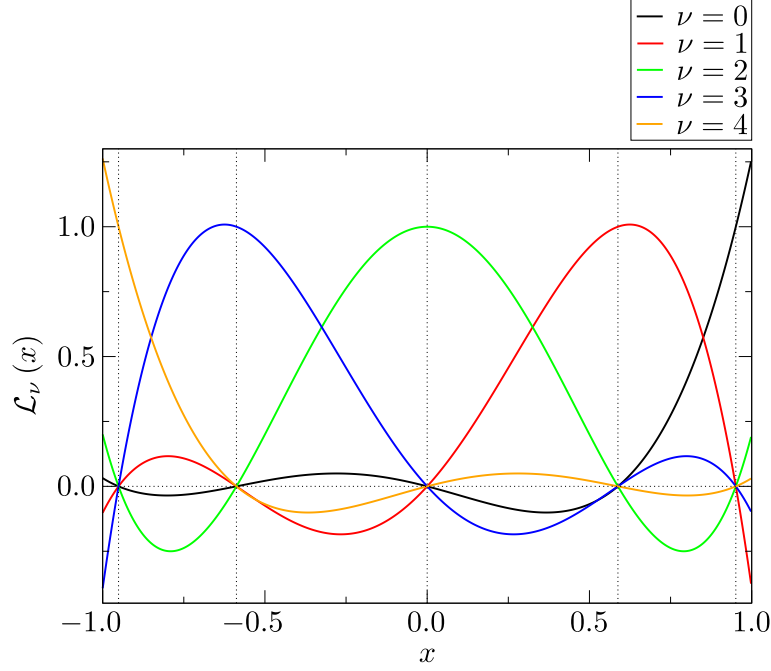


Figure 2.6.: Graphical illustration of the 4-th order Lagrange polynomials on the interval $[-1,1]$. The vertical, dotted lines denote the Chebyshev points.

interpolate $f(x)$ between a set of points ξ_ν , we use Lagrange polynomials \mathcal{L}_μ :

$$\mathcal{L}_\mu(x) = \prod_{\mu=0, \mu \neq \nu}^m \frac{x - \xi_\mu}{\xi_\nu - \xi_\mu} \quad \mu \in \{0, 1, \dots, m\}. \quad (2.62)$$

For interpolation, m -th order Chebyshev points are chosen:

$$\xi_\nu = \cos\left(\frac{2\nu + 1}{2m + 2}\pi\right) \quad \text{for all } \nu \in \{0, 1, \dots, m\}. \quad (2.63)$$

Note that the identity:

$$\mathcal{L}_\mu(\xi_\nu) = \delta_{\mu,\nu} \quad (2.64)$$

holds. This can also be seen in Figure 2.6, where a graphical illustration of 4-th order Lagrange polynomials is given. At each Chebyshev interpolation point, one polynomial is equal to 1, while the other polynomials are 0. The expansion of a function $f(x)$ reads:

$$f(x) \approx \sum_{\nu=0}^m f(\xi_\nu) \mathcal{L}_\nu(x). \quad (2.65)$$

The extension from this one-dimensional case to the expansion of the kernel $g(\vec{R}, \vec{r})$ on a sub-domain of ∂R is relatively straightforward, when replacing this sub-domain by a bounding box Q_S on which the interpolation points

are defined (see also Figure 2.3). As shown in [72] the corresponding three-dimensional Lagrange polynomials read:

$$\mathcal{L}_{\vec{\nu}}^t = \mathcal{L}_{\nu_1, \nu_2, \nu_3}^{[a_1, b_1], [a_2, b_2], [a_3, b_3]}(\vec{r}) = \prod_{i=1}^3 \prod_{\mu=0, \mu \neq \nu_i}^m \frac{x_i - \xi_{\mu}^{[a_i, b_i]}}{\xi_{\nu_i}^{[a_i, b_i]} - \xi_{\mu}^{[a_i, b_i]}}, \quad (2.66)$$

where x_i denotes the Cartesian components of the vector \vec{r} and the intervals $[a_i, b_i]$ the dimensions of the bounding box in x , y or z -directions. The index t in $\mathcal{L}_{\vec{\nu}}^t(\vec{r})$ refers to the fact that the three-dimensional Lagrange polynomials are defined as the tensor product of the corresponding one-dimensional Lagrange polynomials

$$\mathcal{L}_{\nu}^{[a, b]}(x) = \prod_{\mu=0, \mu \neq \nu}^m \frac{x - \xi_{\mu}^{[a, b]}}{\xi_{\nu}^{[a, b]} - \xi_{\mu}^{[a, b]}}.$$

The Chebyshev points $\xi_{\nu}^{[a, b]}$ on the interval $[a, b]$ are defined as

$$\xi_{\nu}^{[a, b]} = \frac{a+b}{2} + \frac{b-a}{2} \xi_{\nu}, \quad (2.67)$$

where ξ_{ν} are the corresponding Chebyshev points on the interval $[-1, 1]$ (see equation 2.63). Thus, a function defined in three-dimensional space can be approximated by:

$$\begin{aligned} f(\vec{r}) = f(x_1, x_2, x_3) &= \sum_{\nu_1, \nu_2, \nu_3=0}^m f(\xi_{\nu_1}^{[a_1, b_1]}, \xi_{\nu_2}^{[a_2, b_2]}, \xi_{\nu_3}^{[a_3, b_3]}) \mathcal{L}_{\nu_1, \nu_2, \nu_3}^t(\vec{r}) \\ &= \sum_{\nu_1, \nu_2, \nu_3=0}^m f(\xi_{\vec{\nu}}^t) \mathcal{L}_{\nu_1, \nu_2, \nu_3}^t(\vec{r}), \end{aligned}$$

where, for brevity, we write the three-dimensional Chebyshev interpolation points as $\xi_{\vec{\nu}}^t$. We use interpolation to perform the degenerate expansion of the kernel. For this, we consider the following cases, which follow from the admissibility condition of equation (2.57). If the cluster in the source space is smaller than in the image space, i.e. $\text{diam}(Q_S) < \text{diam}(Q_I)$, the kernel is expanded with respect to the variable in the source space, i.e. \vec{r} . If $\text{diam}(Q_I) < \text{diam}(Q_S)$ holds, the kernel function is expanded with respect to \vec{R} . In the former case we obtain:

$$g(\vec{R}, \vec{r}) \approx \tilde{g}(\vec{R}, \vec{r}) = \sum_{\vec{\nu}} g(\vec{R}, \xi_{\vec{\nu}}^t) \mathcal{L}_{\vec{\nu}}^t(\vec{r}), \quad (2.68)$$

which, according to equations (2.58) to (2.61), leads to:

$$\phi(\vec{R}) = \int q(\vec{r}) g(\vec{R}, \vec{r}) d^2r$$

2. Theoretical fundamentals

$$\approx \sum_{\vec{\nu}} g(\vec{R}, \xi_{\vec{\nu}}^t) \int \mathcal{L}_{\vec{\nu}}^t(\vec{r}) q(\vec{r}) d^2 r.$$

After discretising this equation, we obtain the matrices:

$$S_{i\vec{\nu}} = g(\vec{R}_i, \xi_{\vec{\nu}}^t)$$

and

$$T_{\vec{\nu}j} = \int \mathcal{L}_{\vec{\nu}}^t(\vec{r}) \psi_j(\vec{r}) d^2 r.$$

Following the same approach for the case of $(\text{diam}(Q_I) < \text{diam}(Q_S))$, we obtain:

$$\begin{aligned} \phi(\vec{R}) &= \int q(\vec{r}) g(\vec{R}, \vec{r}) d^2 r \\ &\approx \sum_{\vec{\nu}} \mathcal{L}_{\vec{\nu}}^t(\vec{R}) \int g(\xi_{\vec{\nu}}^t, \vec{r}) q(\vec{r}) d^2 r. \end{aligned}$$

The matrices S and T read

$$S_{i\vec{\nu}} = \mathcal{L}_{\vec{\nu}}^t(\vec{R}_i)$$

and

$$T_{\vec{\nu}j} = \int g(\xi_{\vec{\nu}}^t, \vec{r}) \psi_j(\vec{r}) d^2 r.$$

The maximal rank of the matrix $\mathbf{S} \mathbf{T}$ is $(m+1)^3$, as this is the number of Chebyshev interpolation points. Instead of N_s^2 matrix entries, $2(m+1)^3 N_s$ matrix elements only have to be stored.

2.3.3. Algorithms for low-rank approximation

We now want to introduce the different algorithms, that can be used to assemble R_k -matrices.

Adaptive cross approximation (ACA)

The probably most frequently used algorithm is adaptive cross approximation (ACA) [84, 85, 86]. As a purely algebraic method, it does not require the expansion of the kernel function as most other algorithms do, but uses only a few entries of the original matrix for the computation of the approximation. Thus, only a small part of the original matrix needs to be computed. The method has the advantage that one can easily plug it into existing code without much change [85]. It has already been used for micromagnetic applications [80], and

benchmark tests have shown that the algorithm performs well concerning data compression and speed of matrix vector product [70]. However, considering the time needed for the set-up of the boundary element matrix, it shows worse results than a tree-code algorithm [70]. It has been stated that ACA does not converge for certain situations (e.g. for the double layer potential on domains with edges) [87, 72, 88], and an alternative variant of the original ACA, ACA+, has been proposed [88], which, despite being an improved version of ACA, still exhibits the same convergence problems. According to [85], one can avoid these problems by modifying ACA. These modifications are not implemented in HLib, so that they will not be addressed in this work. The accuracy of ACA and ACA+ is primarily determined by a heuristic parameter ϵ_{aca} . A second parameter k_{\max} defines the maximal rank for the admissible leaves.

Interpolation

Interpolation [89] has already been discussed in Sub-section 2.3.2. This method starts with an integral equation (as in equation (2.56)) and uses Lagrange polynomials to expand the kernel of the integral. The R_k -matrix can then be readily obtained (see Sub-section 2.3.2 or [83]). The accuracy of the method is determined by the order of expansion p . The disadvantage of this technique compared to other methods is that it requires more time to assemble the boundary element matrix [72]. The approximation of large matrices by an \mathcal{H} -matrix using interpolation is therefore often not feasible.

Hybrid Cross Approximation (HCA)

Hybrid cross approximation (HCA) was introduced as an alternative to ACA and ACA+ [87]. Unlike the previous algorithms, it is not purely algebraic but, like interpolation, also relies on the expansion of the kernel function. According to its character as a hybrid between interpolation and ACA, the accuracy of HCA can be tuned with two parameters p and ϵ_{aca} . There are two different types of algorithm: HCA I is closer to interpolation while HCA II is more similar to ACA. The more efficient variant, HCA II, has proven to be comparable to ACA+ concerning performance, while being more accurate [87]. By default, HLib uses a strong admissibility criterion when computing the R_k -matrices with HCA I or HCA II. Using the notation of equation (2.57) and Figure 2.3, it reads (see also [87]):

$$\max(\text{diam}(Q_I), \text{diam}(Q_S)) \leq \eta \text{dist}(Q_I, Q_S). \quad (2.69)$$

2. Theoretical fundamentals

Adaptive recompression

Once assembled, the efficiency of an \mathcal{H} -matrix can be optimised by exploiting an adaptive re-compression procedure [88]. This is done by optimising the rank within the admissible leaves and coarsening the hierarchical structure itself. The accuracy of the re-compression can be adjusted with a parameter ϵ .

In Chapter 3 the efficiency of the introduced algorithms for the compression of the boundary element matrix B (see equation (2.53)) is tested. It appears in the Fredkin-Koehler approach to hybrid FEM/BEM. For completeness, it should also be mentioned that there exists a slightly different type of hierarchical matrix, namely \mathcal{H}^2 -matrices [90, 72], which are also implemented in HLib. Concerning the scaling of the data compression and the speed of the matrix-vector product with N , N being the number of rows and columns of the full matrix, it shows a slightly better behaviour than conventional hierarchical matrices ($\sim N$ instead of $\sim N \cdot \log(N)$). Applications have been reported in the fields of electromagnetism [73] and micromagnetics [81]. However, some initial tests using \mathcal{H}^2 -matrices showed just comparable efficiency with respect to conventional \mathcal{H} -matrices, so that it was decided not invest resources into further investigation.

2.3.4. \mathcal{H} -matrix assembly in HLib

This sub-section discusses the steps to be taken in order to assemble a hierarchical matrix in HLib. As a first step, an object `grid` of the structure `bemgrid3d` is created using the statement:

```
grid = new_bemgrid3d( number_vertices, number_edges,  
                      number_triangles);
```

where the number of vertices, edges and triangles of the surface mesh is passed to the routine `new_bemgrid3d`. Then the arrays of the object `grid`, which store the vertex coordinates and other relevant mesh data, are initialised in for-loops. The computation of the local surface normals \hat{n} is performed with the routine:

```
dyn_prepare_bemgrid3d( grid);
```

As a next step, an object `ct` of the structure `clustertree`, which hierarchically organises the sub-clusters of our surface mesh, is created using the routine `buildvertexcluster_bemgrid3d`: 2.2.

```
ct = buildvertexcluster_bemgrid3d( grid, HLIB_REGULAR,
```

```
nmin, 0);
```

The argument `nmin` is the minimal leaf size, which has been introduced in section 2.3.1. By passing the identifier `HLIB_REGULAR`, a regular clustering strategy for the creation of the cluster tree (see Sub-section 2.1.3 in [72]) is used, which is slightly different from the strategy presented in Figure 2.2. Then, an object `sbf` of the structure `surfacebemfactory` is created, which contains all the information needed for the construction of a hierarchical matrix. This is done with the routine `new_surfacebemfactor_dlp`:

```
sbf = new_surfacebemfactory_dlp( grid,
                                HLIB_LINEAR_BASIS, ct,
                                HLIB_LINEAR_BASIS, ct,
                                quadorder, quadorder,
                                polyorder, 0.0);
```

Here, the `clustertree` object `ct` is passed twice, as it represents the row and column cluster tree. The identifier `HLIB_LINEAR_BASIS` makes sure that we use linear basis functions for the discretisation in the integration space. The reason why this argument is passed twice, is that, by default, HLib uses a Galerkin discretisation (see also Section 3.1), which is different from the collocation discretisation of equation 2.50 or 2.53. Therefore, we modified HLib internally by adding corresponding routines, which in turn render some arguments of HLib's top-level routines redundant. The arguments `quadorder` and `polyorder` correspond to the order q of the Gaussian quadrature, which is used for the numerical integration, and the order p of the polynomial expansion. Finally, the hierarchical matrix is created by

```
hmatrix = onthefly_hca_coarsen_supermatrix( ct->root,
                                             ct->root,
                                             sbf, eps_aca,
                                             kmax, eps, 1,
                                             algorithm, 0,
                                             eta, 0);
```

The argument `ct->root` refers to the root cluster of the cluster tree `ct`. The arguments `eps_aca`, `kmax`, `eps` and `eta` correspond to the parameters ϵ_{aca} , k_{max} , ϵ and η , which have been introduced earlier. The \mathcal{H} -matrix assembly algorithm (e.g. ACA or HCA II) is specified through the variable `algorithm`. When assembling hierarchical matrices with ACA and without adaptive recompression, the routine `onthefly_hca_coarsen_supermatrix` is replaced by

```
bcluster = build_blockcluster( ct->root, ct->root,
                               HLIB_MINADMISSIBILITY,
```

2. Theoretical fundamentals

```
HLIB_BLOCK_INHOMOGENEOUS,  
eta, 0);  
  
hmatrix = build_supermatrix_from_blockcluster( bcluster,  
                                                0, 0.0);  
  
bufacafillold_surfacebem_supermatrix( hmatrix,  
                                       ct->root,  
                                       ct->root,  
                                       sbf,  
                                       eps_aca,  
                                       kmax);
```

Here, a block cluster `bcluster` is built and from that an empty hierarchical matrix `hmatrix`. The latter is filled using the routine `bufacafillold_surfacebem_supermatrix`.

3. Compression of the boundary element matrix

The hybrid finite element method / boundary element method (FEM/BEM), which was introduced in Section 2.2, is an often-used method for the computation of long-range, magnetostatic interaction in micromagnetic finite-element solvers [25, 91, 37, 45]. One of its main advantages is that it only requires the meshing of the ferromagnetic region. On the other hand, the use of this method includes the assembly and storage of a dense boundary element matrix with N_S^2 elements, where N_s is the number of surface nodes of the unstructured mesh. Approximating a boundary element matrix by a hierarchical matrix (see Section 2.3) improves the computational complexity of the method significantly [70]. This chapter uses hierarchical matrices to optimise the Fredkin-Koehler approach of the hybrid FEM/BEM. In particular, it compares the accuracy and efficiency of different algorithms (see Sub-section 2.3.3) used for the assembly of a hierarchical matrix. Parts of this investigation were published in [92].

3.1. Introduction

[70] showed that hierarchical matrices constitute a useful tool in optimising the BEM part of hybrid FEM/BEM [70]. Besides reducing the memory footprint of the dense boundary element matrix B and its assembly time, they also speed up the matrix-vector product. In the aforementioned study [70], adaptive cross approximation (ACA, see Sub-section 2.3.3) was used to assemble hierarchical matrices. This study uses the HLib library, which is an implementation of the hierarchical matrix methodology, together with the micromagnetic finite element solver Nmag [93], and compares the different algorithms presented in Sub-section 2.3.3, concerning their accuracy, memory savings and matrix assembly time. The speed of the matrix vector product is not addressed, mainly because its speed-up should be closely related to the memory footprint of the resulting hierarchical matrix.

HLib contains implementations to build hierarchical matrix approximations of

3. Compression of the boundary element matrix

the discretised boundary element matrix of the single and double layer potentials (see Chapter 2, [72]). However, it employs Galerkin discretisation instead of the collocation discretisation of equation (2.51). A Galerkin discretisation of equation (2.35) results in:

$$\mathbf{M} \cdot \Phi_2 = \mathbf{B}_{\text{Gal}} \cdot \Phi_1, \quad (3.1)$$

where \mathbf{M} , the so called mass matrix, is a sparse, symmetric matrix. Its elements read:

$$M_{ij} = \int_{\Omega_i \cap \Omega_j} \psi_i(\vec{r}) \psi_j(\vec{r}) d^2 \vec{r}. \quad (3.2)$$

The elements of the Galerkin discretised boundary element matrix \mathbf{B}_{Gal} read:

$$\begin{aligned} B_{\text{Gal},ij} = & \frac{1}{4\pi} \int_{\Omega_j} \int_{\Omega_i} \psi_i(\vec{r}) \frac{\langle \vec{R} - \vec{r}, \vec{n}(\vec{r}) \rangle}{|\vec{R} - \vec{r}|^3} \psi_j(\vec{R}) d^2 \vec{r} d^2 \vec{R} \\ & + \int_{\Omega_i \cap \Omega_j} \psi_i(\vec{R}) \left(\frac{\Omega(\vec{R})}{4\pi} - 1 \right) \psi_j(\vec{R}) d^2 \vec{R}. \end{aligned} \quad (3.3)$$

The values for ϕ_2 can be retrieved by multiplying equation (3.1) with \mathbf{M}^{-1} . However, the solid angle term in equation (3.3) has to be correctly evaluated. We have followed another route and used the collocation discretisation of equation (2.53). For this, we wrote corresponding routines, which compute collocation-type matrix elements within the admissible and inadmissible leaves. Technically this task was simplified by the fact that the original HLib routines could be used as a template. Then, the integration over the second variable (the solution space in the language of Section 2.2) had just to be replaced by a point evaluation. There are two ways of computing the matrix elements B_{ij} (see equation (2.53)) within the inadmissible leaves of a hierarchical matrix. First, a Gaussian quadrature [73] can be used to compute the matrix elements numerically. This is also how HLib computes the Galerkin-type matrix elements. Secondly, the analytical formula of Sub-section 2.2.4 may be used. Initially, numerical quadrature was implemented and the results were published in [92]. However, in order to test whether its use increases the accuracy of an \mathcal{H} -matrix approximation, we also implemented the corresponding analytical expressions.

The chapter is structured as follows: this section introduces the studied geometry (thin, square platelets, Sub-section 3.1.1), contains a discussion of how to quantify errors (Sub-section 3.1.2), concluding with the determination of adequate parameter sets for the investigated algorithms (Sub-section 3.1.3). The efficiency of the algorithms is compared in Section 3.2. This section also

contains a comparison between a numerical and an analytical computation of the matrix elements $B_{i,j}$ during hierarchical matrix assembly. A discussion of the numerical errors from hybrid FEM/BEM (Sub-section 3.3.1) and from the use of a hierarchical matrix approximation (Sub-section 3.3.2) is given in Section 3.3. Finally, the findings are summarised and an outlook for potential future work is given in Section 3.3.

3.1.1. The studied system

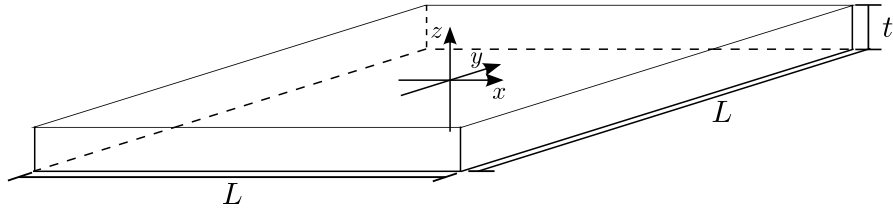


Figure 3.1.: Geometry for the numerical investigations: a square thin platelet with an edge length L and a thickness t . The normal vectors of the two large faces are parallel to the z -direction.

In order to investigate the efficiency of the algorithms implemented in HLib, thin, square platelets are studied (see Fig. 3.1). For ease of discussion a coordinate system is introduced, whose z -direction is aligned parallel to the normals of the square surfaces. The thickness of the platelets is $t = 5$ nm and their edge lengths L vary in 10 nm steps from 10 to up to 260nm. There are different reasons for choosing platelets. First, because of their cuboidal shape they can be efficiently meshed by subdivision into cubes, which in turn are split into tetrahedrons using Kuhn triangulation [62]. Most tetrahedral meshes in this chapter are created with a programme, which is based on a Kuhn triangulation and was written by Matteo Franchin. Secondly, these systems constitute a useful test case for studying the compression of the boundary element matrix, as there are only few volume nodes. Furthermore, in the case of homogeneous magnetisation analytical formulae for the demagnetisation field (see Appendix C) and derived properties such as the magnetometric demagnetising factor exist. The latter property is introduced under the assumption that the magnetisation is homogeneous and points in the z -direction. Then, the magnetometric demagnetising factor in the z -direction, D_z , is defined such that the magnetostatic self energy per unit volume is equal to $\mu_0 D_z M_S^2 / 2$ with M_S being the saturation magnetisation. Using the expression for magnetostatic energy (see equation (2.15)) one readily obtains:

$$D_z = -\frac{1}{L^2 t \mu_0 M_S} \int_{\mathcal{R}_m} \hat{e}_z \cdot \vec{H}_{\text{demag}}(\vec{r}) d^3 r, \quad (3.4)$$

3. Compression of the boundary element matrix

where the volume V of the thin film is expressed in terms of the edge length L and thickness t .

3.1.2. Error analysis

As can be seen from equation (3.4), D_z is computed by spatially averaging over the z-component of the demagnetisation field \vec{H}_{demag} . Therefore, D_z does not constitute a rigorous way of quantifying the error of a demagnetisation field evaluation, as it, first, only depends on one component of the demagnetisation field and, second, leaves the possibility that errors cancel each other out. Nevertheless, we use it as an indicator of the error, as the corresponding analytical expression [94] is easy to implement and thus provides a quick way to compare and test algorithms. In the same way we compare relaxed micromagnetic states in terms of the spatially averaged magnetisation. For a more accurate analysis of the different demagnetisation field evaluations, we subsequently use the rms error [95, 96], which is defined as

$$\delta_{\text{rms}} = \sqrt{\sum_{i=1}^N \sum_{j=1}^3 (H_{ij}^k - H_{ij}^l)^2 / \left(\sum_{i=1}^N \sum_{j=1}^3 (H_{ij}^l)^2 \right)}. \quad (3.5)$$

The indices i and j run over all nodes of the mesh and the three Cartesian coordinates, respectively. The tags k and l refer to the method, with which the field values were computed. We follow the convention that k denotes the more inaccurate and l the more accurate method, e.g. the pair ($k = \text{hlib}$, $l = \text{full}$) corresponds to the rms error introduced by the application of a hierarchical matrix and the pair ($k = \text{full}$, $l = \text{analytic}$) to the rms error from the hybrid FEM/BEM calculation (for the analytical formula see Appendix C).

3.1.3. Determination of parameter sets

This section presents adequate parameter sets for the algorithms introduced in Sub-section 2.3.3. The following parameters have to be set in order to create \mathcal{H} -matrices: η and n_{min} are the defining parameters for the tree structure of a hierarchical matrix. Algorithm-specific parameters are ϵ_{aca} and k_{max} for ACA and ACA+, the polynomial order p for interpolation and the parameters p and ϵ_{aca} for HCA I and HCA II. Finally, the parameters ε and q control the accuracy of adaptive re-compression and numerical quadrature, respectively.

The dependency of the efficiency of the hierarchical matrix assembly on the tree parameters n_{min} and η is relatively complex and there do not seem to be parameter values which yield particularly efficient results. We have chosen $\eta =$

2.0 and $n_{\min} = 30$ for all the simulations presented in this work. This choice lies within the range of commonly used values [76, 72, 97, 98]. The maximal rank k_{\max} of the low-rank matrices assembled with ACA or ACA+ does not have an impact on the efficiency of the algorithm when it is set sufficiently high. We set $k_{\max} = 500$, which ensures that the accuracy of these algorithms virtually only depends on the parameter ϵ_{aca} . For the investigation of different parameter sets, the near-field entries of the \mathcal{H} -matrices were computed numerically by Gaussian quadrature.

We use the demagnetising factor D_z (Sub-section 3.1.2) as an indicator for the accuracy of the hierarchical matrix approximation. Figure 3.2 shows the error in D_z for differently sized platelets and mesh resolutions. According to

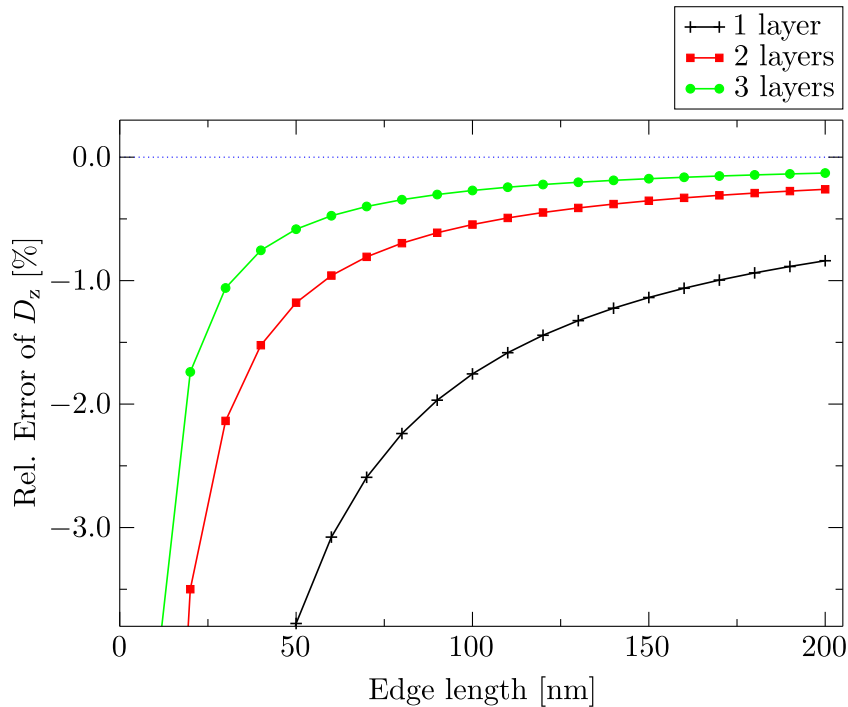


Figure 3.2.: The relative error of the demagnetising factor D_z , as obtained with the full BEM calculation, with respect to its analytical value (equation 3.4) is computed for platelets with different edge lengths L (see figure 3.1). The calculations have been performed for three different discretisations, corresponding to one, two and three tetrahedron layers along the z -direction (no internal nodes, only surface nodes). The meshes have been created with a Kuhn triangulation.

this figure the relative error in D_z seems to diverge towards small edge lengths, with the degree of the divergence increasing with a decreasing mesh resolution. We will later see that this can be explained by the diverging demagnetisation field around the edges of cuboidal geometries (see also Appendix C). The error of D_z lies above 0.1 % for all edge length and mesh resolutions. For the

3. Compression of the boundary element matrix

determination of adequate parameter sets for the algorithms we have used a mesh resolution with two tetrahedron layers along the z -direction. Details on the accuracy and the speed of the matrix assembly of the algorithms as a function of corresponding parameters are given in the Appendix B. Our choices for the algorithm-specific parameters are summarised in table 3.1. Furthermore, adaptive re-compression has been applied with $\epsilon = 10^{-3}$ and Gaussian quadrature with a quadrature order of $q = 3$.

algorithm	p	ϵ_{aca}	k_{\max}
ACA	-	10^{-4}	500
ACA+	-	10^{-4}	500
Interpolation	5	-	-
HCA I	6	10^{-7}	-
HCA II	4	10^{-7}	-

Table 3.1.: The table summarises our choices for the algorithm-specific parameters. Details on how the efficiency of the algorithms depends on the parameter choice are given in Appendix B.

3.2. Efficiency of \mathcal{H} -matrix assembly algorithms

This section is split into three sub-sections. In Sub-section 3.2.1 the algorithms introduced in Section 2.3.3 are compared with regard to deviations in the demagnetising factor D_z , the memory footprint and assembly time of a hierarchical matrix. Each algorithm is used with the corresponding parameter set as given in the previous section (3.1.3). The matrix elements B_{ij} are computed by Gaussian quadrature (quadrature order 3). In the second sub-section (3.2.2) the same investigations as in Sub-section 3.2.1 are conducted, the only difference being that the matrix elements B_{ij} are computed by an analytical formula. Furthermore, both methods to evaluate the matrix elements B_{ij} are compared concerning their efficiency. We will summarise our findings in Sub-section 3.2.3.

3.2.1. B_{ij} by Gaussian quadrature

Figure 3.3 shows the deviation in the demagnetisation factor computed with hybrid FEM/BEM either using \mathcal{H} -matrix approximations assembled through different algorithms or using the full BE matrix. All errors are more than one order of magnitude smaller than the error introduced through hybrid

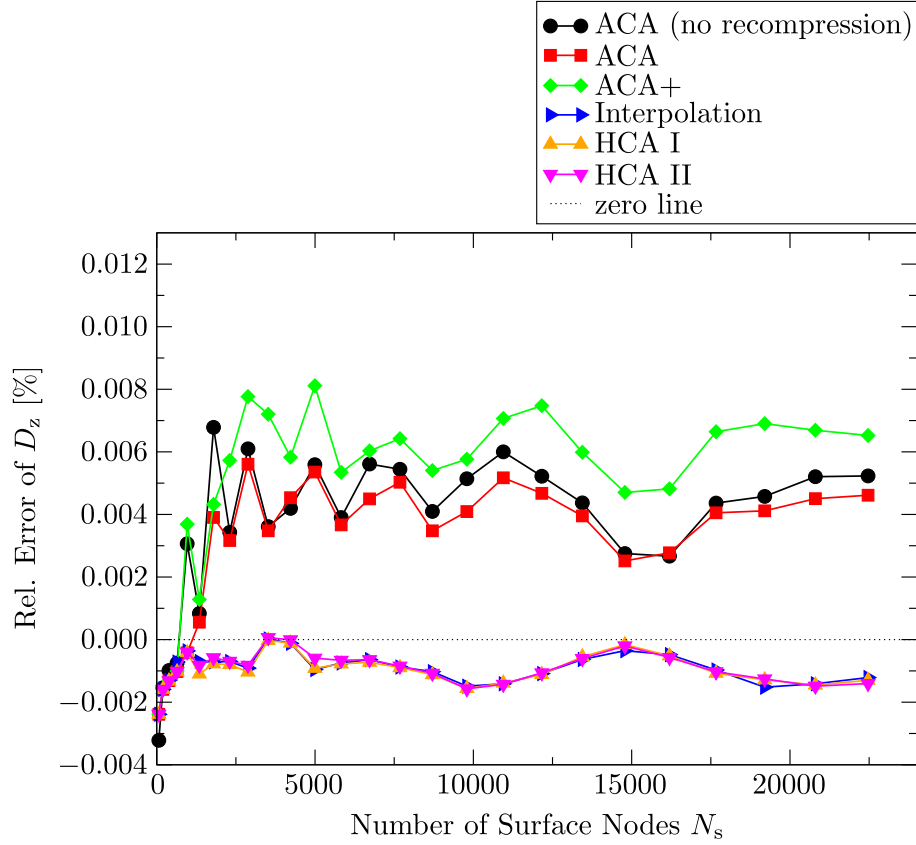


Figure 3.3.: The magnetometric demagnetising factor D_z of equation (3.4) has been computed with hybrid FEM/BEM using either an \mathcal{H} -matrix approximation or the full BE matrix. For different \mathcal{H} -matrix assembly algorithms (see legend) this figure shows the relative deviation from the result, obtained with the full BE matrix, as a function of the number of surface nodes N_s . The computations using ACA have been performed with and without adaptive recompression (see Section 2.3.3). The matrix elements B_{ij} of each hierarchical matrix approximation have been computed by numerical quadrature (quadrature order 3). The elements of the full BE matrix have been evaluated with the analytical formula of Section 2.2.4.

3. Compression of the boundary element matrix

FEM/BEM (see Fig. 3.2) and stable with an increasing number of surface nodes. The latter fact is essential since the application of \mathcal{H} -matrices becomes important for large structures with many surface nodes. A comparison of the curves for ACA with and without adaptive recompression yields that the use of recompression only has a minor effect on the error. Generally the deviations observed for ACA and ACA+ are higher than for the other algorithms and could not be reduced by further decreasing ϵ_{ACA} (see the Figures B.2 and B.3 in Appendix B).

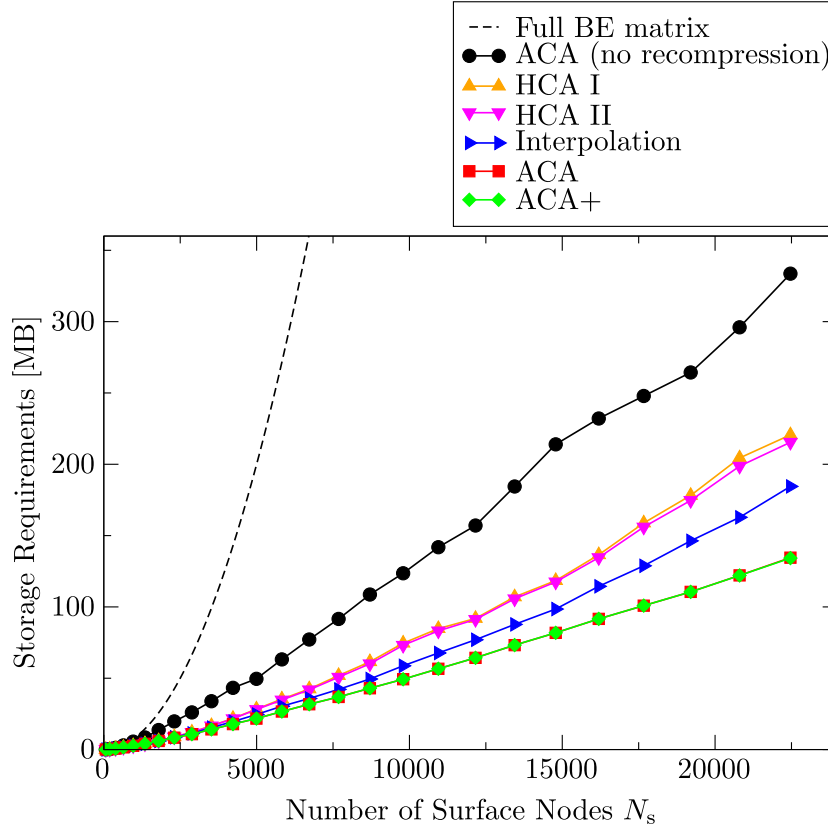


Figure 3.4.: The memory footprint of \mathcal{H} -matrix approximations is given as a function of the number of surface nodes N_s . Additional memory costs due to the storage of the hierarchical tree are included. The matrix elements B_{ij} of the hierarchical matrices have been computed by numerical quadrature (quadrature order 3). As a comparison the memory footprint of a full BE matrix is given. This graph is not based on a numerical computation but has been derived from the expected memory requirements of a dense matrix with N_s^2 elements.

Figure 3.4 shows a comparison of the storage requirements. As expected hierarchical matrices assembled through all algorithms show a crucial improvement as compared to the conventional, full boundary element matrix, whose memory footprint scales quadratically with the number of surface nodes. Instead,

3.2. Efficiency of \mathcal{H} -matrix assembly algorithms

their memory footprint exhibits the almost linear behaviour, which has also been proven theoretically [72, 83]. Comparing the algorithms, ACA without recompression shows the poorest compression rates, indicating the efficiency of adaptive recompression. Using recompression, the compression rates of ACA and ACA+ are better than those of interpolation, HCA I, and HCA II. Until recently, the use of hierarchical matrices in the framework of hybrid FEM/BEM was limited to ACA without recompression [70, 80] (with the entries computed by the Lindholm formula, however). Thus, a result of our work is that the use of adaptive recompression [88] substantially improves the efficiency of hierarchical matrices in micromagnetics.

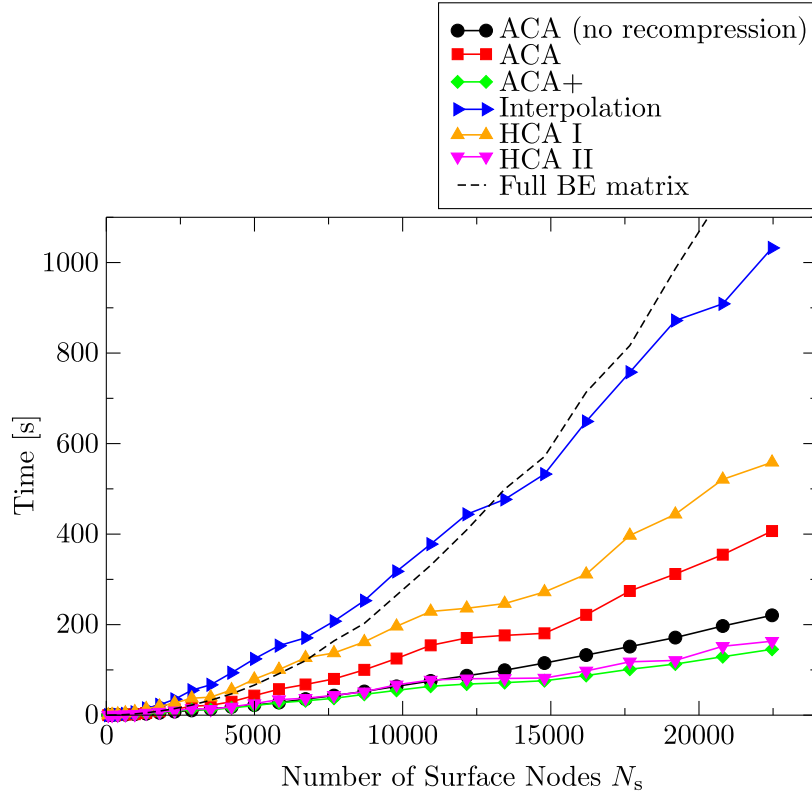


Figure 3.5.: The assembly times of \mathcal{H} -matrices, assembled through different algorithms, are given as a function of the number of surface nodes N_s . The algorithms, which have been used to assemble \mathcal{H} -matrix approximations are given in the legend. The elements B_{ij} of the hierarchical matrices have been computed by numerical quadrature (quadrature order 3). As a comparison the matrix assembly times of the full BE matrices, the elements of which are evaluated by the analytical formula of Section 2.2.4, are given.

The \mathcal{H} -matrix assembly times for different algorithms are compared in Figure 3.5. As expected (see Section 2.3.3) the assembly of a hierarchical matrix by interpolation is very slow. For the studied matrix sizes it is about as fast as the setup of the full BE matrix. However, due to its improved scaling behaviour,

3. Compression of the boundary element matrix

interpolation should bring a significant reduction in the setup time as compared to the full BE matrix for larger matrix sizes. Comparing the results for ACA with and without recompression, it turns out that the matrix assembly time is increased significantly by using recompression for ACA. However, the speed of the recompression is dependent on the algorithm used in the first place [88]. The speed of ACA+ (with recompression) in Figure 3.5 already indicates that recompression must be faster for this algorithm. Generally, the best results concerning the matrix assembly time are exhibited by ACA+, with HCA II being only slightly slower.

3.2.2. B_{ij} by analytical formula

In this section we use the analytical formula of Section 2.2.4 (equation (2.55)) to compute full BE matrix elements B_{ij} within the hierarchical matrix approximations. Apart from this we have run the same simulations as in Section 3.2.1 and also used the same type of computer for the computations. Thus, we can make a direct comparison between computations, where the BE matrix elements B_{ij} are calculated with an analytical formula, and computations, where a numerical quadrature is used (quadrature order 3). Since the algorithms ACA and ACA+ build the low-rank blocks within the admissible leaves from some of the original elements of the full BE matrix B_{ij} (see Section 2.3.3), their assembly of a hierarchical matrix approximation either depends entirely on Gaussian quadrature (Section 3.2.1) or on the analytical formula (this section). On the contrary, for interpolation, HCA I and HCA II, the analytical formula may only be applied for filling inadmissible leaves, i.e. the far-field entries are always computed by numerical quadrature (quadrature order $q = 3$). Therefore, one would expect that the efficiency of ACA and ACA+ shows the largest dependence on whether the computation of the matrix entries B_{ij} is performed numerically or analytically. We will see that this is indeed the case.

Figure 3.6 shows the error of the magnetometric demagnetisation factor D_z when the elements B_{ij} of the hierarchical matrices are computed analytically. A comparison with corresponding results obtained with numerical quadrature is made in Figure 3.7. Since this comparison yields qualitatively similar results for ACA and ACA+ as well as for interpolation, HCA I and HCA II, only the results for the algorithms ACA+ and HCA II are shown. The findings are that for HCA I, HCA II, and interpolation the error is only slightly affected by the choice between numerical quadrature and the analytical formula, i.e. there is a small decrease in the error when employing the latter option. For ACA and ACA+, on the contrary, the error is decreased by a factor of about 2 upon using the analytical formula. This decrease appears to stem from the

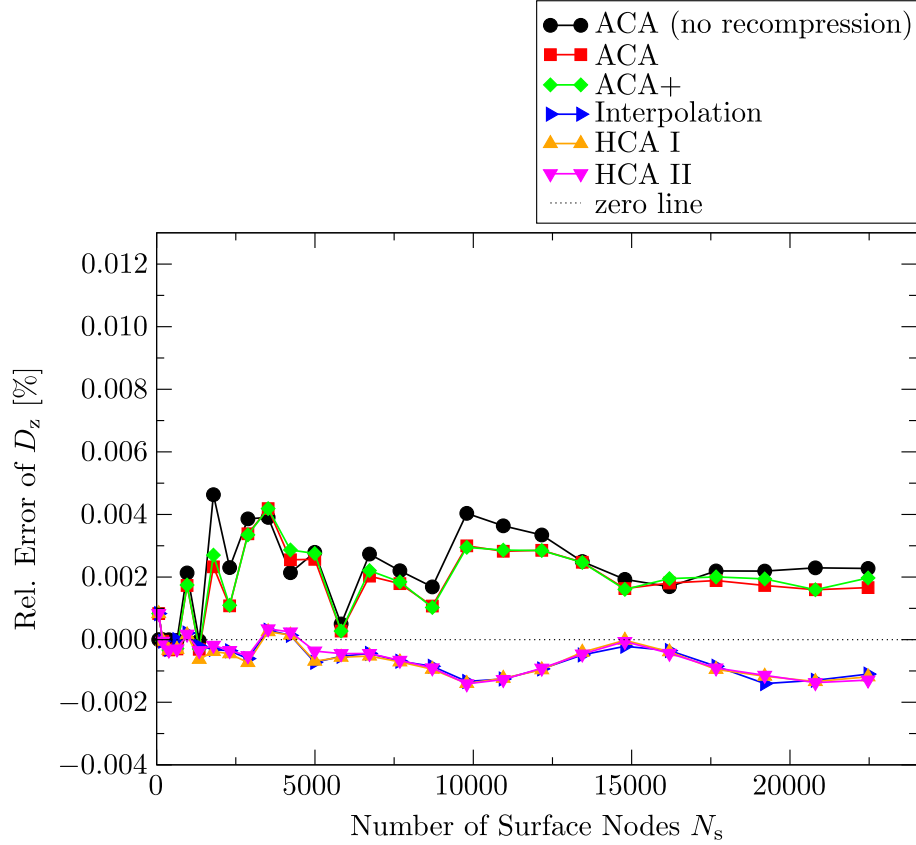


Figure 3.6.: The magnetometric demagnetising factor D_z of equation (3.4) has been computed with hybrid FEM/BEM using either an \mathcal{H} -matrix approximation or the full BE matrix. For different \mathcal{H} -matrix assembly algorithms (see legend) this figure shows the relative deviation from the result, obtained with the full BE matrix, as a function of the number of surface nodes N_s . The matrix elements B_{ij} of each hierarchical matrix approximation and each full BE matrix have been computed with the analytical formula of Section 2.2.4. The y -axis range has been chosen as in Figure 3.3 in order to ease the comparison.

3. Compression of the boundary element matrix

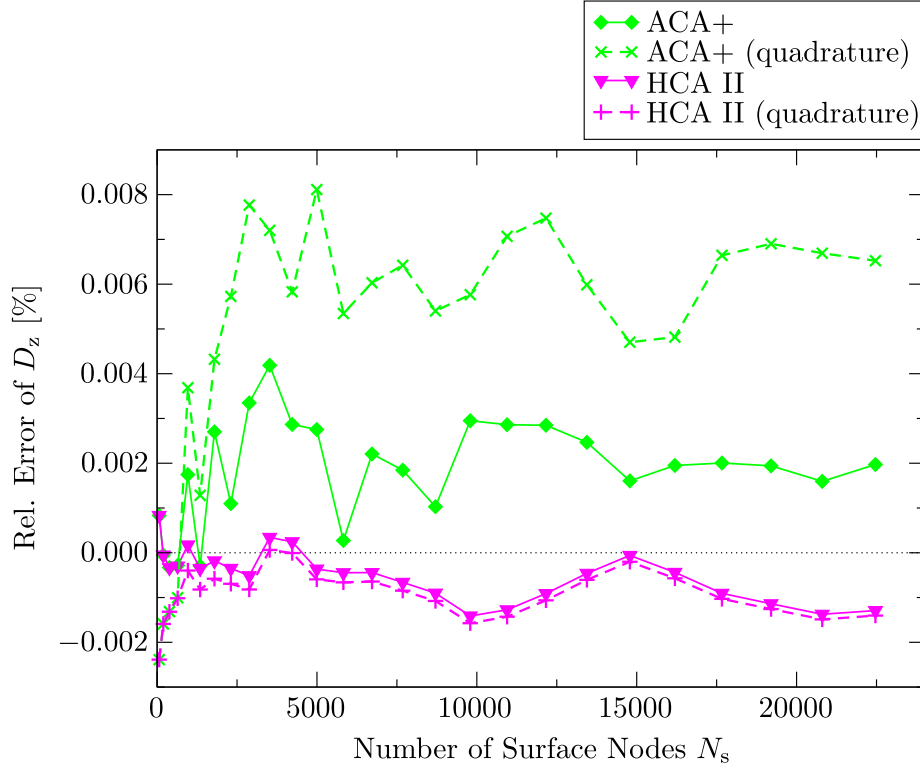


Figure 3.7.: The BE matrix of hybrid FEM/BEM is approximated by a hierarchical matrix and the magnetometric demagnetisation factor D_z is computed. The figure shows the relative deviation with respect the result of a corresponding full BE matrix computation as a function of the number of surface nodes N_s . The dashed data curves correspond to calculations where the matrix elements B_{ij} of the hierarchical matrix approximation have been computed by numerical quadrature (quadrature order 3). Graphs with full lines refer to simulations where the analytical formula of Section 2.2.4 has been used. The latter method has also been employed to compute the full BE matrix. As the dependence of the error in D_z on the method to evaluate the matrix elements B_{ij} is similar for the algorithms ACA and ACA+ as well as for the algorithms HCA I, HCA II and interpolation, only graphs for ACA+ and HCA II are shown.

3.2. Efficiency of \mathcal{H} -matrix assembly algorithms

computation of the far-field entries, for which only ACA and ACA+ use the analytical formula.

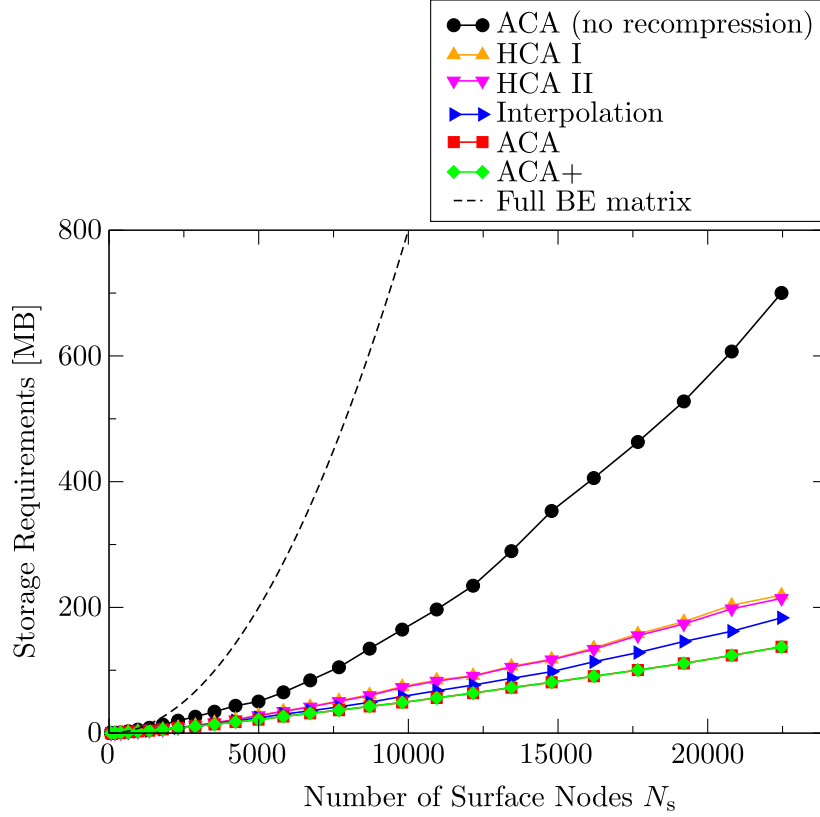


Figure 3.8.: The memory footprint of \mathcal{H} -matrix approximations is given as a function of the number of surface nodes N_s . Additional memory costs due to the storage of the hierarchical tree are included. The data has been taken from computations, where the analytical formula of Section 2.2.4 has been used for the evaluation of the matrix elements B_{ij} within the hierarchical matrix approximations. As a comparison the memory footprint of a full BE matrix is given. The latter graph is not based on a numerical computation but has been derived from the expected memory requirements of a dense matrix with N_s^2 elements.

The results on the memory footprint for the \mathcal{H} -matrix approximations are presented in the Figures 3.8 and 3.9. The former figure shows a comparison between all studied algorithms using the analytical formula for computing the BE matrix elements B_{ij} . In the latter figure the graphs for ACA (with and without recompression) are compared with the corresponding graphs, stemming from computations with a numerical evaluation of the matrix elements B_{ij} . We find, that, when using recompression, the storage requirements virtually do not depend on the whether numerical quadrature or the analytical formula is used. When using ACA without recompression the analytical evaluation increases the memory footprint significantly.

3. Compression of the boundary element matrix

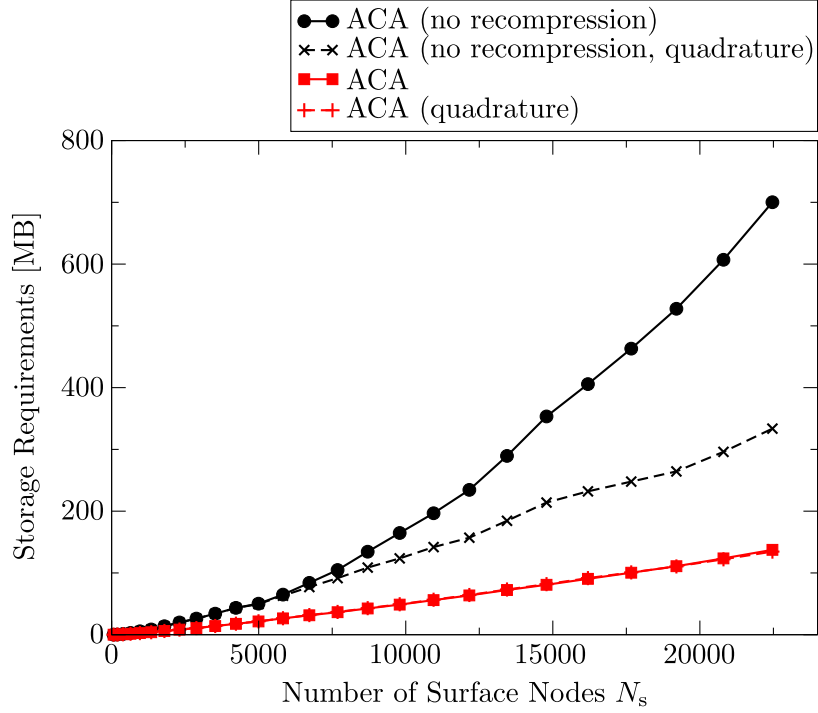


Figure 3.9.: The memory footprint of \mathcal{H} -matrix approximations is given as a function of the number of surface nodes N_s . Additional memory costs due to the storage of the hierarchical tree are included. The graphs with the dashed lines denote computations where Gaussian quadrature (quadrature order 3) has been used to evaluate the matrix elements B_{ij} . Graphs with full lines correspond to computations where the analytical formula (equation 2.55) has been used. The memory footprint of a hierarchical matrix does not depend on the method of evaluating the matrix entries B_{ij} when adaptive recompression is applied. In the figure this is demonstrated using the example of ACA.

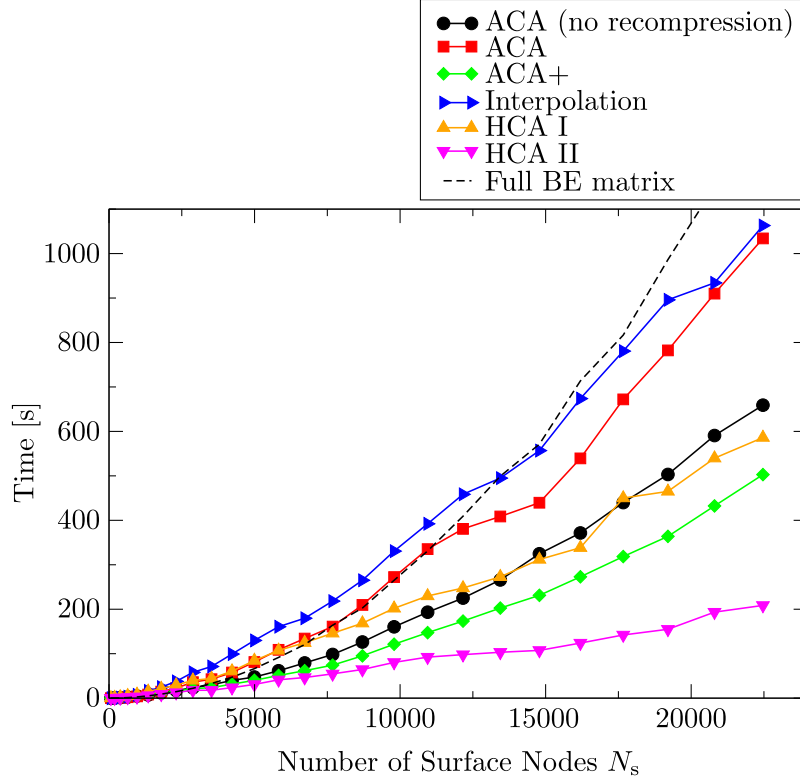


Figure 3.10.: The matrix assembly times of \mathcal{H} -matrix approximations are given as a function of the number of surface nodes N_s . The algorithms, which have been used to assemble \mathcal{H} -matrix approximations are given in the legend. As a comparison the matrix assembly times of the full BE matrices are also given. The data presented in this figure has been obtained from computations, which use the analytical formula (equation 2.55) for the evaluation of the full BE matrix elements B_{ij} .

3. Compression of the boundary element matrix

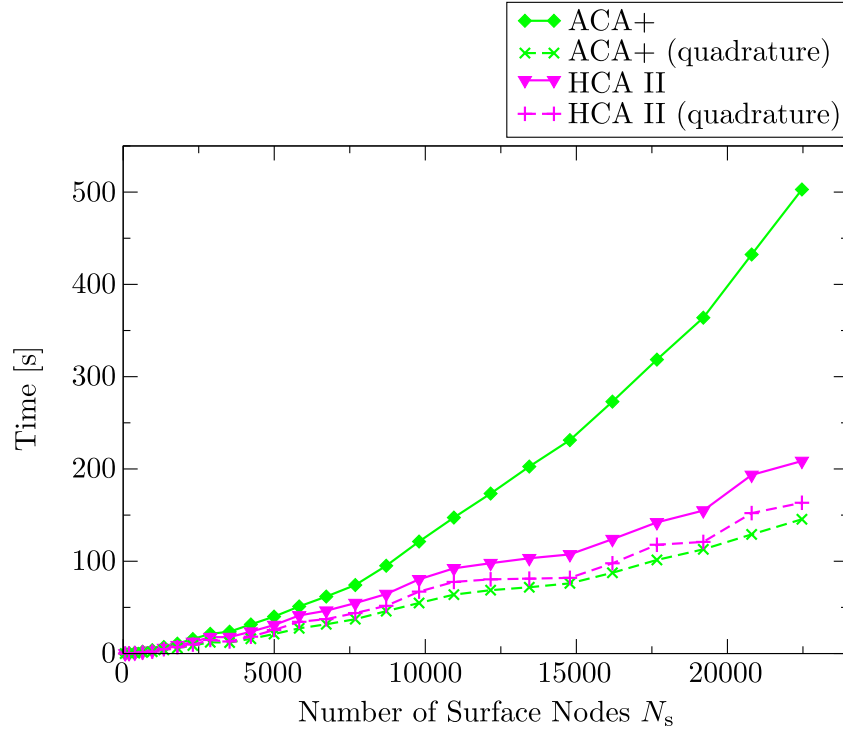


Figure 3.11.: The matrix assembly times of \mathcal{H} -matrix approximations are given as a function of the number of surface nodes N_s . The graphs with the dashed lines denote computations where Gaussian quadrature (quadrature order 3) has been used to evaluate the matrix elements B_{ij} . Graphs with full lines correspond to computations where the analytical formula (equation 2.55) has been used. The influence of the method to evaluate the matrix elements B_{ij} on the matrix assembly time is qualitatively the same for ACA and ACA+ as well as for interpolation, HCA I and HCA II. Therefore, only the results of the algorithms ACA+ and HCA II are shown.

3.2. Efficiency of \mathcal{H} -matrix assembly algorithms

In Figure 3.10 the assembly times of the algorithms are compared. As a general remark one can state that the analytical computation of matrix elements B_{ij} takes more time than Gaussian quadrature with a quadrature order of $q = 3$ (see also Figure 3.11). Please note, that this result only applies for this particular quadrature order. Since the number of quadrature points N_q is equal to q^3 , the complexity of Gaussian quadrature increases significantly with increasing q . As expected, we find that the increase in the assembly time, stemming from the analytical computation of the matrix B_{ij} , is significantly higher for ACA+ than for HCA II (see Figure 3.11). This can be readily explained in terms of the above mentioned fact that, unlike HCA II, ACA+ also uses the analytical formula to build the sub-matrices within admissible leaves. As a consequence, HCA II is the most efficient algorithm in regard to the matrix setup time, when the elements B_{ij} are calculated analytically. Our observation, that the use of equation (2.55) for computing the matrix elements B_{ij} is relatively slow, also seems to comply with earlier investigations. In [70] it is stated that the assembly of hierarchical matrices with ACA (presumably using the formula (2.55) to compute the elements B_{ij}), is clearly slower than a tree code algorithm.

3.2.3. Summary

In this section we have demonstrated the use of hierarchical matrices for the computation of the demagnetisation field in homogeneously magnetised thin, square platelets. The magnetometric demagnetisation factor D_z (equation (3.4)) has been used to estimate the error introduced by the application of hierarchical matrices. By choosing adequate parameter sets for each algorithm, it has been possible to reduce this error significantly (i.e. about one order of magnitude) below the error stemming from the finite element discretisation. Comparing the algorithms for the \mathcal{H} -matrix assembly, interpolation, HCA I and HCA II are more accurate than ACA I and ACA II. The error of the latter two algorithms could not be reduced below $\sim 0.002\%$. Convergence problems of these algorithms have also been discussed in the literature. In the next chapter we will further investigate the effect of errors from \mathcal{H} -matrix approximations on micromagnetic simulations.

The storage requirements can be further reduced by using recompression routines, while the error made by the approximation remains virtually the same. However, dependent on the algorithm, recompression can substantially increase the matrix assembly time. On the other hand, in micromagnetic simulations this should be at least partly compensated by a faster matrix-vector product of the recompressed \mathcal{H} -matrix (not studied here), so that the lower

3. Compression of the boundary element matrix

memory footprint seems to outweigh the higher assembly time.

From the five algorithms, which have been tested in this section, only ACA+ and HCA II have to be considered for the \mathcal{H} -matrix assembly in micromagnetic simulations. This is because HCA II is as accurate as HCA I and interpolation while being more efficient. Especially the use of interpolation is detrimental due to its lengthy \mathcal{H} -matrix assembly times (see also Section 2.3.3). In the same way, ACA and ACA+ show the same accuracy but the \mathcal{H} -matrix setup is faster for ACA+. When choosing between ACA+ and HCA II one has to consider the following points:

1. \mathcal{H} -matrices assembled by ACA+ have a lower memory footprint (about 35 % lower)
2. \mathcal{H} -matrix approximations assembled by HCA II are more accurate
3. ACA+ has the lowest \mathcal{H} -matrix assembly time when the elements B_{ij} are computed numerically. Generally, these have been the fastest \mathcal{H} -matrix assembly times we have found.
4. HCA II has the lowest \mathcal{H} -matrix assembly time when the full BE matrix elements B_{ij} are computed analytically.

In conclusion, the most data-sparse \mathcal{H} -matrices with the lowest assembly time are created by using ACA+ and numerical quadrature (quadrature order $q = 3$). More accurate \mathcal{H} -matrix approximations are created by using HCA II. This advantage may not be significant for the example of this section. However, in Section 3.3 we will see that this changes for a different magnetisation configuration.

3.3. Discussion of Numerical Errors

In the former section (3.2) the efficiency of different algorithms for the assembly of hierarchical matrices has been compared concerning accuracy, matrix assembly time and memory footprint. We have also shown that for the studied system the error introduced by a hierarchical matrix approximation appears to be negligible compared to the error from the finite element discretisation (for example, compare the Figures 3.2 and 3.3). Here we use the term "appears" for various reasons: first, the magnetometric demagnetisation factor D_z , which has been used to estimate the error, does not rigorously define an error for the computation of the vector field \vec{H}_{demag} (see discussion in Section 3.1.2). Second, we have only computed the demagnetisation field for a certain configuration of the magnetisation. However, most micromagnetic simulations will

require the integration of the LLG equation (2.22), involving the subsequent computation of \vec{H}_{demag} for many different configurations of the magnetisation. Thus, errors from the computation of \vec{H}_{demag} may accumulate and lead to wrong results. It is important to test the application of hierarchical matrices with respect to such dynamical simulations. Third, we only have tested hierarchical matrices for thin, square platelets. Their accuracy may also depend on the geometry of the magnetic structure.

In this section we address point 1 and 2 by performing additional numerical tests. Their applicability with respect to a different geometry is demonstrated in Appendix D. However, one should note that such numerical tests can only verify the applicability of hierarchical matrices in micromagnetics. Due to the results of Section 3.2 we will only use the algorithms ACA+ and HCA II. Furthermore, we will evaluate the BE matrix elements $B_{i,j}$ during the \mathcal{H} -matrix assembly analytically using equation (2.55).

3.3.1. FE discretisation in square platelets

Figure 3.2 shows that even without using a hierarchical matrix approximation the deviation of the numerically computed demagnetisation factor D_z from its theoretical value is rather large. In particular, this applies to thin films with a small edge length L . We have computed the demagnetisation field of a homogeneously aligned, in-plane magnetisation along the edge of a thin platelet analytically and with hybrid FEM/BEM. The results are compared in Figure 3.12. The exact solution (dashed line) shows that the y and z -component of the demagnetisation field diverge for $x \rightarrow -50$. The accuracy of the numerical solution clearly increases upon improving the resolution of the mesh. This is due to the occurrence of diverging magnetic fields in corners of cuboidal geometries, an issue which is addressed in Appendix A and in [99]. In the latter article the computation of the demagnetisation field is carried out by a two-dimensional, FFT-based method [95, 100]. As pointed out in this paper, infinite demagnetisation fields do not only occur in artificial configurations of the magnetisation, such as the homogeneous configurations discussed in this chapter, but also in stable micromagnetic configurations and therefore need to be considered. In Section C.2 of Appendix C it is shown that a FFT-based approach to compute the demagnetisation field is very accurate for systems of cuboidal shape and with a homogeneous magnetisation. However, also with this method one would need an infinitely fine grid to take into account the diverging demagnetisation field at the edges. In [99] it is shown that a cubic grid with a cell width of $0.5 \cdot l_{\text{exch}}$, where the exchange length $l_{\text{exch}} = \sqrt{A/K_D}$ is defined in terms of the exchange constant A and the magnetostatic self en-

3. Compression of the boundary element matrix

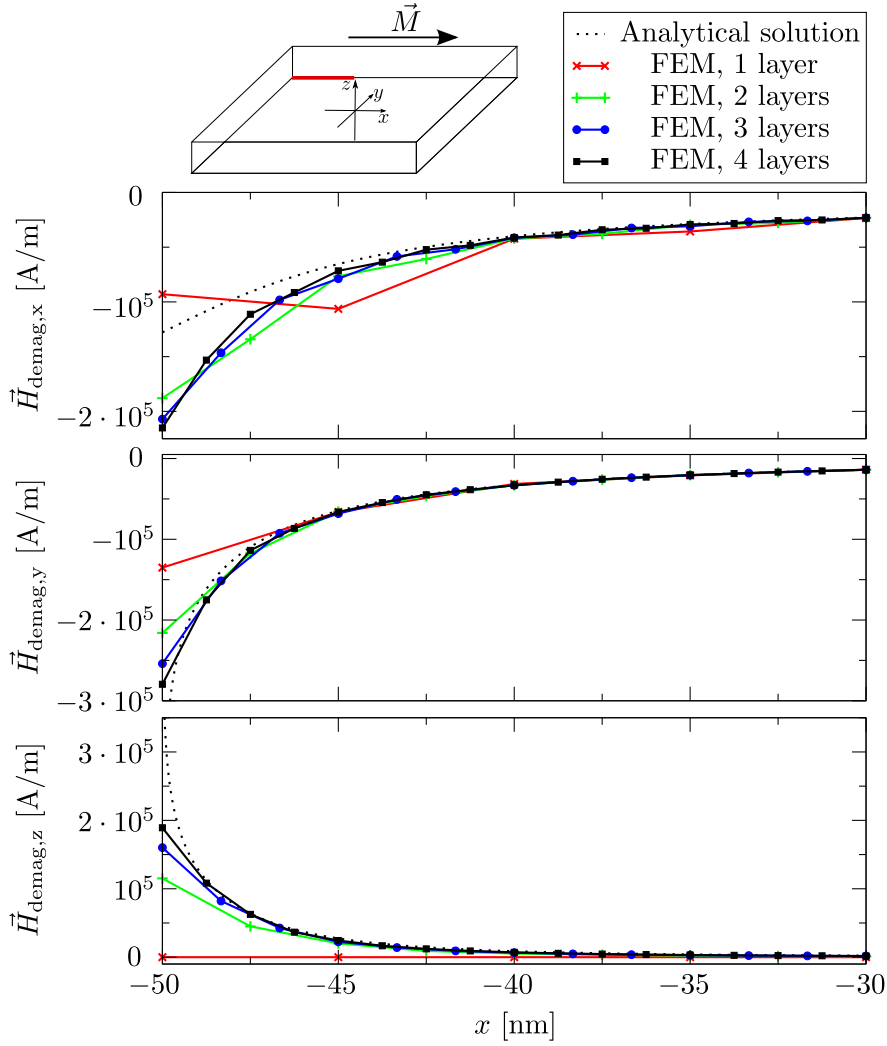


Figure 3.12.: The components of the demagnetisation field are computed along an edge of a thin platelet, which is indicated by the red line in the inset at the top left corner. As indicated by the arrow in the inset, the homogeneous magnetisation points into the positive x -direction. The edge length of the platelet is 100 nm and the thickness is 5 nm. The demagnetisation field is computed by the analytical formula, which has been derived in Appendix C (indicated by the dashed line), and numerically using hybrid FEM/BEM. The unstructured mesh has been derived from cubic grids by using a Kuhn triangulation. Accordingly, the number of layers in the legend refers to the number of cube layers along the z -direction.

ergy $K_d = \frac{\mu_0}{2} \cdot M_S^2$, leads to accurate micromagnetic simulation results for the FFT-based method. In general, the exchange length is an important length scale in the area of micromagnetic simulations. The resolution of FE based simulations, which discretise the magnetic region on a tetrahedral mesh, is usually chosen such that the extension of the tetrahedral elements is below l_{exch} [25, 46, 45]. We will see later (Chapter 4), that, in the case of FE computations, one may have to choose a resolution well below l_{exch} for certain geometries. Table 3.2 compares the results of hybrid FEM/BEM and the FFT on the demagnetisation field of in-plane and out-of-plane magnetisation configurations within a thin, square platelet and reports their rms error (equation (3.5)) with respect to the analytical solution (see Appendix C). The results from the FFT are about 1-2 orders of magnitude more accurate than results from hybrid FEM/BEM. For both methods the rms error is smaller for the out-of-plane configuration. This is due to the fact that for the out-of-plane configuration surface charges on the large square surfaces are created, which in turn create a large demagnetisation field within the entire platelet. Therefore, the errors occurring around the edges of the surface charge carrying surfaces do not have such a big impact on the rms error. On the contrary, the in-plane configuration creates surface charges on two opposing, smaller surfaces, which also lie further apart. The resulting demagnetisation is relatively small, leading to a higher impact of the errors around the edges of the charged surfaces. Table 3.2 also contains results from hybrid FEM/BEM computations using either an unstructured mesh created by a Kuhn triangulation or a mesh created with the automatic mesh generator Netgen. We find that the meshes created by a Kuhn triangulation generally yield more accurate results. Another disadvantage of meshes created with Netgen is that they contain rather many surface nodes, which is the result of a high mesh resolution on the surface. The unstructured mesh of table 3.2, which has been created with a Kuhn triangulation of a cubic grid with 4 cubes over the thickness of the platelet, contains 32805 volume nodes and 14082 surface nodes. The equivalent Netgen grid contains 32912 volume nodes and 21700 surface nodes. In terms of the memory footprint of the full BE matrix 14082 surface nodes correspond to 1.48 GB and 21700 surface nodes to 3.51 GB. Similarly, meshes created by commercial software tool Fluent Gambit 2.4.6. contain fewer surface nodes than equivalent Netgen meshes. This demonstrates that the efficiency of hybrid FEM/BEM is strongly dependent on the used mesh. However, this strong dependence is reduced when matrix compression techniques are used.

We have now seen that, due to the occurrence of diverging demagnetisation fields at the edges, hybrid FEM/BEM may lead to substantial errors in the calculation of the demagnetisation field in cuboidal systems. However, FE-based

3. Compression of the boundary element matrix

magnetisation	resolution	Hy. FEM/BEM ^a	Hy. FEM/BEM ^b	FFT ^c
out-of-plane	1 layer	4.035	4.426	0.011
	2 layers	2.692	4.225	0.122
	3 layers	2.528	3.266	—
	4 layers	1.870	3.113	0.061
in-plane	1 layer	32.731	35.339	0.289
	2 layers	22.624	30.749	0.790
	3 layers	19.482	22.779	—
	4 layers	13.286	18.506	0.382

^a Unstructured mesh created with a Kuhn triangulation [62].

^b Unstructured mesh created with the automatic mesh generator Netgen [101].

^c FFT performed with OOMMF [102].

Table 3.2.: The rms error δ_{rms} (see equation (3.5)) in the demagnetising field with respect to the analytical solution (equations (C.15) to (C.17)) has been computed for different numerical methods, mesh resolutions and directions of the magnetisation. Mesh nodes on the edges of surface charge carrying surfaces have not been considered for the computation of the rms error, as the exact demagnetisation field diverges at these points, leading to an infinite error. The studied geometry is a thin, square platelet with an edge length of 100 nm and a thickness of 5 nm. The direction of the homogeneous magnetisation points either out-of-plane (z -direction in Figure 3.1) or in-plane (x -direction in Figure 3.1). The demagnetisation field has been computed with hybrid FEM/BEM, discretised on an unstructured mesh, and with the FFT on a cubic grid. To test the influence of the unstructured mesh on the accuracy of hybrid FEM/BEM the mesh has been created in two ways, by a Kuhn triangulation and with the automatic mesh generator Netgen. The characterisation of the mesh resolution in terms of the number of cube/tetrahedron layers is straightforward for a FFT grid and an unstructured mesh created by a Kuhn triangulation. For the unstructured meshes, which have been created with Netgen, there is no distinct number of tetrahedron layers as the resolution varies spatially. Therefore, we have created Netgen meshes, which contain about the same number of volume nodes as the corresponding meshes created with a Kuhn triangulation.

micromagnetic simulations have already been used to describe the properties of particles of such a geometry [103, 91, 104, 33, 34, 45]. In particular, hybrid FEM/BEM has been used in [91, 45]. Although we have only studied hybrid FEM/BEM in this chapter, any kind of finite element discretisation should lead to similar errors.

We now want to verify the applicability of micromagnetic, FE based simulations to a thin square platelet, which will also give us some insight into its general applicability to cuboidal shapes. In this thesis micromagnetic simulations are only employed to relax a magnetic system to its ground state, i.e. there are no dynamic simulations with an experimentally determined value of the Gilbert damping constant. Therefore, we will only focus on such relaxations. As a test system we have choose a thin, square platelet with an edge length of 100 nm and a thickness of 5 nm. In our simulations, the exchange constant is set to $A = 1.571 \times 10^{-11} \text{ Jm}^{-1}$ and the saturation magnetisation to $M_s = 10^6 \text{ Am}^{-1}$. These parameters do not correspond to an actual material, but have been chosen such that the exchange length $l_{\text{exch}} = \sqrt{A/K_D}$ is equal to the thickness of the platelet, namely 5 nm. Initially, the magnetisation of the system is homogeneously aligned along the randomly chosen directions (0.265, 0.450, 0.100) or (0.034, 0.021, 1.000) and then relaxed to a stable configuration using the Landau-Lifshitz-Gilbert equation (equation (2.22)). We find that in all simulations the system relaxes to a configuration shown in Figure 3.13, where the spatially averaged magnetisation aligns along the diagonal of the platelet. One refers to this configuration as the so called leaf or onion state. In [105] it is shown that the onion state is the energetic ground state for the chosen geometry and material parameters, thus confirming our findings. In the tables 3.3 and 3.4 the spatially averaged magnetisation of the relaxed configuration is given for FD and FE based simulations and different mesh resolutions. At the given accuracy the spatially averaged magnetisation converges towards a vector of the form $(-0.6943, 0.6891, 5.6 \times 10^{-5})$ when increasing the grid resolution of the FD simulations. Due to the symmetry of the system 16 equivalent solutions exist. The relaxation from both initial configurations leads to such equivalent solutions. The finite element simulations show the qualitatively correct results (onion state). Quantitatively, the deviation of the resulting, spatially averaged magnetisation from a corresponding FD result is less than 1 %, which is also in line with [96]. When relaxing the system from the out-of-plane configuration (see table 3.4) FD and FE simulations relax to different onion states. From this one may argue that micromagnetic FE simulations are not suited to study the dynamics within a cuboidal system. However, in order to align the magnetisation homogeneously (as in the initial configuration) one has to apply a strong external magnetic

3. Compression of the boundary element matrix

resolution	$\langle \vec{M} \rangle / M_s$		
	FDM ^a	FEM ^b	FEM ^c
1 layer	$\begin{pmatrix} 0.6894 \\ 0.6947 \\ 5.6 \cdot 10^{-5} \end{pmatrix}$	$\begin{pmatrix} 0.6973 \\ 0.6933 \\ -5.9 \cdot 10^{-5} \end{pmatrix}$	$\begin{pmatrix} 0.6972 \\ 0.6935 \\ -2.4 \cdot 10^{-4} \end{pmatrix}$
2 layers	$\begin{pmatrix} 0.6892 \\ 0.6944 \\ 5.6 \cdot 10^{-5} \end{pmatrix}$	$\begin{pmatrix} 0.6933 \\ 0.6922 \\ -5.7 \cdot 10^{-5} \end{pmatrix}$	$\begin{pmatrix} 0.6920 \\ 0.6934 \\ -1.1 \cdot 10^{-4} \end{pmatrix}$
3 layers	-	$\begin{pmatrix} 0.6932 \\ 0.6912 \\ -5.4 \cdot 10^{-5} \end{pmatrix}$	$\begin{pmatrix} 0.6934 \\ 0.6910 \\ -7.2 \cdot 10^{-5} \end{pmatrix}$
4 layers	$\begin{pmatrix} 0.6891 \\ 0.6943 \\ 5.6 \cdot 10^{-5} \end{pmatrix}$	$\begin{pmatrix} 0.6930 \\ 0.6910 \\ -5.4 \cdot 10^{-5} \end{pmatrix}$	$\begin{pmatrix} 0.6932 \\ 0.6905 \\ -6.5 \cdot 10^{-5} \end{pmatrix}$
8 layers	$\begin{pmatrix} 0.6891 \\ 0.6943 \\ 5.6 \cdot 10^{-5} \end{pmatrix}$	-	-

^a Simulation performed with OOMMF

^b Simulation performed with Nmag on a mesh created by a Kuhn triangulation

^c Simulation performed with Nmag on a mesh created with Netgen

Table 3.3.: The average magnetisation $\langle \vec{M} \rangle / M_s$ within a thin, square platelet is given. The platelet has an edge length of 100 nm and a thickness of 5 nm. Initially the magnetisation is aligned with the vector (0.265, 0.450, 0.100) and then relaxed to a stable micromagnetic configurations using different numerical methods and mesh resolutions. The exchange constant is set to $A = 1.571 \times 10^{-11} \text{ Jm}^{-1}$, the saturation magnetisation to $M_s = 10^6 \text{ Am}^{-1}$ and the Gilbert damping constant to $\alpha = 1$. We have used the FD (finite difference) based solver OOMMF [102] and the FE (finite element) based solver Nmag [93]. The FE based simulations have been performed on meshes, which have been created with two different methods: with a Kuhn triangulation [62] and with the automatic mesh generator Netgen [101]. The characterisation of the mesh resolution in terms of the number of cube/tetrahedron layers is straightforward for a FFT grid and an unstructured mesh created by a Kuhn triangulation. For the unstructured meshes, which have been created with Netgen, there is no distinct number of tetrahedron layers as the resolution varies spatially. Therefore, we have created Netgen meshes, which contain about the same number of volume nodes as the corresponding meshes created with a Kuhn triangulation.

resolution	$\langle \vec{M} \rangle / M_s$		
	FDM ^a	FEM ^b	FEM ^c
1 layer	$\begin{pmatrix} -0.6947 \\ 0.6894 \\ 5.5 \cdot 10^{-5} \end{pmatrix}$	$\begin{pmatrix} 0.6930 \\ -0.6976 \\ -6.1 \cdot 10^{-5} \end{pmatrix}$	$\begin{pmatrix} 0.6924 \\ -0.6983 \\ 2.4 \cdot 10^{-4} \end{pmatrix}$
2 layers	$\begin{pmatrix} -0.6944 \\ 0.6892 \\ 5.6 \cdot 10^{-5} \end{pmatrix}$	$\begin{pmatrix} 0.6906 \\ -0.6950 \\ -5.6 \cdot 10^{-5} \end{pmatrix}$	$\begin{pmatrix} 0.6914 \\ -0.6941 \\ 1.9 \cdot 10^{-5} \end{pmatrix}$
3 layers	-	$\begin{pmatrix} 0.6908 \\ -0.6937 \\ -5.3 \cdot 10^{-5} \end{pmatrix}$	$\begin{pmatrix} 0.6912 \\ -0.6932 \\ -3.1 \cdot 10^{-5} \end{pmatrix}$
4 layers	$\begin{pmatrix} -0.6943 \\ 0.6891 \\ 5.6 \cdot 10^{-5} \end{pmatrix}$	$\begin{pmatrix} 0.6906 \\ -0.6934 \\ -5.4 \cdot 10^{-5} \end{pmatrix}$	$\begin{pmatrix} 0.6909 \\ -0.6928 \\ -5.5 \cdot 10^{-5} \end{pmatrix}$
8 layers	$\begin{pmatrix} -0.6943 \\ 0.6891 \\ 5.6 \cdot 10^{-5} \end{pmatrix}$	-	-

^a Simulation performed with OOMMF

^b Simulation performed with Nmag on a mesh created by a Kuhn triangulation

^c Simulation performed with Nmag on a mesh created with Netgen

Table 3.4.: The average magnetisation $\langle \vec{M} \rangle / M_s$ within a thin, square platelet is given. The platelet has an edge length of 100 nm and a thickness of 5 nm. Initially the magnetisation is aligned with the vector (0.034, 0.021, 1.000) and then relaxed to a stable micromagnetic configurations using different numerical methods and mesh resolutions. The exchange constant is set to $A = 1.571 \times 10^{-11} \text{ Jm}^{-1}$, the saturation magnetisation to $M_s = 10^6 \text{ Am}^{-1}$ and the Gilbert damping constant to $\alpha = 1$. We have used the FD (finite difference) based solver OOMMF [102] and the FE (finite element) based solver Nmag [93]. The FE based simulations have been performed on meshes, which have been created with two different methods: with a Kuhn triangulation [62] and with the automatic mesh generator Netgen [101]. The characterisation of the mesh resolution in terms of the number of cube/tetrahedron layers is straightforward for a FFT grid and an unstructured mesh created by a Kuhn triangulation. For the unstructured meshes, which have been created with Netgen, there is no distinct number of tetrahedron layers as the resolution varies spatially. Therefore, we have created Netgen meshes, which contain about the same number of volume nodes as the corresponding meshes created with a Kuhn triangulation.

3. Compression of the boundary element matrix

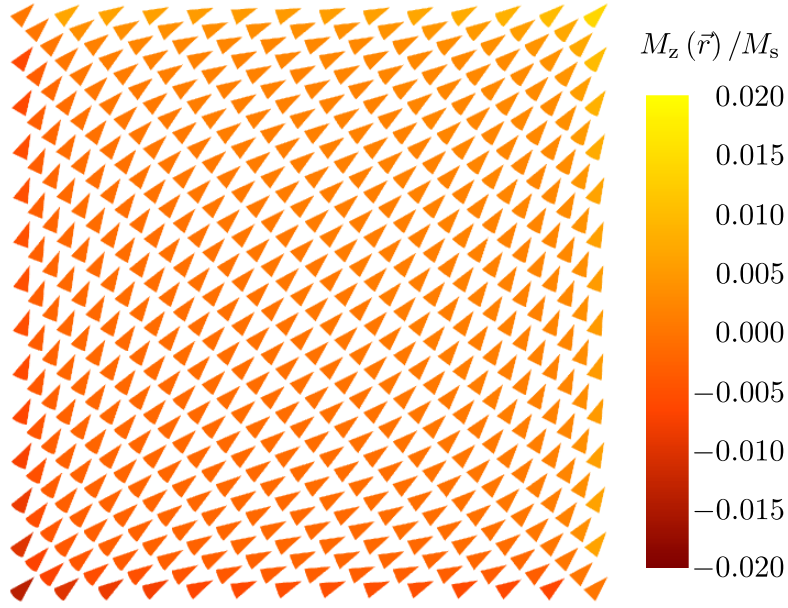


Figure 3.13.: Onion state in a thin, square platelet (edge length 100 nm, thickness 5 nm). The z -direction corresponds to the out-of-plane direction of the platelet. The legend shows the z -component of the normalised magnetisation. The plot has been made from relaxation data obtained with OOMMF (see table 3.3, 2 layers).

field. The process of switching off a magnetic field occurs at a much longer time scale ($\gtrsim \mu\text{s}$, see for example [106]) than the magnetisation dynamics ($\sim \text{ps}$). Therefore, a homogeneous magnetisation in the absence of an external field does not correspond to a realistic scenario. However, a more realistic scenario can be achieved by applying a strong magnetic field along a certain direction, systematically reducing the external magnetic field in discrete, small steps and letting the magnetisation relax after each step. As a test case we investigate the magnetic reversal in a thin, square platelet (edge length 100 nm and thickness 5 nm) by reducing the external magnetic field to zero and then increasing it in opposite direction to its initial absolute value. The physically most interesting part of such simulations is typically located at low external fields, where the interplay between the micromagnetic energy contributions becomes important and the magnetic state of the system may already change through small variations of the external field. Therefore, at low external field values one usually reduces the step size of the external field variation. For our test simulations (Figure 3.14 and 3.15) we have chosen a rather coarse minimal step size of 10 mT ($\equiv 100 \text{ Oe}$). The results are shown in the Figures 3.14 and 3.15, where the components of the spatially averaged magnetisation are plotted as a function of the external field strength. The external field has been aligned along the directions (0.265, 0.450, 0.100) (Figure 3.14) and (0.034, 0.021, 1.000) (Figure 3.15). For brevity we will refer to the former direc-

tion as in-plane direction and to the latter one as out-of-plane direction. The comparison of the simulation results obtained with Nmag and OOMMF yields a good qualitative agreement. At remanence (i.e. at $\vec{H}_{\text{ext}} = 0 \text{ T}$) we obtain an onion state as shown in Figure 3.13 for all simulations. We do not want to concentrate on other intermediate micromagnetic configurations, as our main concern lies with the accuracy of the finite element simulations. There is a clear quantitative difference in the simulation results shown in Figure 3.15. The jumps in the x and y component of the averaged magnetisation occur at different values of the external field, the difference being 20 mT or two steps in the external field. As corners act as nucleation centres for the reversal process in platelets [107], this difference seems to be due to the fact that the FFT computation of \vec{H}_{demag} around the edges of the platelet is more accurate than a corresponding hybrid FEM/BEM computation.

3.3.2. Hierarchical matrices in FE simulation of thin platelets

In this section we will discuss the error, which arises when the BE matrix of the hybrid FEM/BEM is approximated by a hierarchical matrix. From Section 3.3.1 we know that using hybrid FEM/BEM to compute the demagnetisation field is rather inaccurate for certain homogeneous configurations of the magnetisation. This is due to the diverging demagnetisation field at the edges of surface charge carrying surfaces. These inaccuracies may also lead to quantitative errors in the computation of the magnetisation reversal as discussed in Section 3.3.1. Table 3.5 shows the rms error in the demagnetisation field of homogeneous in-plane and out-of-plane configurations in a thin square platelet, which is due to the use of hierarchical matrices. The parameters sets of section 3.2 have been used. The rms error is about two orders of magnitude larger for the in-plane configuration than for the out-of-plane configuration. As already discussed in Section 3.3.1 this is also due to the, on average, smaller demagnetisation field of the in-plane configuration. The observation of the Sections 3.2.1 and 3.2.2, that the assembly of a hierarchical matrix by HCA II leads to more accurate results than the assembly by ACA+, is also verified by the data of table 3.5. Furthermore, disregarding the results for ACA+ and a resolution of one tetrahedron layer, there is no crucial dependence of the error due to a hierarchical matrix approximation on the mesh resolution. Table 3.6 shows the rms error in the demagnetisation field from using hierarchical matrices assembled with ACA+ and HCA II and different parameter sets. We find that the accuracy of ACA+ cannot be reduced below a certain level. This seems to verify the convergence problems of ACA+ which have been discussed in Section 2.3.3. In Figure 3.16 the difference between the demagnetisation field, which has been computed with hybrid FEM/BEM

3. Compression of the boundary element matrix

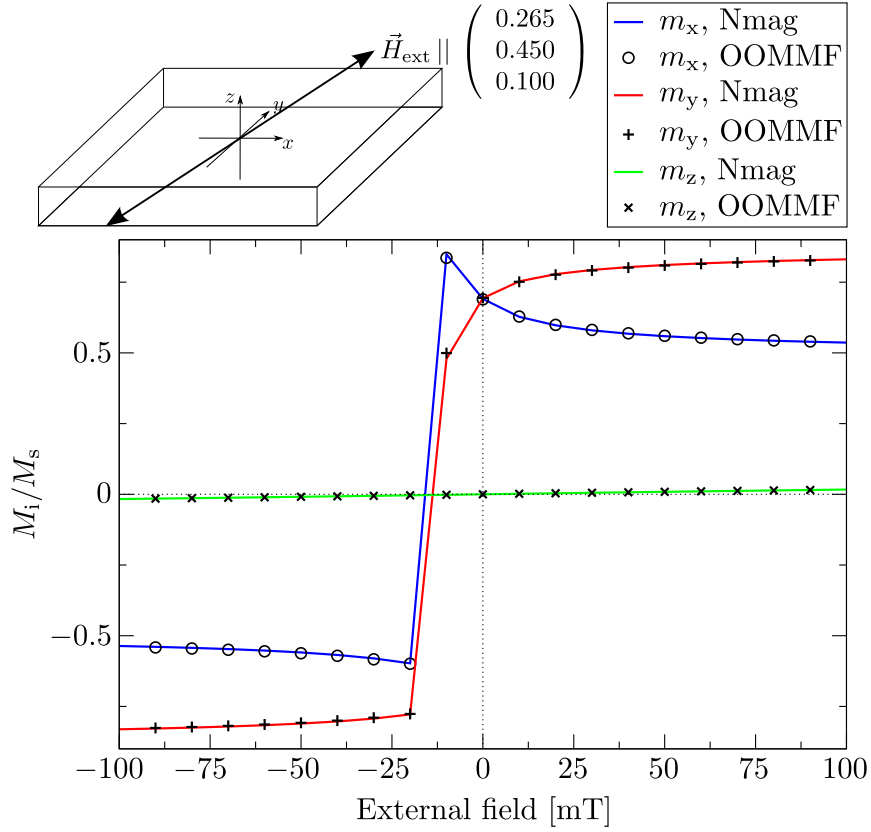


Figure 3.14.: The FDM based solver OOMMF and the FEM based solver Nmag are used to compute the magnetic reversal behaviour within a thin square platelet (edge length 100 nm, thickness 5 nm). The exchange constant is set to $A = 1.571 \times 10^{-11} \text{ Jm}^{-1}$, the saturation magnetisation to $M_s = 10^6 \text{ Am}^{-1}$ and the Gilbert damping constant to $\alpha = 1$. The external magnetic field is aligned along the direction denoted in the inset on the top left and changed in steps of 200 mT between 3 T and 1 T, in steps of 50 mT between 1 T and 200 mT and in steps of 10 mT between 200 mT and 0 mT (for negative field values equivalently). The simulation with Nmag has been performed on an unstructured mesh with three tetrahedron layers along the z -direction. This mesh has been created with a Kuhn triangulation. The FDM based simulation (OOMMF) has been performed on a grid with two cubic layers along the z -direction.

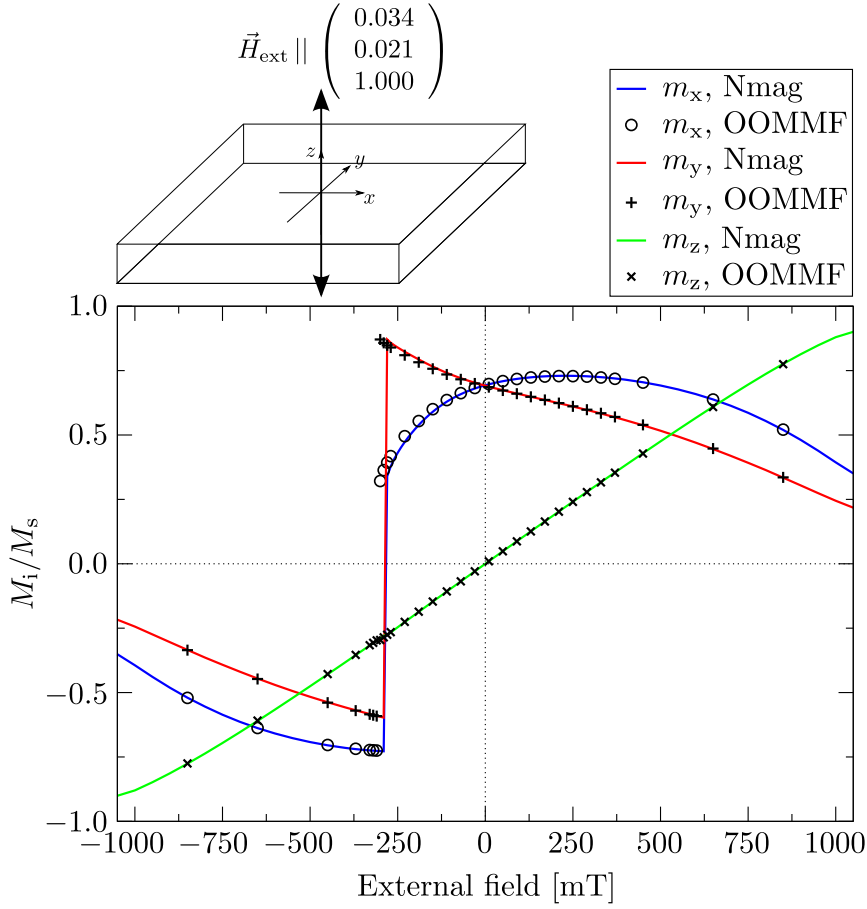


Figure 3.15.: The FDM based solver OOMMF and the FEM based solver Nmag are used to compute the magnetic reversal behaviour within a thin square platelet (edge length 100 nm, thickness 5 nm). The exchange constant is set to $A = 1.571 \times 10^{-11} \text{ Jm}^{-1}$, the saturation magnetisation to $M_s = 10^6 \text{ Am}^{-1}$ and the Gilbert damping constant to $\alpha = 1$. The external magnetic field is aligned along the denoted directions (see inset on top left) and changed in steps of 200 mT between 3 T and 1 T, in steps of 50 mT between 1 T and 400 mT and in steps of 10 mT between 400 mT and 0 mT (for negative field values equivalently). The simulation with Nmag has been performed on an unstructured mesh with three tetrahedron layers along the z -direction. This mesh has been created with a Kuhn triangulation. The FDM based simulation (OOMMF) has been performed on a grid with two cubic layers along the z -direction. Outside the external field range between 270 mT and 330 mT only every 4th data point from the OOMMF simulation results is considered, thus improving the readability of the figure.

3. Compression of the boundary element matrix

resolution	in-plane		out-of-plane	
	ACA+ ^a	HCA II ^b	ACA+ ^a	HCA II ^b
1 layer	0.3199	0.3176	0.004582	0.004546
2 layers	2.566	0.3487	0.01578	0.003600
3 layers	1.614	0.4510	0.01439	0.004925
4 layers	2.172	0.4989	0.01967	0.005099

^a Parameters: $\epsilon = 10^{-3}$, $\epsilon_{aca} = 10^{-4}$, $q = 3$

^b Parameters: $\epsilon = 10^{-3}$, $\epsilon_{aca} = 10^{-7}$, $p = 4$, $q = 3$

Table 3.5.: The rms error δ_{rms} (equation (3.5)) in the demagnetisation field stemming from a hierarchical matrix approximation is given for two homogeneous configurations of the magnetisation (out-of-plane, in-plane) in a thin, square platelet (edge length 100 nm, thickness 5 nm). The most efficient algorithms, ACA+ and HCA II, with the specified parameter sets (see also Section 3.2), are used to assemble the hierarchical matrices. The mesh has been created with a Kuhn triangulation from a corresponding cubic grid. The number of layers of the cubic grid along the z -direction is used to characterise different mesh resolutions.

HCA II			ACA+			Rms Error [%]
ϵ	ϵ_{aca}	p	ϵ	ϵ_{aca}	k_{max}	
10^{-3}	10^{-7}	4	-	-	-	0.4989
10^{-3}	10^{-8}	7	-	-	-	0.4981
10^{-6}	10^{-7}	4	-	-	-	0.06774
10^{-6}	10^{-8}	7	-	-	-	0.000366
-	-	-	10^{-3}	10^{-4}	500	2.172
-	-	-	10^{-3}	10^{-7}	500	1.811
-	-	-	10^{-6}	10^{-7}	500	1.748
-	-	-	10^{-6}	10^{-9}	500	1.748
-	-	-	10^{-6}	10^{-9}	1000	1.748

Table 3.6.: Convergence tests of the algorithms HCA II and ACA+. The demagnetisation field of an in-plane magnetisation within a thin, square platelet (edge length 100 nm, thickness 5 nm) is computed. The field is computed with hybrid FEM/BEM using a \mathcal{H} -matrix approximation. The rms error is defined with respect to the result of the corresponding hybrid FEM/BEM computation using the full BE matrix. The simulations have been performed on a mesh, which has been created with a Kuhn triangulation from a cubic grid with 4 layers along the z -direction.

resolution	$\langle \vec{M} \rangle / M_s$		
	full BE matrix	HCA II ^a	ACA+ ^b
1 layer	$\begin{pmatrix} 0.6973 \\ 0.6933 \\ -5.9 \cdot 10^{-5} \end{pmatrix}$	$\begin{pmatrix} 0.6978 \\ 0.6928 \\ -6.2 \cdot 10^{-5} \end{pmatrix}$	$\begin{pmatrix} 0.6979 \\ 0.6927 \\ -6.8 \cdot 10^{-5} \end{pmatrix}$
2 layers	$\begin{pmatrix} 0.6933 \\ 0.6922 \\ -5.7 \cdot 10^{-5} \end{pmatrix}$	$\begin{pmatrix} 0.6933 \\ 0.6923 \\ -5.9 \cdot 10^{-5} \end{pmatrix}$	$\begin{pmatrix} 0.6933 \\ 0.6923 \\ 5.0 \cdot 10^{-5} \end{pmatrix}$
3 layers	$\begin{pmatrix} 0.6932 \\ 0.6912 \\ -5.4 \cdot 10^{-5} \end{pmatrix}$	$\begin{pmatrix} 0.6939 \\ 0.6906 \\ -7.3 \cdot 10^{-5} \end{pmatrix}$	$\begin{pmatrix} 0.6933 \\ 0.6913 \\ -2.7 \cdot 10^{-4} \end{pmatrix}$
4 layers	$\begin{pmatrix} 0.6930 \\ 0.6910 \\ -5.4 \cdot 10^{-5} \end{pmatrix}$	$\begin{pmatrix} 0.6933 \\ 0.6907 \\ -5.4 \cdot 10^{-5} \end{pmatrix}$	$\begin{pmatrix} 0.6935 \\ 0.6905 \\ -3.6 \cdot 10^{-4} \end{pmatrix}$

^a parameters: $\epsilon = 10^{-3}$, $\epsilon_{aca} = 10^{-7}$, $p = 4$

^b parameters: $\epsilon = 10^{-3}$, $\epsilon_{aca} = 10^{-4}$

Table 3.7.: The spatially averaged magnetisation $\langle \vec{M} \rangle / M_s$ within a thin, square platelet is given. The platelet has an edge length of 100 nm and a thickness of 5 nm. Initially the magnetisation is homogeneously aligned with the vector (0.265, 0.450, 0.100) and then relaxed to a stable micromagnetic configuration using hybrid FEM/BEM with different expressions for the BE matrix (full BE matrix, hierarchical matrix approximations assembled through ACA+ or HCA II). The exchange constant is set to $A = 1.571 \times 10^{-11} \text{ Jm}^{-1}$ and the saturation magnetisation to $M_s = 10^6 \text{ Am}^{-1}$. Different mesh resolutions are chosen. The characterisation of the mesh resolution in terms of the number of tetrahedron layers along the z -direction is straightforward for these unstructured meshes, as they have been created with a Kuhn triangulation.

using different hierarchical matrix approximations, and the demagnetisation field, which has been computed with hybrid FEM/BEM using the full BE matrix, is shown along a line through the platelet. We see that, in a certain region, there is a substantial deviation from the solution, obtained without a hierarchical matrix approximation, when the hierarchical matrix has been assembled with ACA+. These deviations cannot be reduced by fine-tuning the parameters ϵ and ϵ_{aca} , as the comparison of the black (ACA+, $\epsilon = 10^{-3}$ and $\epsilon_{aca} = 10^{-4}$) and red (ACA+, $\epsilon = 10^{-6}$ and $\epsilon_{aca} = 10^{-7}$) curve shows. Thus, deviations of this kind seem to lead to corresponding convergence problems observed in the rms error.

Figure 3.17 shows equipotential surfaces of the magnetic scalar potential $\phi(\vec{r})$

3. Compression of the boundary element matrix

resolution	$\langle \vec{M} \rangle / M_s$		
	full BE matrix	HCA II ^a	ACA+ ^b
1 layer	$\begin{pmatrix} 0.6930 \\ -0.6976 \\ -6.1 \cdot 10^{-5} \end{pmatrix}$	$\begin{pmatrix} 0.6934 \\ -0.6972 \\ -6.2 \cdot 10^{-5} \end{pmatrix}$	$\begin{pmatrix} 0.6933 \\ -0.6972 \\ -5.9 \cdot 10^{-5} \end{pmatrix}$
2 layers	$\begin{pmatrix} 0.6906 \\ -0.6950 \\ -5.6 \cdot 10^{-5} \end{pmatrix}$	$\begin{pmatrix} 0.6906 \\ -0.6950 \\ -5.7 \cdot 10^{-5} \end{pmatrix}$	$\begin{pmatrix} 0.6903 \\ -0.6953 \\ -3.3 \cdot 10^{-5} \end{pmatrix}$
3 layers	$\begin{pmatrix} 0.6908 \\ -0.6937 \\ -5.3 \cdot 10^{-5} \end{pmatrix}$	$\begin{pmatrix} 0.6909 \\ -0.6935 \\ -5.2 \cdot 10^{-5} \end{pmatrix}$	$\begin{pmatrix} 0.6906 \\ -0.6939 \\ -1.3 \cdot 10^{-4} \end{pmatrix}$
4 layers	$\begin{pmatrix} 0.6906 \\ -0.6934 \\ -5.4 \cdot 10^{-5} \end{pmatrix}$	$\begin{pmatrix} 0.6910 \\ -0.6931 \\ -5.3 \cdot 10^{-5} \end{pmatrix}$	$\begin{pmatrix} 0.6915 \\ -0.6925 \\ -5.4 \cdot 10^{-4} \end{pmatrix}$

^a parameters: $\epsilon = 10^{-3}$, $\epsilon_{aca} = 10^{-7}$, $p = 4$

^b parameters: $\epsilon = 10^{-3}$, $\epsilon_{aca} = 10^{-4}$

Table 3.8.: The spatially averaged magnetisation $\langle \vec{M} \rangle / M_s$ within a thin, square platelet is given. The platelet has an edge length of 100 nm and a thickness of 5 nm. Initially the magnetisation is homogeneously aligned with the vector (0.034, 0.021, 1.000) and then relaxed to a stable micromagnetic configuration using hybrid FEM/BEM with different expressions for the BE matrix (full BE matrix, hierarchical matrix approximations assembled through ACA+ or HCA II). The exchange constant is set to $A = 1.571 \times 10^{-11} \text{ Jm}^{-1}$ and the saturation magnetisation to $M_s = 10^6 \text{ Am}^{-1}$. Different mesh resolutions are chosen. The characterisation of the mesh resolution in terms of the number of tetrahedron layers along the z -direction is straightforward for these unstructured meshes, as they have been created with a Kuhn triangulation.

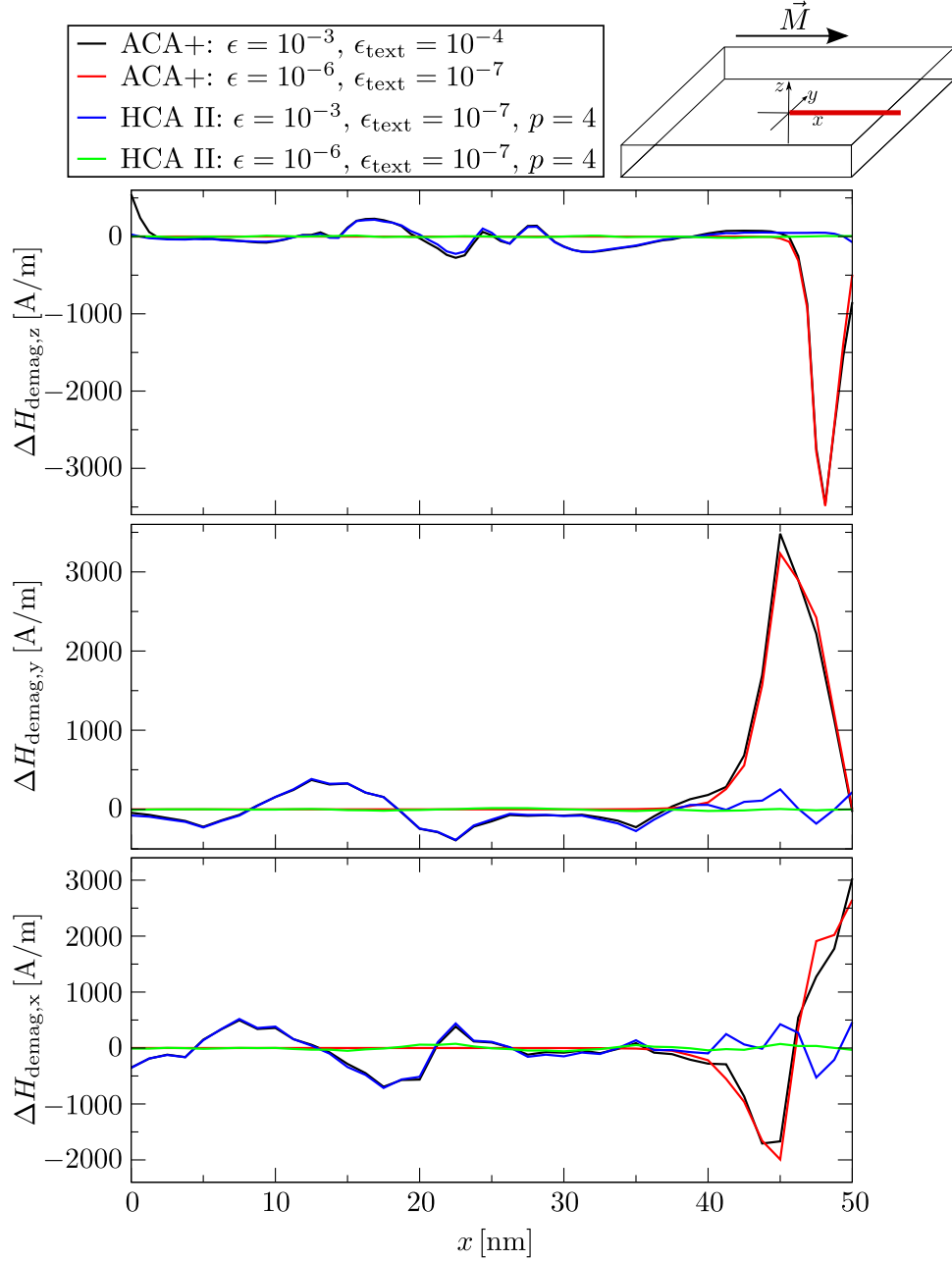


Figure 3.16.: Difference between the demagnetisation fields calculated with hybrid FEM/BEM using hierarchical matrix approximations, assembled through different algorithms and parameter sets, and hybrid FEM/BEM using the full BE matrix. The system is a homogeneously magnetised square platelet (edge length 100 nm, thickness 5 nm) and the field is computed along the line indicated in the sketch at the top-right corner. To put these deviations into a perspective: the demagnetisation field, as computed with hybrid FEM/BEM, is 22500 A/m at $x = 0$ nm and increases to 413000 A/m at $x = 50$ nm.

3. Compression of the boundary element matrix

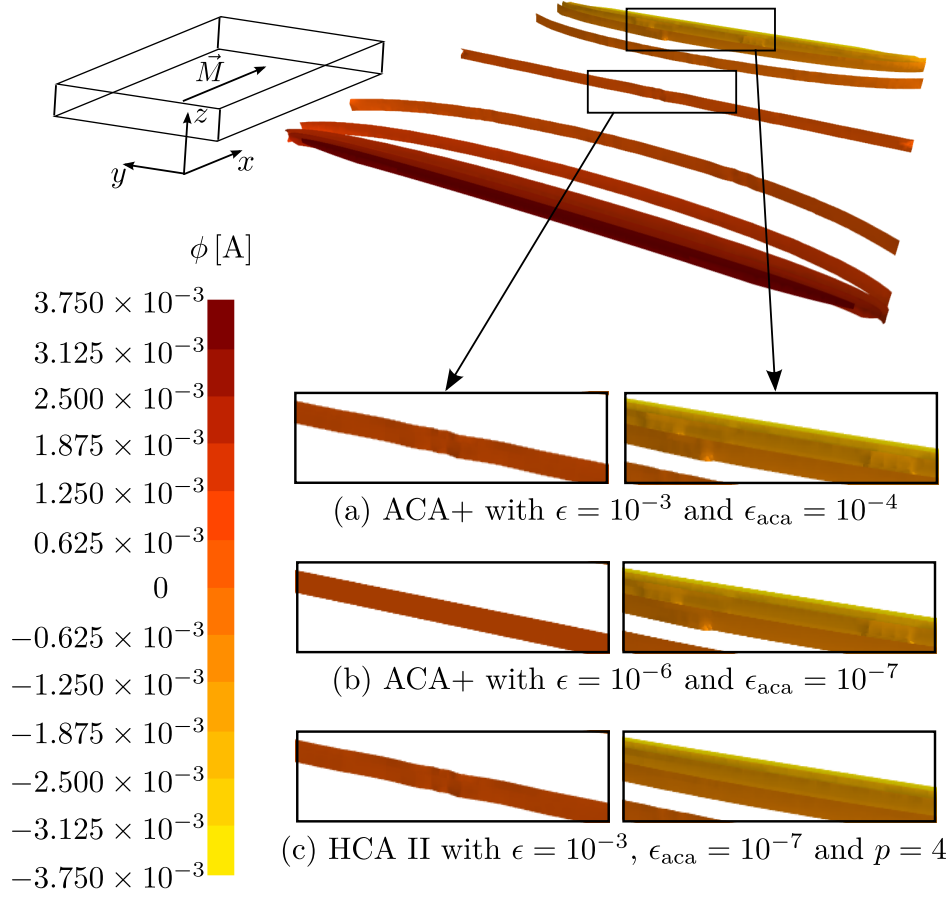


Figure 3.17.: The magnetic scalar potential is computed using the hybrid FEM/BEM for a homogeneous magnetisation along the x -direction within a thin square platelet (see inset on the top left). The platelet's edge length is 200 nm and its thickness is 5 nm. The BE matrix has been approximated by a hierarchical matrix, which is assembled through different algorithms and parameter sets (see (a) to (c)). (a) Equipotential surfaces of the magnetic scalar potential are shown in the region of the thin platelet and magnified within the highlighted boxes. (b) and (c): only the magnified segments are shown. The mesh has been created from a cubic grid (with 3 layers along the z -direction) by using a Kuhn triangulation. Please note that for illustrating the equipotential surface shading effects are used, so that their colours do not rigorously correspond to the colour scheme on the colour bar.

in a thin, square platelet with a homogeneous in-plane magnetisation. These have been computed with hybrid FEM/BEM using hierarchical matrices assembled through ACA+ and HCA II with the parameter sets of table 3.1 (3.17(a) and (c)) and through ACA+ with smaller values for the parameter ϵ and ϵ_{aca} (3.17(b)). Here, the inaccuracy of ACA+ appears in form of locally confined fluctuations in the equipotential surfaces (see the magnified images on the right of Figure 3.17(a) and (b)). Outside of these regions \mathcal{H} -matrices assembled through ACA+ lead to about the same accuracy as \mathcal{H} -matrices assembled through HCA II. Especially we can reduce fluctuations, occurring for ACA+ and HCA II with the parameter choices of table 3.1, by reducing the parameter ϵ from 10^{-3} to 10^{-6} , i.e. increasing the accuracy of the adaptive recompression (see Section 2.3.3). This can be seen in Figure 3.17 where the use of ACA+ with the parameter choices $\epsilon = 10^{-6}$ and $\epsilon_{aca} = 10^{-7}$ leads to smoother equipotential surfaces at the centre of the platelet (compare the left image of (a) and (b)). Likewise we see a substantial reduction in the fluctuations of the demagnetisation field (Figure 3.16) when the parameter ϵ is reduced to 10^{-6} , leading to a significant reduction of the rms error (table 3.6).

Analogous to Section 3.3.1 we check the effect of using hierarchical matrices on the relaxation of the magnetisation in a thin square platelet. We also use the same geometry (edge length 100 nm and thickness 5 nm), micromagnetic parameters ($A = 1.571 \times 10^{-11}$ and $M_s = 10^6 \text{ Am}^{-1}$) and homogeneous initial magnetisation ((0.265, 0.450, 0.100) and (0.034, 0.021, 1.000)). The relaxation results are given in the tables 3.7 and 3.8 and compared to corresponding results, where the full BE matrix has been used. The error arising from hybrid FEM/BEM (without the use of a hierarchical matrix), i.e. the discretisation error, can be estimated from the tables 3.3 and 3.4), where the spatially averaged magnetisation of the relaxed state is compared with corresponding OOMMF results. The OOMMF results seem to be very accurate as they converge quickly with an increasing mesh resolution and the computation of the demagnetisation field with the FFT is very precise (see for example table 3.2 or Appendix C). Therefore we identify the deviation due to the discretisation with the difference from the corresponding OOMMF result. We then find that the deviations introduced by the use of hierarchical matrices are small compared to the deviations due to the FE discretisation. This is true for both algorithms, ACA+ and HCA II, when the parameter sets of table 3.1 are employed. Finally, as in Section 3.3.1 we have performed corresponding simulations of the magnetic reversal behaviour in a thin, square platelet. The results are shown in Figure 3.18 and 3.19. We find that the use of hierarchical matrices has a small effect on the accuracy of the simulation result. Again this holds for both algorithms and the parameter sets of table 3.1. As a comparison, the discrepancy between the simulation results obtained with

3. Compression of the boundary element matrix

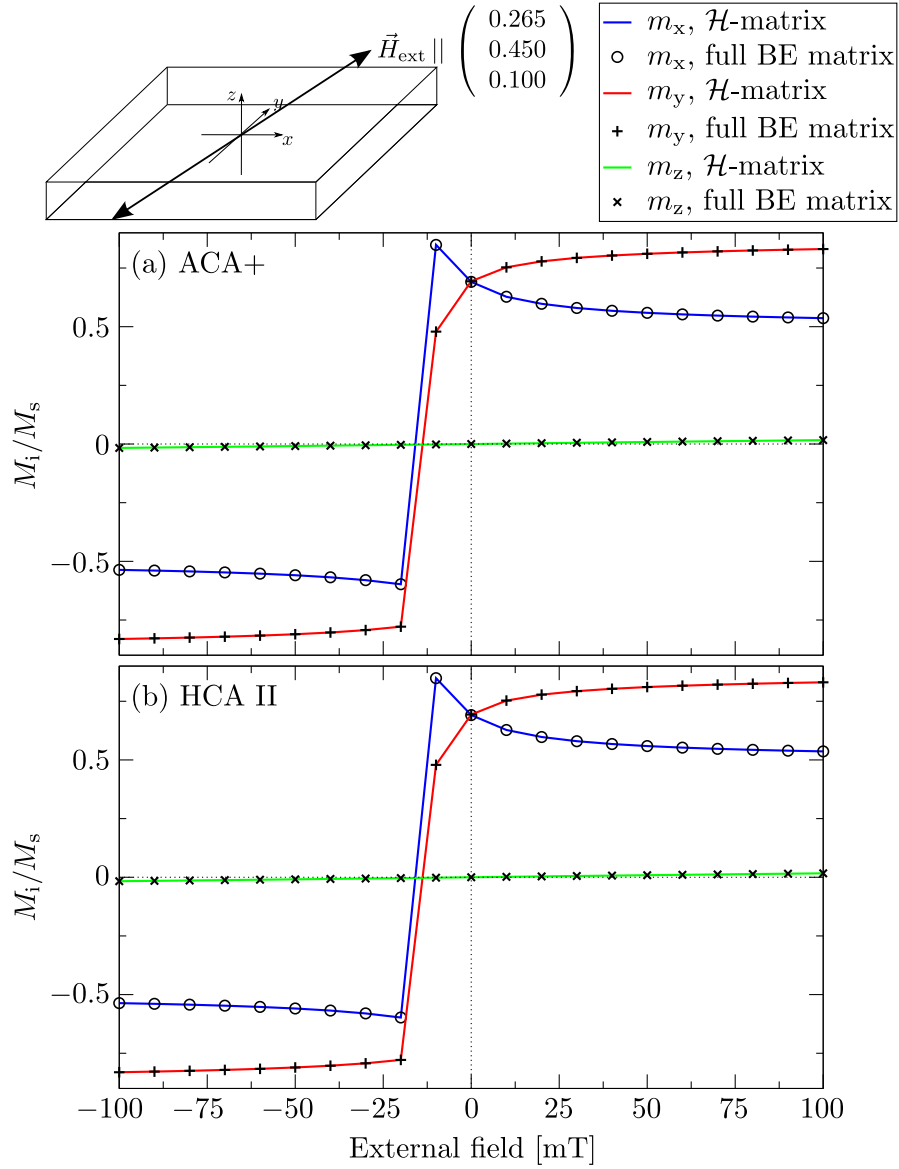


Figure 3.18.: The effect of using a hierarchical matrix approximations in hybrid FEM/BEM on simulation results of the magnetic reversal (along the direction specified in the inset) in a thin, square platelet is investigated. The platelet has an edge length of 100 nm and a thickness of 5 nm. The simulations have been performed with Nmag. The exchange constant is set to $A = 1.571 \times 10^{-11} \text{ Jm}^{-1}$, the saturation magnetisation to $M_s = 10^6 \text{ Am}^{-1}$ and the Gilbert damping constant to $\alpha = 1$. The algorithms ACA+ (upper figure) and HCA II (lower figure) have been used with the parameter sets specified in table 3.1. The external field has been varied in the same way as in Figure 3.14. A Kuhn triangulation from a cubic grid, with three cube layers along the z -direction, has been utilised to create the mesh.

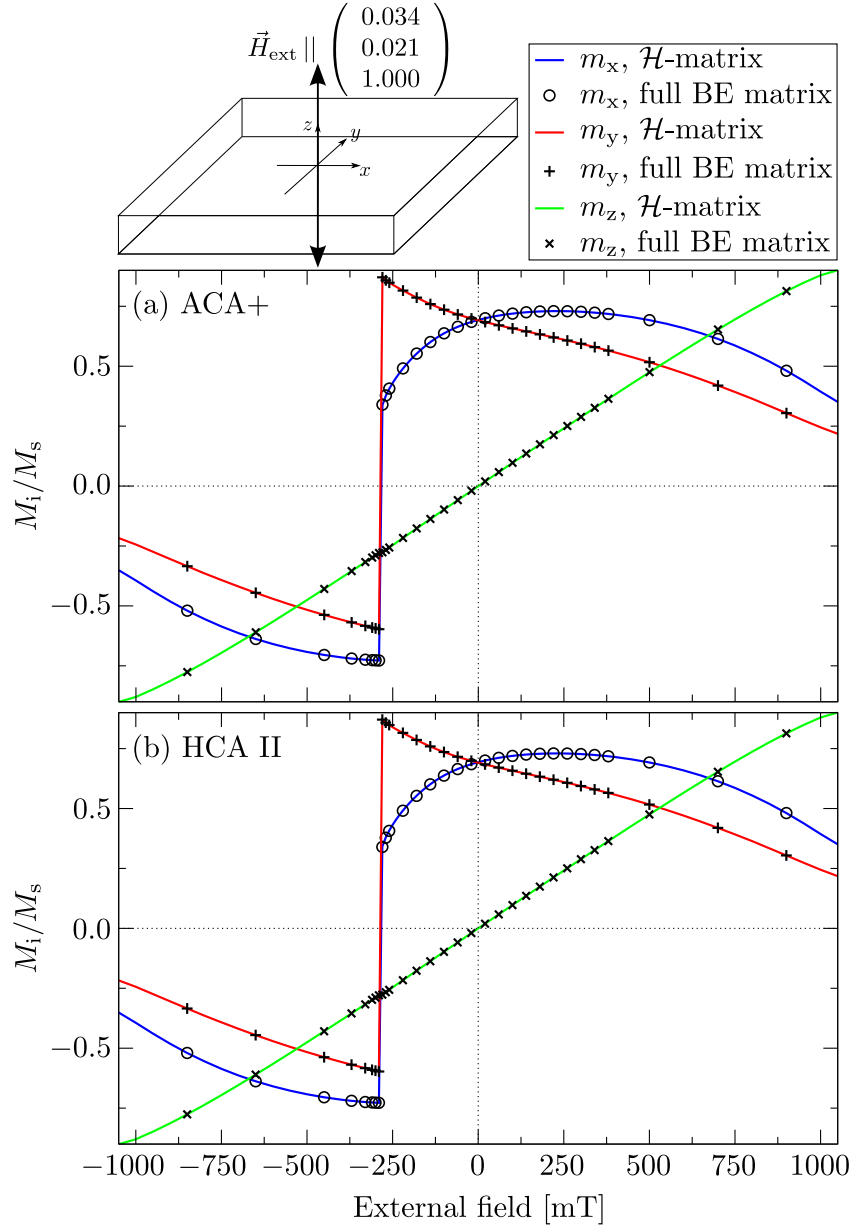


Figure 3.19.: The effect of using a hierarchical matrix approximations in hybrid FEM/BEM on simulation results of the magnetic reversal (along the direction specified in the inset) in a thin, square platelet is investigated. The platelet has an edge length of 100 nm and a thickness of 5 nm. The simulations have been performed with Nmag. The exchange constant is set to $A = 1.571 \times 10^{-11} \text{ Jm}^{-1}$, the saturation magnetisation to $M_s = 10^6 \text{ Am}^{-1}$ and the Gilbert damping constant to $\alpha = 1$. The algorithms ACA+ (upper figure) and HCA II (lower figure) have been used with the parameter sets specified in table 3.1. The external field has been varied in the same way as in Figure 3.15. A Kuhn triangulation from a cubic grid, with three cube layers along the z -direction, has been utilised to create the mesh. Outside the external field range between 270 mT and 330 mT only every 4th data point from the OOMMF simulation results is considered, thus improving the readability of the figure.

3. Compression of the boundary element matrix

OOMMF and Nmag (without a hierarchical matrix approximation) is more notable (Figure 3.15).

3.4. Summary and outlook

The work of this chapter has focused on the use of hierarchical matrices to improve the efficiency of hybrid FEM/BEM. By using the micromagnetic FE solver Nmag in conjunction with the library HLib, we have been able to improve the scaling behaviour of the algorithm. HLib, an implementation of the hierarchical matrix methodology, contains different algorithms for the assembly of a hierarchical matrix. In Section 3.1.3 we have determined reasonable parameter sets for the assembly algorithms interpolation, ACA, ACA+, HCA I and HCA II and compared their efficiency with respect to the demagnetisation field computation within homogeneously magnetised thin, square platelets in Section 3.2. We find that the use of the algorithms ACA+ and HCA II is advantageous, either concerning the memory footprint and matrix assembly time (ACA+) or concerning accuracy and matrix assembly time (HCA II). Furthermore we have compared the computation of BE matrix elements $B_{i,j}$ by numerical Gaussian quadrature and by an analytical formula during the \mathcal{H} -matrix assembly. We find that the use of an analytical formula is more accurate but leads to higher matrix assembly times, especially when using ACA+. In all following simulations we have used the analytical formula to compute matrix elements $B_{i,j}$. In Section 3.3 we have further investigated the numerical error of hybrid FEM/BEM with and without the use of hierarchical matrix approximations. In Section 3.3.1 we have compared the demagnetisation field of a homogeneous magnetisation in a thin, square platelet, as computed with hybrid FEM/BEM and the full BE matrix, with corresponding results from an analytical formula. Due to the occurrence of diverging demagnetisation fields at the edges of surface charge carrying surfaces the numerical results are inaccurate, especially in the vicinity of those edges. For the studied geometries the computation of the demagnetisation field with a fast Fourier transform based on an analytical formula yields more accurate results. Therefore we have used this method to test the accuracy of finite element based simulations. We find that the FE based simulations yield good qualitative results for relaxing systems to a stable configuration. However, we observe quantitative errors in the relaxed configurations, which, using the spatially averaged magnetisation as an error gauge, lie below 1%. When computing the magnetic reversal in a platelet we find that certain jumps, occurring during the reversal process, take place at slightly different external field strengths when using the finite element method. One could try to increase the accuracy of the finite element

simulation for a cuboidal system by using adaptive mesh refinement [103, 33]. The inaccuracies of hybrid FEM/BEM in cuboidal geometries already suggest corresponding difficulties that arise when using a FD discretisation, i.e. a discretisation on a cubic grid, to investigate non-cuboidal geometries. In this case one has to approximate smooth surfaces by cubes, which, even in the case of a fine discretisation, should lead to substantial errors in the demagnetisation field due to the diverging demagnetisation field at the edges of a cube.

The error introduced by a hierarchical matrix approximation is relatively small. We observe convergence problems for ACA+ (see Section 2.3.3), i.e. we cannot tune the accuracy of hierarchical matrices, assembled through ACA+, below a certain threshold. One could potentially overcome these convergence issues by implementing the modifications suggested in [85]. On the contrary, the accuracy of hierarchical matrices created with HCA II seems to be arbitrarily tunable. Although both algorithms seem to work for relaxing micro-magnetic systems, we will use the more reliable HCA II with the parameter set specified in table 3.1 in the following chapters. When simulating the dynamics of a system, one may have to reduce the parameters accordingly.

A direction of future work may be the modification of hybrid FEM/BEM as proposed by García-Cervera and Roma (see Section 2.2.2). In this case the kernel of the boundary integral would be the classical single layer potential (2.43), which is less singular than the classical double layer potential used in the Fredkin-Koehler approach. This, in turn, may lead to a better convergence of the assembly algorithms and thus improve the efficiency of the hierarchical matrix approximation. Another advantage is that no solid angles have to be computed (compare equations (2.50) and (2.53)). Furthermore, a parallelisation of the code involving the \mathcal{H} -matrix assembly and the execution of the \mathcal{H} -matrix-vector product (equation (2.49) or (2.51)) should be relatively straightforward for both variants of hybrid FEM/BEM.

The boundary element matrix becomes symmetric by choosing a Galerkin discretisation, thus reducing the memory footprint of the full BE matrix by about one half. However, disadvantages are a longer \mathcal{H} -matrix assembly time and, analogous to equation 3.1, an additional matrix multiplication with the inverse of a sparse matrix. Generally, when using hierarchical matrix approximations, the limiting factor in the computational complexity of hybrid FEM/BEM is not the BEM part (scales nearly linearly with the number of surface nodes) but the FEM part, as the size of the corresponding coefficient matrices scales linearly with the number of volume nodes. Therefore, the further investigations into the efficiency of hierarchical matrices may not be pertinent.

4. Micromagnetic studies of pyramidal-shaped shell structures

In this chapter we present a numerical study of the magnetic properties of pyramidal-shaped, three-dimensional core-shell structures. The core of these structures (Ag in the experiments) is diamagnetic, while the Nickel shell is ferromagnetic. Typically the magnetic properties of ferromagnetic materials are about a factor of 10^9 times stronger than those of diamagnetic materials (see for example Chapter 1 in [49]), so that the magnetic behaviour of the whole structure is governed by the shell. It is therefore pertinent to only model the properties of the shell by using the micromagnetic model of Chapter 2. For this we employ the finite-element micromagnetic solver Nmag [93]. The bulk of this chapter has been published in [108]. Furthermore, the presented work has also lead to contributions in [109]. The results of Section 4.3.3 are to be published.

As we will see later, the pyramidal-shaped geometry studied in this chapter is fully defined by two parameters, one of which describes the size of the geometry, while the other one determines its shape. Thus we define a two-dimensional parameter space on which we investigate the following questions: what micromagnetic configurations are stable at different geometry sizes and shapes? Which of these configurations has the lowest energy, i.e. is the micromagnetic ground state? Which states occur when one does hysteresis measurements along certain space directions? How does a rounding of the corners and edges of the geometry affect the magnetic properties? Which properties may be interesting for technical applications?

The chapter is structured as follows: in Section 4.1, we briefly discuss the research on core-shell structures and give a summary of corresponding experimental work on the growth of pyramidal core-shell structures. In Section 4.2 details on the methodology are given. We introduce the geometry-defining parameters (Sub-section 4.2.1), present details on the micromagnetic model and the numerics in Sub-section 4.2.2 and describe the approaches used to obtain the results (Sub-section 4.2.3). The results are presented in Section 4.3. It comprises a Sub-section (4.3.1), which characterises all occurring micromagnetic configurations in the absence of an external field \vec{H}_{ext} , and a

4. Micromagnetic studies of pyramidal-shaped shell structures

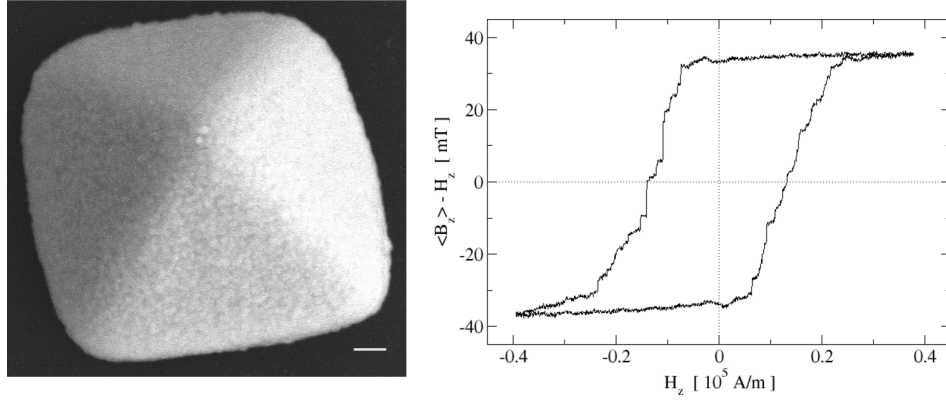


Figure 4.1.: Left: atomic force microscope (AFM) image of a pyramidal core-shell structure with a silver core and a nickel shell. The scale bar length is $1 \mu\text{m}$. Right: hysteresis measurement on a pyramidal Ag/Ni core-shell structure. These measurements have been carried out at 5 Kelvin using a linear array of $2 \mu\text{m} \times 2 \mu\text{m}$ GaAs/AlGaAs heterostructure Hall probes. An individual structure has been taken from the electrode and then placed onto an active Hall probe element with its basal plane facing down. The homogeneous magnetic field has been applied perpendicular to the Hall element, a direction that we identify with the z -direction. The x -axis shows the strength of the applied magnetic field, while the y -axis depicts the magnetic field detected by the Hall element $\langle B_z \rangle$ minus the applied field H_z . The latter quantity corresponds to the stray field generated by the pyramidal shell, which is spatially averaged over the active area of the Hall element. This data has been provided by our co-workers, Farzad Nasirpouri and Simon Bending, from the University of Bath.

Sub-section (4.3.2) describing the intermittent micromagnetic configurations during a hysteresis loop. These investigations are carried out for different shapes and sizes, allowing for an analysis of how the geometry influences the magnetic behaviour. The effect of the rounding of corners and edges is investigated in Section 4.3.3. Finally, we summarise our findings in Section 4.4 and discuss potential directions of future research.

4.1. Experimental growth of Nickel structures

As discussed in the introduction (Chapter 1), most experimental and theoretical research has been devoted to the study of planar structures like square platelets. This is mainly due to practical difficulties that arise in the growth of well-defined, three-dimensional samples. In the context of three dimensional objects, core-shell structures are advantageous for the following reasons: they reduce the amount of magnetic material used compared to filled 3D objects

4.1. Experimental growth of Nickel structures

which, in the case of expensive components, may lead to significant cost reductions. In addition, the interaction between the core and shell regions may lead to interesting physical phenomena. For example the core region could consist of a material which is superconducting below a certain critical field, H_C . In this case the core can exhibit re-entrant superconductivity when the applied magnetic field compensates the stray fields due to the ferromagnetic shell. Furthermore, superconductivity can exist up to applied fields well above the bulk critical field of the core due to these effects (see Chapter 5). On the other hand, if the core material is non-magnetic (e.g., the magnetic field in the core region lies above H_C), then the magnetic behaviour of the core-shell structure will be solely governed by the ferromagnetic shell (the situation assumed in this chapter). The transition between the two magnetic states of the core-shell structure depends on the material properties (within the core and the shell) and on the geometry of the structure. The presented work has been motivated by corresponding experimental work on the electrochemical growth of pyramidal core-shell structures with a silver (Ag) core and a nickel (Ni) shell (Figure 4.1), which was carried out by co-workers at the University of Bath. It is briefly described in the following: for this a two step dual bath method is used. First, single-crystalline pyramidal-shaped silver mesostructures are deposited on a highly ordered pyrolytic graphite (HOPG) working electrode from an aqueous solution of 100 mM AgNO_3 at a pH value between 2 and 2.5. In the process the potential of the HOPG working electrode is first set to 1 V for 60 seconds, then to 0 V for 10 seconds, and finally to -10 mV for 30 seconds. The silver deposition occurs during the last stage via the so-called Volmer-Weber mechanism, in which three-dimensional nuclei are promptly formed. In the second step the electrolyte is replaced by an aqueous solution containing 2.3 M NiSO_4 , 0.6 M NiCl_2 and 0.5 M boric acid. The Nickel is then electrodeposited at a potential of -800 mV versus a Ag/AgCl reference electrode and a pH value of 2. Cyclic voltammograms suggest that at this potential Nickel is only deposited on the metallic silver islands and not elsewhere on the HOPG electrode. A direct deposition of Nickel onto HOPG turns out to be impracticable as it tends to plate rather than to exhibit a three-dimensional growth mode. The pyramidal core-shell structures grown with this method (Figure 4.1) have typically a base side length of $10\text{ }\mu\text{m}$, a height of $5\text{ }\mu\text{m}$ and a shell thickness of about 100 nm.

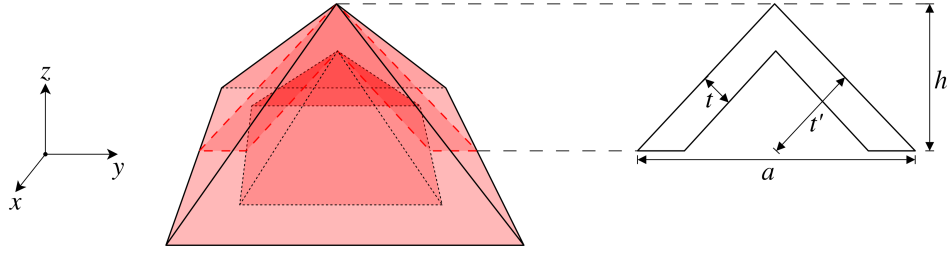


Figure 4.2.: Sketch of a pyramidal shell structure. The left part of the figure shows a three dimensional visualisation. On the right, parameters defining the shell geometry are introduced on the basis of a cross-section through the shell structure's centre. The parameter h is the height of the pyramid, a denotes its edge length and t is the thickness of the shell. t' defines the distance between each outer side face and the centre of the basal plane. Throughout the paper, we define the z-direction as the direction that is represented by the tip, while x and y are aligned with the edges of the basal plane.

4.2. Methodology

4.2.1. The investigated system

We focus our micromagnetic studies on pyramidal shells with a square base. The base of the pyramid is not covered with a ferromagnetic layer as it is sitting face down on the growth substrate (i.e. the HOPG) during electrodeposition. Figure 4.2 shows how such a structure can be defined in terms of three parameters. The pyramidal shape is defined by the edge length a and the height h , while the parameter t is the shell thickness. In order to limit the number of simulations for this study to a reasonable extent, we have restricted our parameter space by setting $h = a/2$, which also appears to concur with the shape of the experimentally grown structures (see Section 4.1). Furthermore, we replace the shell thickness t in absolute units by t_{rel} , which is defined as

$$t_{\text{rel}} = 100.0 \cdot \frac{t}{t'}.$$

Here, $t' = a/(2 \cdot \sqrt{2})$ is the distance between one of the triangular faces of the shell's outside and the centre of the base. t_{rel} ranges between 0.0 and 100.0, with 0.0 being the limit of an infinitely thin shell, and 100.0 representing a completely filled pyramid. Two shells with the same value for t_{rel} , say (a_1, t_{rel}) and (a_2, t_{rel}) , are mathematically similar, i.e. the former can be obtained from the latter by rescaling it by a factor a_1/a_2 . Thus, a may be regarded as a size parameter and t_{rel} as a shape parameter.

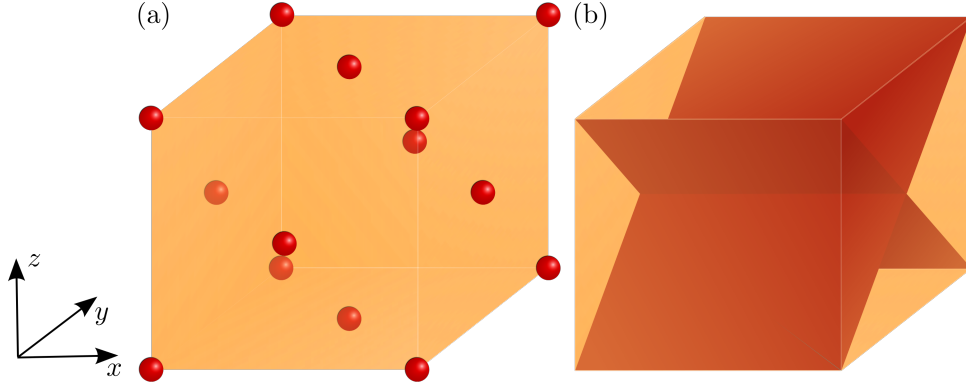


Figure 4.3.: (a) The face-centred cubic crystal structure of Nickel is shown. (b) The crystal planes, which have the right symmetry to describe the geometry of the observed pyramidal shells (basal edge length of a and a height of $h = a/2$), have the Miller indices $(1, 1, 0)$, $(1, 0, 1)$ and $(0, 1, 1)$. The planes with the Miller indices $(0, 1, 1)$ are shown in this figure. So in the case of a single-crystalline Nickel shell one could readily incorporate magnetocrystalline anisotropy into the model as the axes of the cubic lattice correspond to the directions x , y and z of Figure 4.2.

4.2.2. The micromagnetic method

As discussed in Section 4.1 Nickel has been successfully used to grow core-shell structures with a ferromagnetic Nickel shell and a non-magnetic core. Therefore, in our micromagnetic model, we use the corresponding values for the exchange constant $A = 7.2 \times 10^{-12} \text{ J/m}$ and the saturation magnetisation $M_S = 493380 \text{ A/m}$ [50], while we neglect its highly temperature-dependent cubic anisotropy. At room temperature the anisotropy constants are $K_1 = -4500 \text{ J/m}^3$ and $K_2 = -2500 \text{ J/m}^3$, which are small compared to the typical magnitude of the magnetostatic self energy $K_D = \frac{\mu_0}{2} \cdot M_S^2 = 152948 \text{ J/m}^3$. Earlier studies suggest that the omission of the anisotropy term does not qualitatively alter the results within the regime investigated here (i.e. dimensions of about $60 \cdot l_{\text{exch}}$ and below, where l_{exch} is defined by $l_{\text{exch}} = \sqrt{A/K_D}$) [39]. Furthermore, due to the polycrystalline structure of the electrodeposited nickel shell, an inclusion of the magnetocrystalline anisotropy is not straightforward. Only in the case of a singlecrystalline structure one can relate the side faces of the pyramidal structure to the crystal planes of the cubic lattice (see Figure 4.3), rendering the incorporation of magnetocrystalline anisotropy feasible. We do not consider surface anisotropy, which becomes especially important for very thin shells [33], and additional energy contributions that, for example, may arise from magnetoelastic effects such as magnetostriction.

We employ a finite element discretisation on a tetrahedral mesh (using the solver Nmag [93]) in order to numerically compute the different contributions

4. Micromagnetic studies of pyramidal-shaped shell structures

to the effective field \vec{H}_{eff} (equation (2.19)). In particular, we use the hybrid FEM/BEM of Section 2.2 for the computation of the demagnetisation field \vec{H}_{demag} . As this method becomes inefficient for structures with many surface nodes we approximate the BE matrix 2.53 by a hierarchical matrix, which is assembled through the algorithm HCA II using adaptive recompression and the parameter sets given in Sub-section 3.1.3. For this we couple Nmag with the library HLib [31]. We find that the use of hierarchical matrices works well for the studied pyramidal geometries, as the error introduced by this approximation is small compared to other numerical errors in the computation of \vec{H}_{demag} , which are driven by the discretisation (see Section D.1 in Appendix D). Each tetrahedral mesh has been created with the commercial software tool Fluent Gambit 2.4.6. When creating the unstructured mesh its resolution has to be such that the computation of the model's exchange and demagnetisation fields is reasonably accurate. For a sufficient accuracy in the exchange field computation the edge lengths of all tetrahedrons should typically lie below the exchange length l_{exch} [45, 99], which in the case of nickel is equal to 6.86 nm. Since Gambit does not provide a parameter for specifying a maximal edge length, we use an h-type refinement [110], i.e. add a nodal point to the centre of tetrahedron edges a with $|a| > l_{\text{exch}}$ and rearrange adjacent tetrahedrons accordingly, in order to ensure a resolution below l_{exch} (see also Section D.1). For each simulation we have checked whether the maximal angle between the magnetic moments of adjacent mesh nodes (the so-called spin angle) of the relaxed configuration is about 30° or below. Spin angles, which dramatically exceed this limit, underestimate the contribution of the local exchange field and may lead to incorrect results [111]. In Section D.1 we show that, due to the diverging demagnetisation fields around sharp corners (Appendix C), the computation of the magnetostatic energy density becomes inaccurate even if the resolution is below the exchange length l_{exch} . However, a reasonable accuracy is achieved when the edge lengths of the tetrahedrons lie below the values $0.035a$ and $0.5t$, where a and t are the base length of the pyramidal structure and the shell thickness, respectively (see Figure 4.2). In summary, depending on the size and shape of the pyramidal shell geometry we choose the smallest of three threshold values (exchange length, $0.5t$, $0.035a$), to obtain a satisfactory accuracy. For the time integration of (2.22), Nmag uses an implicit time integration scheme as reported in [63] and made available in the Sundials software library [112]. The system is integrated until the angular rate of change of the magnetisation is below 1° ns^{-1} at every mesh node.

4.2.3. Exploring the parameter space

The parameters a and t_{rel} , as introduced in Section 4.2.1, define a 2D phase space. One goal of this chapter is to examine this phase space for micromagnetic ground state configurations in the absence of an externally applied magnetic field. Ground state configurations minimise the micromagnetic energy of (2.17). We start these investigations by relaxing the magnetisation for different parameter sets (a, t_{rel}) and initial configurations. The edge length a is set to values at 20, 50, 100, 150, 200, 250, 300, 350 and 400 nm (i.e. varied between $a_{\text{min}} \approx 3 \cdot l_{\text{exch}}$ and $a_{\text{max}} \approx 60 \cdot l_{\text{exch}}$), while thicknesses of $t_{\text{rel}} = 5, 10, 15, 20, 30, 40, 50, 60, 70, 80, 90$ and 100% are used. As initial configurations we choose different homogeneously aligned magnetisations pointing in directions such as $(1, 0, 0)$, $(0, 0, 1)$, $(1, 1, 0)$ and $(1, 1, 0.5)$ (with respect to the coordinate system defined in Figure 4.2). Obtaining a set of stable configurations for each investigated point (a, t_{rel}) we assume the configuration with the lowest micromagnetic energy to be the ground state. The corresponding results are then most conveniently summarised in a phase diagram which states the micromagnetic ground state as a function of a and t_{rel} .

In order to add phase boundaries to the phase diagram, we use a technique similar to the one described in [113]. We start from the relaxed micromagnetic configuration and rescale the mesh such that the edge length a increases or decreases by Δa , i.e. the rescale factor is $(a + \Delta a)/a$ or $(a - \Delta a)/a$, respectively. One should note that the described procedure does not work with a variation of the shape parameter t_{rel} . We extrapolate the rescaled micromagnetic configuration to a new mesh that discretises the geometry of the new size (otherwise the rescaling procedure would change the resolution of the mesh) and relax the system to a new stable state. Usually the system will relax quickly, since we already start from a very good approximation of the domain structure. However, if the domain structure becomes unstable at the new system size, it will collapse to a qualitatively different micromagnetic configuration. We use this procedure iteratively, when the ground state configuration between adjacent points of the same thickness t_{rel} changes. Starting from a configuration corresponding to a small value of a and gradually increasing a , we get a curve for the total energy as a function of a . Starting from a (different) configuration corresponding to a large a and then decreasing a , we obtain another data set of the total energy as a function of the edge length a . Subsequently, we determine by a low-order polynomial interpolation the point a_{trans} at which the energies of both configurations cross over. When both states decay spontaneously into each other we choose a_{trans} as the arithmetic mean value of the two edge lengths between which the transition occurs. Repeating this proce-

4. Micromagnetic studies of pyramidal-shaped shell structures

For different thicknesses t_{rel} one can draw phase boundaries between areas of different micromagnetic ground states. Depending on the magnitude of a , we use different values for Δa . We choose $\Delta a = 2 \text{ nm}$ for $10 \text{ nm} < a < 20 \text{ nm}$, $\Delta a = 5 \text{ nm}$ for $20 \text{ nm} < a < 50 \text{ nm}$ and $\Delta a = 10 \text{ nm}$ for $50 \text{ nm} < a < 400 \text{ nm}$. A problem in our approach may arise because the primary data points of the phase diagram have been obtained from a finite set of initial states. Thus, it could happen that at a certain parameter point (a, t_{rel}) a magnetisation configuration may not have been found although it is stable or even the ground state.

4.3. Numerical results

4.3.1. Energetic ground states at $H_{\text{ext}} = 0$

In this section, we present results on the micromagnetic states of pyramidal shells (see Section 4.2.1) in the absence of an external magnetic field. In accordance with previous work on soft magnetic structures [39, 45], we find that in the investigated regime two types of ferromagnetic domains occur: the so-called single domain (or quasi-homogeneous) states and vortex states.

Single-domain states

Single-domain states are quasi-homogeneous and have a well-defined mean magnetisation direction. They usually occur in the limit of very small structures, i.e. at dimensions of just a few exchange lengths. While the exchange interaction leads to the quasi-homogeneity, magnetostatic effects govern the direction of the mean magnetisation. In the literature, one distinguishes between two types of anisotropies arising from the magnetostatic contribution to the micromagnetic energy functional (2.17). Shape anisotropy describes the anisotropy of a completely aligned magnetisation due to the shape of the ferromagnet. However, the deviations from homogeneous alignment may lead to a change in the character of the anisotropy, i.e. the assumption of homogeneous magnetisation becomes invalid. This interaction between an inhomogeneous magnetisation and the shape is called configurational anisotropy. The name derives from the fact that an inhomogeneous state generally changes with the direction in space, and the anisotropy follows from the different energies of those configurations. Configurational anisotropy is usually studied for quasi-homogeneous states [32, 45], while an analysis of more complex states (e.g. vortex states) turns out to be problematic [45]. We investigate the shape

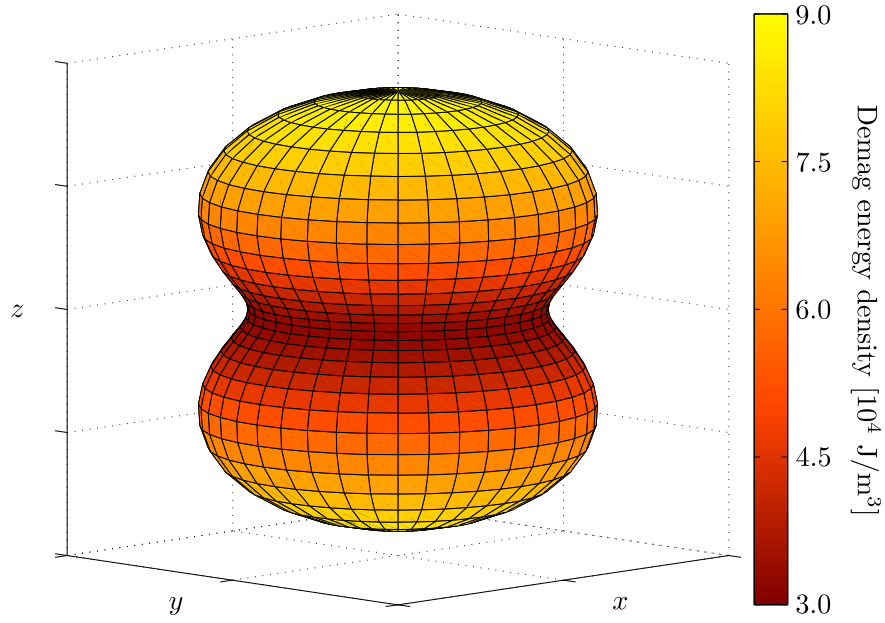


Figure 4.4.: The polar plot shows the shape anisotropy of a pyramidal shell with $t_{\text{rel}} = 50\%$ ($a = 150\text{ nm}$). For this geometry we find a minimal magnetostatic energy density of $w_{\text{min}} = 32085\text{ J/m}^3$ in the xy -plane and a maximum energy density of $w_{\text{min}} = 88690\text{ J/m}^3$ along the z -direction. This corresponds to an anisotropy constant of $K = 56605\text{ J/m}^3$ and thus exceeds the magnetocrystalline anisotropy by more than one order of magnitude.

4. Micromagnetic studies of pyramidal-shaped shell structures

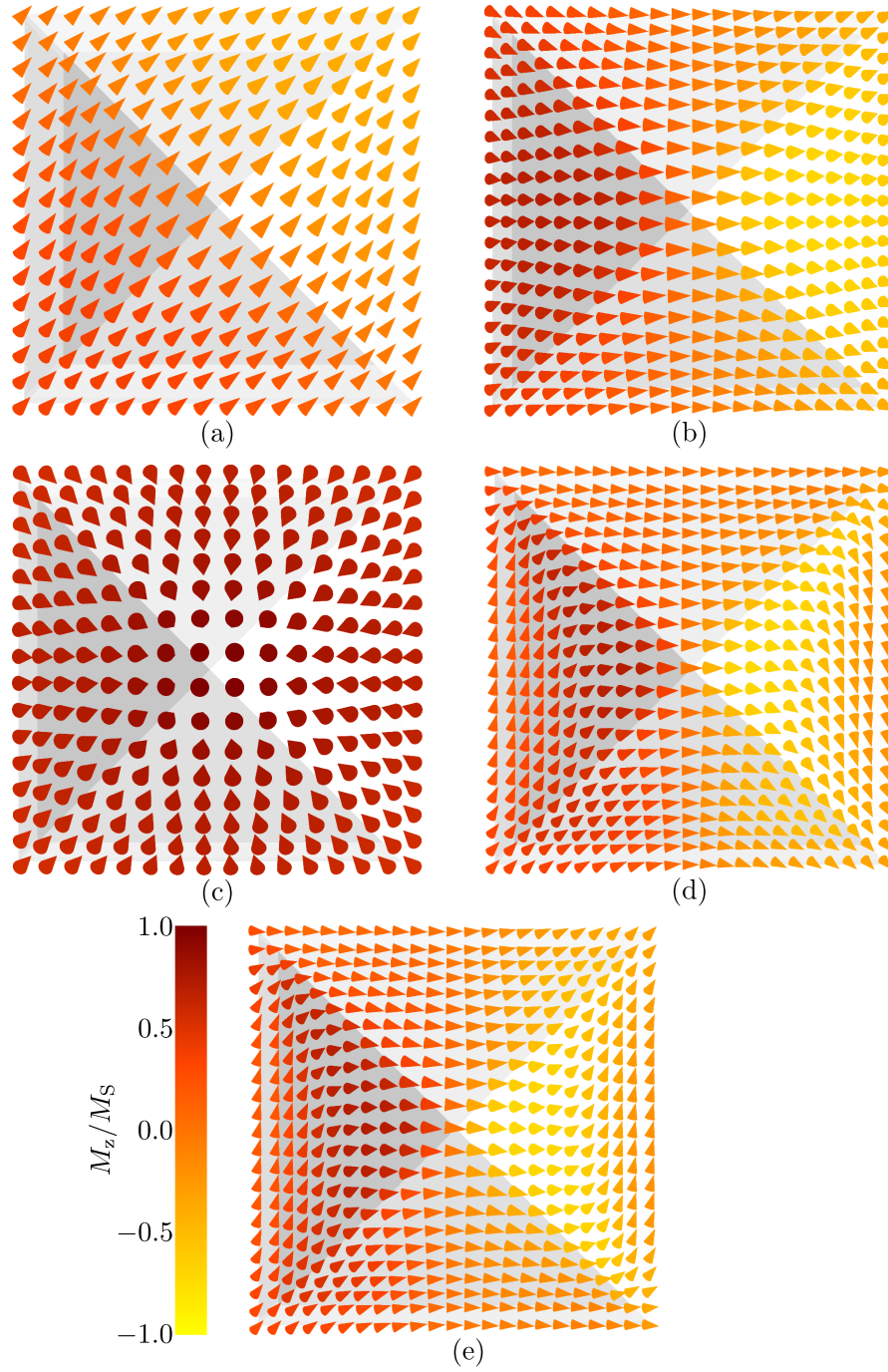


Figure 4.5.: Top view (in negative z -direction) of stable single domain states. The observed states are (a) an onion state, (b) a flower state, (c) a single-domain state aligned along the z -direction, (d) a C state, and (e) an S state. The pyramidal geometries correspond to the following parameter sets: $a = 35$ nm and $t_{\text{rel}} = 20$ % for the onion state, $a = 120$ nm and $t_{\text{rel}} = 10$ % for the flower state, $a = 60$ nm and $t_{\text{rel}} = 10$ % for the single-domain state in Figure (c), and $a = 300$ nm, and $t_{\text{rel}} = 10$ % for the C and the S state. For illustration purposes a semi-transparent depiction of the pyramidal shells has been added to each picture.

anisotropy by varying the spatial orientation of the homogeneous magnetisation in pyramidal shells with $t_{\text{rel}} = 10\%$, 50% and 100% . Please note that the shape anisotropy only depends on the shape parameter t_{rel} but not on the size parameter a . We introduce spherical polar coordinates (ϕ, θ) , i.e. the points \hat{e} on the unit sphere are described by

$$\hat{e} = \begin{pmatrix} \cos(\phi) \sin(\theta) \\ \sin(\phi) \sin(\theta) \\ \cos(\theta) \end{pmatrix}.$$

We systematically vary the angle ϕ in 40 steps between 0 and 2π and the angle θ in 20 steps between 0 and π , so that 800 spatial directions are probed. For each spatial direction we align the magnetisation accordingly and compute the magnetostatic energy density w_{demag} numerically using Nmag. We find that the shape anisotropy has a uni-axial symmetry with the structure's basal plane being the easy plane. This could be established by fitting the data to the phenomenological formula

$$w_{\text{demag}} = w_{\text{min}} + (w_{\text{max}} - w_{\text{min}}) \cos^2(\theta), \quad (4.1)$$

which corresponds to the expression for uni-axial anisotropy given in equation 2.3. The two fitting parameters w_{min} and w_{max} are the numerically computed energy densities at $\theta = \pi/2$ and $\theta = 0$, respectively. We quantify the deviation Δ from the fitting curve through

$$\Delta = \frac{\sqrt{\sum_i \sum_j (w_{\text{num}}(\phi_i, \theta_j) - w_{\text{fit}}(\phi_i, \theta_j))^2}}{\sqrt{\sum_i \sum_j w_{\text{fit}}(\phi_i, \theta_j)^2}},$$

and find that $\Delta \sim 10^{-5}$ holds for all studied geometries ($a = 150\text{ nm}$ and $t_{\text{rel}} = 10\%$, 50% and 100%). A graphical illustration of the shape anisotropy is given in Figure 4.4 for the pyramidal shell with $t_{\text{rel}} = 50\%$. However, it turns out that due to configurational anisotropy quasi-homogeneous states, whose mean magnetisation aligns either along the x (or y) direction (as defined in Figure 4.2) or the diagonal of the basal plane, are energetically favoured. Figure 4.5 shows the observed single-domain states. Every state (apart from the state of Figure 4.5c) corresponds to a state observed in square nanostructures [105, 33], i.e. shows a similar symmetry. However, the states of the pyramidal system are more inhomogeneous in the sense that there is a significant variation of the magnetisation's z -component. This is due to the fact that the magnetisation tries to avoid surface charges on the inner and outer side faces of the shell by aligning parallel to those faces.

4. Micromagnetic studies of pyramidal-shaped shell structures

We refer to the single-domain state, whose mean magnetisation is aligned along the diagonal of the basal plane as an onion state (sometimes also called the leaf state). Figure 4.5a shows the magnetisation of the onion state on the outer surface of a pyramidal shell with ($a = 35 \text{ nm}$, $t_{\text{rel}} = 20 \%$). Moving from the lower left to the upper right corner the magnetisation tries to follow the surface geometry by pointing upwards on the lower left and pointing downwards on the upper right half. Due to the symmetry of this state the z-component of the magnetisation is zero across the crest, around which the proximity of negative and positive surface charges leads to a high magnetostatic energy density. The latter effect is inherent to the onion state.

The state of Figure 4.5b is called a flower state. It features the typical tilting in the vicinity of corners, which gives a flower-like impression. We observe that the spatially averaged magnetisation, which is aligned with either the x- or y-axis, increases with growing shell thickness. This is due to surface charges that can be created on the basal plane of the pyramidal shell. The area of the latter grows with increasing shell thickness. Thus, the higher impact of the basal plane leads to a generally better alignment of the magnetisation along the x (or y) axis for thick shells.

Figure 4.5d shows a so-called buckle or C state. The latter name derives from the shape of the flux lines, which, in the perspective of Figure 4.5d, resembles the letter C rotated 90° in the clockwise direction. Compared to a flower state, a C state reduces the magnetostatic energy by a higher degree of flux closure. This happens at the expense of a higher exchange energy.

The so-called S state is shown in Figure 4.5e. Analogous to the C state, it gets its name from the shape of the flux lines that follow the shape of the letter S. Compared to the flower and the C state the mean magnetisation of the S state is shifted towards a diagonal of the basal plane, i.e. from $(1, 0, 0)$ to typically about $(0.75, 0.25, 0)$.

Figure 4.5c shows a quasi-homogeneous metastable state with a mean magnetisation pointing in the z-direction. As this state is only metastable for very thin and small structures ($a \lesssim 100 \text{ nm}$, $t_{\text{rel}} \lesssim 10\%$) but unstable otherwise, we will not discuss it in what follows.

Vortex states

There is no mathematically rigorous definition of a vortex state in micromagnetics [114]. For thin platelets a vortex state consists of a small, out-of-plane vortex core and an in-plane magnetisation curling around the core. The in-plane magnetisation helps form closed flux lines, i.e. reduces surface charges,

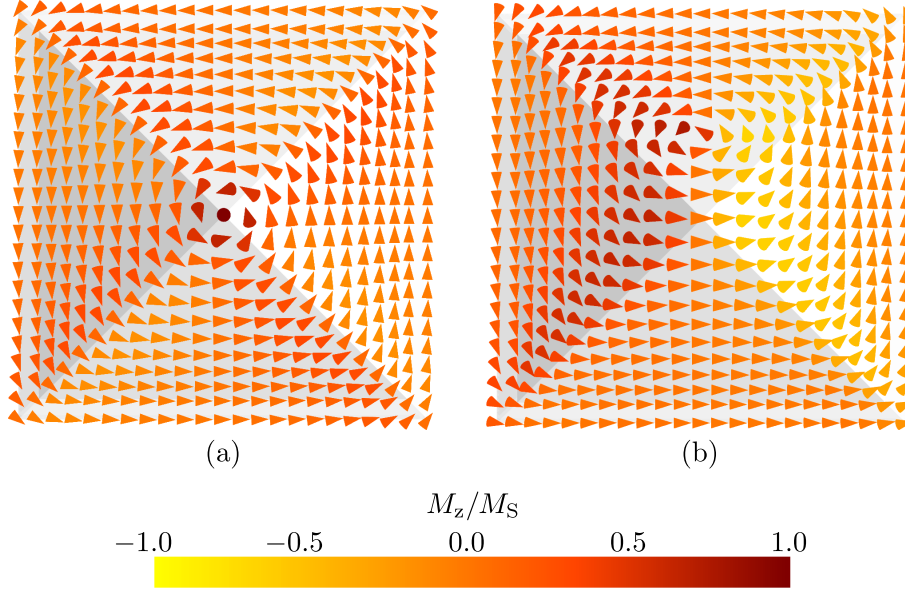


Figure 4.6.: Top view (in negative z -direction) of stable vortex states. We observe a symmetric vortex state (a) and an asymmetric vortex state (b). The pyramidal structure has an edge length of $a = 300$ nm and a thickness of $t_{\text{rel}} = 10$ %.

at the expense of a higher exchange energy especially in the vicinity of the vortex core. However, the magnetostatic energy of the vortex core cannot be neglected [33, 34]. For our geometries we observe two different vortex states (figure 4.6).

Figure 4.6a shows a vortex state with a core aligned along the direction of the pyramid’s tip (i.e. the z -direction). Due to the core position in the symmetry centre of the geometry, we will refer to this state as the symmetric vortex state. We note two features: firstly, the z -component of the curling magnetisation fluctuates around the edges between two adjacent side faces. This effect is just visible in the form of colour variations in Figure 4.6a but more pronounced in the warp plane representation of Figure 4.11 (top image). Secondly, the vortex core broadens towards the top of the pyramid (see Figure 4.7a). A consequence of this broadening is a decrease in the exchange energy density within the vortex core towards the top of the pyramid.

Figure 4.6b shows the asymmetric vortex state whose core is sitting on one of the four (outer) side faces of the shell. A characteristic of the asymmetric vortex state is that its remanent magnetisation is not only carried by the vortex core but also has a component parallel to the basal plane. This can be seen in Figure 4.6b where more “magnetic moments” point to the right than to the left. We discuss in Section 4.3.2 that this leads to an interesting magnetic reversal behaviour. Figure 4.7 shows that the character of the state

4. Micromagnetic studies of pyramidal-shaped shell structures

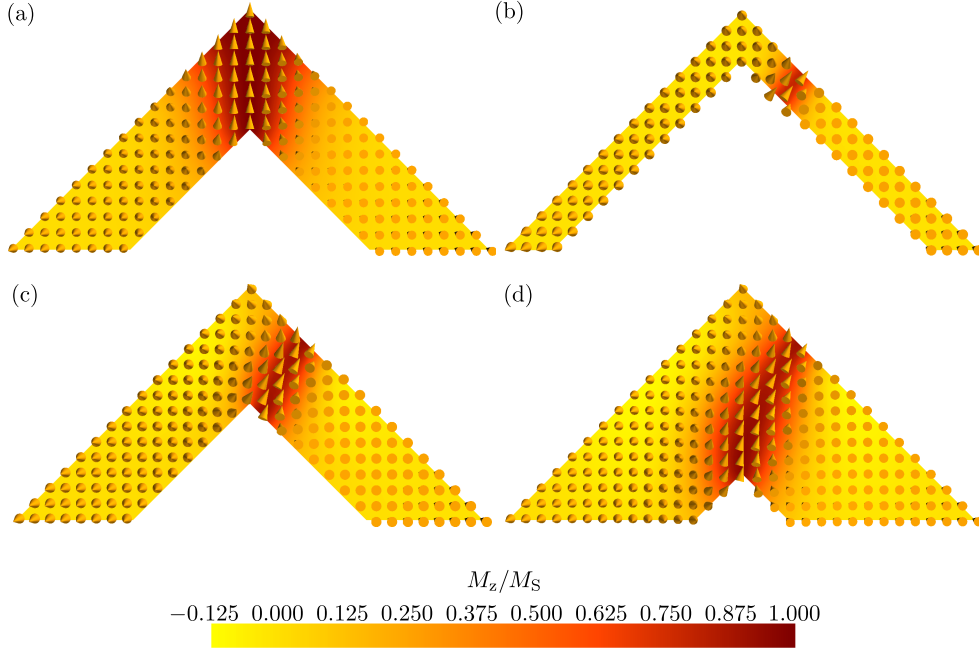


Figure 4.7.: (a) Cross-sectional view of the symmetric vortex state. The pyramidal shell has an edge length of $a = 150$ nm and a shell thickness of $t_{\text{rel}} = 50\%$. (b-d) Cross-section through an asymmetric vortex state for a pyramidal shell with an edge length of $a = 300$ nm and three different thicknesses t_{rel} : 20 % (b), 50 % (c) and 80 % (d). The cross-sectional plane centrally cuts the pyramidal structure in all depicted images.

changes with varying shell thickness. While for thin shells ($t_{\text{rel}} \lesssim 50\%$) the vortex core runs from the outer face straight to the corresponding inner face (see Figures 4.7b and c), it tends to bend towards the tip of the structure's core for larger values of t_{rel} (Figure 4.7d). This vortex core bending is also illustrated in Figure 4.8 for a conventional pyramid, i.e. t_{rel} equals 100 %. The position of the vortex on the outer side face lies in the vicinity of the pyramid tip for most values of t_{rel} , but is shifted towards the centre of the triangular face for very thin shells below 10 %. We show in [109] that, for a pyramidal shell with $a = 500$ nm and $t_{\text{rel}} = 10\%$, metastable asymmetric vortex states exist, whose cores are at different positions on the (same) side face.

Phase diagram and metastability

The phase diagram of Figure 4.9 summarises which state minimises the total micromagnetic energy, i.e. is the ground state, for which geometry (defined by the parameter set (a, t_{rel})). Physically the ground state can be interpreted as the state which should be formed when a ferromagnetic structure is slowly cooled below its Curie temperature to 0 K [105]. According to [105], in the

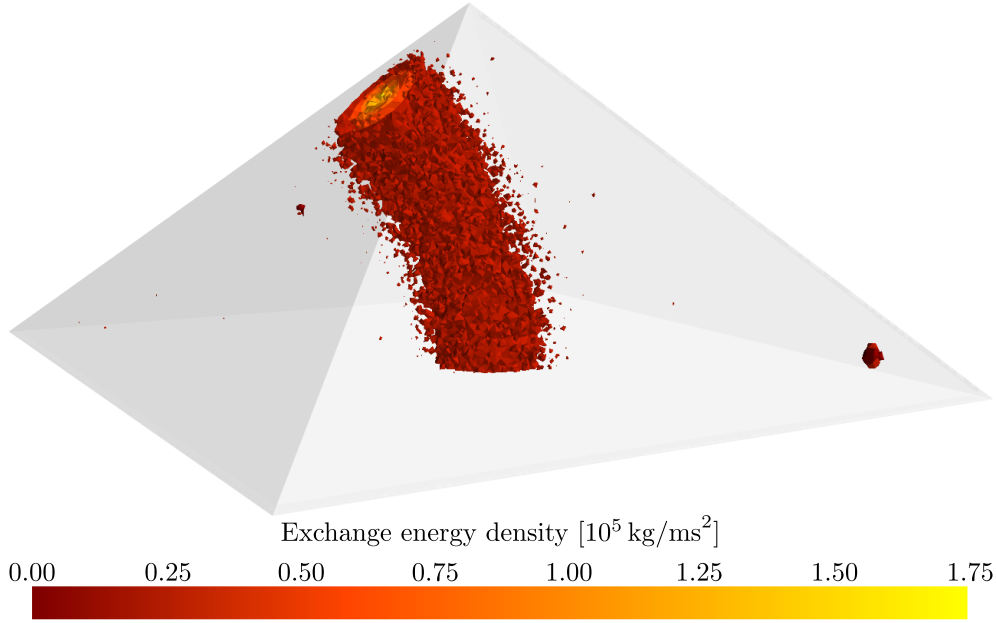


Figure 4.8.: Equipotential surfaces of the exchange energy density displaying a vortex state with a bent vortex core. The geometry is a full pyramid with a basal plane edge length of 300 nm and a height of 150 nm. The exchange energy density is defined as $u_{\text{exch}} = \vec{M} \cdot \vec{H}_{\text{exch}} = 2A \vec{m} \cdot \nabla^2 \vec{m}$. Artifacts from the numerical calculation of the exchange energy appear to lead to non-smooth surfaces.

limit of large thermal activation, the ground state tends to be the same as the remanence state after saturation by an applied field. However, due to the complicated energy landscape of ferromagnetic systems it is difficult to make a general remark on the tendency of systems to adopt the micromagnetic ground state. In particular, for soft magnetic structures, metastable states may occur. Therefore, we will later discuss the stability regimes of all domain structures, which have been observed at the shell thicknesses $t_{\text{rel}} = 10, 50$ and 100 % (Figure 4.10). One should note that our model does not consider the effects of thermal activation on the stability of different configurations.

For small structure sizes (i.e. $a < 100 \text{ nm}$) only the flower and the onion state are energetic ground states. As can be seen from Figure 4.9 the onion state minimises the energy roughly for edge lengths a below 25 nm and shell thicknesses t_{rel} smaller than 55 %. The simulation results do not give obvious reasons why the onion state becomes metastable at $t_{\text{rel}} \gtrsim 55 \%$. However, corresponding investigations on square platelets have shown that the onion state becomes energetically favourable with respect to the flower state for larger values of the ratio between size and thickness [32, 105], which is qualitatively in agreement with our findings. These investigations have also shown that for small platelet thicknesses the onion state is the micromagnetic ground state

4. Micromagnetic studies of pyramidal-shaped shell structures

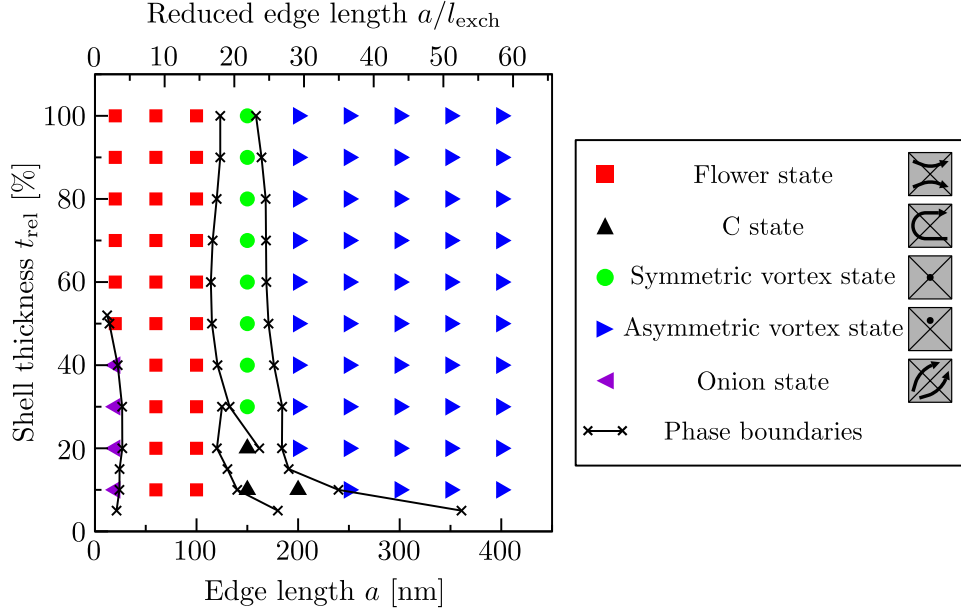


Figure 4.9.: Phase diagram showing the ground states for different pyramidal structures. The two parameters are the edge length of the outer pyramid and the thickness of the pyramid shell. For a better readability we have added schematic plots to the legend, which highlight the main features of each ground state from a top-down perspective.

in a wide size range. Thus, we observe a suppression of the onion state for the pyramidal structures. The reason seems to be the high magnetostatic energy density in the vicinity of the crest, which is inherent to the onion state.

At larger edge lengths a the micromagnetic ground state crucially depends on the shell thickness t_{rel} . For thicknesses t_{rel} above 30 % the symmetric vortex state becomes the ground state in a range between 120 and 180 nm, above which the asymmetric vortex state minimises the micromagnetic energy. The edge length a_{trans} at which these transitions occur depends weakly on the shell thickness. Below $t_{\text{rel}} = 20\%$ the situation is different: with increasing edge length a the lowest energy state changes from the flower state to the C state and from the C state to the asymmetric vortex state. The transition edge length a_{trans} strongly depends on the shell thickness t_{rel} in this region of the phase diagram. The occurrence of the C state at low values of t_{rel} can be readily understood: the penalty in the magnetostatic energy for the C state decreases with decreasing t_{rel} , as fewer surface charges on the basal plane are created.

Another feature of very thin shells is a growth in the number of metastable states (Figure 4.10). The number of stable configurations (i.e. curves in Figure 4.10) is 7 for $t_{\text{rel}} = 10\%$, 5 for $t_{\text{rel}} = 50\%$ and 4 for $t_{\text{rel}} = 100\%$. Furthermore,

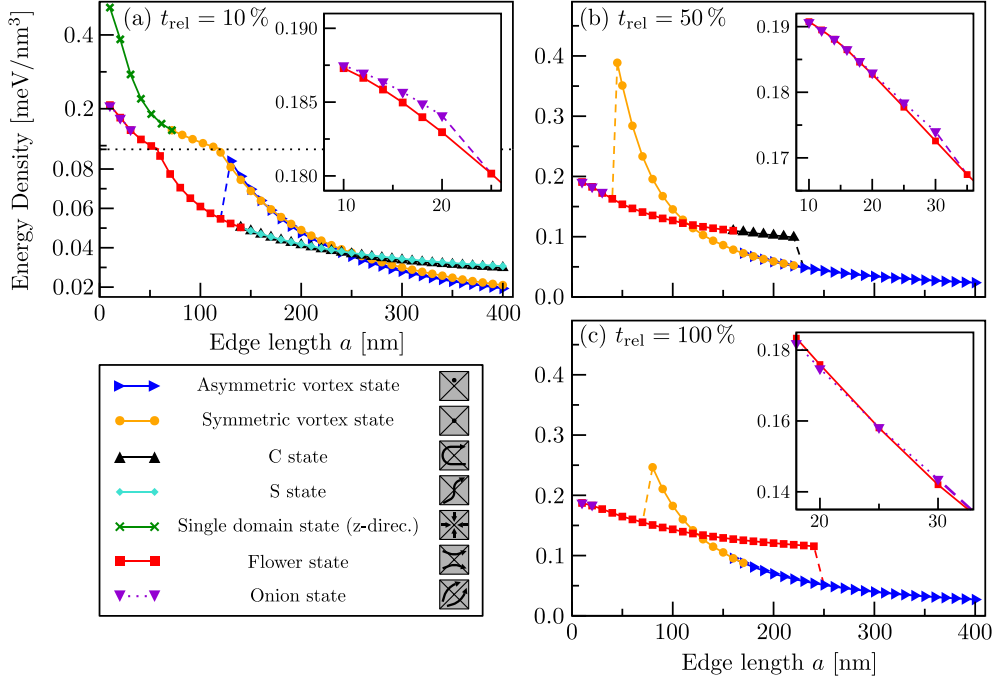


Figure 4.10.: Dependency of the energy density of different micromagnetic configurations on the size of the shell structure. Three different thicknesses t_{rel} are considered: (a) 10%, (b) 50%, and (c) 100%. The dashed lines denote transitions between different states, i.e. the state with the higher total energy becomes unstable and the lower-energy state develops. For a better readability we added schematic plots to the legend, which highlight the main feature of each ground state from a top-down perspective.

the stability range of the quasi-homogeneous states (C and S states) and the symmetric vortex state extends to $a_{\text{max}} = 400$ nm for $t_{\text{rel}} = 10\%$, while for $t_{\text{rel}} = 50\%$ and $t_{\text{rel}} = 100\%$, only the asymmetric vortex state is stable at large a . Thus the energy landscape becomes more complex, i.e. it contains more local minima, for very thin shells.

Figure 4.10 shows that the S state only occurs as a metastable state. We find that its total micromagnetic energy is always higher than the energy of the C state, a result that also has been found for square films [33, 35]. A possible explanation is the larger distance between positive and negative surface charges for the S state [33].

Why does the asymmetric vortex state occur?

The phase transitions from a flower state to a C state, and from a flower or C state to a vortex state (both symmetric and asymmetric), can be qualitatively explained in terms of (partial) flux closure and a corresponding reduction

4. Micromagnetic studies of pyramidal-shaped shell structures

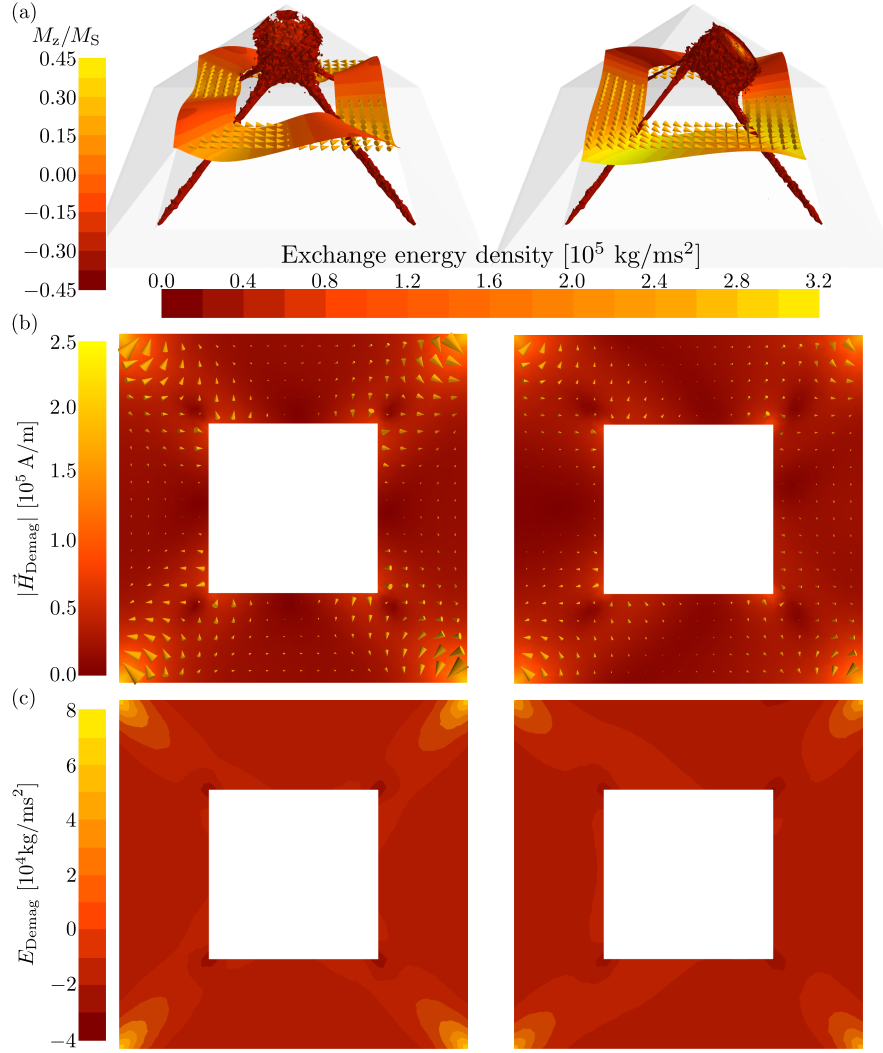


Figure 4.11.: Different fields in a cross-sectional plane are shown for the symmetric (left) and the asymmetric (right) vortex state. The cross-section is perpendicular to the z -axis and intersects it at $z = 50 \text{ nm}$ ($z = 0 \text{ nm}$ corresponds to the basal plane). Within all images of the asymmetric vortex state the bent vortex core points towards the right. The geometry parameters are $a = 240 \text{ nm}$ and $t_{\text{rel}} = 30\%$. (a) The arrows in the plane represent the magnetisation. Supplementary information is given by the warp plane, which bends out of the cross-plane. The displacement is proportional to m_z . Quantitative values of m_z can be taken from the colouration of the warp plane and the colour bar on the left. The exchange energy density of both configurations is represented in the form of contour surfaces. These reveal the location of the vortex core. (b) Demagnetisation field. The arrows are scaled according to the strength of the local demagnetisation field. (c) Magnetostatic energy density.

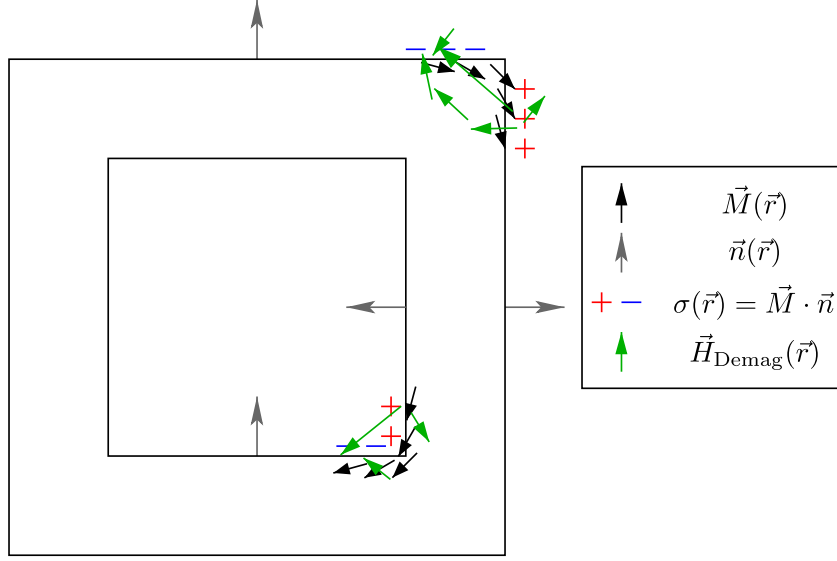


Figure 4.12.: Cross-section of a pyramidal shell illustrating the creation of surface charges near corners on the shell's inner and outer surfaces. The symbols defined in the plot correspond to the magnetisation $\vec{M}(\vec{r})$, the surface normals $\vec{n}(\vec{r})$, magnetic surface charges $\sigma(\vec{r})$, and the demagnetisation field \vec{H}_{demag} . The resulting demagnetisation fields and their orientation with respect to the magnetisation govern the magnetostatic energy density (see equation (4.2)). The plot gives a qualitative idea of the physical behaviour, but the lengths of vectors and the number of each symbol do not rigorously mirror corresponding physical quantities.

of the magnetostatic energy. In contrast, the physics driving the transition between the symmetric and the asymmetric vortex state is less evident and one has to take a closer look at the interplay between the geometry and the magnetisation. In this section, we will qualitatively explain this transition, and thus the occurrence of the asymmetric vortex state. The fact that the asymmetric vortex state is the ground state at large sizes a suggests that it reduces the magnetostatic energy with respect to the symmetric vortex state. A key role in this reduction is played by the edges separating adjacent side faces on the outside of the shell. Figure 4.11 compares the magnetisation, the demagnetisation field, and the magnetostatic energy density of the symmetric and the asymmetric vortex states for a cross-section, which lies perpendicular to the z axis. The magnetostatic energy density is defined as

$$u_{\text{demag}} = -\frac{1}{2} \vec{M} \cdot \vec{H}_{\text{demag}}, \quad (4.2)$$




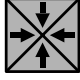
























so that a parallel alignment of magnetisation $\vec{M}(\vec{r})$ and demagnetisation field \vec{H}_{demag} is favoured. Let us first discuss the symmetric vortex state: surface charges close to the edges of the outer surface, i.e. the corners of the

4. Micromagnetic studies of pyramidal-shaped shell structures

cross-section in Figure 4.11, create a local demagnetisation field, which approximately aligns anti-parallel to the magnetisation (see top left and middle left image of Figure 4.11), corresponding to a local increase in the magnetostatic energy density. Therefore, the observed fluctuations of the magnetisation around the edges of the outer side faces (see Figure 4.11 (top)) can be understood in terms of a reduction of surface charges and a resulting lower demagnetisation field. Towards the tip of the pyramid the area of the cross-section decreases and the impact of the edges becomes more significant. As a consequence the magnetisation is increasingly driven out of the xy-plane so that this effect qualitatively explains the broadening of the vortex core as observed in Figure 4.7(a). Effects at the edges between the inner side faces of the shell are far weaker. This is mainly because the large demagnetisation fields, which are created between the areas of positive and negative surface charges, lie in the vacuum region, and therefore do not contribute to the micromagnetic energy functional. This is illustrated in the sketch of Figure 4.12.

When comparing the micromagnetic energy densities of an asymmetric and a symmetric vortex state (Figure 4.11 (bottom)), a reduction of magnetostatic energy density at the edges of the outer surface can be observed for the asymmetric vortex state. It can be attributed to the significant z-component of the magnetisation in the vicinity of the edges (Figure 4.11 (top)). Firstly, this reduces surface charges and thus the magnitude of the local demagnetisation field as shown by Figure 4.11 (middle). Secondly, Figure 4.11 (middle) also shows that the symmetry (i.e. the direction) of the demagnetisation field remains basically unaltered, so that magnetisation and demagnetisation field subtend a smaller angle, i.e. are not anti-parallel any more. According to (4.2), this leads to a reduction in the magnetostatic energy density u_{demag} .

In Section 4.3.1, we have discussed that the core of the symmetric vortex state broadens towards the tip of the pyramidal structure. Accordingly, Figure 4.11 (top) shows a very low exchange energy density at the top of the pyramidal structure for the symmetric vortex state, compared to the values shown for the core of the asymmetric vortex state. The much higher exchange energy density at the tip of the pyramidal core is not shown in this figure. Generally we find that the exchange and magnetostatic energy densities are higher within the displaced core. As other energetic differences (e.g. at the edges of the inner surface) are relatively small, the transition between the symmetric and the asymmetric vortex state seems to be governed by the competition between the magnetostatic energy density at the edges of the outer surface and the total micromagnetic energy density within the vortex core. More generally, we can conclude that a vortex configuration, whose core ends at a corner with converging edges, leads to high magnetostatic energy densities around

a	t_{rel}					
	$\vec{H}_{\text{ext}} x$			$\vec{H}_{\text{ext}} z$		
	10 %	50 %	100 %	10 %	50 %	100 %
50 nm	 ^a			 ^b	 ^d	
100 nm						
150 nm	 ^c					
250 nm		 ^e				
300 nm		-	-		-	-
400 nm		-	-		-	-

^a Flower state ^b Single domain state (z-direction) ^c C state
^d Symmetric vortex state ^e Asymmetric vortex state

Table 4.1.: Remanent states for different shell geometries (a, t_{rel}) when subsequently decreasing a strong magnetic field (3 Tesla), which is aligned along the x or z -direction, to zero (see Figure 4.2). To denote the different magnetic configurations we have used the same schematic plots as in the Figures 4.9 and 4.10.

the edges. This also may be an important factor in octahedrons and cubes, where, for large enough structures, a vortex core aligned along a diagonal (i.e. the core ends in corners) switches to a vortex configuration with its core aligned along face normals [45]. Also the twisted vortex state, which has been observed for cubes in the limit of soft materials [39], could be driven by similar edge effects.

4.3.2. Hysteresis

Although a direct observation of ferromagnetic states by a direct measurement of the magnetisation is possible (for example by using magnetic force (MFM) [115] or spin-polarised scanning tunnelling microscopy (SP-STM) [116]), hysteresis measurements are often more pertinent for a characterisation of the ferromagnetic properties of a structure. This is especially true for 3D struc-

4. Micromagnetic studies of pyramidal-shaped shell structures

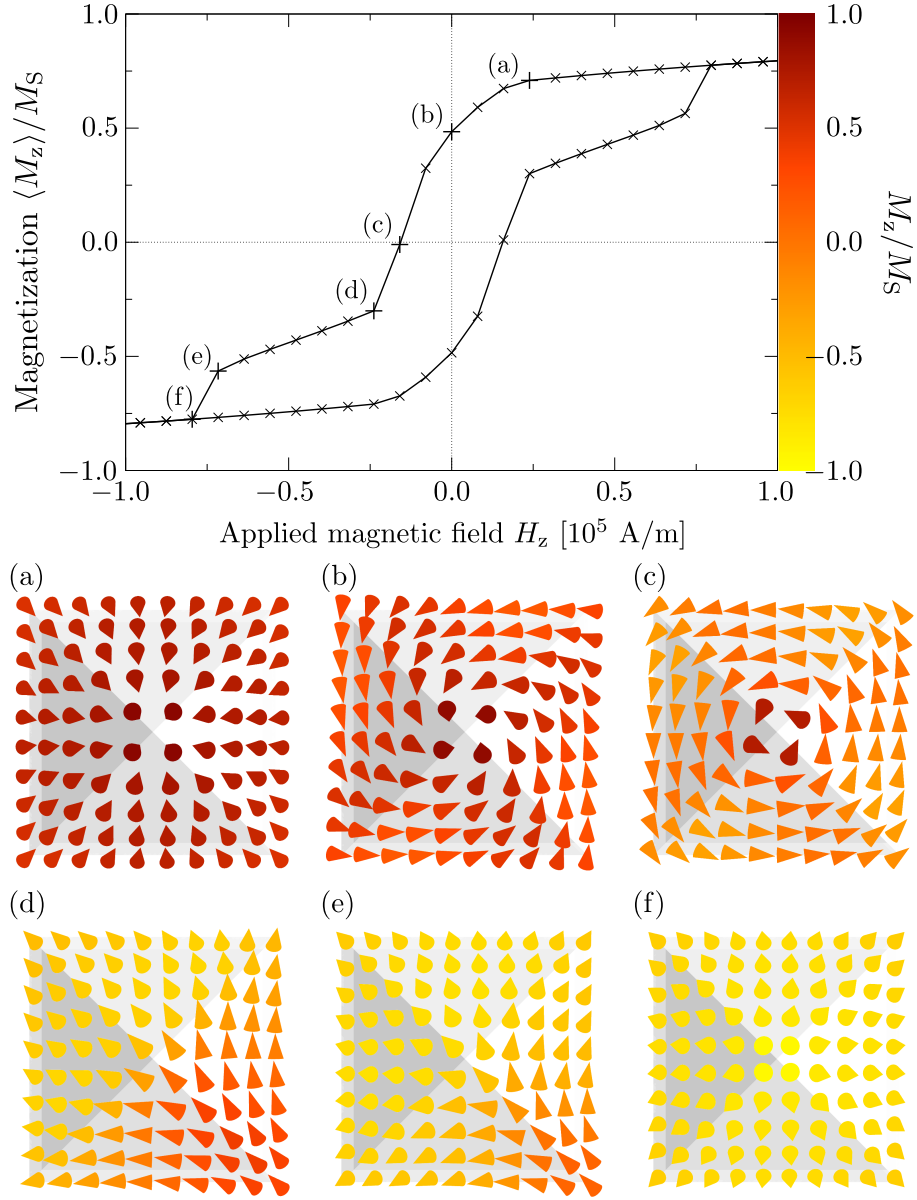


Figure 4.13.: Hysteresis of a pyramidal shell with an edge length of 100 nm and $t_{\text{rel}} = 10\%$. The external field \vec{H}_{ext} is applied along the z-direction, i.e. along the direction of the pyramid's tip. For selected points (a)-(f) magnetisation patterns are shown from a top-down perspective: (a) at higher external field the magnetisation subsequently aligns along side faces. (b) At zero field a symmetric vortex configuration develops. (c) Magnetisation partially reverses within vortex state. (d) Switch to a quasi-homogeneous state with the mean magnetisation mainly aligned along a diagonal of the structure's basal plane (onion state). (e) Reversal continues within onion state. (f) Switch to state where the magnetisation is aligned along side faces again.

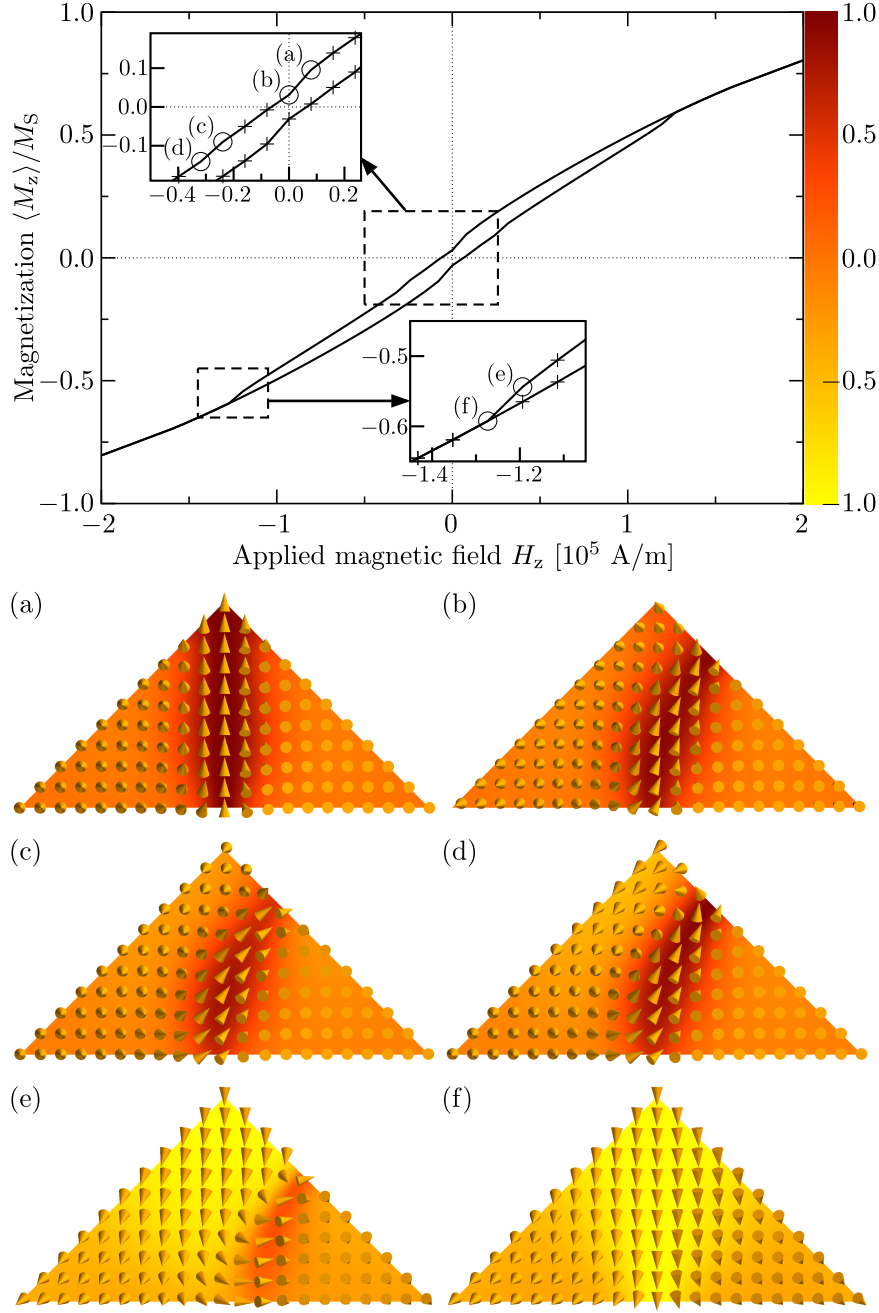


Figure 4.14.: Hysteresis curve of a full pyramid with an edge length of 250 nm. The external field \vec{H}_{ext} is applied along the z -direction, i.e. along the direction of the pyramid's tip. At selected points (a)-(f) magnetisation patterns within a cross-section of the pyramid are presented. The cross-section lies in the xz -plane and intersects the pyramid centrally. (a) With decreasing external field a symmetric vortex state subsequently develops. (b) System switches to an asymmetric vortex state at remanence. (c) The asymmetric vortex state remains stable at low external fields. (d) Nucleation of what will become the core of a reversed symmetric vortex state. (e) The displaced vortex core is gradually pushed out by the developing core of the reversed symmetric vortex state. (f) Reversed symmetric vortex configuration after the displaced vortex core has been annihilated.

4. Micromagnetic studies of pyramidal-shaped shell structures

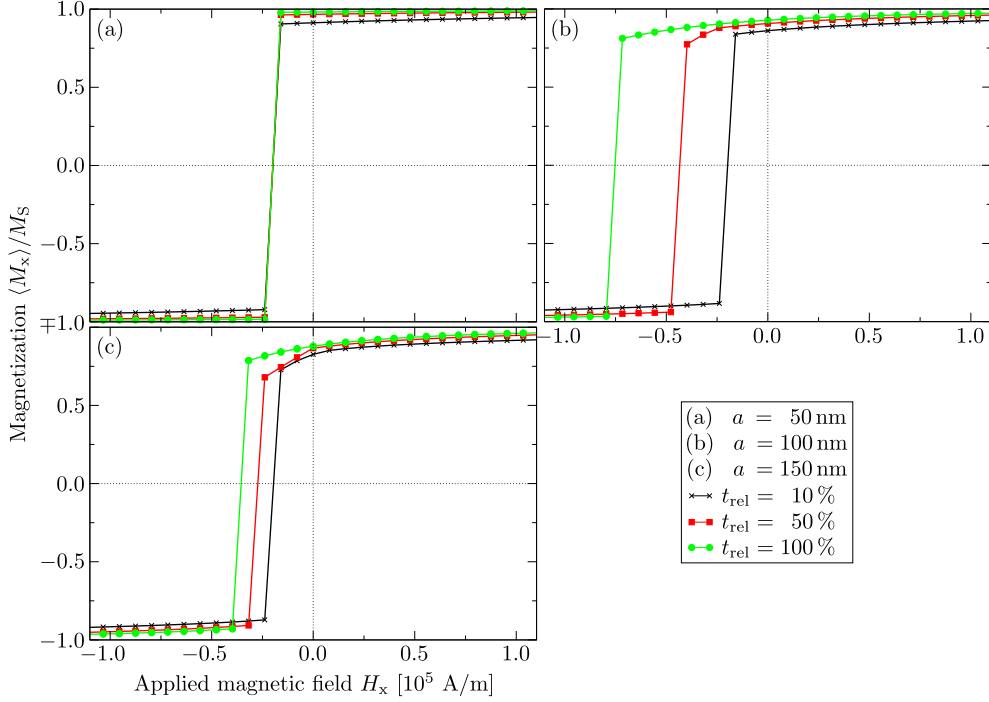


Figure 4.15.: The magnetic reversal along the x -direction is performed for different pyramidal shells (as indicated in the legend).

tures like the pyramidal shells studied in this paper, as the above-mentioned methods are surface techniques and only relatively straightforward to use on planar, 2D structures. From a hysteresis measurement one can obtain parameters such as the coercivity, susceptibility and the hysteresis [16], which quantify the magnetic properties. Furthermore, the knowledge of which state develops from a configuration, where the magnetisation is homogeneously aligned along a certain direction in space, is essential to the research on ferromagnetic structures as it provides the opportunity to establish desired magnetic states. In the following section, we focus on the qualitative behaviour of the magnetic reversal and investigate intermediate magnetic configurations occurring between the saturated states and their effect on the hysteresis curve.

We apply and change the external magnetic field \vec{H}_{ext} along one of the edges of the structure's basal plane (i.e. the x - or the y -direction in Figure 4.2) and along the direction of the pyramid tip (z -direction). We choose the former direction since it corresponds to the system's easy axis (for reasonable large system sizes where configurational anisotropy becomes important). The latter one is a suggested direction because it is perpendicular to the bottom layer. Therefore, the external magnetic field can be aligned accordingly and corresponding hysteresis measurements are easily realisable in experiments. The reversal simulations are performed by systematically changing the external field in small steps, and relaxing the magnetisation to a stable configuration

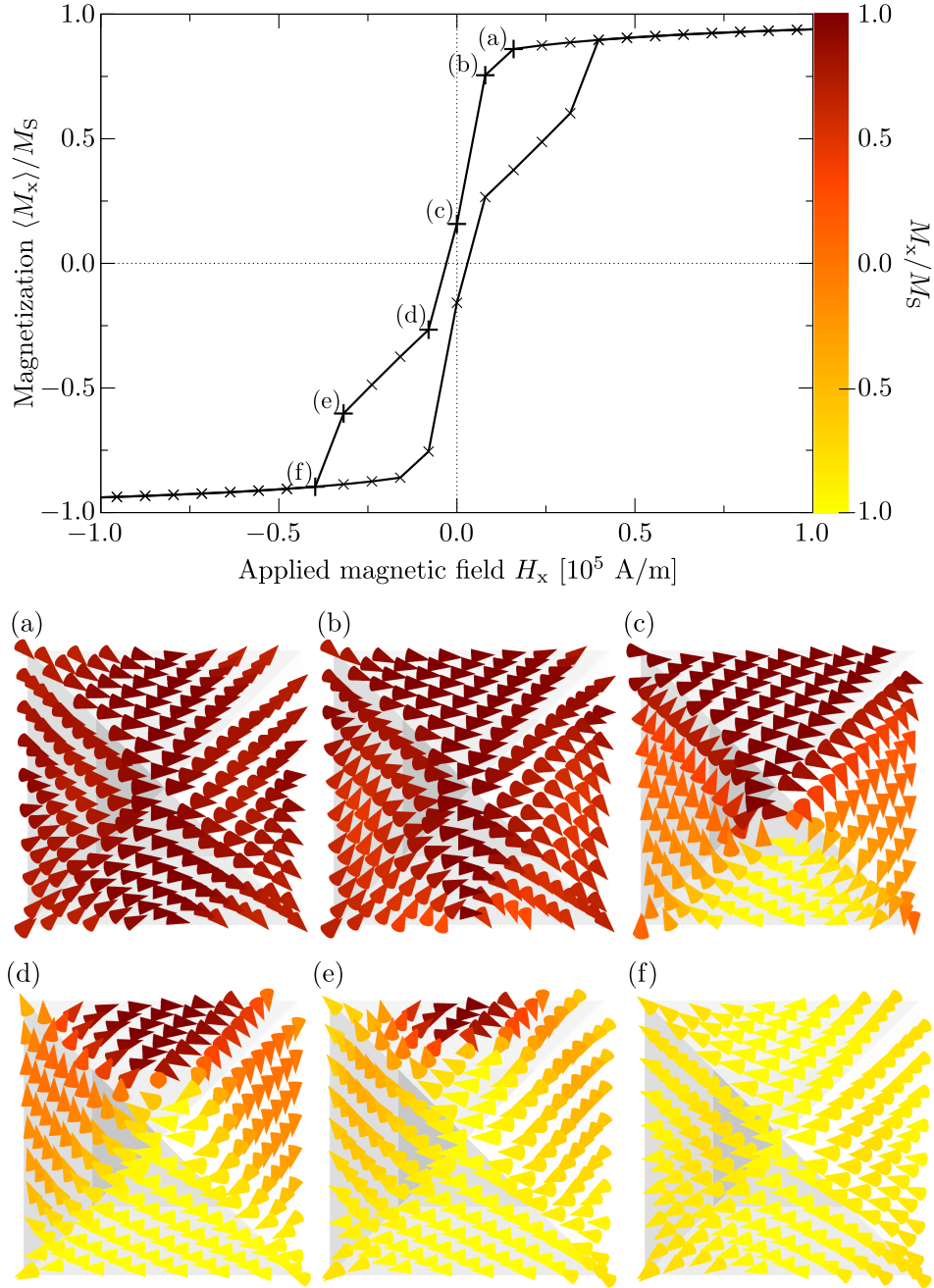


Figure 4.16.: Hysteresis of a pyramidal shell with an edge length of 250 nm and $t_{\text{rel}} = 50\%$. The external field \vec{H}_{ext} is applied along the x-direction. For selected points (a)-(f) magnetisation patterns are shown from a top-down perspective: (a) as the external field is reduced a flower state develops. (b) Switch to a C state at very low fields. (c) An asymmetric vortex configuration is formed at remanence. (d) At a low negative field the vortex core moves to the opposite side. (e) Vortex core subsequently moves down the side. (f) After the annihilation of the vortex core a reversed flower state becomes stable.

4. Micromagnetic studies of pyramidal-shaped shell structures

after each step. For every simulation, the external field is initially set to 3.0 T. From there the field is first reduced in steps of 0.2 T to 1.0 T, then in finer intervals of 0.05 T to 0.2 T, and finally to zero in 0.01 T steps. Afterwards the external field is changed equivalently from zero to -3.0 T. We have performed hysteresis simulations at the system sizes $a = 50$ nm, $a = 100$ nm, $a = 150$ nm and $a = 250$ nm for a thin shell ($t_{\text{rel}} = 10\%$), a shell ($t_{\text{rel}} = 50\%$) and a conventional pyramid ($t_{\text{rel}} = 100\%$). Those parameter sets (a, t_{rel}) correspond to regimes where either the flower state, the C state or symmetric vortex state, or the asymmetric vortex state are the ground state.

The remanent states of these hysteresis simulations are shown in table 4.1. Varying the external field along the x -direction, the remanent state tends to be a single-domain state. A variation along the z -direction tends to result in a vortex state at remanence. Hysteresis simulations along the z -direction exhibit a large variety of reversal mechanisms with different intermittent states. A specific reversal mechanism is strongly dependent on the size and shape of the geometry. Generally we observe that the magnetic reversal often occurs via an onion-like configuration for small structures ($a = 50$ nm and $a = 100$ nm) and via an asymmetric vortex state for larger structures ($a = 150$ nm and $a = 250$ nm). The former case is exemplified in Figure 4.13 where the magnetic reversal for a shell with ($a = 100$ nm, $t_{\text{rel}} = 10\%$) is shown. The remanent state is a symmetric vortex state (Figure 4.13b). At a magnetic field of about -20000 Am^{-1} the vortex state becomes unstable and switches to the onion-like configuration (see Figures 4.13c and d). This transition leads to a distinctive kink in the hysteresis curve and therefore may well be identifiable in an experiment. The reversal via an asymmetric vortex configuration is shown in Figure 4.14 for a full pyramid ($t_{\text{rel}}=100\%$). The hysteresis curve only contains subtle indications of changes in the micromagnetic configuration. Due to the discrepancy between the structure sizes accessible by experiment ($\sim \mu\text{m}$) and simulation (~ 100 nm), a comparison with the experimentally measured hysteresis curve of Figure 4.1 is currently not feasible. Interestingly the experimental curve exhibits a more square-like shape. This could be due to a pinning of the magnetisation, which may arise from the polycrystalline structure of the shell and additional anisotropies (enhanced magnetocrystalline anisotropy of nickel at low temperatures, strain-induced anisotropy) not included in the used model. Another possible explanation is that the reversal involves the nucleation and propagation of domain walls, which may get pinned at imperfections of the sample, such as grain boundaries.

Varying the external magnetic field along the x -direction, we find two reversal mechanisms. results in rectangular-shaped hysteresis curves similar to those of Stoner-Wohlfarth particles. Figure 4.15 compares the reversal curves for

pyramidal shells with $a = 50, 100$ and 150 nm and $t_{\text{rel}} = 10, 50$ and 100% . We observe direct transitions between quasi single domain states (flower, C and S state) pointing in opposite directions, which results in rectangular-shaped hysteresis curves similar to those of Stoner-Wohlfarth particles. For potential intermediate states occurring during these transitions one would have to reduce the step width for the external field (see also [117]). As expected, the remanent magnetisation decreases with increasing shell thickness t_{rel} due to the larger impact of the basal plane (see also Section 4.3.1). Furthermore, the remanent magnetisation decreases with an increasing system size since larger systems generally allow for more inhomogeneous configurations. More interesting is the dependence of the coercivity on the shell thickness and the system size. We find that the coercivity increases with an increasing shell thickness (Figure 4.15(b) and (c)). The dependency on the system size is more complex. For the depicted system sizes the coercivity of the pyramidal shells with $t_{\text{rel}} = 10\%$ does not vary with a . At larger system sizes (i.e. $a = 250, 300, 400$ nm), however, a slight reduction in the coercivity can be observed (not shown in the figure). For $t_{\text{rel}} = 50\%$ and $t_{\text{rel}} = 100\%$ we observe a maximal coercivity at $a = 100$ nm. A similar peak in the coercivity has also been found for square platelets [16]. The following two effects seem to lead to this behaviour: first, an increase of the systems size enhances the configurational anisotropy of the flower state, leading to a higher coercivity. Second, at higher system sizes the C state is formed during the reversal process, apparently reducing the coercivity.

Geometries with an edge length of $a = 250$ nm and thicknesses of $t_{\text{rel}} = 50$ and 100% exhibit a reversal mechanism that comprises a transition between two asymmetric vortex states whose cores end on opposing side faces (see Figures 4.16c and d). The switching between the asymmetric vortex states can easily be understood, as both states have a relatively large magnetisation component either parallel or anti-parallel to the external field. Generally, the reversal mechanism resembles the one observed for circular nanodots [36]. The main difference, however, is that for the pyramidal shells the hysteresis curve passes through two different remanent states, which correspond to the asymmetric states on opposite side faces. According to Figure 4.16, this transition occurs at relatively low fields, i.e. at fields below our step width of $7958 \text{ Am}^{-1} \equiv 100 \text{ Oe}$. Due to the fourfold symmetry of the pyramidal shell, one cannot only switch between two but four equivalent asymmetric vortex states.

4. Micromagnetic studies of pyramidal-shaped shell structures

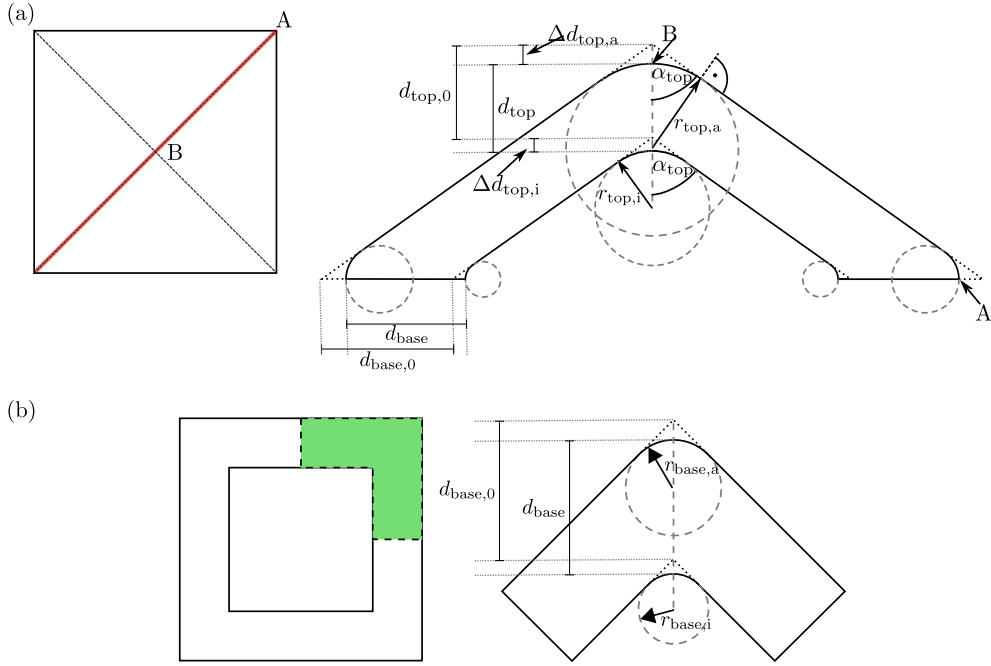


Figure 4.17.: (a) Left: pyramidal shell from a top-down perspective. The red line refers to the cross-section shown on the right. In the cross-section the shell's interior and exterior tip appear as corners. These corners are replaced by part-circles with the radii $r_{\text{top},i}$ and $r_{\text{top},a}$. Instead of using these radii as parameters for the rounding we use the variables d_{top} , $r_{\text{top},a}$ and $d_{\text{base},i}$, $r_{\text{base},a}$. d_{top} can be readily obtained from $r_{\text{top},i}$, $r_{\text{top},a}$, $d_{\text{top},0}$ and α_{top} . First, the illustrated quantities $\Delta d_{\text{top},a}$ and $\Delta d_{\text{top},i}$ are computed via $\Delta d_{\text{top},x} = r_{\text{top},x}(\sin^{-1}(\alpha_{\text{top}}) - 1)$ (with $x = a, i$), so that d_{top} is obtained by $d_{\text{top}} = d_{\text{top},0} - \Delta d_{\text{top},a} + \Delta d_{\text{top},i}$. For the studied pyramidal shells (with $h = a/2$) $\sin(\alpha_{\text{top}}) = \sqrt{2/3}$ holds. (b) Left: illustration of the shell's basal plane. As shown on the right, the corners of this cross-section are replaced by part-circles, the corresponding radii being $r_{\text{base},a}$ and $r_{\text{base},i}$. Again we control the rounding procedure by the parameters d_{base} and $r_{\text{base},a}$ (with $\alpha_{\text{base}} = \pi/4$). To create a pyramidal shell with rounded corners we then follow the following steps: we rigidly sweep the indicated green section of the base along the indicated red path (top left) between the points A and B in order to create a three dimensional (3D) solid. This is done for all four equivalent base sections so that four corresponding solids are created. By forming the union of these solids a pyramidal shell with rounded edges and corners is created. In summary, we introduce four dimensionless parameters, namely $d_{\text{top}}^{\text{rel}} = d_{\text{top}}/d_{\text{top},0}$, $r_{\text{top}}^{\text{rel}} = 2/\sqrt{3} r_{\text{top},a}/a$, $d_{\text{base}}^{\text{rel}} = d_{\text{base}}/d_{\text{base},0}$ and $r_{\text{base}}^{\text{rel}} = 2 r_{\text{base},a}/a$. The relative radii have been normalised such that $0 \leq r_{\text{top}}^{\text{rel}} < 1$ and $0 \leq r_{\text{base}}^{\text{rel}} < 1$ holds, with $r_{\text{top}}^{\text{rel}} = 0$ and $r_{\text{base}}^{\text{rel}} = 0$ corresponding to the shell with sharp corners.

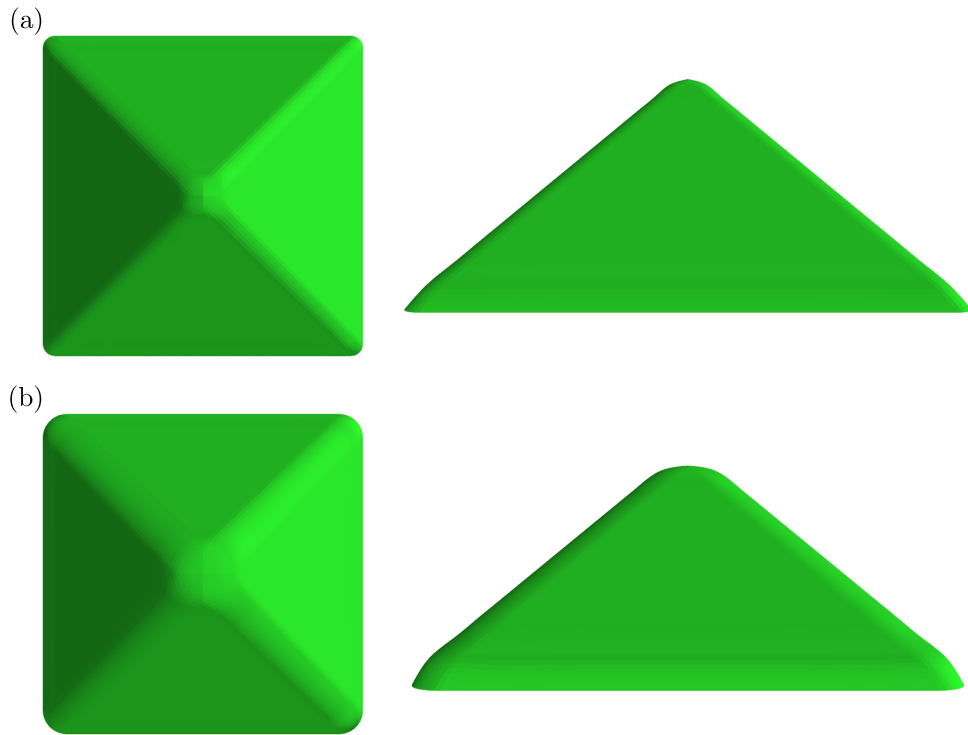


Figure 4.18.: Pyramidal shells with the parameters $a = 250$ nm and $t_{\text{rel}} = 50$ % are shown from a top-down perspective and from the side. The corners have been rounded off using the relative parameters (a) $r_{\text{top}}^{\text{rel}} = 0.075$, $d_{\text{top}}^{\text{rel}} = 1.0$, $r_{\text{base}}^{\text{rel}} = 0.075$ and $d_{\text{base}}^{\text{rel}} = 1.0$ and (b) $r_{\text{top}}^{\text{rel}} = 0.220$, $d_{\text{top}}^{\text{rel}} = 1.0$, $r_{\text{base}}^{\text{rel}} = 0.150$ and $d_{\text{base}}^{\text{rel}} = 1.0$.

4. Micromagnetic studies of pyramidal-shaped shell structures

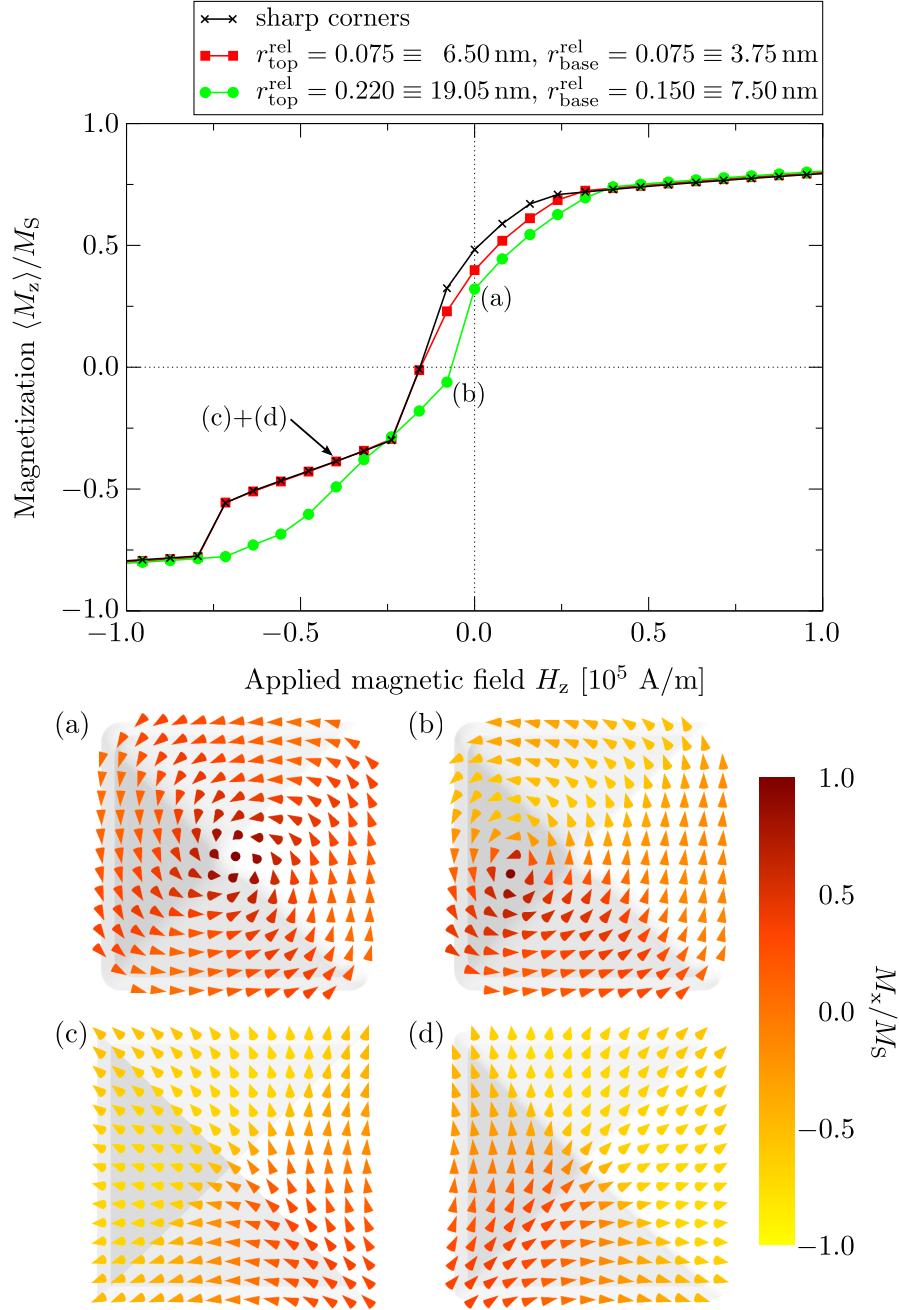


Figure 4.19.: The magnetic reversal along the z -direction is shown for pyramidal shells with $a = 100$ nm and $t_{\text{rel}} = 10\%$ and different degrees of rounding at the corners and edges. The black curve corresponds to the reversal of a pyramidal shell with sharp corners and edges (see also Figure 4.13). The geometries, which correspond to the green and red curve respectively, have been created with $d_{\text{bottom}}^{\text{rel}} = 1.0$ and $d_{\text{top}}^{\text{rel}} = 1.0$ and the indicated values for the parameters $r_{\text{bottom}}^{\text{rel}}$ and $r_{\text{top}}^{\text{rel}}$. The distribution of the magnetisation is shown for indicated points (a), (b), (c) and (d). Point (c) corresponds to the black curve and point (d) to the red curve.

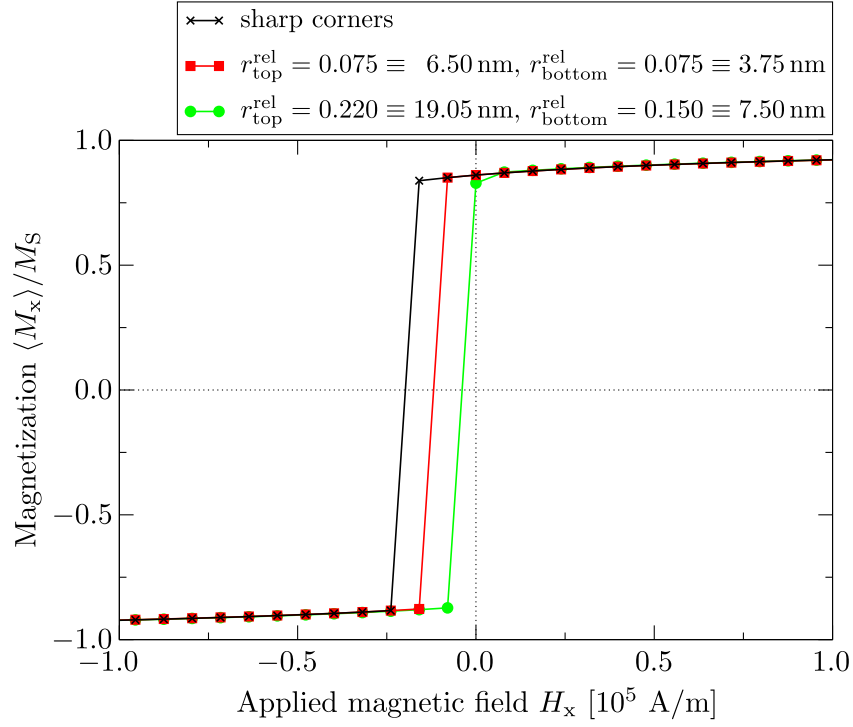


Figure 4.20.: The magnetic reversal along the x -direction is shown for pyramidal shells with $a = 100$ nm and $t_{\text{rel}} = 10\%$ and different degrees of rounding at the corners and edges. The black curve corresponds to the reversal of a pyramidal shell with sharp corners and edges (see also Figure 4.13). The geometries, which correspond to the green and red curve respectively, have been created with $d_{\text{bottom}}^{\text{rel}} = 1.0$ and $d_{\text{top}}^{\text{rel}} = 1.0$ and the indicated values for the parameters $r_{\text{bottom}}^{\text{rel}}$ and $r_{\text{top}}^{\text{rel}}$.

4. Micromagnetic studies of pyramidal-shaped shell structures

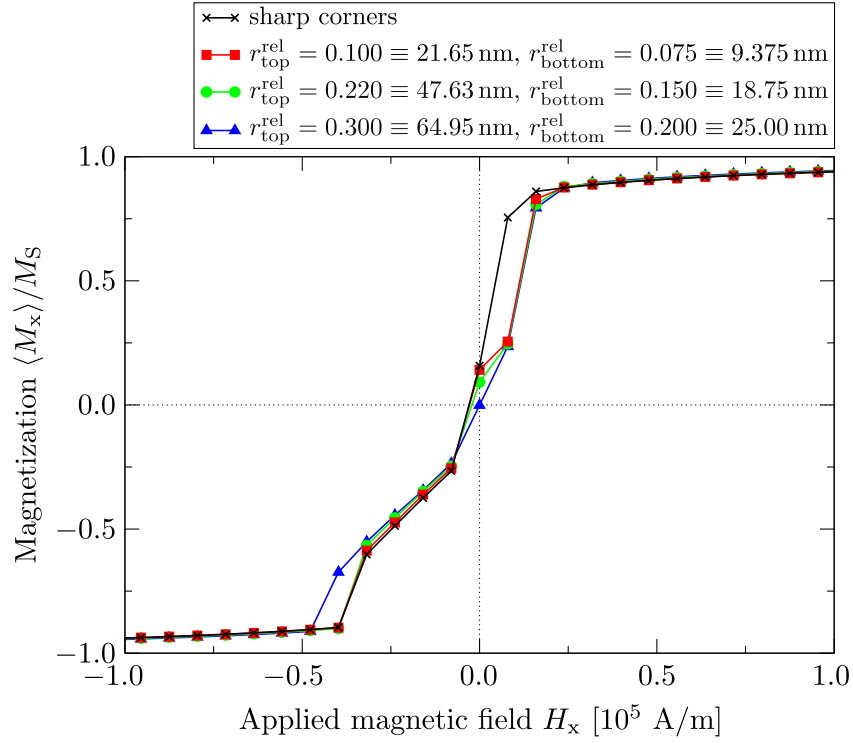


Figure 4.21.: The magnetic reversal along the x -direction is shown for pyramidal shells with $a = 250$ nm and $t_{\text{rel}} = 50\%$ and different degrees of rounding at the corners and edges. The black curve corresponds to the reversal of a pyramidal shell with sharp corners and edges (see also Figure 4.16). The geometries, which correspond to the green, red and blue curve respectively, have been created with $d_{\text{bottom}}^{\text{rel}} = 1.0$ and $d_{\text{top}}^{\text{rel}} = 1.0$ and the indicated values for the parameters $r_{\text{bottom}}^{\text{rel}}$ and $r_{\text{top}}^{\text{rel}}$. The remanent state of the black, red and green data curve is a asymmetric vortex state, while the remanent state of the blue data curve (corresponding to the highest degree of rounding) is a symmetric vortex state.

4.3.3. Pyramidal shells with rounded edges and corners

In Sub-section 4.3.1 we have already seen that the occurrence of sharp corners has an important effect on the formation of magnetic states (see also similar studies [118, 119]). Especially it has been argued that the occurrence of the asymmetric vortex state in pyramidal shell structures is a consequence of the high demagnetisation field in the vicinity of sharp edges. Furthermore, in realistic structures, as shown in Figure 4.1, edges are generally not sharp but slightly rounded off. In this section we want to investigate the effect of slightly rounded corners and edges on the magnetic properties of the structure. In order to define the rounding of edges in our pyramidal shells, Figure 4.17 introduces additional shape-defining parameters: $d_{\text{top}}^{\text{rel}}$, $r_{\text{top}}^{\text{rel}}$, $d_{\text{base}}^{\text{rel}}$ and $r_{\text{base}}^{\text{rel}}$. Figure 4.18 shows geometries which have been created with two different parameter sets. In the following we address three magnetic reversal scenarios which have already been discussed in the previous section (4.3.2). The first example is given in Figure 4.19, where the magnetic reversal along the z -direction is shown for pyramidal shells with $a = 100 \text{ nm}$, $t_{\text{rel}} = 10 \%$ and sharp corners as well as a rounding of corners as shown in Figure 4.18. We find that curvature radii of $r_{\text{tip}} = 6.50 \text{ nm}$ and $r_{\text{base}} = 3.75 \text{ nm}$ do not qualitatively alter the results, i.e. we still observe a symmetric vortex state at remanence, which at negative external fields transforms into a onion-like configuration. However, please note that the onion state within the pyramidal shell with the rounded corners aligns along a different diagonal in the xy plane (compare the configurations 4.19 (c) and (d)), which may also be observed by plotting the component $\langle M_x \rangle$ versus the external field H_z (not shown). When further increasing the curvature radii ($r_{\text{tip}} = 19.05 \text{ nm}$ and $r_{\text{base}} = 7.50 \text{ nm}$ in Figure 4.19) we find more significant changes in the magnetic behaviour. The remanent state is a symmetric vortex state, which changes to an asymmetric vortex state at a sufficiently reversed external field. We have performed the same comparison for a reversal along the x -direction in Figure 4.20. We find that increasing the rounding of the corners leads to a decrease in the coercivity, thus confirming the important role of corners during a reversal process of quasi single domain states [38]. Finally, we have investigated the reversal along the x -direction within a pyramidal shell with $a = 250 \text{ nm}$ and $t_{\text{rel}} = 50 \%$. The results are shown in Figure 4.21. For a pyramidal shell with sharp corners this reversal process usually contains the transition between two asymmetric vortex states. The vortex cores of these states end on opposite side faces of the geometry (see Figure 4.16). In Sub-section 4.3.1 we have seen that the occurrence of the asymmetric vortex state is due to high demagnetisation fields in the vicinity of sharp corners and edges. Therefore, our aim is to check how stable this state and the corresponding switching process is with respect to

4. Micromagnetic studies of pyramidal-shaped shell structures

the rounding of corners and edges. We find that the remanent state is an asymmetric vortex state even in the presence of rounding. This can be seen from Figure 4.21 where a geometry with curvature radii of $r_{\text{top}} = 47.63 \text{ nm}$ and $r_{\text{base}} = 18.75 \text{ nm}$ (green curve) accommodates a remanent state with a significant value for $\langle M_x \rangle$ (corresponding to an asymmetric vortex state). Further increasing these radii (blue curve) leads to a suppression of the asymmetric vortex state at remanence ($\langle M_x \rangle = 0.0$).

4.4. Conclusions

We have used micromagnetic simulations to conduct an in-depth analysis on the micromagnetic behaviour of pyramidal core-shell structures in the limit of soft magnetic materials. We have identified and characterised several stable and metastable states in a regime of sizes below $60 \cdot l_{\text{exch}}$. A phase diagram, which presents the energetic ground states at different structure sizes and shell thicknesses, with accurately computed phase boundaries has been created. By carefully examining the results of our micromagnetic simulations we have been able to qualitatively understand the phase transitions between different ground states. Additionally, we have investigated the stability regimes of all occurring states at different thicknesses. From our findings we conclude that the physics changes crucially in the limit of very thin shells. This implies a higher number of metastable states, generally extended stability regimes of quasi-homogeneous and vortex states (especially towards larger sizes) and differences in the ground state configurations. In particular, the reduction of metastable states with increasing thickness may be technologically relevant as the occurrence of metastable states can lead to problems. Analysing the magnetic reversal with respect to selected directions, we have found a switching mechanism between two equivalent vortex states that can be induced with low magnetic fields. This switching mechanism even works with a significant rounding of the corners and edges, which may be important regarding potential technological applications. Magnetic sensing is a typical area of application for soft magnetic materials with a high relative permeability and no hysteresis [16]. The studied pyramidal shells do not seem to exhibit these properties in a way that would make them a potential candidate for such an application. The asymmetric vortex state seems to be more interesting in regard to magnetic data storage. This field of application would require a certain thermal stability, i.e. an energy barrier E_B between the magnetic states, which is often estimated to be about $50 k_B T$ [120, 121]. A method of estimating the energy barrier between different stable configurations has been presented in [122] and may also be used to investigate the stability of the asymmetric vortex state. Another

aspect is the system size. From the phase diagram of Figure 4.9 we know that the asymmetric vortex state is stable for $a \geq 150$ nm (for Nickel), which is rather large compared to the elements of modern storage media [123, 124], even considering that one could store two bits within one pyramidal shell (corresponding to four equivalent asymmetric vortex states). Finally, the fast switching of magnetic domains induced by spin-polarised currents has been a topic of intensive research over the last decade [125]. It would be interesting to see whether these mechanisms could be used to switch between equivalent asymmetric vortex states. However, before spending resources on any further theoretical research on these structures one would probably wait until there has been a substantial progress on the experimental side. The disadvantages of grown, state-of-the-art structures (see for example Figure 4.1) have been discussed in this chapter (size $\sim 10 \mu\text{m}$, polycrystalline texture) and render medium-term, technical applications unfeasible.

5. Stray field investigations on core-shell-structures

In this chapter simulation results on core-shell structures, which have the shape of a triangular platelet and a rectangular prism, are presented. The study of these particular geometries has been motivated by the experimental work of our co-workers at the University of Bath. The core material is lead (Pb) in the case of the triangular platelets and tin (Sn) in the case of the rectangular prisms. These materials are type-I superconductors and become superconducting below $T_{\text{crit}}(\text{Pb}) = 7.2\text{ K}$ and $T_{\text{crit}}(\text{Sn}) = 3.7\text{ K}$, respectively. Superconductors are perfect diamagnets and as such completely expel an applied magnetic field, so that $\vec{B} = 0$ holds within their volume. As a consequence, the core exhibits a strong magnetic response to low magnetic fields below T_{crit} , which will have an effect on the physical behaviour of the core-shell structure. The shell material is Nickel, which is ferromagnetic and therefore can be described with the micromagnetic model introduced in Chapter 2. Some results of this chapter have been published in [1]. This article also contains references to relevant publications in the field of superconducting-ferromagnetic hybrid structures.

5.1. Experimental background

In this section we want to give some background on the experimental work conducted by our co-workers at the university of Bath. Figure 5.1 contains two three-dimensional atomic force microscope images of a Pb/Ni core-shell structure, which has the shape of a triangular platelet (5.1a), and a Sn/Ni core-shell structure, which has the shape of a rectangular prism (5.1b). These core-shell structures are classified as mesoscopic [4], as their typical dimensions are in the micrometre range. They are grown by electrodeposition [22, 23, 1]. The procedure is very similar to the two-step method, which has been discussed in Section 4.1. First, the core material, i.e. single crystalline Pb or Sn, is deposited onto the working electrode of an electrochemical cell via the island formation of a Volmer Weber growth mode. In contrast to the growth of the Ag/Ni core-shell structures of Section 4.1 the working electrode consists

5. Stray field investigations on core-shell-structures

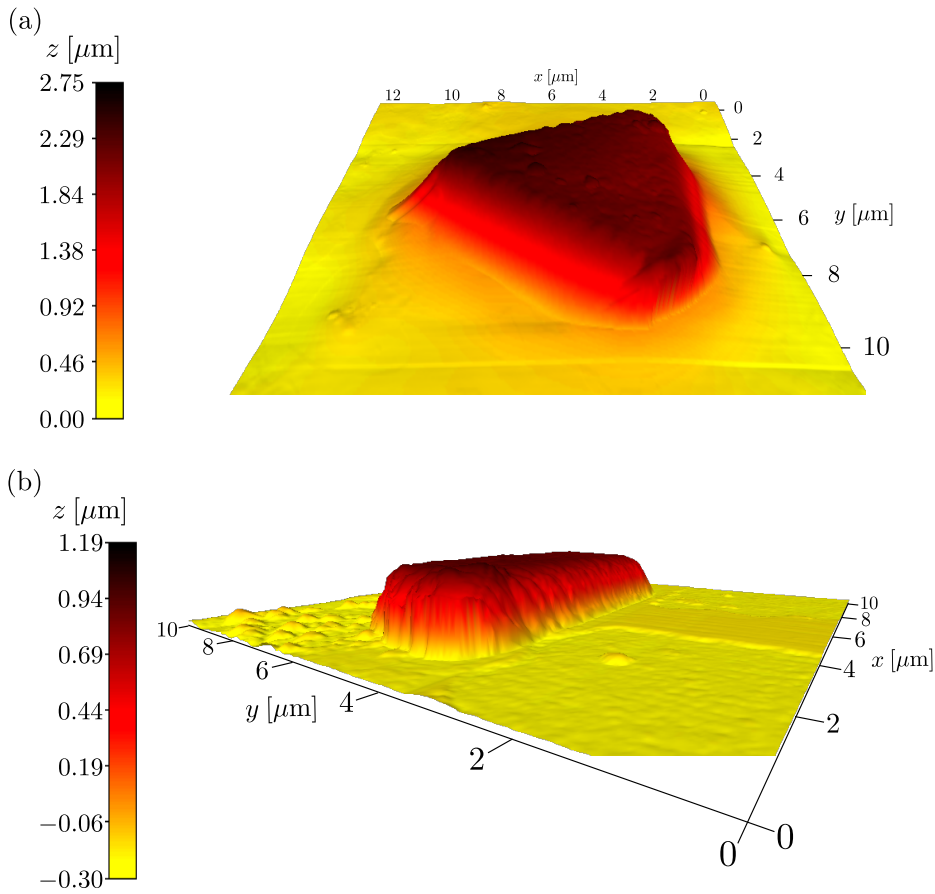


Figure 5.1.: Three-dimensional atomic force microscope images of (a) a triangular Pb-Ni platelet and (b) a Sn-Ni rectangular prism. These images have been provided by our co-workers, André Müller and Simon Bending, at the University of Bath (see also [1]).

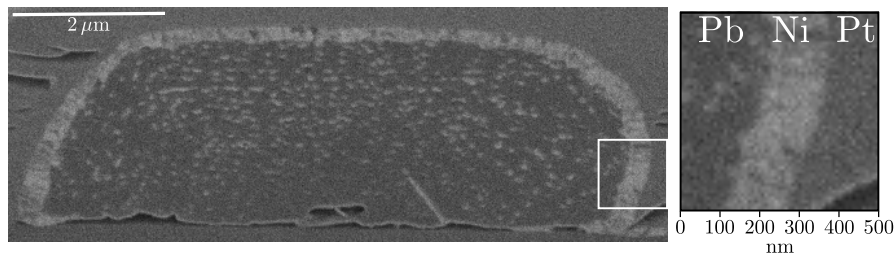


Figure 5.2.: Atomic force microscope image showing the cross-section through a triangular Pb-Ni platelet. The section within the white-rimmed box is magnified and shown in the illustration on the right. The cross-section has been obtained by sectioning the core-shell with a focused ion beam (FIB). Before this milling procedure a Pt layer has been deposited onto the region of interest in order to protect it [1]. This image has also been provided by our co-workers, André Müller and Simon Bending, at the University of Bath.

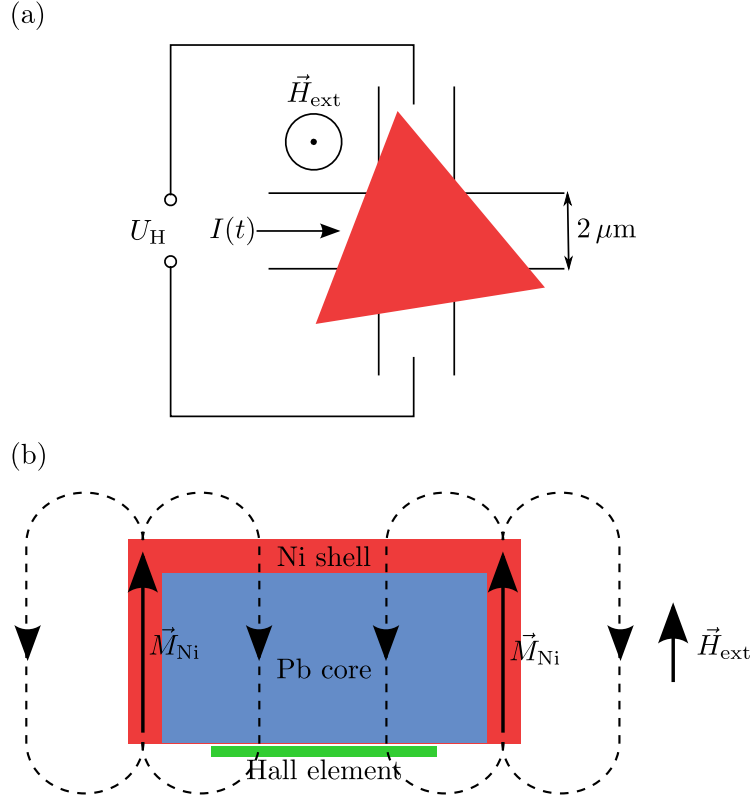


Figure 5.3.: (a) Sketch of the experimental setup: a triangular Pb/Ni core-shell structure is placed onto a $2\mu\text{m} \times 2\mu\text{m}$ active element of a two-dimensional GaAs/AlGaAs heterostructure Hall probe array. The latter is used in order to measure the perpendicular component of the local magnetic field $H_{\text{total},z} = H_{\text{demag},z} + H_{\text{ext},z}$. The external field is applied perpendicularly with respect to the plane of the Hall element. (b) Cross-sectional view of the experimental setup. The dashed lines illustrate the stray field, which is induced by a vertically aligned magnetisation within the side faces of the shell. Both figures have been adopted from [1].

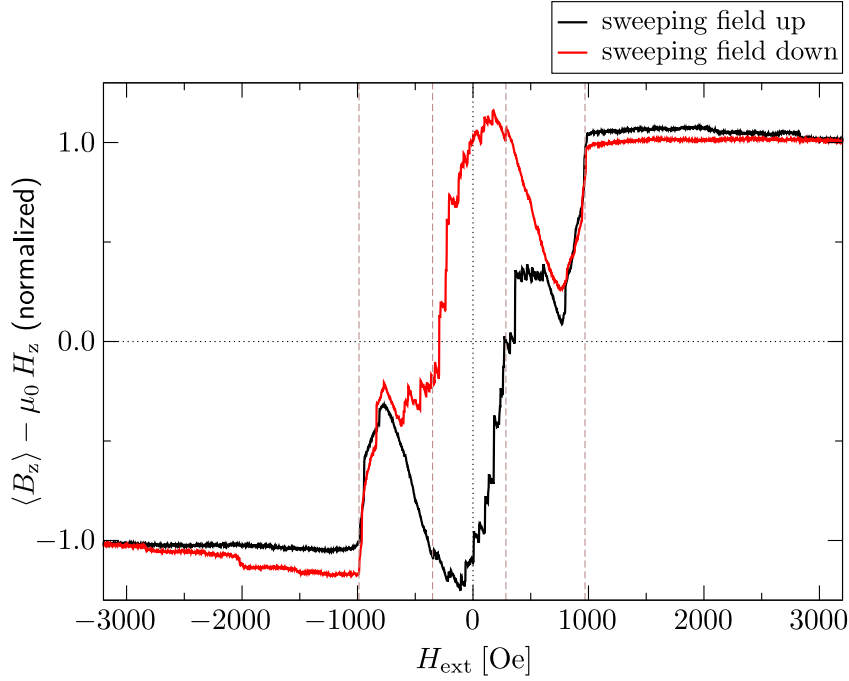


Figure 5.4.: Experimentally observed magnetic reversal of a Pb-Ni triangular platelet at $T = 4.2$ Kelvin. The investigated structure has a side length a of about $5.7 \mu\text{m}$ and a height h of about $2.2 \mu\text{m}$ (see also Figure 5.5). The abscissa shows the external field in Oersted, which is applied perpendicularly with respect to the triangular base of the platelet. The ordinate shows the z -component of the magnetic field measured by a $2 \mu\text{m} \times 2 \mu\text{m}$ active element of a two-dimensional GaAs/AlGaAs heterostructure Hall probe array, upon which the core-shell structure is placed, minus the externally applied field. The latter quantity is normalised with respect to its saturation value at high magnetic fields (i.e. $|H_{\text{ext}}| > 3000$ Oe), which for the presented case is about 115 Oe. The data clearly shows the occurrence of a diamagnetic cone for $H_{\text{min}} = 285 \text{ Oe} < H_{\text{ext}} < H_{\text{max}} = 970 \text{ Oe}$ when reducing the external field from positive values (red curve) and for $H_{\text{min}} = -985 \text{ Oe} < H_{\text{max}} = -350 \text{ Oe}$ upon the increase from negative values (black curve.). The values of H_{min} and H_{max} are marked by the vertical, dashed lines in the graph. The experimental data shown in this plot has been provided by our co-workers from the University of Bath.

of polycrystalline boron doped diamond (BDD), which, compared to highly oriented pyrolytic graphite (HOPG) can be prepared more uniformly and has a fairly constant low density of nucleation sites [23]. The latter property is important in order to avoid the overlap of islands from different nucleation sites. In a second step the electrolyte of the electrochemical cell is replaced and Nickel is electroplated onto the Pb or Sn islands. For details on the electrochemical growth, such as the composition of the electrolyte and the potential of the working electrode with respect to a reference electrode, the reader is referred to [1]. A cross section of a typical triangular core-shell structure is shown in Figure 5.2, demonstrating the sharp interface between the core and the shell region. The shell thickness varies from about 100 nm at the top of the structure to up to 200 nm at the sides, which confirms estimates between 100 and 300 nm made from the electrodeposition parameters [1]. Figure 5.3 shows the experimental setup for the measurement of the magnetic hysteresis of a triangular Pb/Ni core-shell structure. In a first step, the core-shell structure is removed from the BDD electrode, which is facilitated by the chemical inertness of the boron doped diamond, and placed on one of the $2\text{ }\mu\text{m} \times 2\text{ }\mu\text{m}$ active elements of a two-dimensional GaAs/AlGaAs heterostructure Hall probe array (see Figure 5.3). This process is carried under a long focal length optical microscope, the resolution of which is limited by the wavelength of visible light ($\sim 400 - 800\text{ nm}$). Therefore, only structures of dimensions in the micrometre range (and above) can be identified in order to move them from the working electrode and use them for further investigations. Thus, our restriction to relatively large structure sizes is not due to limitations of the growth process itself but rather a consequence of size limitations when preparing individual structures for experiments. The hysteresis measurements are carried out by subsequently sweeping the external magnetic field, which is aligned perpendicularly with respect to the base of the core-shell structure ($= z$ -direction), from high positive field values $> 3000\text{ Oe}$ to high negative field values $< -3000\text{ Oe}$ and vice versa. The Hall element measures a spatial average of the magnetic field, which is taken over its extension. From this value one has to deduct the value of the homogeneous external field in order to determine the spatial average of the magnetic stray field stemming from the core-shell structure. The experimental result for a triangular Pb/Ni core-shell structure is shown in Figure 5.4. The most interesting feature is the diamagnetic dome, which occurs in the range $285\text{ Oe} < H_{\text{ext}} < 970\text{ Oe}$, when sweeping the external field down (red curve), and in the range $-985\text{ Oe} < H_{\text{max}} = -350\text{ Oe}$, when sweeping the field up (black curve). Its occurrence can be interpreted in terms of the core becoming superconducting in the denoted range of external fields: lead becomes superconducting at temperatures below $T_{\text{crit}}^{\text{Pb}} = 7.2\text{ K}$. Furthermore, superconductivity is destroyed, when the magnetic field exceeds

5. Stray field investigations on core-shell-structures

a temperature-dependent critical field value $H_{\text{crit}}^{\text{Pb}}(T)$, which can be approximated by the formula

$$H_{\text{crit}}^{\text{Pb}}(T) = H_{\text{crit}}^{\text{Pb}}(0) \left(1 - (T/T_{\text{crit}}^{\text{Pb}})^2\right) \quad (5.1)$$

with $H_{\text{crit}}^{\text{Pb}}(0)$ being 803 Oe [126]. The simulation results have been obtained at $T = 4.2\text{ K}$, a temperature, which can be accurately adjusted in experiments, as the system only has to be left until it has settled at the boiling point of Helium and no additional heating is required [127]. With equation 5.1 we then find $H_{\text{crit}}^{\text{Pb}}(T) = 530\text{ Oe}$. Figure 5.3b illustrates that the magnetic field in the core region is the sum of the external field and the stray field stemming from the ferromagnetic Nickel shell, i.e.

$$\vec{H}_{\text{total}}(\vec{r}) = \vec{H}_{\text{ext}} + \vec{H}_{\text{stray}}. \quad (5.2)$$

At 4.2 K superconductivity is destroyed in the region of the Pb core, where $|\vec{H}_{\text{total}}| > 530\text{ Oe}$ holds. When decreasing the field from high external field strengths (red curve of Figure 5.4), the diamagnetic dome can then be interpreted as follows: before its onset ($\vec{H}_{\text{ext}} \gtrsim 970\text{ Oe}$), the strong external field destroys superconductivity within the Pb core. With its onset, the external field and the stray field from the ferromagnetic shell, which tends to oppose the external magnetic field (see also Figure 5.3), compensate each other, so that locally $\vec{H}_{\text{tot}} < 530\text{ Oe}$ may hold. At low external field strengths ($\vec{H}_{\text{ext}} \lesssim 285\text{ Oe}$), the uncompensated stray field destroys superconductivity within the core region. In Sub-section 5.2.1, we will see that this scenario is qualitatively confirmed using a simple micromagnetic model.

5.2. Simulation results

This section is structured as follows: in Sub-section 5.2.1 the simulation results on the triangular Pb/Ni core-shell structures are presented, which, in parts, have been published in Section [1]. Simulation results on the cuboidal core-shell structures, which show the reversal in an external field \vec{H}_{ext} , are presented in Sub-section 5.2.2. Figure 5.5 defines the idealised cuboidal (5.5a) and triangular platelet-shaped (5.5b) core-shell geometries in terms of corresponding geometry parameters.

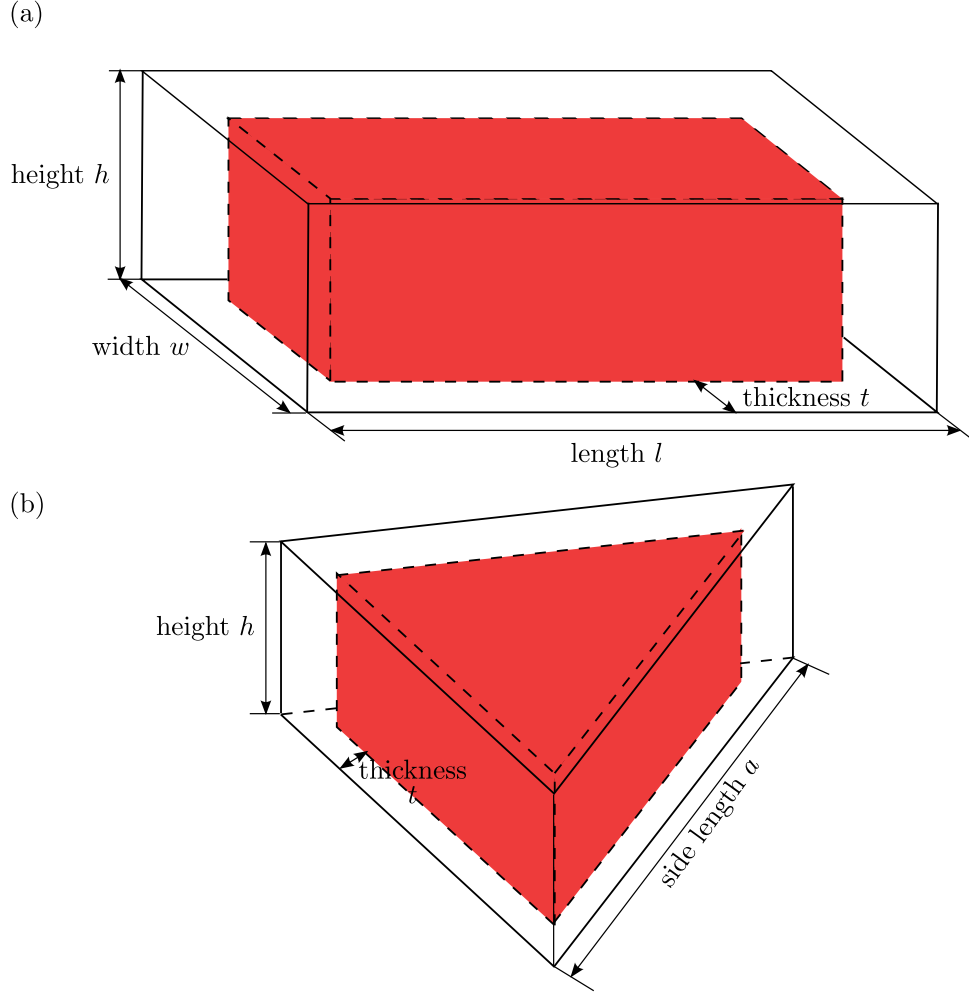


Figure 5.5.: Geometrical definition of the core-shell structures which have been investigated. (a) Core-shell structure in the shape of a prism: the parameters h , l and w determine the dimensions of the prism as measured at the outside of the shell. The parameter t is the thickness of the shell. (b) Core-shell structure with a triangular shape: the dimensions of the structure are determined by the two parameters a and h (as measured with respect to the structure's outside). The parameter a is the side length of the isosceles triangle, which forms the base of this structure. The third parameter t is the thickness of the shell.

5.2.1. Superconducting regions in triangular Pb/Ni core shell structures

In this sub-section we want to present a simple micromagnetic model, which allows for a simple interpretation of the experimental results of Figure 5.4. As in Chapter 4 we use the finite-element based solver Nmag [93] to conduct our simulations. The experimentally grown structures have typical dimensions of several micrometres and a shell thickness ≥ 100 nm. Such structure sizes are not accessible by micromagnetic simulations, so that we have to scale the system down by a factor 10.

Computation of the superconducting fraction

In our approach, we assume that the diamagnetic signal (see Figure 5.4), which has been measured at the Hall element, is proportional to the superconducting volume within the core region. Thus, after relaxing the magnetisation of the Ni shell we compute the superconducting volume within the core region, i.e. the volume where $|\vec{H}_{\text{stray}} + \vec{H}_{\text{ext}}| < H_{\text{crit}} = 530$ Oe holds. This is done by defining a tetrahedral mesh within the core region, on which the stray field from the Nickel shell can be computed numerically. If the above mentioned criterion for superconductivity holds at a certain mesh node i , a corresponding volume

$$V_i = \frac{1}{4} \sum_{i \in k,l,m,n} T_{k,l,m,n} \quad (5.3)$$

is assumed to be superconducting. $T_{k,l,m,n}$ is the volume of the tetrahedron, which is formed by the mesh nodes k , l , m and n . Thus, the sum runs over all tetrahedrons, of which the node i is a corner. Repeating this procedure for all nodes of the core mesh and adding up the corresponding volumes yields the superconducting volume within the core. In the following, we will normalise the superconducting volume with respect to the full volume of the core mesh and refer to this quantity as the superconducting fraction. In order to be able to probe the stray field on the core mesh, the core region needs to be defined within Nmag and material parameters such as A , M_S have to be set. Nmag will then also integrate the micromagnetic equations on the core mesh. The exchange constant A and anisotropy constants can just be set to zero. However, M_S^{Vac} has to be given a finite value in order to avoid divisions by 0. The value of M_S^{Vac} should be small, so that it does not affect the calculated stray field within the core region. In Section D.2 of Appendix D it is shown that for the studied system the condition $M_S^{\text{Vac}} < 10$ A/m ensures a sufficient accuracy.

The tetrahedral mesh

The commercial software tool Fluent Gambit 2.4.6 is used in order to create tetrahedral meshes of the shell and the core. The resolution of the shell mesh is chosen such that the maximal tetrahedron edge length does not exceed the exchange length l_{exch} . Unlike Chapter 4 we do not have to use a smaller mesh resolution in order to increase the accuracy of the stray field calculation. First, because the dimensions of the studied structures ($\gtrsim 500 \text{ nm}$) and the shell thicknesses ($\geq 10 \text{ nm}$) are larger than those of Chapter 4. Second, because we do not compare the total energies of different micromagnetic states, a task which requires an accurate computation of the micromagnetic energies (see Section D.1 of Appendix D). To limit the complexity of our simulations, the core mesh is chosen to be coarser than the shell mesh. This can be done since no resolution below l_{exch} is required. We leave a gap of 5 nm between the shell mesh and the core mesh. Otherwise, the core mesh would have to adopt the resolution of the shell mesh at the interface and would only gradually become coarser towards the centre of the core, leading to a significant increase in the size of the core mesh. Beside these efficiency considerations the introduction of such a gap is physically justifiable, as in the vicinity of the Ni/Pb interface superconductivity is suppressed due to the proximity effect. This effect extends into the volume of the superconductor on a length scale of one coherence length ($\approx 80 \text{ nm}$ for lead) [1]. Considering that we have to reduce the size of the experimental structures by a factor 10, it is perfectly reasonable to not consider a surface region of the core with a depth of a few nanometres. The chosen gap width of 5 nm even rather underestimates this effect. For the structure sizes of this section we choose a resolution, which corresponds to a mean tetrahedron edge length of about 20 nm. In Section D.2 in Appendix D it is shown that this leads to a reasonable accuracy.

The micromagnetic model

In our approach, we first relax the micromagnetic configuration of the Nickel shell from a homogeneous state, which is aligned along the normal of the base of the triangular platelet (z -direction). Furthermore, a homogeneous external field of variable strength is applied along the z -direction. As in Chapter 4, we set the exchange constant A to $7.2 \times 10^{-12} \text{ J/m}$ and do not consider the cubic anisotropy of Nickel. Due to the polycrystalline structure of the Nickel shell an inclusion of the magnetocrystalline anisotropy is not straightforward. The saturation magnetisation M_S is set to 510000 A/m , which is the value at $T = 0 \text{ K}$ [49]. Hence, the exchange length l_{exch} is equal to 6.64 nm . To enhance the efficiency of the algorithm, hierarchical matrices are used to op-

5. Stray field investigations on core-shell-structures

timise the computation of the stray field. For the assembly of the hierarchical matrices we use the algorithm HCA II with parameters as given in Section 3.1.3. We find that the micromagnetic model cannot account for the annihilation of superconductivity at remanence ($|\vec{H}_{\text{ext}}| = 0 \text{ Oe}$), which is suggested by the experimental data of Figure 5.4. Therefore, we have chosen the following approach: first, the magnetisation of the Nickel shell is relaxed at a relatively high external field (e.g. 1000 Oe). Then, the magnetisation is pinned, while the strength of the external field is gradually changed. As a result we obtain a data curve showing the computed superconducting fraction as a function of the external field. Such a pinning is also suggested by the experimental data outside of the diamagnetic dome shown in Figure 5.4: before its onset the measured stray field is constant without any decay, after leaving the regime of the diamagnetic dome the measured stray field returns to very high values. Physically, the polycrystalline structure of the Nickel shell may lead to the pinning of magnetic structures like vortices and domain walls at imperfections such as grain boundaries (see also discussion in Section 4.3.2 and [108, 1]). Finally, it should be noted that the stray field from the shell is scale-invariant, i.e. for a certain micromagnetic configuration it will not depend on the size of the studied geometry. Therefore, if we obtain the qualitatively correct micromagnetic configuration in our scaled-down geometries, we should also get qualitatively good results concerning the superconducting fraction. However, one should keep in mind that our approach does not consider the presence of screening currents and associated magnetic fields within the Pb core. The inclusion of such effects would require the solution of the coupled micromagnetic and the Ginzburg-Landau equations [1].

Micromagnetic configuration in triangular platelet-shaped shell

Figure 5.6 shows the micromagnetic configuration of a thin (10 nm) Nickel shell in differently strong external magnetic fields. At each external field strength we observe a vortex configuration, with the vortex core sitting at the centre of the triangular top face. Furthermore, we see that, at low external field strengths, the magnetisation of the side walls tends to orient parallel to the base plane of the triangular structure (see 5.6(a)). Only in the vicinity of those edges, which separate the side faces, the magnetisation is pinned along the z direction. We find that the stray field of such a configuration cannot account for the annihilation of superconductivity at low external fields, so that a pinning of the magnetisation is introduced when computing the superconducting fraction as a function of the external field (see previous paragraph). When increasing the external field the magnetisation of the side walls starts to align along the z -direction. At very high magnetic fields also an increased z -

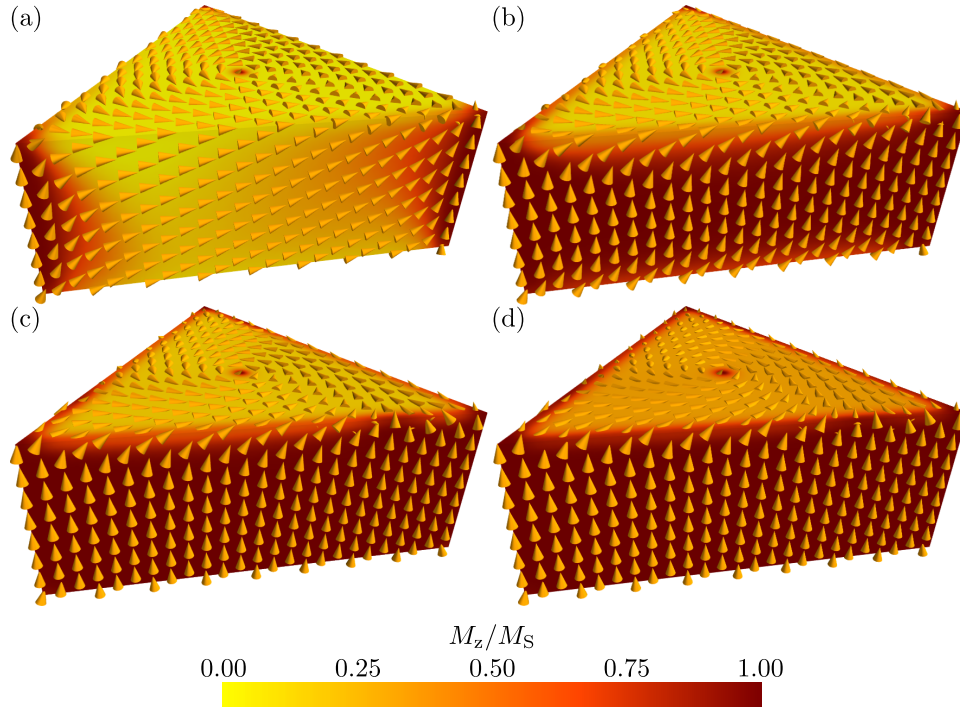


Figure 5.6.: The micromagnetic configuration of a triangular platelet-shaped shell structure (edge length $a = 570$ nm, height $h = 220$ nm and thickness $t = 10$ nm) is shown at different external field strengths. The external field is aligned with the z direction, i.e. perpendicularly with respect to the base of the structure. The images correspond to the following field strengths: (a) 100 Oe, (b) 500 Oe, (c) 1000 Oe and (d) 2000 Oe.

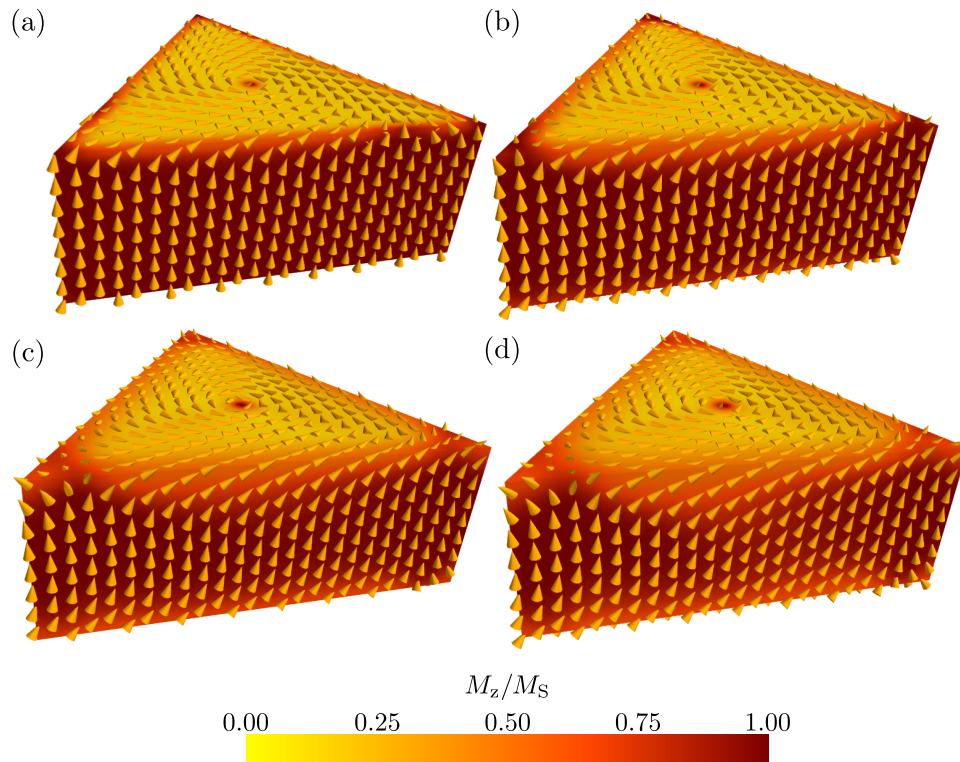


Figure 5.7.: The micromagnetic configuration at an external field strength of 1000 Oe is shown for triangular shell structures with a side length $a = 570$ nm, a height $h = 220$ nm and different shell thicknesses: (a) $t = 10$ nm, (b) $t = 20$ nm, (c) $t = 30$ nm and (d) $t = 40$ nm. The external field is aligned with the z direction, i.e. perpendicularly with respect to the base of the structure.

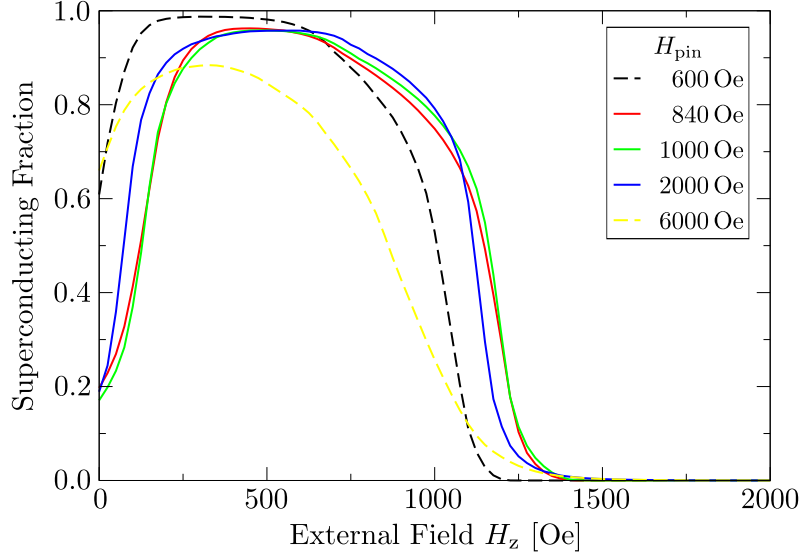


Figure 5.8.: The dependence of the superconducting fraction within the core on the external magnetic field is shown for different pinning field strengths. The investigated triangular shell structure has a side length of $a = 655.9$ nm, a height of $h = 295$ nm and a thickness of $t = 40$ nm.

component of the magnetisation within the top layer becomes apparent (colour change from yellow in Figure 5.6(c) to orange in Figure 5.6(d)). Figure 5.7 shows the micromagnetic configuration at an external field of $|\vec{H}_{\text{ext}}| = 1000$ Oe for different shell thicknesses. We clearly see that the magnetisation within the side walls becomes more inhomogeneous with an increasing shell thickness. This can be qualitatively understood as a homogeneous alignment of the magnetisation along the z -direction leads to the creation of surface charges σ_M at the bottom and the top of the structure, which according to the equations (2.7), (2.13) and (2.15) increases the magnetostatic energy. For a larger shell thickness this energy penalty and thus, the tendency of the system to avoid these surface charges, becomes more significant.

Computation of the superconducting fraction

We now want to discuss the dependence of the superconducting fraction within the core on strength of the external field \vec{H}_{ext} . As stated above our approach is to relax the micromagnetic configuration of the shell at a certain external field strength. Then the magnetisation and thus, its stray field, is pinned, while the external field is systematically varied to compute the corresponding superconducting fraction within the core. Figure 5.8 shows how the superconducting fraction within a core-shell structure with a thickness of 40 nm depends on the strength of the used pinning field. When a relatively low pinning field of

5. Stray field investigations on core-shell-structures

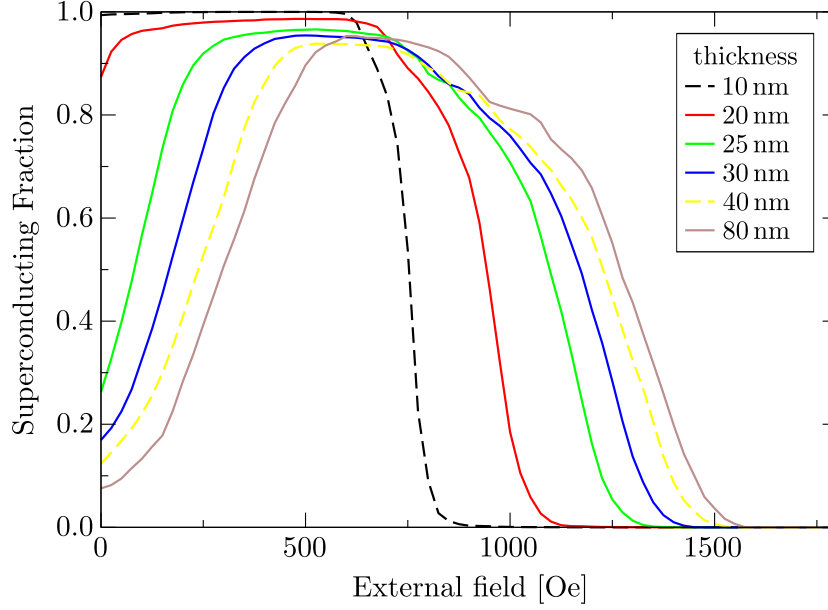


Figure 5.9.: Graph showing the superconducting fraction as a function of the external field for different shell thicknesses. The magnetisation has been pinned at an external magnetic field of 1000 Oe. The investigated structures have a side length of 570 nm, a height of 220 nm.

600 Oe is chosen, the stray field is not strong enough to annihilate superconductivity at $|\vec{H}_{\text{ext}}| = 0$ in the bulk of the core region. Increasing the pinning field to 840 Oe leads to the annihilation of superconductivity at $|\vec{H}_{\text{ext}}| = 0$ in most parts of the core region (about 80 %). The stronger stray field also leads to an extension of superconductivity to higher external fields, i.e. the observed dome shape shifts towards positive external field values. Generally, we find that the dependence of the superconducting fraction on the external field is insensitive to the used pinning field for a wide range of values (between 800 Oe to more than 2000 Oe). Only for very strong pinning fields (here: 6000 Oe) we observe a reduction of the stray field, i.e. the survival of superconductivity at $|\vec{H}_{\text{ext}}| = 0$. Furthermore, the shape of the dome changes significantly, especially towards high external fields, and the superconducting fraction never exceeds a value of 0.9. This is due to a partial magnetisation of the top layer of the shell (along the z -direction), which screens the stray field stemming from the side walls of the structure. Figure 5.9 shows the superconducting fraction within the core region as a function of the external field for different shell thicknesses. The geometry of the core-shell structure (side length $a = 570$ nm, height $h = 220$ nm) has been scaled down from the dimensions of the experimental structure (see Figure 5.1) by a factor of 10. We see that a very thin shell thickness of 10 nm cannot account for the annihilation of superconductivity in the absence of an external field. For this, the shell thickness

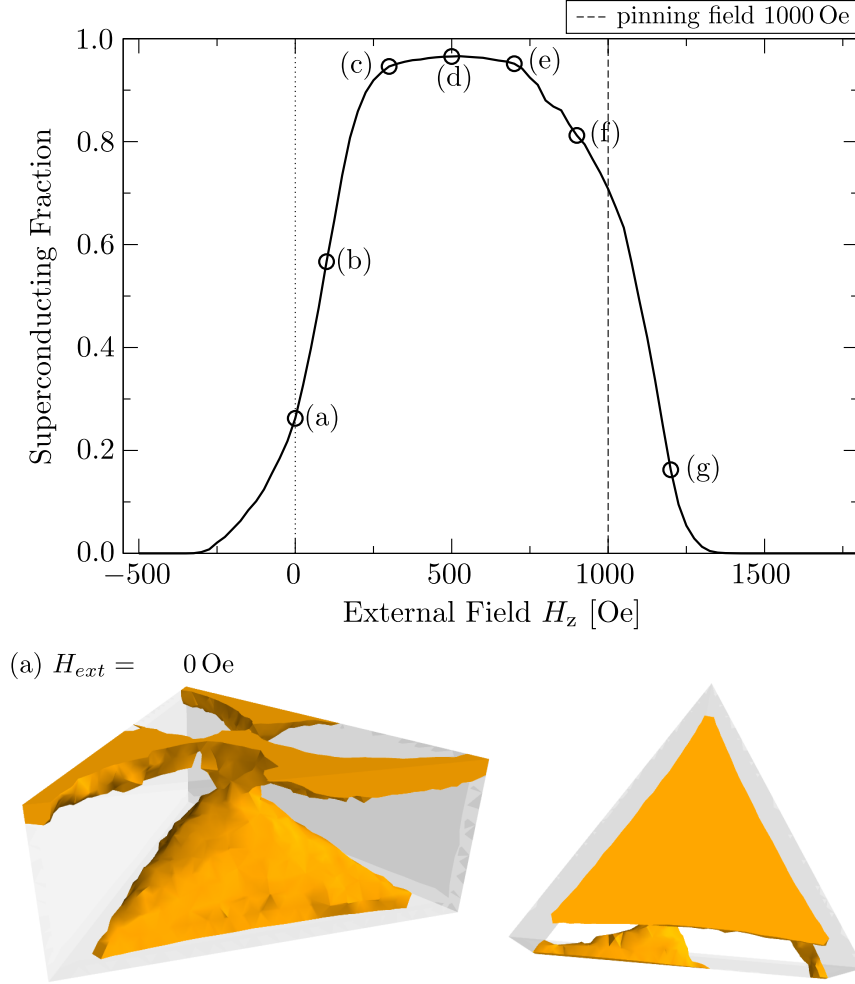
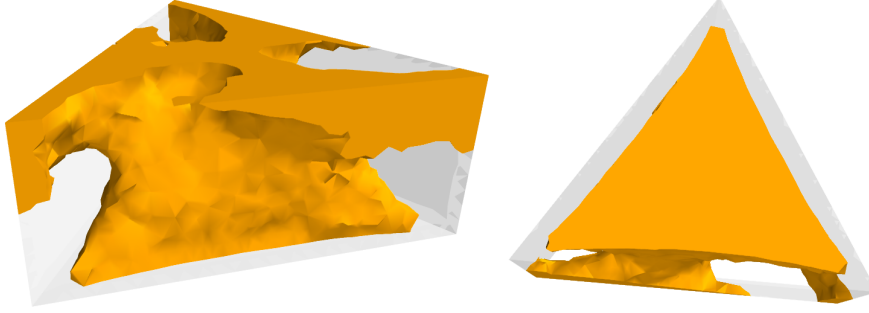


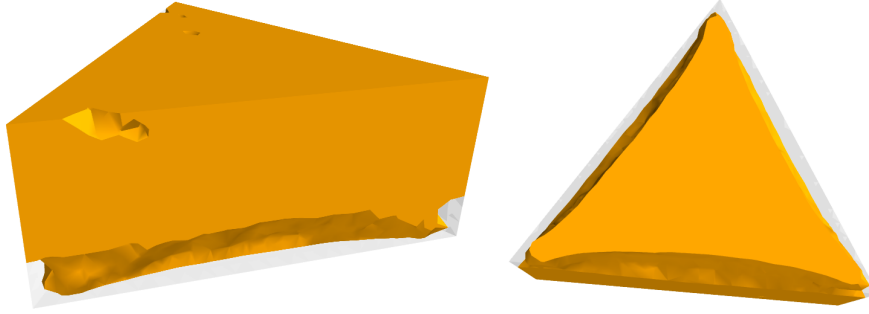
Figure 5.10.: Top: the superconducting fraction within the core domain of a triangular platelet-shaped Pb/Ni core-shell structure (edge length $a = 570$ nm, height $h = 220$ nm and thickness $t = 25$ nm) is shown as a function of the external field, which is applied perpendicular to the base of the triangular platelet. The magnetisation is relaxed at an external field strength of 1000 Oe. The data curve is then computed by keeping the magnetisation of the shell fixed and varying the external field. At the marked external field strengths images show the superconducting region from two perspectives, a lateral top view (left) and a bottom view (right). The images, which correspond to the data points (b)-(d), are shown in Figure 5.11, those of the data points (e)-(g) in Figure 5.12.

5. Stray field investigations on core-shell-structures

(b) $H_{ext} = 100$ Oe



(c) $H_{ext} = 300$ Oe



(d) $H_{ext} = 500$ Oe

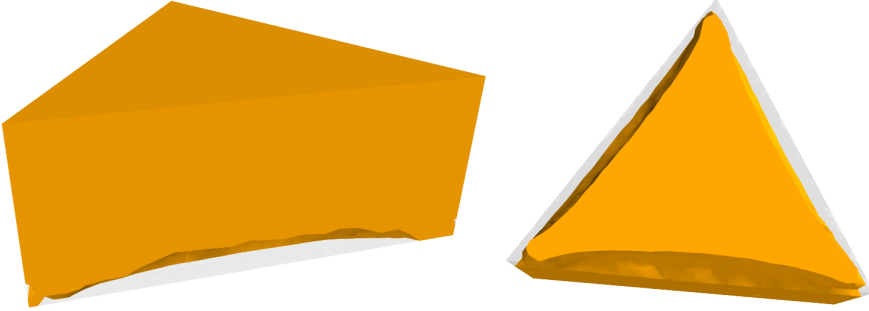
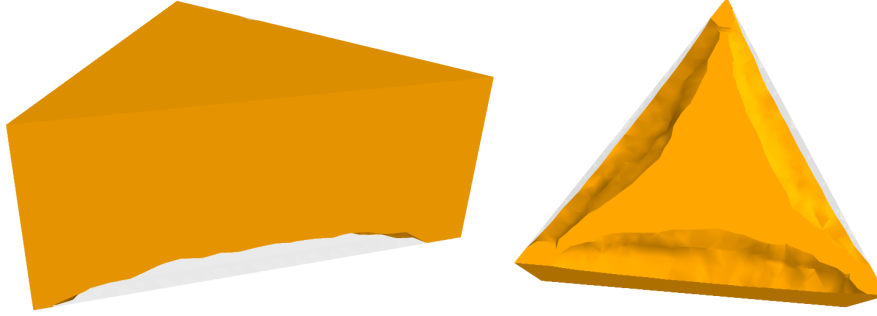
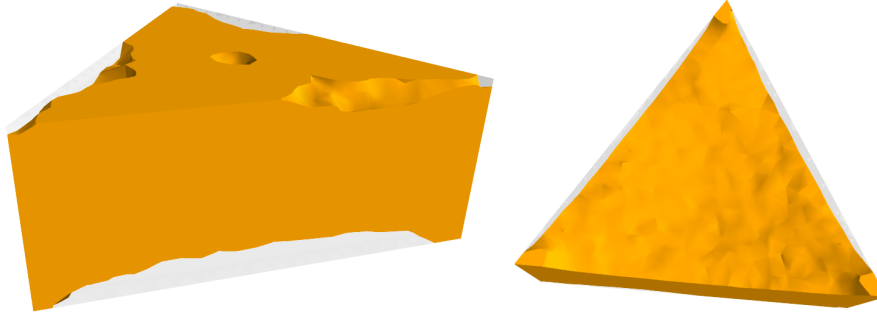


Figure 5.11.: Images of the superconducting region at different external field strengths. These images correspond to the data points (b)-(d) of Figure 5.10.

(e) $H_{ext} = 700$ Oe



(f) $H_{ext} = 900$ Oe



(g) $H_{ext} = 1200$ Oe

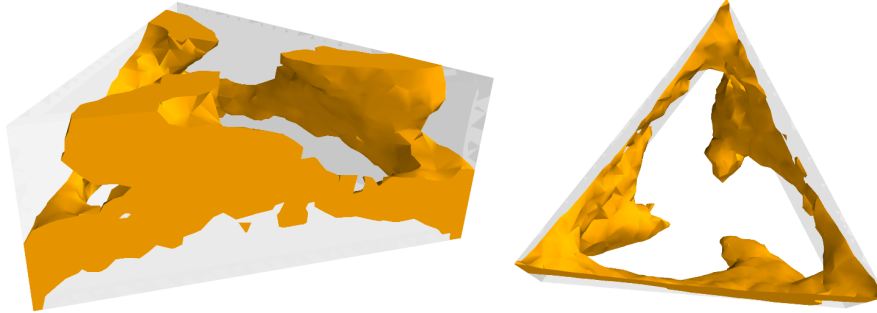


Figure 5.12.: Images of the superconducting region at different external field strengths. These images correspond to the data points (e)-(g) of Figure 5.10.

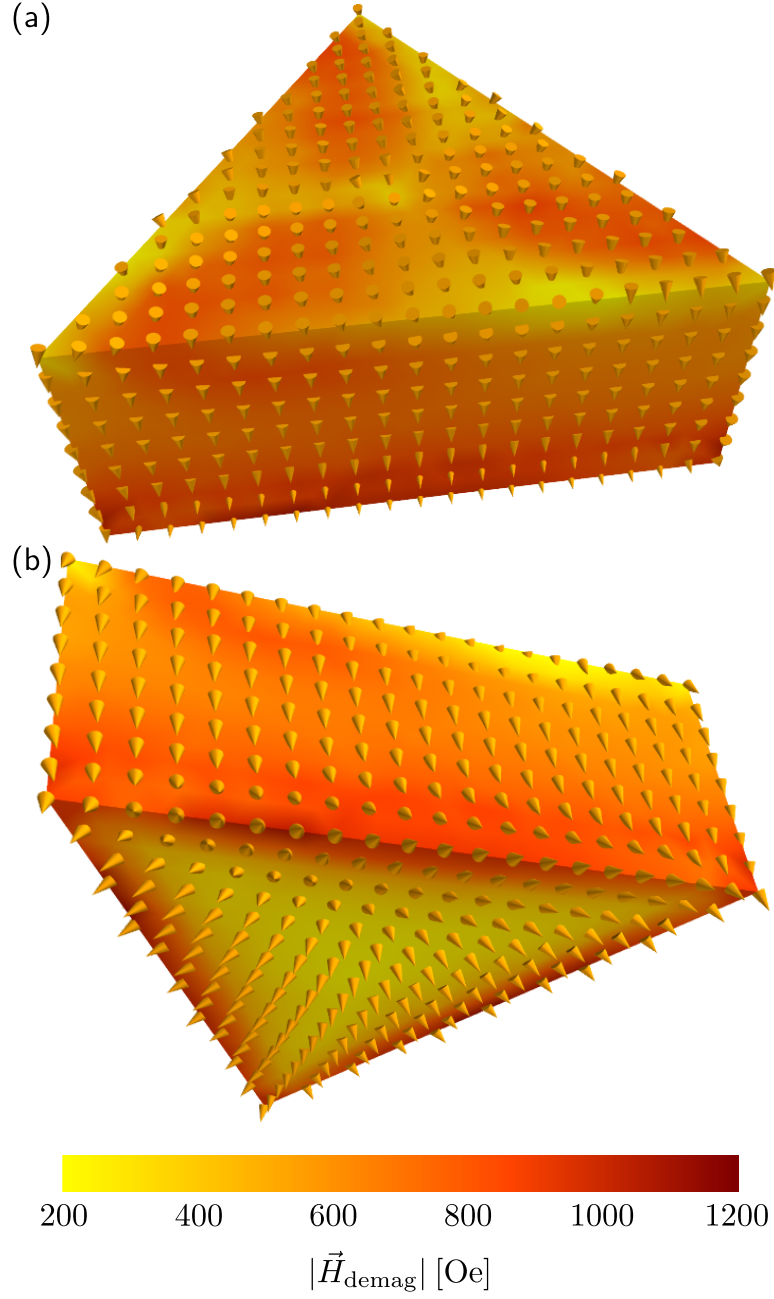


Figure 5.13.: Image showing the stray (demagnetisation) field within the core region of a triangular platelet-shaped Pb/Ni core-shell structure. (a) Core region as seen from a top view on the core-shell structure. (b) Core region as seen from a bottom view on the core-shell structure. The structure has a side length of $a = 570$ nm, a height of $h = 220$ nm and a shell thickness of $t = 25$ nm. The locally resolved magnitude of the stray field is given by the colour scheme, while the arrows denote its local orientation.

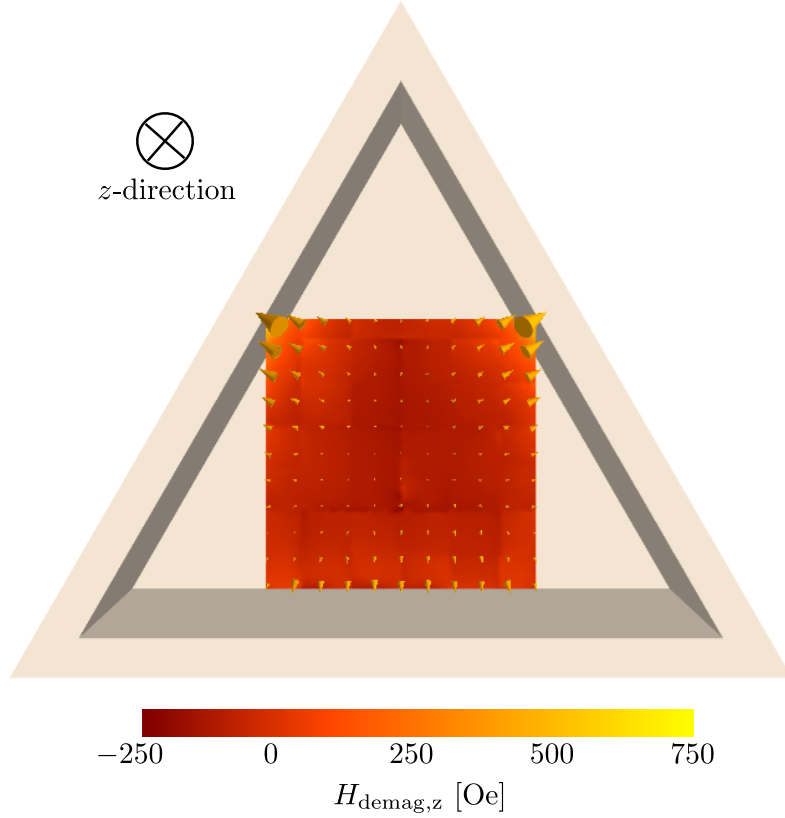


Figure 5.14.: The spatially resolved stray field at a Hall element, which is generated by the Nickel shell placed above this element, is shown. The z -component of \vec{H}_{demag} is displayed by the colour scheme, while the size of the arrows is proportional to the magnitude of the stray field. The magnetisation of the Nickel shell is relaxed at an external field strengths of 1000 Oe, leading to a vortex configuration as shown in Figure 5.7. The Nickel shell has an edge length of $a = 570$ nm, a height of 220 nm and a shell thickness of 25 nm. The Hall element is a square platelet of the size $200 \text{ nm} \times 200 \text{ nm}$ and has a thickness of 5 nm. It is positioned 8 nm below the base of the triangular platelet. These dimensions have been obtained by scaling down the experimental setup by a factor 10.

5. Stray field investigations on core-shell-structures

needs to be 25 nm or more. The general trend, that the stray field increases with an increasing shell thickness and thus the diamagnetic dome shifts to higher external field strengths, is readily understood as it is generated by the magnetised side walls. This is also illustrated in Figure 5.3(b). That this trend is attenuated towards larger shell thickness (e.g. the data curves, which correspond to the thicknesses $t = 40$ nm and $t = 80$ nm, only exhibit a comparably small relative shift) is due to the surface-charge avoidance principle, which has been discussed in the former sub-section. As pointed out before, the annihilation of superconductivity at $\vec{H}_{\text{ext}} = 0$ Oe can only be described by a shell thickness $t \geq 25$ nm. Therefore, the Figures 5.10, 5.11 and 5.12 give a more detailed account of the simulation results for $t = 25$ nm, with additional, spatially resolved images of the superconducting region within the core at different external field strengths. We see that at $|\vec{H}_{\text{ext}}| = 0$ superconductivity survives in a region around the centre of the bottom of the core and in local regions at the top of the core (Figure 5.10(a)). The survival of superconductivity in the former regions can be qualitatively explained when considering the side walls as magnets with the north pole at the top and the south pole at the bottom. With respect to the z -direction the discussed region lies on about the same level as the south pole of all three magnets, but is laterally displaced. Thus, as this region does not lie between south and north pole, the corresponding stray field is relatively small. This can also be seen in Figure 5.13(b), where the stray field within the core region is shown. The superconducting region at the top of the core is due to the fact, that a partial magnetisation of the Nickel layer at the top screens the stray field stemming from the side walls. Therefore, we observe a lower stray field below the vortex core (see 5.13(a)). Local fluctuations in the z -component of the magnetisation, which curls around the vortex core, lead to the observed pattern in the superconducting volume, which has a threefold symmetry. When increasing the external field the superconducting region successively grows. At a field strength of $|\vec{H}_{\text{ext}}| = 500$ Oe nearly the entire core is superconducting (see Figure 5.11(d)). Upon further increasing the external field the superconducting decreases again. At a field strength of $|\vec{H}_{\text{ext}}| = 1200$ Oe superconductivity only survives in the vicinity of the side wall at the fringe of the core, where the strongest stray field is generated.

Stray field computation at the Hall element

Finally, we check whether the studied triangular platelet-shaped Pb/Ni core-shell structure ($a = 570$ nm, $h = 220$ Oe and $t = 25$ nm) and the used pinning field of $|\vec{H}_{\text{ext}}| = 1000$ Oe reproduces a stray field of 115 Oe, which is experimentally measured at a Hall element below the Pb core (see Figure 5.4). To

do this we model the Hall element (Figure 5.3) by placing a square platelet, which has a side length of 200 nm and a thickness of 5 nm, 8 nm below the Pb core and fill this structure with a fine tetrahedral mesh (two tetrahedron layers along the z -direction). The micromagnetic parameters A and M_S are set as in the core region. Figure 5.14 shows the stray field, which is generated by the vortex state of the Ni shell ($|\vec{H}_{\text{ext}}| = 1000 \text{ Oe}$), at this square platelet. By probing and adding up the stray field at the mesh nodes of the square platelet, we obtain the spatial average of its z -component $\langle H_{\text{stray},z}^{\text{hall}} \rangle$. We find $\langle H_{\text{stray},z}^{\text{hall}} \rangle \approx 60 \pm 5 \text{ Oe}$, which lies significantly below the experimentally measured value. The error margin is roughly estimated and due to the dependence of $\langle H_{\text{stray},z}^{\text{hall}} \rangle$ on the orientation of the square platelet with respect to the Ni shell. Here, orientation refers to a rotation of the platelet about the z -direction (see Figure 5.14). The underestimation of $\langle H_{\text{stray},z}^{\text{hall}} \rangle$ in our simulations seems to be due the inhomogeneous stray field at the fringes of the Hall element, especially in regions which are close to the side walls of the Nickel shell. Indeed, the effective size of the Hall element will be smaller than its actual dimensions, since there is always a dead layer around its etched perimeter where the electronic system is fully depleted [128]. The size of this depletion layer may be expected to be 250 nm at each side of the Hall element, reducing the effective size of the Hall element to $1.5 \mu\text{m}$ (150 nm within the computer simulations) [128]. To investigate this effect we have gradually reduced the side length a of the Hall element in our simulations to 150 nm, 125 nm and 100 nm. We find $\langle H_{\text{stray},z}^{\text{hall}} \rangle \approx -94 \pm 5 \text{ Oe}$ for $a = 150 \text{ nm}$, $\langle H_{\text{stray},z}^{\text{hall}} \rangle \approx -106 \pm 3 \text{ Oe}$ for $a = 125 \text{ nm}$ and $\langle H_{\text{stray},z}^{\text{hall}} \rangle = -120 \pm 3 \text{ Oe}$ for $a = 100 \text{ nm}$. Thus, in order to reproduce the experimentally measured stray field with the presented approach, we have to assume that a substantial part of the Hall element is not active.

Discussion of the results

We conclude this section by discussing its results and having an outlook at future work. It has been shown that it is possible to understand the occurrence of the superconducting dome in the hysteresis curve of a Pb/Ni core-shell structure (see Figure 5.4) in terms of a simple micromagnetic model. However, the width of the experimentally measured superconducting dome is smaller and its shape is more pointed. There are several factors which may lead to these discrepancies:

1. In our approach we have assumed that the diamagnetic signal, which is measured at the Hall element, is directly proportional to the calculated superconducting fraction within the core. This is only an approximation.
2. In its superconducting state the Pb core shows a strong magnetic re-

5. Stray field investigations on core-shell-structures

sponse to a magnetic field, which should also have an impact on the magnetic state of the Nickel shell. Such an interaction between the Ni shell and the Pb core is not considered in the model.

3. The pinning of the magnetisation at a strong external field $|\vec{H}_{\text{ext}}|$ is an approximation. In the real system a partial relaxation of the magnetisation will take place, which is also indicated by Figure 1(c) of [1].
4. The experimentally grown structure is about a factor 10 larger than the modelled geometry and its shape deviates from the geometry of an idealised triangular platelet (see Figures 5.1(a) and 5.2). The Nickel shell is polycrystalline instead of single-crystalline as assumed in the micromagnetic model. These differences affect the magnetic state of the Nickel shell and thus also its stray field within the core region. Other effects (for example magnetocrystalline anisotropy and magnetoelastic effects), which are not included in the micromagnetic model, may have an impact on the physical behaviour of the experimental system, as well.

Beside the occurrence of the diamagnetic dome, there are aspects in the experimental results, which cannot be explained by the used model: the measured stray field at $|\vec{H}_{\text{ext}}| = 0 \text{ Oe}$ is larger than the stray field at saturation (see Figure 5.4 and [1]), which is a somewhat counterintuitive result and can only be due to the screening of the stray field of the partially reversed shell by superconducting puddles, that survive within the core region and throw out magnetic flux towards the Hall element [1]. The behaviour of the core-shell structure during the magnetic reversal at low external fields is very complex, exhibiting the occurrence of Barkhausen jumps within the ferromagnetic shell, which are coupled to changes in the diamagnetic state of the Pb core [1]. Our simple model cannot account for such a physical scenario as it assumes a pinning of the magnetisation and does not consider the magnetic response of the core, which in turn leads to a complex magnetic interplay between the superconducting core and the ferromagnetic shell. To correctly model such an interplay one would need to solve the micromagnetic equations and the Ginzburg-Landau (GL) equations of superconductivity in a self-consistent way. This approach presents a very interesting direction of future research, since, to the best of our knowledge, a numerical solution of coupled micromagnetic and GL equations has not been performed so far, and should enhance the understanding of ferromagnetic-superconducting hybrid systems.

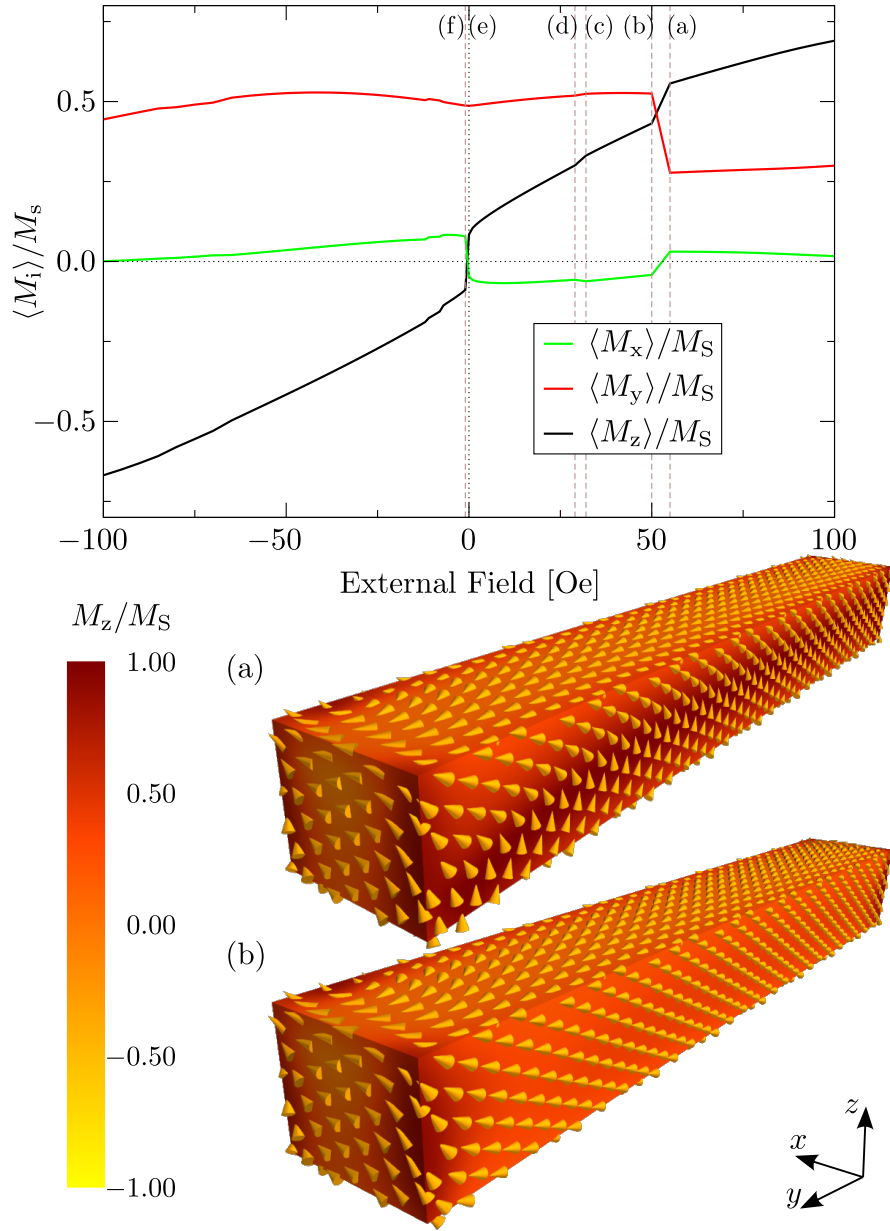


Figure 5.15.: The magnetic reversal within a core-shell structure in the shape of a rectangular prism is illustrated. The dimensions of this structure are $h = 122.5 \text{ nm}$, $l = 1043.0 \text{ nm}$ and $w = 143.5 \text{ nm}$ as measured with respect to the shell outside (see Figure 5.5). The thickness of the shell is $t = 21 \text{ nm}$. The upper graph shows the components of the spatially averaged magnetisation $\langle \vec{M} \rangle$ as a function of the external magnetic field which is aligned along the z -direction. Images of the spatially resolved magnetisation are shown for those external field strengths, which are marked by the vertical lines, namely: (a) $H_{\text{ext},z} = 55 \text{ Oe}$, (b) $H_{\text{ext},z} = 50 \text{ Oe}$, (c) $H_{\text{ext},z} = 32 \text{ Oe}$, (d) $H_{\text{ext},z} = 29 \text{ Oe}$, (e) $H_{\text{ext},z} = 0 \text{ Oe}$ and (f) $H_{\text{ext},z} = -1 \text{ Oe}$. Image (c), (d), (e) and (f) are shown in Figure 5.16.

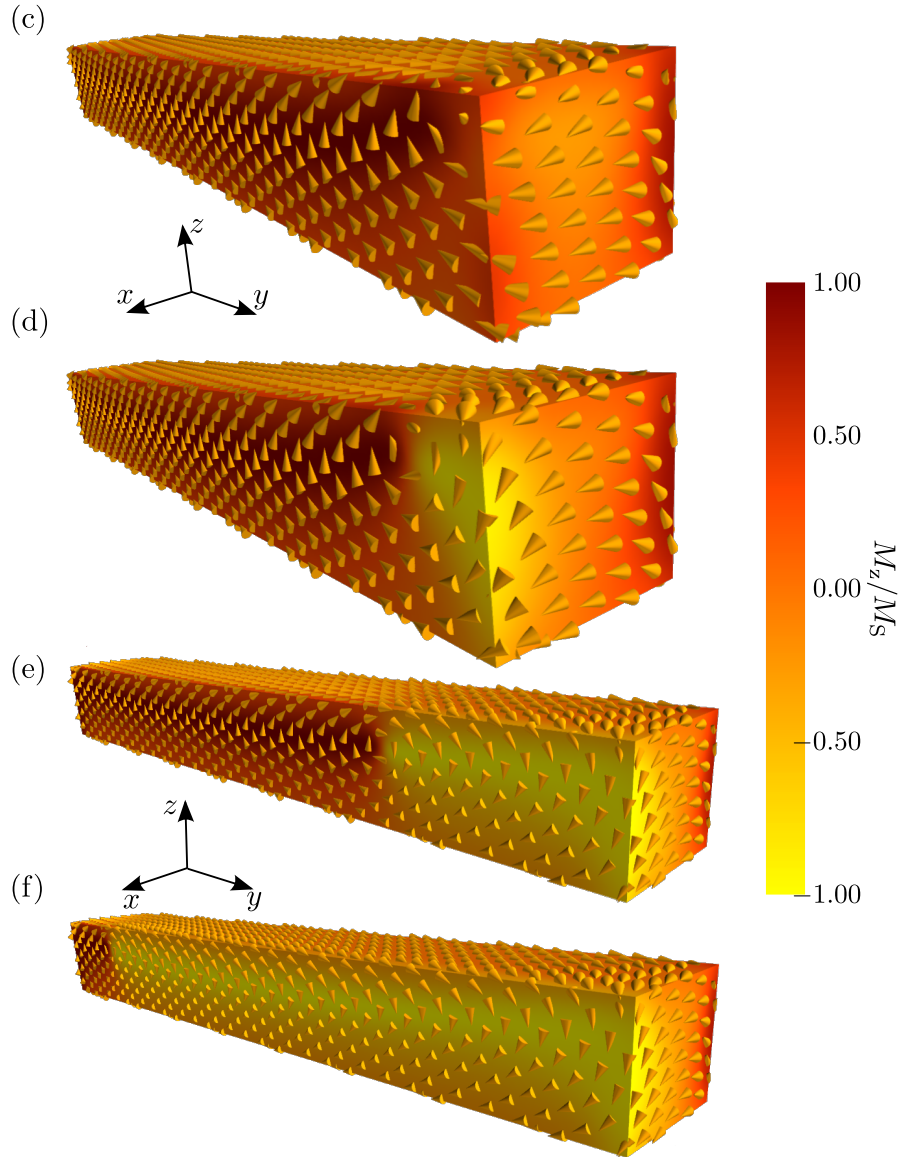


Figure 5.16.: Illustration of the spatially resolved magnetic configuration for the system defined in Figure 5.15 and the external field strengths (c) $H_{\text{ext},z} = 32$ Oe, (d) $H_{\text{ext},z} = 29$ Oe, (e) $H_{\text{ext},z} = 0$ Oe and (f) $H_{\text{ext},z} = -1$ Oe. The added coordinate axes denote the Cartesian directions for the images (c), (d) and (e), (f), respectively.

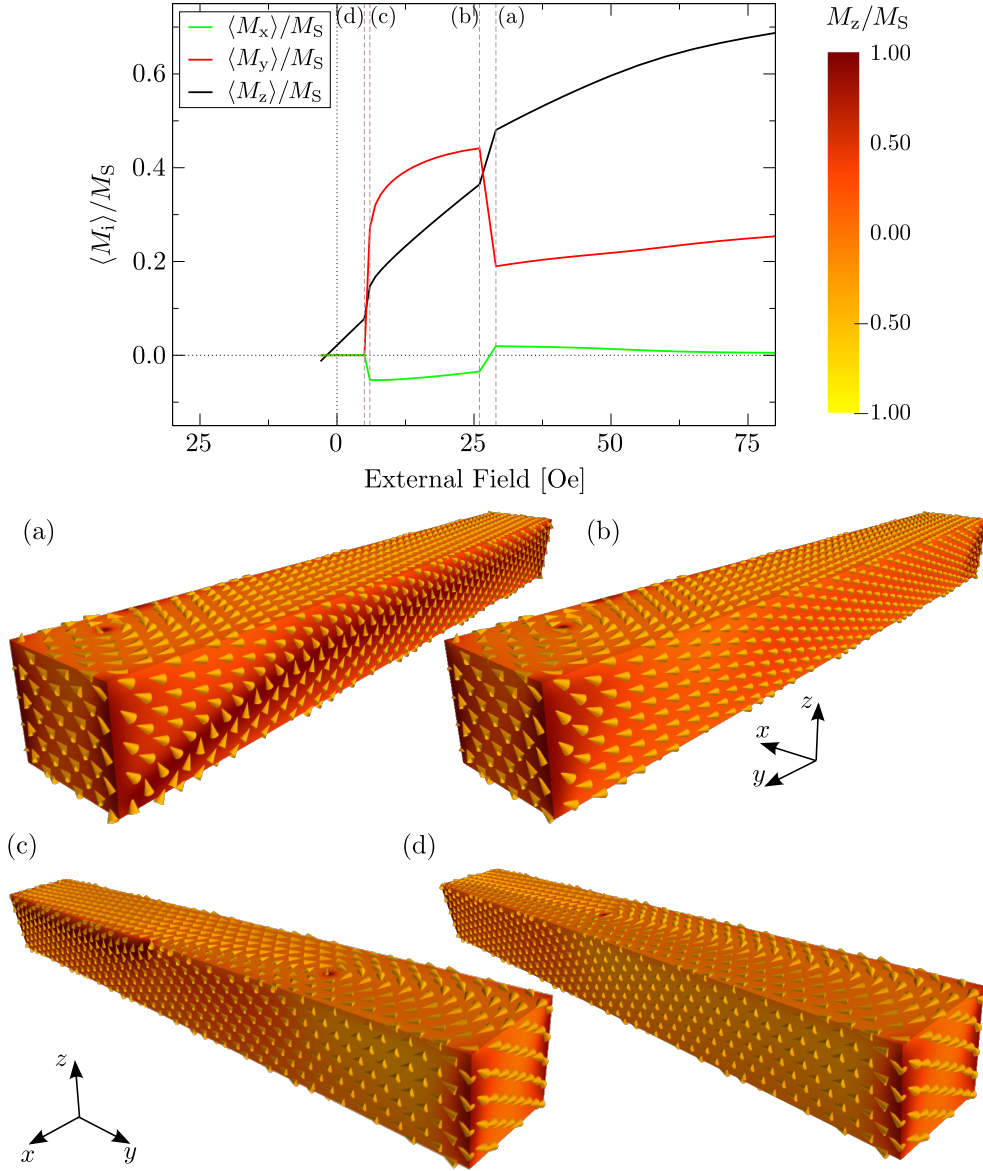


Figure 5.17.: The components of the spatially averaged magnetisation $\langle \vec{M} \rangle$ within a rectangular prism are shown (graph on top) as a function of the external magnetic field H_z , which is subsequently reduced to a field strength of -3 Oe. The dimensions of the rectangular prism are $h = 220.5$ nm, $l = 2044.0$ nm and $w = 241.5$ nm as measured with respect to the shell outside (see Figure 5.5). The thickness of the shell is $t = 21$ nm. Images of the spatially resolved magnetisation are shown for external field strengths, between which irreversible jumps in the magnetisation occur (see vertical, dashed lines). The image correspond to the following magnetic field strengths: (a) $H_{\text{ext},z} = 29$ Oe, (b) $H_{\text{ext},z} = 26$ Oe, (c) $H_{\text{ext},z} = 6$ Oe, (d) $H_{\text{ext},z} = 5$ Oe. The added coordinate axes denote the Cartesian directions for the images (a), (b) and (c), (d), respectively.

5.2.2. Magnetic reversal in cuboidal Nickel shells

In this section we present micromagnetic simulation results on the magnetic reversal of a core-shell structure (core: Sn, shell: Ni), which has the shape of a rectangular prism (see Figure 5.5(a)). The simulations have been performed with the micromagnetic finite-difference (FD) based solver OOMMF [102]. Similar to Chapter 4 we use a model, which only considers the magnetic properties of the ferromagnetic Ni shell. Although the Sn core becomes superconducting below a critical temperature of 3.7 K, we do not consider it in this sub-section. One reason is that the experimental hysteresis curve of a rectangular prism-shaped Sn/Ni core-shell structure (recorded at $T = 2$ K) only shows evidence of a diamagnetic signal at relatively low external fields when a substantial relaxation of the system has taken place (see Figure 1 of [1]). Additionally, the diamagnetic signal is less distinct than that of Figure 5.4, which occurs at higher fields. The simple approach of Section 5.2.1, which assumes the pinning of the magnetisation, is not suited to describe this data and a more sophisticated model, which directly takes the superconductivity of the core into account, needs to be employed (see discussion in Sub-section 5.2.1). Such a model is beyond the scope of this work.

The method

We use the micromagnetic model of Section 4.2.2, i.e. the exchange constant A is set to 7.2×10^{-12} J/m and the saturation magnetisation M_S to 493380 A/m, while the magnetocrystalline anisotropy of Nickel is neglected. The exchange length $l_{\text{exch}} = \sqrt{A/K_D}$, with K_d being $\frac{\mu_0}{2} M_S^2$, is equal to 6.86 nm. The FD discretisation of the micromagnetic equations is performed on a cubic grid, whose cells have a uniform side length. The side length should be equal to $0.5 \cdot l_{\text{exch}}$ or smaller, in order to ensure that the micromagnetic simulations are sufficiently accurate [99]. Accordingly, we choose an edge length of 3.5 nm $\approx 0.51 \cdot l_{\text{exch}}$. Since OOMMF uses a fast Fourier transform (FFT) for the computation of the magnetostatic interaction, it requires a grid, which models a cuboidal shape. As a consequence our evenly spaced grid comprises the Ni shell as well as the Pb core. Although the cells within the core do not correspond to degrees of freedom, on which magnetic spins are defined, they increase the complexity of the simulations via the FFT. The computation of the magnetostatic interaction via the FFT generally constitutes the bottleneck of simulations, which are performed with OOMMF. To perform OOMMF simulations with an optimal efficiency one should consider the following issues:

- One may use a new version of OOMMF, which can be run in parallel

on a shared-core memory system in order to reduce the simulation time [129]. We run the simulations on eight CPU cores, which according to [129] should roughly bring a total speed-up by a factor between 3 and 5, depending on the used hardware.

- One should arrange the grid such, that the inequalities $N_x \geq N_y \geq N_z$ hold. N_x , N_y and N_z are the number of cells along the x , y and z direction. For certain geometries this reduces the memory footprint substantially [129].
- Internally, OOMMF will store a number of cells, which is equal to a power of 2 along each Cartesian direction. The memory footprint of OOMMF for a cube ($N = N_x = N_y = N_z$) in terms of the number of cells along its side lengths is illustrated in Figure 2.16 of [130] and shows a typical step-wise behaviour. Thus, one can avoid an unfavourable memory footprint, if one chooses N_x , N_y and N_z such, that they can be expressed as $2^i - j$ with $i, j \in \mathbb{N}$, where j is 0 or a small, positive integer.

We study the magnetic reversal along the z -direction, which in Figure 5.5(a) corresponds to the direction parallel to the height h of the structure. We systematically vary the external field $H_{\text{ext},z}$ from 400 Oe to 200 Oe in steps of $\Delta H_z = 20$ Oe, from 200 Oe to 100 Oe in steps of 10 Oe, from 100 Oe to 50 Oe in steps of 5 Oe, from 50 Oe to 20 Oe in steps of 3 Oe and finally from 20 Oe to 0 Oe in steps of 1 Oe. Accordingly, $H_{\text{ext},z}$ is then successively changed to -400 Oe. Initially, we also set $H_{\text{ext},x} = H_{\text{ext},y} = 0.04$ Oe and vary these components by $\Delta H_x = \Delta H_y = 0.0001 \Delta H_z$ with the step sizes ΔH_z as given above. We set $H_{\text{ext},x} \neq 0$ and $H_{\text{ext},y} \neq 0$ in order to break the symmetry of the problem and avoid an artificial pinning of the magnetisation. Each time the external field has been changed, the magnetisation is relaxed using OOMMF's conjugated-gradient based solver `Oxs_CGEvolve` with the stopping criterion `stopping_mxHxm` of 0.1 A/m [131].

Results

In Figure 5.15 and 5.16 results for the magnetic reversal of a rectangular prism-shaped core-shell structure with a height of $h = 122.5$ nm, a length of $l = 1043.0$ nm a width of $w = 143.5$ nm and a shell thickness of $t = 21$ nm are shown. Looking at the components of the spatially averaged magnetisation $\langle \vec{M} \rangle$ (Figure 5.15top), we observe mayor jumps between $H_{\text{ext},z} = 55$ Oe and 50 Oe and between $H_{\text{ext},z} = 0$ Oe and -1 Oe. Furthermore several minor kinks occur (for example between 32 Oe and 29 Oe). The images (a) and (b) of Figure 5.15 show how the micromagnetic state changes between $H_{\text{ext},z} = 55$ Oe and

5. Stray field investigations on core-shell-structures

50 Oe. At $H_{\text{ext},z} = 55$ Oe there is a C-like configuration on one of the larger side faces of the prism, whose mean magnetisation is aligned along the z -direction. Upon setting $H_{\text{ext},z}$ to 50 Oe it changes to a homogeneous configuration, which is approximately aligned along the y -direction. The images (c) and (d) of Figure 5.15 show the evolution of a vortex at a corner of the opposite large side face. This only corresponds to a minor jump in the components of the spatially averaged magnetisation. At remanence (Figure 5.15(e)) the vortex core has moved towards the centre of the large side face. Interestingly, it is not exactly at its centre, but is slightly shifted along the y and z directions. This seems to be due to the relatively complicated shell geometry, which comprises several edges. To avoid a high magnetostatic energy (see also the discussion in Section 4.3.1), the magnetisation will always try to align parallel with these edges, leading to rather complicated micromagnetic configurations, which are not always intuitively comprehensible. Upon changing the field to $H_z = -1$ Oe we see a major shift in the vortex core position (Figure 5.16(e) and (f)), which leads to a negative z -component of $\langle \vec{M} \rangle$. Figure 5.17 shows an incomplete reversal process for a rectangular prism-shaped structure with a height of $h = 220.5$ nm, a length of $l = 2044.0$ nm a width of $w = 241.5$ nm and a shell thickness of $t = 21$ nm. The simulation has been stopped after about 2 months in order to free computer resources. The images, which show the spatially resolved magnetisation, reveal that a vortex core sits on the top face of the structure. Again we observe two mayor changes in the spatially averaged magnetisation when we reduce the external field. Between $H_{\text{ext},z} = 29$ Oe and 26 Oe we observe a change in the magnetisation of one of the larger side faces (see Figure 5.17(a) and (b)). Afterwards, the vortex core subsequently moves towards the centre of the top face. This core movement has an effect onto the opposite side face. This can be seen nicely when, upon changing the external field from 6 Oe to 5 Oe, the vortex core jumps from a more lateral position to the centre of the core (5.17(c) and (d)): at the same time the magnetisation on the side face (in the far end of Figure 5.17(c)) changes from a C-like configuration along the z -direction to a homogeneous configuration along the y -direction. This leads to the jumps in the y and z -component of the spatially averaged magnetisation. The jump in in the x -component is due to the changed magnetisation on the top face. At remanence the x and y component of the spatially averaged magnetisation are 0 due to the symmetry of the micromagnetic state.

Conclusions

We have seen that the occurrence of vortices and their movement is key to the understanding of the reversal process within rectangular prism-shaped shell

structures of a soft-magnetic material. The elongation of the studied structures along the y -direction partially leads to a relatively strong magnetisation along this direction during reversal. This study has not been exhaustive. The shape and the size of the structure may be changed through the geometry parameters h , l , w and t in order to conduct a more in-depth study of the dependence of the magnetic reversal on the geometry. Also, the effect of the slight canting of the external field, which has been introduced to avoid artificial pinning effects, on the reversal process may be investigated. Judging from our simulations it seems plausible to assume that the sign of $H_{\text{ext},y}$ determines the sign of $\langle m_y \rangle$.

6. Summary and outlook

The present work deals with the optimisation of a finite element-based micromagnetic code (Nmag) and its use for the study of ferromagnetic shell structures in the sub-micrometer regime. The code uses the hybrid finite element method / boundary element method (FEM/BEM) to compute the long-range magnetostatic interaction, which involves the assembly and storage of a dense boundary element matrix. The matrix size scales quadratically with the number of surface nodes of the mesh, which discretises the region of the ferromagnetic material. Hierarchical matrices are used in order to approximate the boundary element matrix and thus improve the scaling behaviour of the algorithm.

The micromagnetic model, the hybrid FEM/BEM and the concept of hierarchical matrices are introduced in the theory chapter (Chapter 2). This chapter also introduces different algorithms for the assembly of hierarchical matrices, namely interpolation, ACA, ACA+, HCA I and HCA II. These algorithms are implemented in the library HLib, an implementation of the hierarchical matrix methodology. In the first result chapter (Chapter 3) these algorithms are compared with respect to the assembly time, the memory footprint of the resulting hierarchical matrix and the introduced error. The second result chapter (Chapter 4) deals with the micromagnetic analysis of pyramidal-shaped Ni shell structures. Finally, Chapter 5 focuses on the analysis of the magnetic reversal of triangular platelet-shaped Ni shell structures, which contain a superconducting Pb core. In the following the content of these result chapters is summarised and potential directions of future research are pointed out.

6.1. Hierarchical matrices in FE-based micromagnetic simulations.

To compare the efficiency of different hierarchical matrix assembly algorithms (interpolation, ACA, ACA+, HCA I and HCA II), the FE based solver Nmag is used in conjunction with the library HLib and thin square platelets of different sizes are considered. Calculating the demagnetisation field of configurations with a homogeneous magnetisation, it is found that HCA II yields

6. Summary and outlook

the most reliable results, independent of whether the full BE matrix elements $B_{i,j}$ are computed via a numerical Gaussian quadrature or an analytical formula (see Sub-section 3.2.1 and 3.2.2). By default, this algorithm is used in all simulations where hierarchical matrices are used. In Section 3.3 a thin, square platelet is used to compare the error, which results from the hierarchical matrix approximation, with the discretisation error of the hybrid FEM/BEM. This corresponds to a comparison of FE-based micromagnetic simulations with and without the use of hierarchical matrices. The comparison is done with respect to the demagnetisation field computation of configurations with a homogeneous magnetisation, the relaxation of the magnetisation and hysteresis simulations. It is found that the errors arising from the use of a hierarchical matrices are small in comparison with the discretisation errors. The reason is that for cuboidal systems, such as the thin square platelets studied in this chapter, diverging demagnetisation fields exist in the vicinity of sharp edges and corners, leading to relatively inaccurate results for a FE-based discretisation. However, FE-based micromagnetic simulations still yield acceptable results and are widely used for such systems, which in turn demonstrates the applicability of hierarchical matrices. To improve the accuracy of FE-based micromagnetic simulations one could try to use an adaptive mesh refinement, i.e. a locally finer discretisation in regions where the demagnetisation field computation is inaccurate.

The application of hierarchical matrices to the hybrid FEM/BEM improves the computational complexity of the BEM part of this method, which, without the approximation, limits the efficiency of the method. After the application of hierarchical matrices its efficiency is limited by the FEM part of the method. Therefore, it does not seem pertinent to fine-tune the hierarchical matrix approximation of the boundary element (BE) matrix, although potential approaches are discussed in section 3.4. Instead, it appears to be more promising to use hierarchical matrices in order to improve the FEM part of the method, where they could be used as preconditioners. Another important aspect is the optimisation of Nmag's parallel capabilities. The simulations, on which the results of this work are based on, have not been performed in parallel, because there has been a significant memory overhead when running Nmag in parallel. Thus, optimising Nmag's parallel mode with respect to a more effective memory partition seems to be a promising pathway towards more efficient simulations.

6.2. Micromagnetic studies of pyramidal-shaped shell structures.

In Chapter 4 hierarchical matrix-optimised, FE-based micromagnetic simulations are used to conduct an in-depth analysis on the magnetic behaviour of pyramidal-shaped core-shell structures in the limit of soft magnetic materials. These structures contain a pyramidal-shaped Ag core with a square base, which is covered by a thin Ni layer (the shell). The core is weakly magnetic, so that within the micromagnetic model only the properties of the ferromagnetic Nickel shell are considered.

The micromagnetic analysis includes the identification and characterisation of several stable and metastable states in a size regime below $60 \cdot l_{\text{exch}}$. Furthermore, a phase diagram, which presents the energetic ground states at different structure sizes (the aspect ratio is fixed) and shell thicknesses, with accurately computed phase boundaries is created. By carefully examining the results of the micromagnetic simulations a qualitative understanding of the phase transitions between different ground states is gained. The stability regimes of all occurring states are investigated at different shell thicknesses. Finally, the magnetic reversal is studied along selected directions. These reversal simulations are partly repeated for pyramidal shell structures with rounded corners and edges in order to investigate the physical impact of such a rounding.

As a result several stable magnetic configurations are found, which, in line with the naming conventions for equivalent micromagnetic states in thin, square platelets, are called flower state, onion state, C state and S state. There are also two vortex-like configurations, which are called symmetric and asymmetric vortex state, the latter of which does not have an equivalent configuration occurring in thin, square platelets. Apart from the S state all these states are ground states, i.e. occur within the corresponding phase diagram. During magnetic reversal simulations the vortex core of the asymmetric vortex state may be switched between opposite side faces of the pyramidal shell, a behaviour which is potentially interesting with respect to data storage applications. This switching is also reasonably stable with respect to a rounding of corners. Finally, it is found that such a rounding generally leads to a decrease in the coercivity.

Further research may be directed towards studying the technological applicability of the asymmetric vortex state, especially with respect to applications in the area of data storage. Possible directions would be an investigation of its thermal stability, its fast switching by spin-polarised currents and its occurrence for different aspect-ratios of the pyramidal-shaped shell. However,

6. Summary and outlook

any potential application of these structures hinges on corresponding improvements of their experimental fabrication. A growth method based on electrodeposition currently only yields pyramidal-shaped shells in the regime of several micrometers, which is about two orders of magnitude larger than elements of state-of-the-art memory devices.

6.3. Stray field investigations on core-shell-structures

The emphasis of Chapter 5 is placed on the micromagnetic analysis of triangular platelet-shaped core-shell structures with a Pb core and a Ni shell. Lead becomes superconducting below a critical temperature of $T_{\text{crit}}^{\text{Pb}} = 7.2 \text{ K}$ and below a temperature-dependent critical external field strength $H_{\text{ext}}^{\text{Pb}}(T)$. In this case the core also exhibits strong magnetic properties, which cannot be neglected when studying such core-shell structures. Experimental data on these structures exhibits a characteristic diamagnetic dome at field strengths between 1000 and 300 Oe. Thus, a diamagnetic signal also occurs at field strengths, which exceed the critical field of lead $H_{\text{crit}}^{\text{Pb}}(T)$ ($H_{\text{crit}}^{\text{Pb}}(4.2) = 530 \text{ Oe}$), demonstrating that these core-shell structures show novel (dia-)magnetic properties.

A simple micromagnetic model is used in order to understand this behaviour, especially the survival of superconductivity towards higher magnetic field strengths. The approach is that at first only the magnetisation of the ferromagnetic shell is considered. It is relaxed at an external field strength of $\vec{H}_{\text{ext}} = 1000 \text{ Oe}$. Afterwards the magnetisation, and thus also its demagnetisation field \vec{H}_{demag} , is pinned while the external field is successively varied. After each variation of the external field the core volume, within which $|\vec{H}_{\text{demag}} + \vec{H}_{\text{ext}}| < H_{\text{crit}}^{\text{Pb}}(4.2) = 530 \text{ Oe}$ holds, is computed. Thus, a data curve of the superconducting core volume as a function of the external field is obtained. Under the approximate assumption that the experimental signal, which is measured at a Hall element positioned below the core-shell structure, is proportional to the computed volume of superconducting material, both data curves are compared. Given the simplicity of the computational model, a good qualitative agreement between experiment and model is found. The survival of a superconducting signal at external fields $H_{\text{ext}} > H_{\text{crit}}^{\text{Pb}}$ can be attributed to the partial compensation of the external field \vec{H}_{ext} by the stray field \vec{H}_{demag} stemming from the shell. However, there are still quantitative discrepancies between experiment and model.

For a quantitatively more accurate analysis the impact of the Pb core needs to be considered by an incorporation of the Ginzburg-Landau (GL) equations

6.3. Stray field investigations on core-shell-structures

of superconductivity into the model. This would amount to solving the micro-magnetic and the Ginzburg-Landau (GL) equations in a self-consistent way. Other (presumably) less important aspects are listed in Section 5.2.1, for example: due to computational restrictions the modelled geometry is about a factor of 10 smaller than the actual experimental geometry. Narrowing this size gap would certainly be desirable.

The chapter concludes with simulation results on the magnetic reversal of cuboidal Ni shell structures, which contain a Sn core. These simulations have been conducted with the finite-element (FE) based micromagnetic solver OOMMF. The superconductivity of tin is neglected, i.e. only the ferromagnetism of the Ni shell is considered. The results show that the reversal processes occur via the movement of a vortex core. However, for a more general understanding of the magnetic reversal within such structures more simulations (different structure sizes, aspect ratios, shell thicknesses and external field directions) would be needed.

A. Notes on potential theory

In this chapter we want to outline how the equations (2.30-2.32), which represent a Laplace equation with open boundary conditions, can be transformed into an integral equation. In literature [66] it is often stated that the equivalence of both formulations is shown by potential theory while no details are given. This has been the main motivation to write this chapter. Figure A.1 gives a summary of the mathematical problem.

A.1. Some definitions

Before deriving the integral equation for the potential $\phi_2(\vec{r})$ we want to introduce some definitions which will be used later. The 3D free-space Green function is given by

$$G(\vec{r}, \vec{R}) = \frac{1}{4\pi} \frac{1}{|\vec{R} - \vec{r}|}. \quad (\text{A.1})$$

It has the property

$$\nabla^2 G(\vec{R}, \vec{r}) = \delta(\vec{R} - \vec{r}). \quad (\text{A.2})$$

Here, $\delta(\vec{R} - \vec{r})$ is the so called Dirac δ distribution which is defined as

$$\int_V f(\vec{r}) \delta(\vec{R} - \vec{r}) d^3\vec{r} = \begin{cases} f(\vec{R}) & \text{for } \vec{R} \in V \\ 0 & \text{for } \vec{R} \notin V \end{cases}. \quad (\text{A.3})$$

Furthermore, we will use Green's second identity:

$$\int_S \left(\phi \frac{\partial \psi}{\partial n} - \psi \frac{\partial \phi}{\partial n} \right) dS = \int_V (\phi \nabla^2 \psi - \psi \nabla^2 \phi) dV. \quad (\text{A.4})$$

The functions ψ and ϕ must be differentiable to the second order. The volume V is bounded by the surface S .

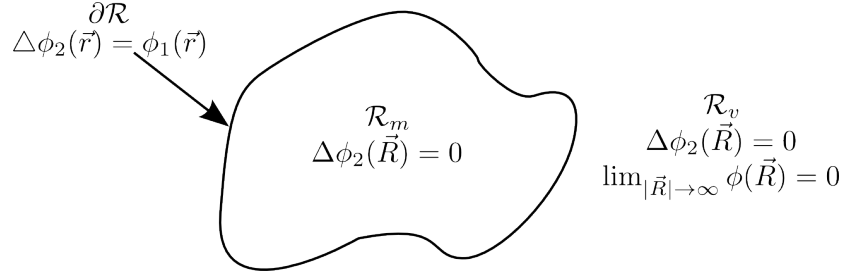


Figure A.1.: Two-dimensional depiction of the mathematical problem to solve. The magnetic region \mathcal{R}_m is bound by the surface ∂R . On the other side of ∂R the vacuum region \mathcal{R}_v extends to infinity. In \mathcal{R}_m and \mathcal{R}_v Laplace's equation holds. Crossing the boundary ∂R from \mathcal{R}_m to \mathcal{R}_v , $\phi_2(\vec{r})$ exhibits a jump, which is equal to the corresponding value of $\phi_1(\vec{r})$, while its normal derivative remains continuous. $\phi_2(\vec{r})$ approaches zero in the limit $|\vec{R}| \rightarrow \infty$. The latter condition is usually referred to as open-boundary condition.

A.2. Derivation

Let us assume that $\phi_2(\vec{r})$ is the solution of Laplace's equation in either region \mathcal{R}_m or \mathcal{R}_v . Then we can use equation A.2 and A.3 to rewrite $\phi_2(\vec{r})$ as follows¹:

$$\phi_2(\vec{R}) = \int_{\mathcal{R}_i} \Delta G(\vec{R}, \vec{r}) \phi_2(\vec{r}) d^3 \vec{r} \quad (\text{A.5})$$

$$\begin{aligned} &= \int_{\partial R} \left(\phi_{2,i}(\vec{r}) \frac{\partial G(\vec{R}, \vec{r})}{\partial \hat{n}} - \frac{\partial \phi_{2,i}(\vec{r})}{\partial \hat{n}} G(\vec{R}, \vec{r}) \right) d^2 \vec{r} \\ &= \underbrace{\int_{\partial R} \phi_{2,i}(\vec{r}) \frac{\partial G(\vec{R}, \vec{r})}{\partial \hat{n}} d^2 \vec{r}}_{\text{Double Layer Potential}} - \underbrace{\int_{\partial R} \frac{\partial \phi_{2,i}(\vec{r})}{\partial \hat{n}} G(\vec{R}, \vec{r}) d^2 \vec{r}}_{\text{Single Layer Potential}} \quad (\text{A.6}) \end{aligned}$$

Here, we have also used the fact that $\Delta \phi = 0$ applies. The index i can either be m or v , depending on whether the point \vec{R} lies within the ferromagnetic or the vacuum region. Equation A.6 shows that we can express the potential $\phi_2(\vec{R})$ in terms of a single layer potential and a double layer potential, which are both defined on the boundary ∂R . Physically the single layer potential corresponds to a layer, on which a surface charge density of $\sigma(\vec{r}) = \partial \phi_2(\vec{r}) / \partial \hat{n}$ sits. The double layer potential is due to a layer of dipoles, which can be constructed from two oppositely charged layers. For this let us describe the first of those two layers by a mapping $\vec{r}_1(\vec{u})$, where $\vec{u} = (u_1, u_2)$ is a vector in a 2D parameter space and the vector \vec{r}_1 a position vector in the 3D space. The local normal vector is defined as $\hat{n} = \vec{n}_1 / |\vec{n}_1|$ with $\vec{n}_1 = \partial \vec{r}_1 / \partial u_1 \times \partial \vec{r}_1 / \partial u_2$.

¹Formally one has to treat \mathcal{R}_v as a finite region by, for example, introducing a spherical surface with a radius R , which serves as an outer boundary. In the limiting case $R \rightarrow \infty$ the contribution of this surface vanishes due to the open boundary conditions (equation (2.10) in Chapter 2). Therefore, equation (A.6) also holds for the vacuum region.

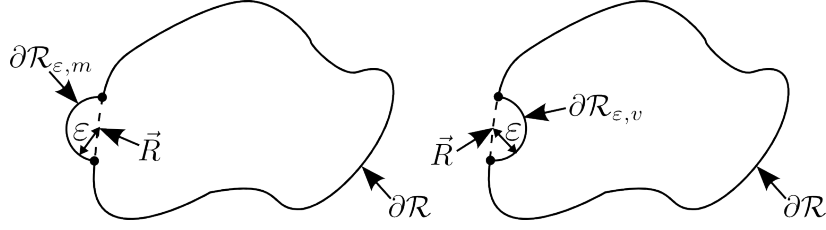


Figure A.2.: Two-dimensional depiction of the approach to evaluate equation A.5 at a point \vec{R} on the boundary ∂R . We consider two limiting cases. On the left the limit is taken from the magnetic region \mathcal{R}_m and on the right from the vacuum region \mathcal{R}_v . Its idea is to put \vec{R} at the center of a part-spherical surface $\partial R_{\epsilon,m}$ or $\partial R_{\epsilon,v}$, respectively. In the case of a smooth surface ∂R , $\partial R_{\epsilon,m}$ and $\partial R_{\epsilon,v}$ will be half-spheres.

The second layer is parallel to the first one, i.e. its position vectors \vec{r}_2 can be described by $\vec{r}_2 = \vec{r}_1 + h\vec{n}_1$, with $h \in \mathbb{R}$. Furthermore, both layers carry opposite surface charge densities $\sigma(\vec{r}_1) = -\sigma(\vec{r}_1 + h\vec{n}_1)$. The dipole layer is then defined by the limiting case $\lim_{h \rightarrow 0, \sigma \rightarrow \infty} h\sigma(\vec{r}_1) = \psi(\vec{r}_1)$. $\psi(\vec{r})$ is a dipole surface charge density. From the first term of equation (A.6) we can identify $\psi(\vec{r}) = \phi_2(\vec{r})$.

An advantage of equation (A.6) is that it automatically satisfies the condition $\lim_{\vec{r} \rightarrow \infty} \phi_2(\vec{r}) = 0$ within \mathcal{R}_v (see Chapter 2.3.4 in [132]). This goes along with our physical intuition, which tells us that a spatially confined charge or dipole layer will always create a potential which vanishes for $\vec{r} \rightarrow \infty$. However, equation (A.6) cannot be used as we are lacking the knowledge of $\phi_2(\vec{r})$ and $\partial\phi_2(\vec{r})/\partial\hat{n}$ on ∂R . Thus we take another step and derive an expression for $\phi_2(\vec{r})$ on ∂R . One should note that, since equation (A.5) does not define the behavior of the Dirac δ distribution on the boundary, equation (A.6) does not hold for points $\vec{R} \in \partial R$. This problem can be resolved by the approach depicted in Figure A.2. The idea is to construct a small spherical surface around \vec{R} . The distance between \vec{R} and the surface be ϵ . This way \vec{R} either belongs to \mathcal{R}_m or \mathcal{R}_v and the usual definition of the Dirac δ distribution holds. The case $\vec{R} \in \partial R$ is then established in the limit of $\epsilon \rightarrow 0$. This calculation is carried out in the following.

According to equation 2.31 $\phi_2(\vec{r})$ is discontinuous when crossing ∂R from \mathcal{R}_m to \mathcal{R}_v . Therefore, for each $\phi_2(\vec{r})$ with $\vec{r} \in \partial R$, there are two distinct values:

$$\phi_{2,m}(\vec{r}) = \lim_{\epsilon \rightarrow 0} \phi_2(\vec{r} \in \mathcal{R}_m) \quad (\text{A.7})$$

$$\phi_{2,v}(\vec{r}) = \lim_{\epsilon \rightarrow 0} \phi_2(\vec{r} \in \mathcal{R}_v) = \phi_{2,m}(\vec{r}) + \phi_1(\vec{r}). \quad (\text{A.8})$$

A. Notes on potential theory

The normal derivative is continuous, i.e.

$$\frac{\partial \phi_2(\vec{r})}{\partial \hat{n}} = \frac{\partial \phi_{2,m}(\vec{r})}{\partial \hat{n}} = \frac{\partial \phi_{2,v}(\vec{r})}{\partial \hat{n}}. \quad (\text{A.9})$$

We can now use equation (A.6), which, in the case of $\vec{r} \in \mathcal{R}_m$ (left image of Figure A.2), becomes

$$\phi_{2,m}(\vec{R}) = \int_{\partial R + \partial R_{\varepsilon,m}} \phi_{2,m}(\vec{r}) \frac{\partial G(\vec{R}, \vec{r})}{\partial \hat{n}} d^2 \vec{r} - \int_{\partial R + \partial R_{\varepsilon,m}} \frac{\partial \phi_2(\vec{r})}{\partial \hat{n}} G(\vec{R}, \vec{r}) d^2 \vec{r}, \quad (\text{A.10})$$

and finally

$$\begin{aligned} \phi_{2,m}(\vec{R}) = & \int_{\partial R} \phi_{2,m}(\vec{r}) \frac{\partial G(\vec{R}, \vec{r})}{\partial \hat{n}} d^2 \vec{r} - \int_{\partial R} \frac{\partial \phi_{2,m}(\vec{r})}{\partial \hat{n}} G(\vec{r}, \vec{R}) d^2 \vec{r} \quad (\text{A.11}) \\ & + \lim_{\varepsilon \rightarrow 0} \underbrace{\int_{\partial R_{\varepsilon,m}} \left(\phi_{2,m}(\vec{r}) \frac{\partial G(\vec{R}, \vec{r})}{\partial \hat{n}} - \frac{\partial \phi_{2,m}(\vec{r})}{\partial \hat{n}} G(\vec{R}, \vec{r}) \right) d^2 \vec{r}}_{I_{\varepsilon,m}}. \end{aligned}$$

The first two terms are just the result of equation (A.6). For the evaluation of the latter two terms we choose spherical polar coordinates with the origin at \vec{R} .

$$\begin{aligned} \Delta \vec{r} = \vec{r} - \vec{R} &= \varepsilon \begin{pmatrix} \cos(\phi) \sin(\theta) \\ \sin(\phi) \sin(\theta) \\ \cos(\theta) \end{pmatrix} \quad (\text{A.12}) \\ &= \varepsilon \vec{e}_\varepsilon \end{aligned}$$

The standard angles θ and ϕ are used to describe the spherically-shaped surface. The infinitesimal surface element $d\vec{r}$ reads

$$\begin{aligned} d^2 \Delta \vec{r} = d^2 \vec{r} &= \varepsilon^2 \sin(\theta) d\theta d\phi \quad (\text{A.13}) \\ &= \varepsilon^2 d\Omega. \end{aligned}$$

$d\Omega$ denotes an infinitesimal element of the solid angle. Finally the following expressions hold:

$$\hat{n} = \vec{e}_\varepsilon \quad (\text{A.14})$$

$$G(\vec{R}, \vec{r}) = G(\varepsilon) = \frac{1}{4\pi\varepsilon} \quad (\text{A.15})$$

$$\frac{\partial G(\vec{R}, \vec{r})}{\partial \hat{n}} = \frac{\partial G(\varepsilon)}{\partial \hat{n}} = \nabla G(\varepsilon) \hat{n} = -\frac{1}{4\pi\varepsilon^2} \quad (\text{A.16})$$

Thus, $\lim_{\varepsilon \rightarrow 0}$ evaluates to

$$\begin{aligned} \lim_{\varepsilon \rightarrow 0} I_{\varepsilon, m} &= - \lim_{\varepsilon \rightarrow 0} \int_{\Omega_m} \frac{\phi_{2, m}(\vec{R} + \varepsilon \hat{n}) \varepsilon^2}{4\pi \varepsilon^2} d\Omega - \underbrace{\lim_{\varepsilon \rightarrow 0} \int_{\Omega_m} \frac{\partial \phi_2(\vec{R} + \varepsilon \hat{n})}{\partial \hat{n}} \frac{\varepsilon^2}{4\pi \varepsilon} d\Omega}_{=0} \\ &= - \frac{\Omega_m(\vec{R})}{4\pi} \phi_{2, m}(\vec{R}) \end{aligned} \quad (\text{A.17})$$

The last step implies that $\phi_2(\vec{r})$ is finite on ∂R , while its normal derivative $\partial \phi_2(\vec{r}) / \partial \hat{n}$ may diverge at an order weaker than $\sim O(\varepsilon^{-1})$. $\Omega_m(\vec{r})$ is the solid angle subtended by ∂R at $\vec{r} \in \mathcal{R}_m \rightarrow \vec{R} \in \partial R$. For a smooth boundary ∂R , $\Omega_m(\vec{r})$ will be equal to 2π . The equations (A.11) and (A.17) yield:

$$\begin{aligned} \phi_{2, m}(\vec{R}) &= \int_{\partial R} \left(\phi_{2, m}(\vec{r}) \frac{\partial G(\vec{R}, \vec{r})}{\partial \hat{n}} - \frac{\partial \phi_2(\vec{r})}{\partial \hat{n}} G(\vec{R}, \vec{r}) \right) d^2 \vec{r} \\ &\quad - \frac{\Omega_m(\vec{R})}{4\pi} \phi_{2, m}(\vec{R}). \end{aligned} \quad (\text{A.18})$$

Analogously we can derive an expression for $\phi_{2, v}(\vec{r})$ (right part of Figure A.2). The only difference is that equation (A.14) changes to $\hat{n} = -\vec{e}_\varepsilon$, which leads to the following result for $I_{\varepsilon, v}$:

$$I_{\varepsilon, v} = \frac{\Omega_v(\vec{R})}{4\pi} \phi_{2, v}(\vec{R}). \quad (\text{A.19})$$

$\Omega_v(\vec{R})$ is the solid angle subtended by ∂R at $\vec{r} \in \mathcal{R}_v \rightarrow \vec{R} \in \partial R$. The sum of $\Omega_m(\vec{R})$ and $\Omega_v(\vec{R})$ yields the full solid angle, i.e.

$$\Omega_m(\vec{R}) + \Omega_v(\vec{R}) = 4\pi. \quad (\text{A.20})$$

Thus, we obtain

$$\begin{aligned} \phi_{2, v}(\vec{R}) &= \int_{\partial R} \left(\phi_{2, v}(\vec{r}) \frac{\partial G(\vec{R}, \vec{r})}{\partial \hat{n}} - \frac{\partial \phi_2(\vec{r})}{\partial \hat{n}} G(\vec{R}, \vec{r}) \right) d^2 \vec{r} \\ &\quad + \frac{\Omega_v(\vec{R})}{4\pi} \phi_{2, v}(\vec{R}). \end{aligned} \quad (\text{A.21})$$

Now, we compute the difference $\phi_{2, m}(\vec{R}) - \phi_{2, v}(\vec{R})$ and use the equations (A.8), (A.9) and (A.20)

$$\phi_{2, m}(\vec{R}) = \int_{\partial R} \phi_1(\vec{r}) \frac{\partial G(\vec{R}, \vec{r})}{\partial \hat{n}} d^2 \vec{r} - \frac{\Omega_m(\vec{R})}{4\pi} \phi_1(\vec{R}) \quad (\text{A.22})$$

$$= \int_{\partial R} \phi_1(\vec{r}) \frac{\partial G(\vec{R}, \vec{r})}{\partial \hat{n}} d^2 \vec{r} + \left(\frac{\Omega_v(\vec{R})}{4\pi} - 1 \right) \phi_1(\vec{R}) \quad (\text{A.23})$$

A. Notes on potential theory

Combining the equations (A.6), (A.11), (A.17) and (A.22) and we can finally write down an expressions for $\phi_2(\vec{r})$ for $\vec{r} \in \mathcal{R}_m$, namely

$$\phi_2(\vec{R}) = \int_{\partial R} \phi_1(\vec{r}) \frac{\partial G(\vec{R}, \vec{r})}{\partial \hat{n}} d^2 \vec{r}. \quad (\text{A.24})$$

This is the well-known result, which is used in the Hybrid FEM/BEM [66]. The alternative approach, as introduced by García-Cervera and Roma, makes use of a boundary integral equation (see equations (2.41) and (2.42)), which can derived analogously.

B. Determining HLib parameters

In this appendix we want show simulation results which have been used to derive adequate parameter sets (see table 3.1 in Chapter 3) for the algorithms ACA, ACA+, HCA I, HCA II and interpolation. As described in Section 3.1 a thin, square platelet system with a homogeneous out-of-plane magnetization is chosen as a test system. The error is estimated from the magnetometric demagnetizing factor D_z defined in equation 3.4. All computations of this section have been conducted on a mesh which has been created with a Kuhn triangulation from a cubic grid with two cube layers along the z -direction (see Figure 3.1 of Chapter 3). We know from Figure 3.2 that the corresponding error from the hybrid FEM/BEM (using the full boundary element (BE) matrix) is $\gtrsim 0.1\%$. As a first step we demand that the error due to the application of a hierarchical matrix should lie at least about one order of magnitude below 0.1% . This is just an estimation of an acceptable error, which has to be tested by performing more realistic micromagnetic simulations (see Section 3.3). For most algorithms we only compare the \mathcal{H} -matrix assembly time and the error for different parameter sets, as the memory footprint of an \mathcal{H} -matrix, which has been assembled with a certain algorithm, is virtually independent of the used algorithm-specific parameters. There is only a slight dependence of the memory footprint for HCA I and HCA II, which we do not consider here. Please note, that one should not compare assembly times of different algorithms, which are presented in this section, as these may have been measured on different machine. For such a comparison the reader is referred to Section 3.2. In this section only numerical quadrature is used to compute the BE matrix elements $B_{i,j}$. The section contains the following figures (in the order as they appear):

- Dependency of the efficiency of interpolation on the polynomial order (Figure B.1)
- Dependency of the efficiency of ACA on the parameter ϵ_{aca} (Figure B.2)
- Dependency of the efficiency of ACA+ on the parameter ϵ_{aca} (Figure B.3)
- Dependency of the efficiency of HCA I on the polynomial order and ϵ_{aca} (Figure B.4)

B. Determining HLib parameters

- Dependency of the efficiency of HCA II on the polynomial order and ϵ_{aca} (Figure B.5)
- Dependency of the efficiency of HCA II with $\epsilon_{aca} = 10^{-7}$ on the polynomial order (Figure B.6)
- Effect of the parameter ϵ on the efficiency of the algorithm HCA II (Figure B.7)
- Effect of the quadrature order q on the efficiency of the algorithm HCA II (Figure B.8)

Additional information (e.g. why a certain value of a parameter has been chosen for an algorithm) are given in the captions.

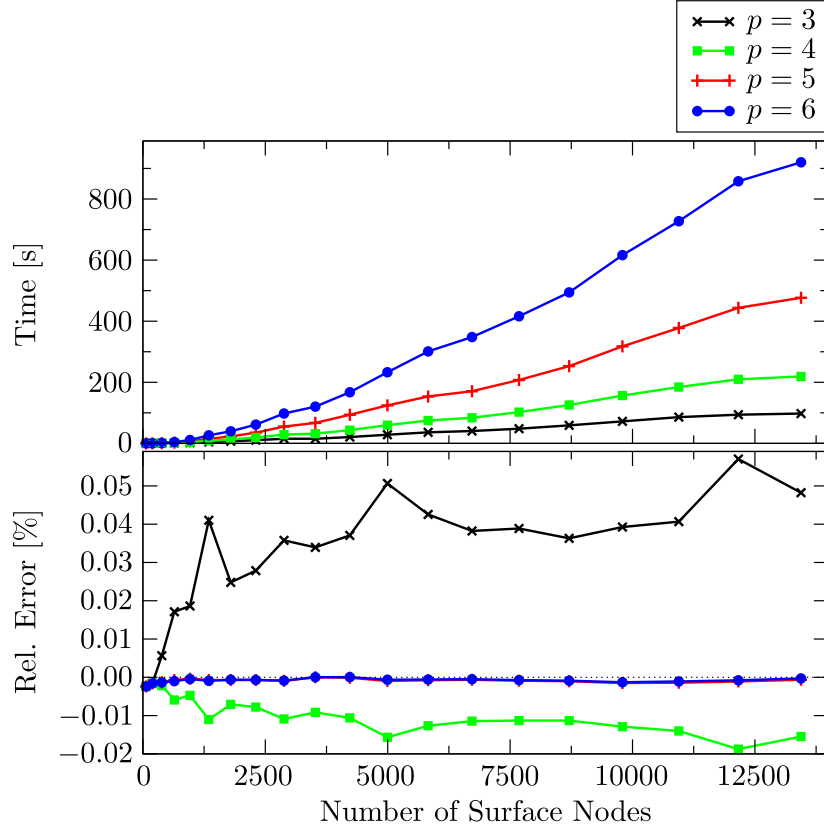


Figure B.1.: Interpolation is used to assemble hierarchical matrix approximations for differently-sized thin, square platelets. The polynomial order of the interpolation is varied between 3 and 6. The parameter ϵ for the adaptive re-compression is set to 0.001 and the order of the numerical quadrature to 3. Top: the assembly time of the hierarchical matrices increases with increasing polynomial order. Bottom: the error in D_z with respect to the corresponding result, obtained with hybrid FEM/BEM and the full BE matrix, is given. It decreases significantly below 0.01 % when the polynomial order is larger or equal to 5. As a consequence we will use a polynomial order of $p = 5$ when using interpolation (if no different value is explicitly given).

B. Determining HLib parameters

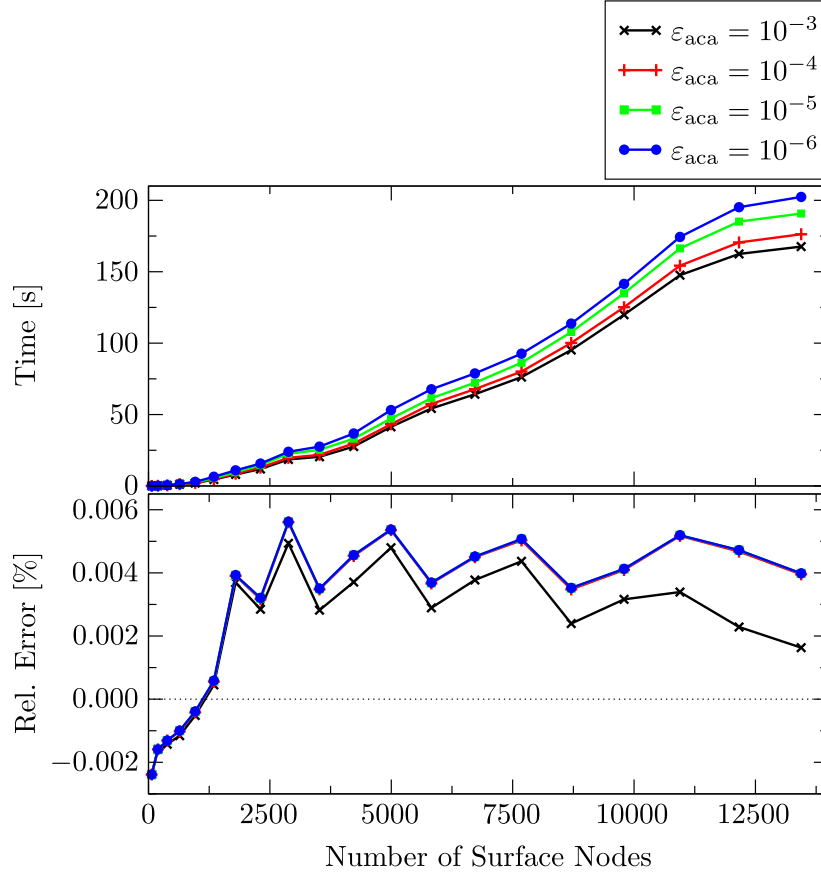


Figure B.2.: Hierarchical matrix approximations for differently-sized thin, square platelets are assembled using ACA. The parameter ε for the adaptive re-compression is set to 0.001 and the order of the numerical quadrature to 3. Different values for the parameter ϵ_{aca} are tested concerning the assembly times of the hierarchical matrices (top) and the deviations from simulation results obtained with the full BE matrix (bottom). The assembly time increases with a decreasing value for ϵ_{aca} , while the deviation from the full matrix computation does not converge to zero but to a finite value below 0.01 %. Although the smallest deviations are observed for $\epsilon_{aca} = 0.001$, we will use ACA with $\epsilon_{aca} = 0.0001$ in subsequent simulations, if not explicitly stated otherwise. The higher accuracy for $\epsilon_{aca} = 0.001$ seems to be the result of a cancellation of errors, namely an error, which is independent of ϵ_{aca} , and an error resulting from a too large value for ϵ_{aca} . For another situation (different geometry and magnetization) these errors may not cancel but amplify.

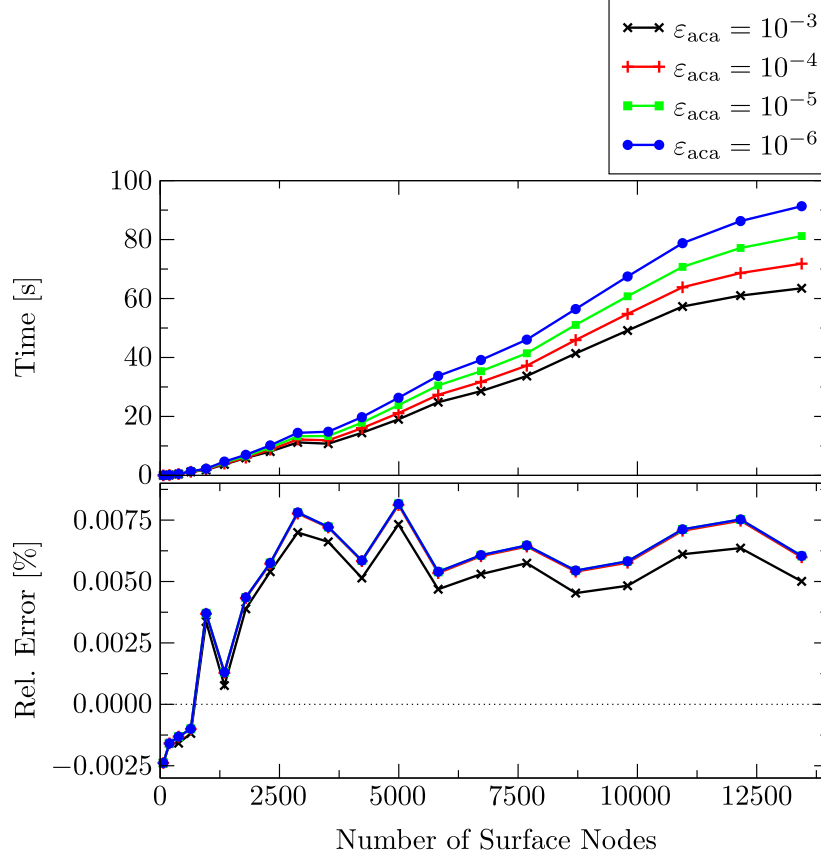


Figure B.3.: Hierarchical matrix approximations for differently-sized thin, square platelets are assembled using ACA+. The parameter ϵ for the adaptive re-compression is set to 0.001 and the order of the numerical quadrature to 3. Different values for the parameter ϵ_{aca} are tested concerning the assembly times of the hierarchical matrices (top) and the deviations from simulation results obtained with the full BE matrix (bottom). The assembly time increases with a decreasing value for ϵ_{aca} , while the deviation from the full matrix computation does not converge to zero but to a finite value below 0.01%. In all subsequent simulations we will use ACA+ with $\epsilon_{aca} = 0.0001$, if not explicitly stated otherwise. For an explanation see Figure B.2.

B. Determining HLib parameters

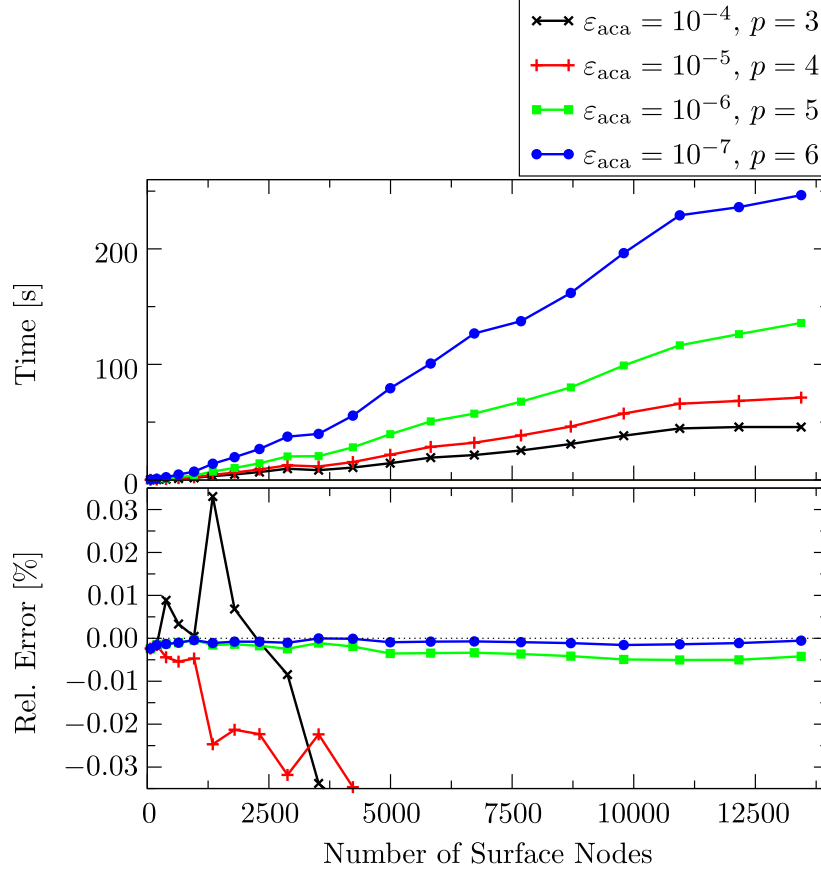


Figure B.4.: Dependency of the accuracy and the assembly time of the \mathcal{H} -matrix assembly by HCA I on the polynomial order and the parameter ϵ_{aca} . In accordance with [72] we find that a choice p , $\epsilon = 10^{-p-1}$ seems to be adequate. Furthermore, we have chosen $\epsilon = 0.001$ for the adaptive re-compression and $q = 3$ for the numerical integration. The deviation from the simulation result obtained with the full BE matrix becomes significantly smaller than 0.01% when we set $p = 6$ and $\epsilon = 10^{-7}$ (bottom figure). We will use these values in all subsequent simulations, if not explicitly stated otherwise.

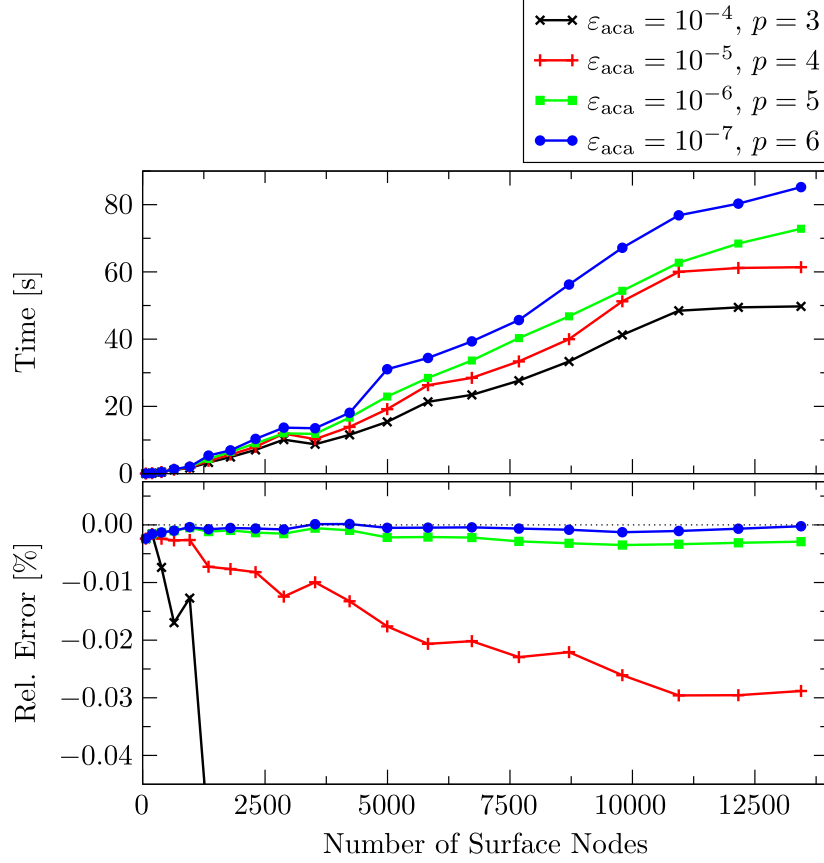


Figure B.5.: Dependency of the accuracy and the assembly time of the \mathcal{H} -matrix assembly by HCA II on the polynomial order and the parameter ε_{aca} . As for HCA I we vary both parameters according to $p = 3, 4, 5, 6$, $\varepsilon = 10^{-p-1}$. Adaptive re-compression is used with $\epsilon = 0.001$ and for the Gaussian quadrature a quadrature order of $q = 3$ is chosen. At $p = 6$ and $\varepsilon = 10^{-7}$ the deviation from the simulation result obtained with the full BE matrix becomes significantly smaller than 0.01%. At the same time the additional computation time for the matrix assembly is moderate (upper figure), so that $(p = 6, \varepsilon = 10^{-7})$ appears to be the most adequate parameter set of this figure. Also note the improved convergence of HCA II as compared to HCA I (Figure B.4). For HCA II one can reduce the parameter p somewhat. This is shown in Figure B.6.

B. Determining HLib parameters

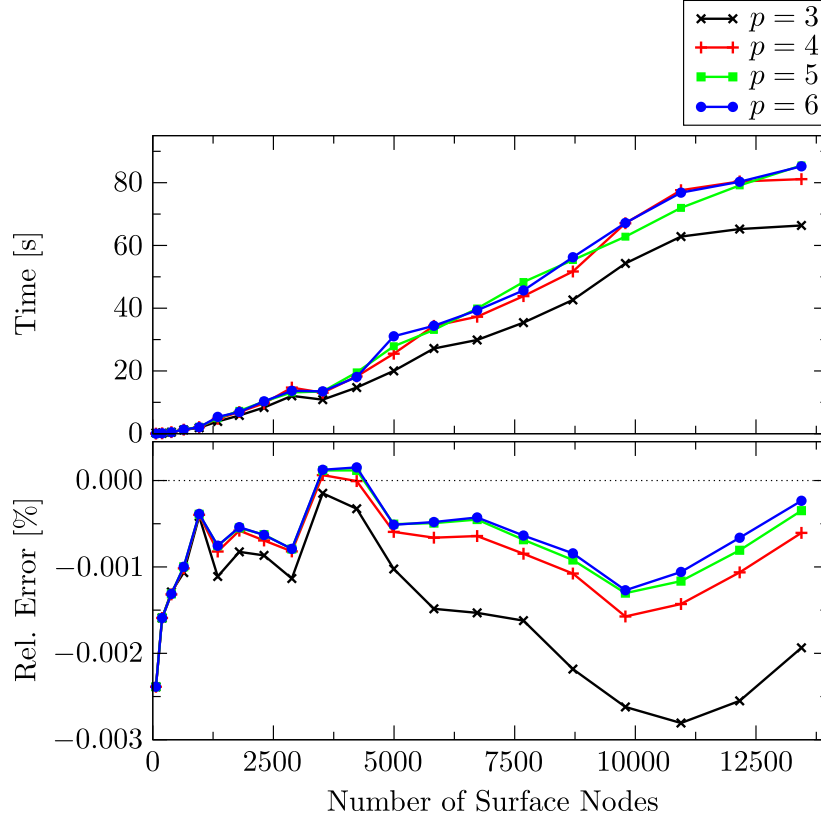


Figure B.6.: Hierarchical matrix approximations for differently-sized thin, square platelets are assembled using HCA II. The dependency of the efficiency of HCA II on the polynomial order p , which is varied between 3, 4, 5 and 6, is investigated. The other parameters are set to $\varepsilon = 0.001$, $\epsilon_{aca} = 10^{-7}$ and $q = 3$. This investigation has been motivated by Steffen Börm, one of the authors of the library HLib, who remarked that, due to its improved convergence compared to HCA I, one may use a lower polynomial order for HCA II. Indeed, a reduction of the polynomial order from 6 to 4 only has a minor effect on the accuracy of the algorithm (lower figure). However, the matrix assembly time is also insensitive to this reduction in the polynomial order (upper figure). Therefore, there is no obvious pick for the polynomial order of HCA II. In subsequent simulations we will use HCA II with $p = 4$, if not explicitly stated otherwise.

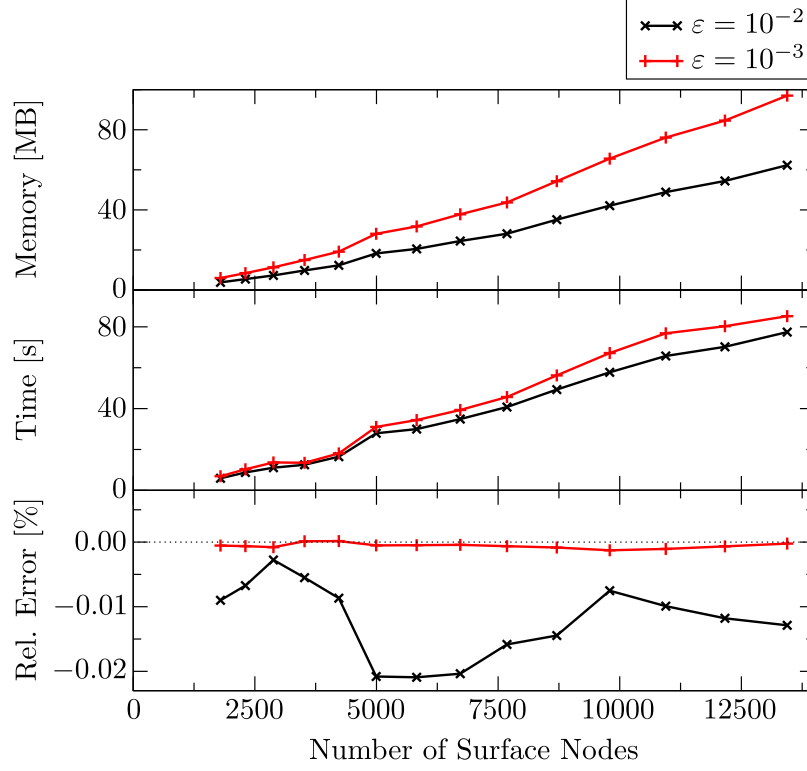


Figure B.7.: The effect of the parameter ε , which controls the adaptive re-compression, on the efficiency of the hierarchical matrix approximation is investigated. As adaptive re-compression has a significant effect on the memory footprint of a hierarchical matrix, this figure is subdivided into three sub-figures: a comparison of the memory footprint (top), a comparison of the matrix assembly times (middle) and a comparison of the deviations from corresponding computations using a full BE matrix. The other parameters are set as follows: $q = 3$ (numerical quadrature), $\varepsilon_{\text{aca}} = 10^{-7}$ and $p = 6$ (HCA II). We see that the error decreases significantly when ε is changed from 10^{-2} to 10^{-3} while the assembly time and the memory footprint moderately increase. As a consequence we will use $\varepsilon_{\text{aca}} = 10^{-3}$ in all simulations of this thesis, if not explicitly stated otherwise.

B. Determining HLib parameters

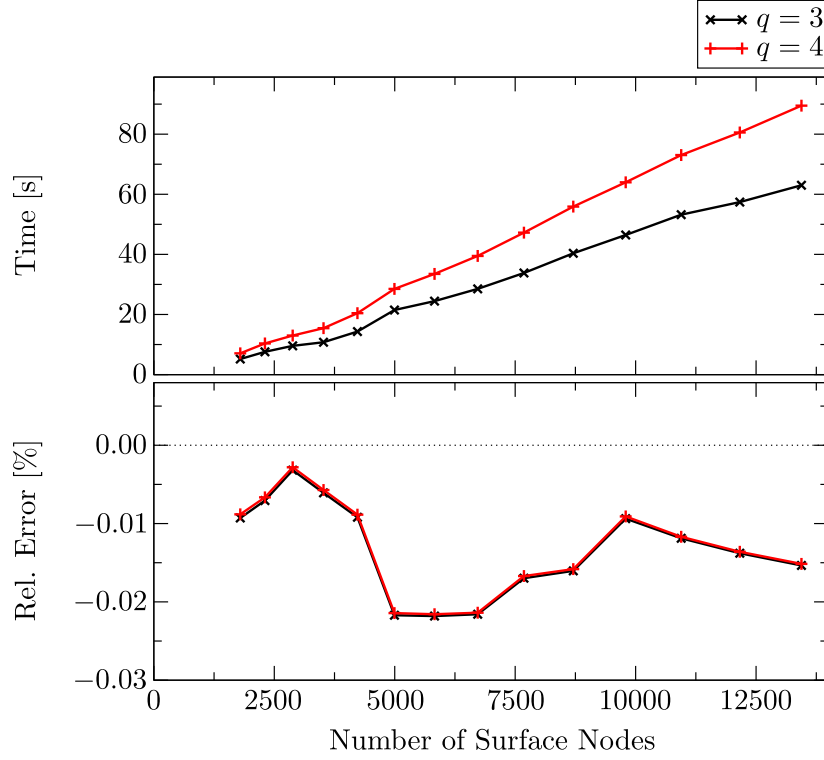


Figure B.8.: The order of the numerical quadrature, which is used to compute the elements of the hierarchical matrix, is varied in order to investigate its effect on the efficiency of the hierarchical matrix approximation. The hierarchical matrices are assembled with HCA II. The following set of parameters has been used in those simulations: $\varepsilon = 0.01$, $\epsilon_{\text{aca}} = 10^{-6}$ and $p = 6$. The accuracy of the hierarchical matrix approximation is not significantly improved upon changing the quadrature order from 3 to 4 (bottom), while the matrix assembly time increases by about 30 % (top). In the following, when using numerical quadrature, we set the quadrature order to 3, if not explicitly stated otherwise.

C. Analytical expression for the stray field in a rectangular prism

In this section we want to derive an analytical formula for the stray field of a homogeneously magnetised, rectangular prism. This formula can then be used to test the numerical calculation of the demagnetisation field using the hybrid FEM/BEM (see Section 2.2 and Chapter 3). This chapter is structured as follows: the derivation of the formula is given in the first part of this chapter (Section C.1). Afterwards the formula is tested (Section C.2).

C.1. Derivation of the formula

For simplicity let us assume the case shown in Figure C.1, where the magnetisation is aligned along one of the principal axes of the prism, which is chosen to be the x direction. The magnetic potential ϕ of this arrangement reads

$$\phi = \frac{\sigma}{4\pi} \overbrace{\left(\int_{-h}^h \int_{-w}^w \frac{dy' dz'}{\sqrt{(x+l)^2 + (y-y')^2 + (z-z')^2}} \right)}^{I_1} \quad (\text{C.1})$$

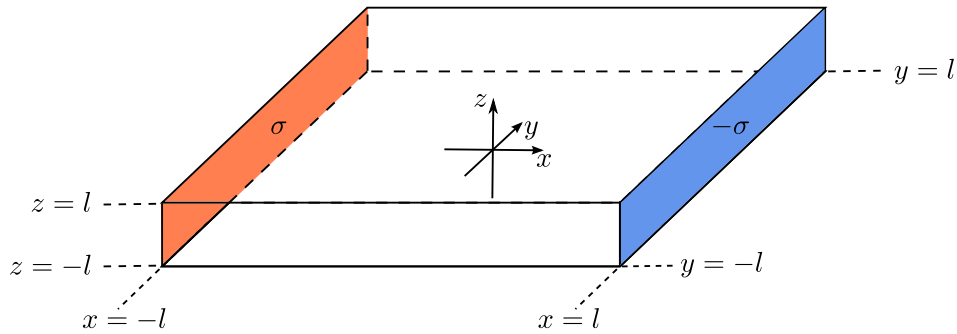


Figure C.1.: Sketch of a rectangular prism. The faces at $x = l$ and $x = -l$ have a surface charge of σ and $-\sigma$, respectively. The coordinate system is chosen such that its origin sits at the geometric centre of the structure with the axes being parallel to the surface normals.

C. Analytical expression for the stray field in a rectangular prism

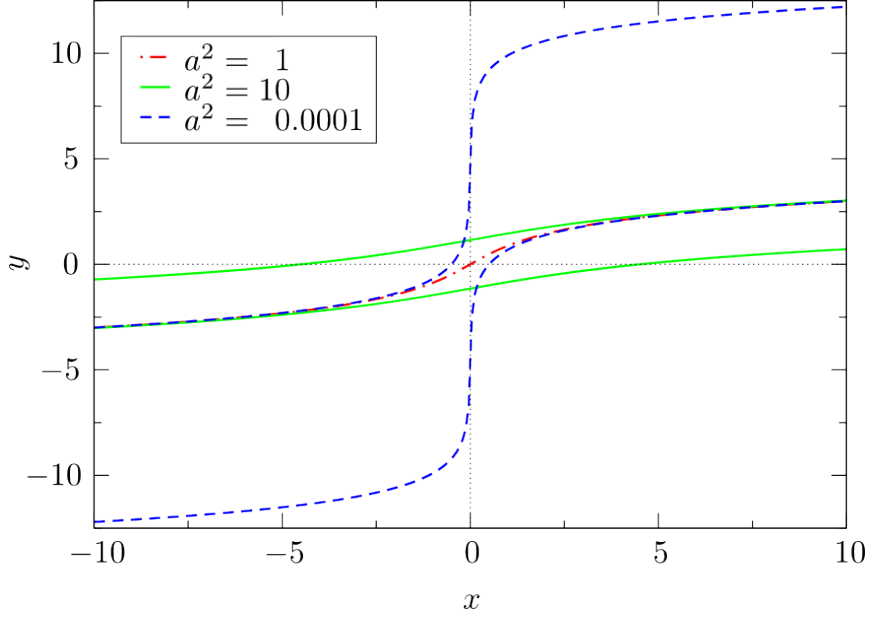


Figure C.2.: Visualisation of solutions of the integral (C.4), which do not diverge in the limiting case of $a \rightarrow 0$ for either $x > 0$ or $x < 0$ (see equation (C.4)). In the case of $a^2 = 1$ these solutions correspond to the inverse function of the hyperbolic sine.

$$\begin{aligned}
 & - \underbrace{\int_{-h}^h \int_{-w}^w \frac{dy' dz'}{\sqrt{(x-l)^2 + (y-y')^2 + (z-z')^2}}}_{I_2} \\
 & = (I_1 - I_2)/4\pi.
 \end{aligned}$$

The stray field simply follows from equation (2.7), i.e.

$$\vec{H}_{\text{demag}} = -\nabla\phi. \quad (\text{C.2})$$

As the calculation for I_2 is completely analogous we only give the details for the calculation of I_1 . For brevity we will also set the surface charge density σ equal to 1. As a first step we want to give some thought to solving integrals of the form

$$\int \frac{dx}{\sqrt{a^2 + x^2}} = \sinh^{-1} \left(\frac{x}{|a|} \right) + C(a), \quad (\text{C.3})$$

where the integration is accomplished by the simple substitution $x = \sinh(y)/|a|$. In the case of $|a| \rightarrow 0$ the solution diverges logarithmically to $-\infty$ for $x < 0$ and to ∞ for $x > 0$. Choosing $C(a) = \mp \log(a)$ one can find two solutions, which do not diverge for either $x > a$ or $x < a$, respectively. Using the relation

$$\sinh^{-1}(x) = \log \left(\sqrt{1+x^2} + x \right)$$

we can rewrite equation (C.3) as

$$\begin{aligned}\int \frac{dx}{\sqrt{a^2 + x^2}} &= \sinh^{-1}(x/|a|) - \log(a) \\ &= \log(\sqrt{a^2 + x^2} + x)\end{aligned}$$

and

$$\begin{aligned}\int \frac{dx}{\sqrt{a^2 + x^2}} &= \sinh^{-1}(x/|a|) + \log(a) \\ &= -\log(\sqrt{a^2 + x^2} - x).\end{aligned}$$

These two solution branches are visualised in Figure C.2 for the cases $a^2 = 0.0001, 1$ and 10 . According to [133] the physically relevant solution is the non-diverging branch, leading to the following equation:

$$\int \frac{dx}{\sqrt{a^2 + x^2}} = \begin{cases} \log(\sqrt{a^2 + x^2} + x) & \text{for } x > 0 \\ -\log(\sqrt{a^2 + x^2} - x) & \text{for } x < 0 \end{cases}. \quad (\text{C.4})$$

Equation C.4 has a discontinuity of $\log(a^2)$ at $x = 0$, which leads to unphysical artifacts when computing the demagnetising tensor of an array of rectangular blocks [133]. For the computation of the demagnetising tensor this can be circumvented by exploiting the symmetry of the problem [134, 133]. By contrast, at this stage we just pick one of the branches of identity (C.4) in order to carry out the integration of equation (C.1) and consider the limiting case $a^2 \rightarrow 0$ later. Thus, equation (C.1) becomes

$$\begin{aligned}I_1 &= \int_{z-h}^{z+h} \int_{y-w}^{y+w} \frac{dy' dz'}{\sqrt{(x+l)^2 + y'^2 + z'^2}} \\ &= \int_{z-h}^{z+h} \log\left(\sqrt{(x+l)^2 + (y+w)^2 + z'^2} + y+w\right) dz' - \\ &\quad \int_{z-h}^{z+h} \log\left(\sqrt{(x+l)^2 + (y-w)^2 + z'^2} + y-w\right) dz'.\end{aligned} \quad (\text{C.5})$$

For the integration over z we use the identity

$$\begin{aligned}\int \log(\sqrt{a^2 + x'^2} + c) dx' &= -\sqrt{a^2 - c^2} \arctan \frac{cx}{\sqrt{a^2 - c^2}\sqrt{a^2 + x^2}} \\ &\quad + \sqrt{a^2 - c^2} \arctan \frac{x}{\sqrt{a^2 - c^2}} \\ &\quad + x \log\left(\sqrt{a^2 + x^2} + c\right) \\ &\quad + c \log\left(\sqrt{a^2 + x^2} + x\right) - x\end{aligned} \quad (\text{C.6})$$

C. Analytical expression for the stray field in a rectangular prism

and obtain the following expression for I_1 :

$$I_1 = f_+(x+l, y+w, z+h) - f_+(x+l, y-w, z+h) \quad (C.7) \\ - f_+(x+l, y+w, z-h) + f_+(x+l, y-w, z-h)$$

with

$$f_+(x, y, z) = -|x| \arctan\left(\frac{yz}{|x|r}\right) + z \log(r+y) + y \log(r+z) \quad (C.8)$$

and

$$r = r(x, y, z) = \sqrt{x^2 + y^2 + z^2}.$$

Deriving an analogous expression for I_2 equation (C.1) can be rewritten as

$$\phi = f_+(x+l, y+w, z+h) - f_+(x-l, y+w, z+h) \quad (C.9) \\ - f_+(x+l, y-w, z+h) + f_+(x-l, y-w, z+h) \\ - f_+(x+l, y+w, z-h) + f_+(x-l, y+w, z-h) \\ + f_+(x+l, y-w, z-h) - f_+(x-l, y-w, z-h).$$

The difficulty with this expression for the potential ϕ is that the argument of the logarithm may become zero, which in turn leads to diverging terms in the demagnetisation field. As an example, let us consider the following two terms of equation (C.9):

$$(z-h) \log(\sqrt{(x-l)^2 + (y+w)^2 + (z-h)^2} + y+w) \quad (C.10) \\ - (z-h) \log(\sqrt{(x-l)^2 + (y-w)^2 + (z-h)^2} + y-w).$$

The argument of the logarithm in the first term is 0 when $x = l$, $z = h$, and $y \leq -w$. For the second term this is true when $x = l$, $z = h$ and $y \leq w$. Therefore, we do not have to worry about diverging terms in the case of $y > w$. Due to the symmetry of our problem this should also be true for $y < -w$. Indeed, we can use the relation

$$\log(\sqrt{a^2 + x^2} + x) = -\log(\sqrt{a^2 + x^2} - x) - \log(a^2)$$

and rewrite expression (C.10) as

$$- (z-h) \log(\sqrt{(x-l)^2 + (y+w)^2 + (z-h)^2} - y-w) \quad (C.11) \\ + (z-h) \log(\sqrt{(x-l)^2 + (y-w)^2 + (z-h)^2} - y+w).$$

The terms of this expression do not diverge when $x = l$, $z = h$ and $y < w$. However, in the case of $x = l$, $z = h$ and $-w \leq y \leq w$, which corresponds to the

edge of one of the charged faces (see Figure C.2), both formulations, equation C.10 and C.11, contain one diverging term. From this we can conclude the occurrence of infinite demagnetisation fields at the edges of a homogeneously magnetised cuboid. Using the function

$$f_{-}(x, y, z) = -|x| \arctan\left(\frac{yz}{|x|r}\right) - z \log(r - y) - y \log(r - z),$$

allows us to introduce an equivalent formulation of equation (C.9), which does not contain diverging logarithms for the cases $(x = \pm l, y = \pm w, z < -h)$ and $(x = \pm l, y < -w, z \pm h)$:

$$\begin{aligned} \phi = & f_{-}(x + l, y + w, z + h) - f_{-}(x - l, y + w, z + h) \\ & - f_{-}(x + l, y - w, z + h) + f_{-}(x - l, y - w, z + h) \\ & - f_{-}(x + l, y + w, z - h) + f_{-}(x - l, y + w, z - h) \\ & + f_{-}(x + l, y + w, z + h) - f_{-}(x - l, y - w, z - h). \end{aligned} \quad (\text{C.12})$$

We can now obtain the stray field \vec{H}_{demag} by computing the gradient of ϕ . Forming the derivative of f_{+} and f_{-} in terms of x , y , and z yields

$$\begin{aligned} \frac{\partial f_{+}}{\partial x} &= \frac{x}{|x|} \arctan\left(\frac{yz}{|x|r}\right) - \frac{xyz}{1 + \frac{y^2 z^2}{x^2 r^2}} \left(\frac{1}{x^2 r} + \frac{1}{r^3}\right) \\ &\quad - \frac{xz}{(r + y)r} - \frac{xy}{(r + z)r} \\ \frac{\partial f_{+}}{\partial y} &= \frac{z}{r \left(1 + \frac{y^2 z^2}{x^2 r^2}\right)} \left(1 - \frac{y^2}{r^2}\right) - \frac{z}{r + y} \left(1 + \frac{y}{r}\right) \\ &\quad - \log(r + z) - \frac{y^2}{(r + z)r} \\ \frac{\partial f_{+}}{\partial z} &= \frac{y}{r \left(1 + \frac{y^2 z^2}{x^2 r^2}\right)} \left(1 - \frac{z^2}{r^2}\right) - \log(r + y) \\ &\quad - \frac{z^2}{(r + y)r} - \frac{y}{r + z} \left(1 + \frac{z}{r}\right) \end{aligned} \quad (\text{C.13})$$

and

$$\begin{aligned} \frac{\partial f_{-}}{\partial x} &= \frac{x}{|x|} \arctan\left(\frac{yz}{|x|r}\right) - \frac{xyz}{1 + \frac{y^2 z^2}{x^2 r^2}} \left(\frac{1}{x^2 r} + \frac{1}{r^3}\right) \\ &\quad + \frac{xz}{(r - y)r} + \frac{xy}{(r - z)r} \\ \frac{\partial f_{-}}{\partial y} &= \frac{z}{r \left(1 + \frac{y^2 z^2}{x^2 r^2}\right)} \left(1 - \frac{y^2}{r^2}\right) - \frac{z}{r - y} \left(1 - \frac{y}{r}\right) \\ &\quad + \log(r - z) + \frac{y^2}{(r - z)r} \end{aligned} \quad (\text{C.14})$$

C. Analytical expression for the stray field in a rectangular prism

$$\begin{aligned}\frac{\partial f_-}{\partial z} = & \frac{y}{r \left(1 + \frac{y^2 z^2}{x^2 r^2}\right)} \left(1 - \frac{z^2}{r^2}\right) + \log(r - y) \\ & + \frac{z^2}{(r - y)r} - \frac{y}{r - z} \left(1 - \frac{z}{r}\right).\end{aligned}$$

The components of the demagnetisation field \vec{H}_{demag} then read

$$\begin{aligned}\vec{H}_{\text{demag},x} = & \frac{\partial f_+}{\partial x}(x + l, y + w, z + h) - \frac{\partial f_+}{\partial x}(x - l, y + w, z + h) \\ & - \frac{\partial f_+}{\partial x}(x + l, y + w, z - h) + \frac{\partial f_+}{\partial x}(x - l, y + w, z - h) \\ & - \frac{\partial f_+}{\partial x}(x + l, y - w, z + h) + \frac{\partial f_+}{\partial x}(x - l, y - w, z + h) \\ & + \frac{\partial f_+}{\partial x}(x + l, y - w, z - h) - \frac{\partial f_+}{\partial x}(x - l, y - w, z - h) \\ = & \frac{\partial f_-}{\partial x}(x + l, y + w, z + h) - \frac{\partial f_-}{\partial x}(x - l, y + w, z + h) \\ & - \frac{\partial f_-}{\partial x}(x + l, y + w, z - h) + \frac{\partial f_-}{\partial x}(x - l, y + w, z - h) \\ & - \frac{\partial f_-}{\partial x}(x + l, y - w, z + h) + \frac{\partial f_-}{\partial x}(x - l, y - w, z + h) \\ & + \frac{\partial f_-}{\partial x}(x + l, y - w, z - h) - \frac{\partial f_-}{\partial x}(x - l, y - w, z - h), \quad (\text{C.15})\end{aligned}$$

$$\begin{aligned}\vec{H}_{\text{demag},y} = & \frac{\partial f_+}{\partial y}(x + l, y + w, z + h) - \frac{\partial f_+}{\partial y}(x - l, y + w, z + h) \quad (\text{C.16}) \\ & - \frac{\partial f_+}{\partial y}(x + l, y + w, z - h) + \frac{\partial f_+}{\partial y}(x - l, y + w, z - h) \\ & - \frac{\partial f_+}{\partial y}(x + l, y - w, z + h) + \frac{\partial f_+}{\partial y}(x - l, y - w, z + h) \\ & + \frac{\partial f_+}{\partial y}(x + l, y - w, z - h) - \frac{\partial f_+}{\partial y}(x - l, y - w, z - h) \\ = & \frac{\partial f_-}{\partial y}(x + l, y + w, z + h) - \frac{\partial f_-}{\partial y}(x - l, y + w, z + h) \\ & - \frac{\partial f_-}{\partial y}(x + l, y + w, z - h) + \frac{\partial f_-}{\partial y}(x - l, y + w, z - h) \\ & - \frac{\partial f_-}{\partial y}(x + l, y - w, z + h) + \frac{\partial f_-}{\partial y}(x - l, y - w, z + h) \\ & + \frac{\partial f_-}{\partial y}(x + l, y - w, z - h) - \frac{\partial f_-}{\partial y}(x - l, y - w, z - h)\end{aligned}$$

and

$$\begin{aligned}\vec{H}_{\text{demag},z} = & \frac{\partial f_+}{\partial z}(x + l, y + w, z + h) - \frac{\partial f_+}{\partial z}(x - l, y + w, z + h) \quad (\text{C.17}) \\ & - \frac{\partial f_+}{\partial z}(x + l, y + w, z - h) + \frac{\partial f_+}{\partial z}(x - l, y + w, z - h)\end{aligned}$$

$$\begin{aligned}
& -\frac{\partial f_+}{\partial z}(x+l, y-w, z+h) + \frac{\partial f_+}{\partial z}(x-l, y-w, z+h) \\
& + \frac{\partial f_+}{\partial z}(x+l, y-w, z-h) - \frac{\partial f_+}{\partial z}(x-l, y-w, z-h) \\
= & \frac{\partial f_+}{\partial z}(x+l, y+w, z+h) - \frac{\partial f_+}{\partial z}(x-l, y+w, z+h) \\
& - \frac{\partial f_-}{\partial z}(x+l, y+w, z-h) + \frac{\partial f_-}{\partial z}(x-l, y+w, z-h) \\
& - \frac{\partial f_-}{\partial z}(x+l, y-w, z+h) + \frac{\partial f_-}{\partial z}(x-l, y-w, z+h) \\
& + \frac{\partial f_-}{\partial z}(x+l, y-w, z-h) - \frac{\partial f_-}{\partial z}(x-l, y-w, z-h).
\end{aligned}$$

Please note, that the formulation of the demagnetisation field \vec{H}_{demag} in terms of the derivatives of either the function f_+ or f_- are equivalent. The advantage of using two expressions lies solely in the numerical implementation of the formula. Just using an expression in terms of f_+ would complicate the task of computing the field at those points, which are specified by $(x = \pm l, y = \pm w, z < -h)$ and $(x = \pm l, y < -w, z = \pm h)$, as it contains diverging terms. Likewise, expressing the demagnetisation field in terms of f_- leads to equivalent issues in the case of $(x = \pm l, y = \pm w, z > h)$ and $(x = \pm l, y > w, z = \pm h)$. For an implementation of the formula one also has to give special attention to terms of the form

$$\begin{aligned}
& \frac{x-l}{|x-l|} \arctan \left(\frac{(y-w)(z-h)}{|x-l| \sqrt{(x-l)^2 + (y-w)^2 + (z-h)^2}} \right) \\
& - \frac{x-l}{|x-l|} \arctan \left(\frac{(y+w)(z-h)}{|x-l| \sqrt{(x-l)^2 + (y+w)^2 + (z-h)^2}} \right).
\end{aligned}$$

In the case of $x \rightarrow l, y \neq -w, y \neq w$ and $z \neq h$ the tangent terms are equal to $\text{sgn}((y-w)(z-h)) \pi/2$ or $\text{sgn}((y+w)(z-h)) \pi/2$, respectively. The term $(x-l)/|x-l|$ is either equal to -1 or 1 , depending on the side, from which the limit $x \rightarrow l$ is taken. If $x \rightarrow l$ and $z = h$ holds, there are two possibilities: in case of $y < -w$ or $y > w$ the two terms cancel each other out. In case of $-w \leq y \leq w$ the result is undefined.

C.2. Testing the formula

Although the derivation of the magnetic field within a homogeneously magnetised prism is not very complicated, the result is a rather lengthy formula. Therefore it is always advantageous to have some tests which can verify the correctness of the formula and its implementation in a programming language. The tests of this section include checks of the formula's physical plausibility

C. Analytical expression for the stray field in a rectangular prism

(symmetry, behaviour in limiting cases) and comparisons with numerical simulations done with the Object Oriented MicroMagnetic Framework (OOMMF) [102]. OOMMF solves the micromagnetic equations using a finite difference (FD) discretisation on a cubic mesh. The demagnetisation field is computed from the analytical expression for the magnetostatic energy of an array of cubes with a homogeneous magnetisation [133, 135] and should be very accurate.

The first two tests concern the asymptotic behaviour of our system. In the case of $l \rightarrow \infty$, $w \rightarrow \infty$ and $h \rightarrow \infty$ the system behaves like a sphere [133], i.e. the demagnetisation field takes the form

$$\vec{H}_{l \rightarrow \infty, w \rightarrow \infty, h \rightarrow \infty} = \frac{\sigma}{3} \begin{pmatrix} 1 \\ 0 \\ 0 \end{pmatrix}. \quad (\text{C.18})$$

The case of an infinitely extended plate capacitor is realised when $l = \text{const.}$, $y \rightarrow \infty$ and $z \rightarrow \infty$. Its demagnetisation field writes

$$\vec{H}_{w \rightarrow \infty, h \rightarrow \infty} = \sigma \begin{pmatrix} 1 \\ 0 \\ 0 \end{pmatrix} \text{ for } -l \leq x \leq l, \quad \vec{H}_{w \rightarrow \infty, h \rightarrow \infty} = \begin{pmatrix} 0 \\ 0 \\ 0 \end{pmatrix} \text{ otherwise.} \quad (\text{C.19})$$

Figure C.3 shows that the implementation of the formula yields the correct asymptotic behaviour. Before starting with the actual calculation let us discuss some properties of \vec{H}_{demag} . Due to the symmetry of the arrangement shown in Figure C.1, the demagnetisation field \vec{H}_{demag} possesses corresponding symmetry properties, which can be used to verify the correctness of our formula. Under reflection \vec{H}_{demag} behaves as follows:

$$\begin{pmatrix} H_x(-x) \\ H_y(-x) \\ H_z(-x) \end{pmatrix} = \begin{pmatrix} H_x(x) \\ -H_y(x) \\ -H_z(x) \end{pmatrix}, \quad \begin{pmatrix} H_x(-y) \\ H_y(-y) \\ H_z(-y) \end{pmatrix} = \begin{pmatrix} H_x(y) \\ -H_y(y) \\ H_z(y) \end{pmatrix}, \quad (\text{C.20})$$

$$\begin{pmatrix} H_x(-z) \\ H_y(-z) \\ H_z(-z) \end{pmatrix} = \begin{pmatrix} H_x(z) \\ H_y(z) \\ -H_z(z) \end{pmatrix}. \quad (\text{C.21})$$

To check whether the derived formula exhibits the expected symmetry (see equation (C.21)), we have calculated the demagnetisation field in a prism ($2l = 50 \text{ nm}$, $2w = 80 \text{ nm}$, $2h = 60 \text{ nm}$) along lines parallel to x , y , and z . A graphical representation of the geometry and the lines is given in Figure C.4. The saturation magnetisation is set to $M_S = \sigma = 1 \text{e6 A/m}$. The results are presented in the Figures C.5-C.7. First, we observe the expected symmetries.

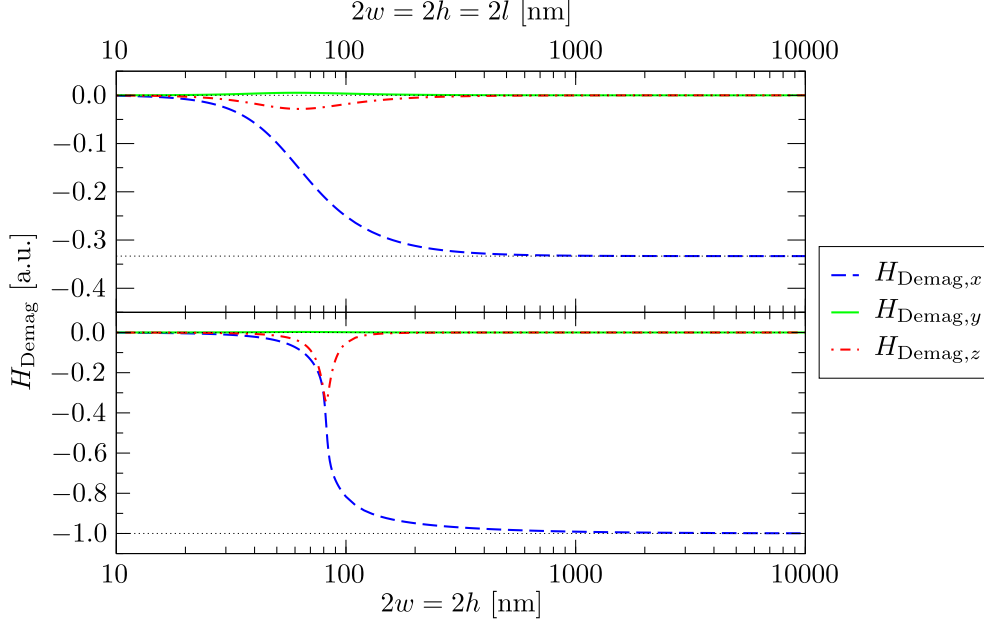


Figure C.3.: Test of the asymptotic behaviour of the formula for the demagnetisation field of a prism. In both cases the surface charge density has been set to $\sigma = -1$.

Top: demagnetisation field at the point $\vec{r} = (5, 10, -41)$ when subsequently increasing l , w and h . It converges towards the field of a sphere, which is indicated by the dotted line (see also equation (C.18)), thus displaying the correct asymptotic behaviour.

Bottom: w and h are subsequently increased while l is set to $2l = 10$. Computing the field at $\vec{r} = (4, 11, -41)$ yields the correct asymptotic behaviour (field of an infinitely extended capacitor indicated by the dotted line, see equation (C.19)). When choosing a point, which is not located between the plates of the capacitor, the computed field decreases towards 0 (not shown in figure), thus also complying with equation (C.19). So we observe a discontinuity of σ in the demagnetisation field, when crossing a plate of the infinitely extended capacitor. This is a well-known feature of basic electrostatics. In its general form it states that, when crossing a surface with a charge density σ , the component of the demagnetisation field, which is parallel to the surface normal, will feature a discontinuity of σ . In equation (C.15) this discontinuity is realised by the arc tangent term of the functions $\frac{\partial f_+}{\partial x}$ (or $\frac{\partial f_-}{\partial x}$).

C. Analytical expression for the stray field in a rectangular prism

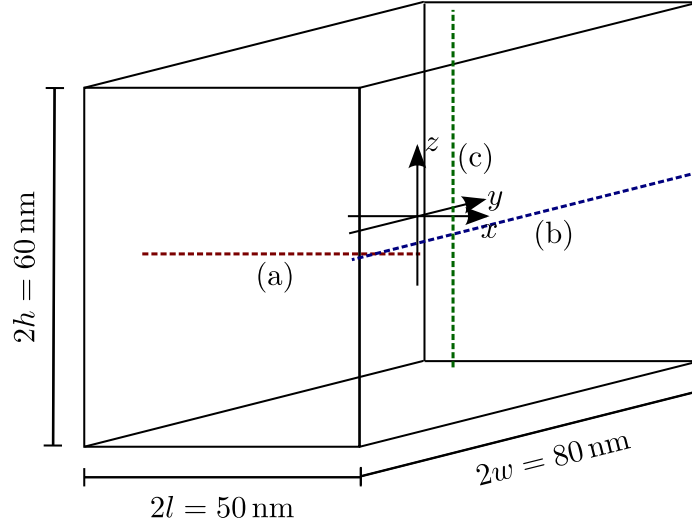


Figure C.4.: Drawing of a prism of the denoted dimensions. The coordinate origin is set to the centre of the prism. The demagnetisation field is computed along the lines (a) $y = -18.75$, $z = -3.75$, (b) $x = 23.75$, $z = -1.25$ and (c) $x = -13.75$, $y = 36.25$.

cube length [nm]	rms error [%]
5.0	0.2887
2.5	0.7900
1.25	0.3816
0.625	0.1891

Table C.1.: Deviation between the numerical (OOMMF) and analytical computation of the demagnetisation field of a homogeneously magnetised thin, square platelet. The platelet's edge length is 100 nm and its thickness is 5 nm. The resolution of the mesh has been gradually reduced.

More importantly, we find an excellent agreement with the numerical results, which have been obtained using the OOMMF code. For the geometry of Figure C.4 we find the rms error (see equation 3.5 in Chapter 3) between the numerical and the analytical result is 0.094 %. As a last test we want to compare analytical and numerical results for the thin, square platelets (see Figure 3.1 of Section 3.1.1). The considered square thin film has an edge length of 100 nm and a height of 5 nm. We successively reduce the resolution of the OOMMF mesh and compare the computed demagnetisation field with the corresponding value from the analytical expression. The results are summarised in table C.1. The deviation between the numerical and analytical result is below 0.1 % for all resolution. If we disregard the result for a resolution of 5nm, the deviation decreases with decreasing resolution. This indicates that the derived

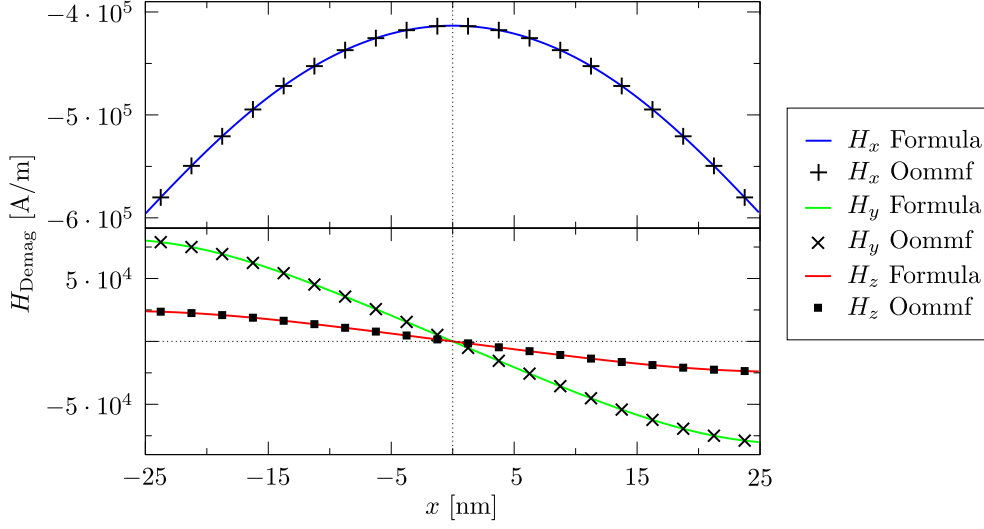


Figure C.5.: Computation of the demagnetisation field along the line $y = -18.75$, $z = -3.75$ within the geometry presented in Figure C.4 (line (a)). The results of the analytic formula are compared with the numerical results obtained with OOMMF.

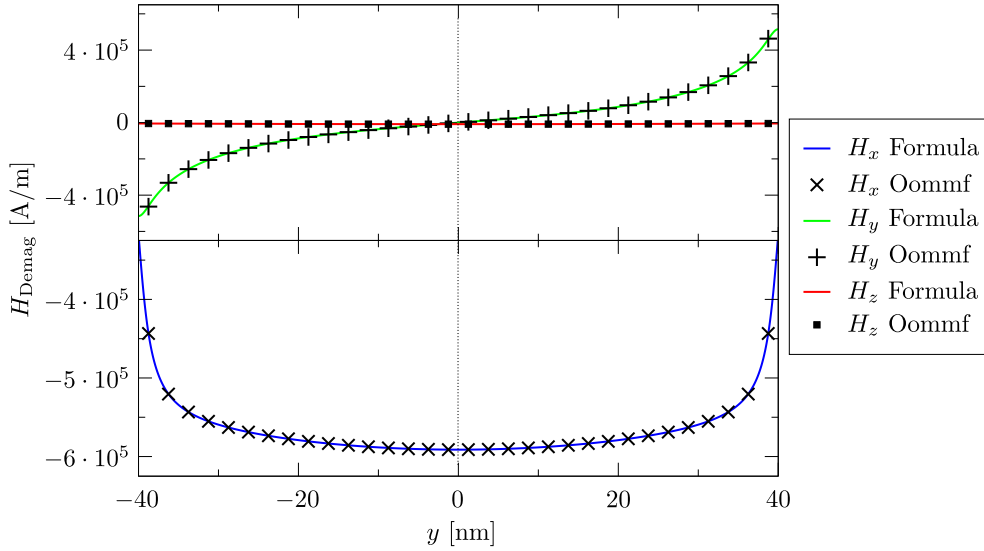


Figure C.6.: Computation of the demagnetisation field along the line $x = 23.75$, $z = -1.25$ within the geometry presented in Figure C.4 (line (b)). The results of the analytic formula are compared with the numerical results obtained with OOMMF.

C. Analytical expression for the stray field in a rectangular prism

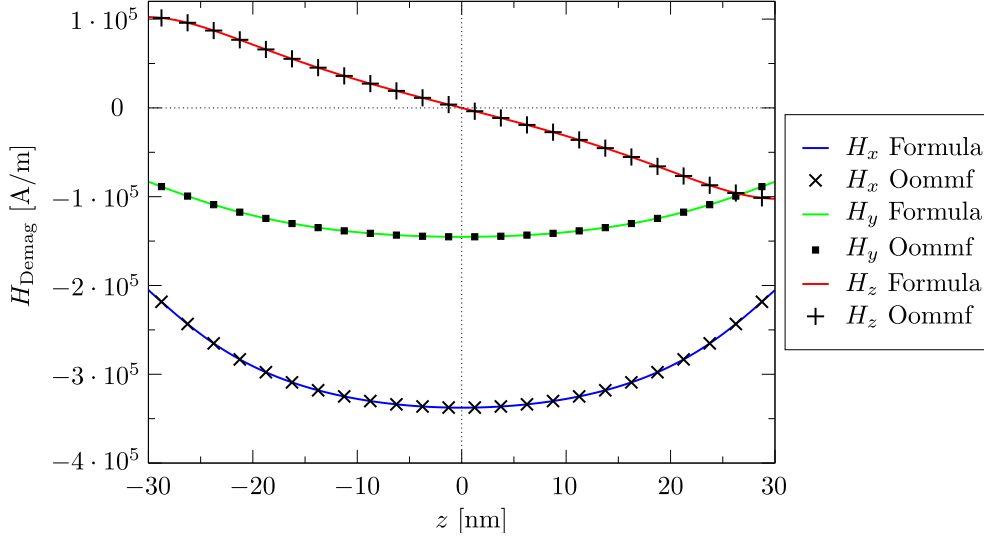


Figure C.7.: Computation of the demagnetisation field along the line $x = -13.75$, $y = 36.25$ within the geometry presented in Figure C.4 (line (c)). The results of the analytic formula are compared with the numerical results obtained with OOMMF.

analytical expressions correctly describes the diverging demagnetisation field in the vicinity of the edges of the charged surfaces. According to table C.1 the computation of the demagnetisation field with only one cube layer over the thickness of the platelet is surprisingly accurate. OOMMF computes local average values of the demagnetisation field, where the spatial average is taken over the cubes of the grid. The accuracy of the computation with one cube layer is probably due to the asymmetry of certain components of the demagnetisation field. Finally, we can conclude that the derived expression for the demagnetisation field is correct. Thus, it can be used to test corresponding finite element computations.

D. Accuracy of the finite element discretisation

Numerical tests are presented, which have been performed in order to ensure that the simulation results, presented in this work, are sufficiently accurate. The first section (D.1) will be mostly concerned with the accuracy of the finite element discretisation with respect to the investigation of the pyramidal shells (Section 4). The second section (D.2) investigates how the accuracy of the superconducting volume, which is computed in Chapter 5, depends on certain mesh and simulation parameters.

D.1. Tests on the accuracy of micromagnetic simulations on pyramidal shells.

In this section we want to analyse the impact of the mesh resolution on the accuracy of the employed finite-element, micromagnetic code. The emphasis of this study is put onto the pyramidal Nickel shells of Chapter 4. We also use the same set of micromagnetic parameters, so that for the exchange length $l_{\text{exch}} = 6.86 \text{ nm}$ holds, and create the meshes with the commercial software tool Fluent Gambit 2.4.6.. A typical distribution of edge lengths of these meshes is shown in Figure D.1 (left). We observe the occurrence of few tetrahedron edge lengths, which are about a factor 1.75 larger than the average value. An h-type refinement (see also [110, 136]) can be employed in order to remove edges, whose length exceeds a certain threshold h_{crit} . The idea of the method is to add an extra node half way between two adjacent nodes, whose distance is larger than h_{crit} , and split those tetrahedrons, which contain the initial two nodes. This splitting is demonstrated in Figure D.2. The effect of such an h-type refinement on the edge length distribution of a mesh is shown in Figure D.1 ($h_{\text{crit}} = 6.5 \text{ nm}$). After the refinement the maximal edge length is only 1.5 times larger than the average edge length. One should note that an h-type refinement leads to a higher computational complexity due to the addition of nodes. Choosing an appropriate h_{crit} is therefore a trade-off between the accuracy and the computational complexity. Especially for large meshes (\geq

D. Accuracy of the finite element discretisation

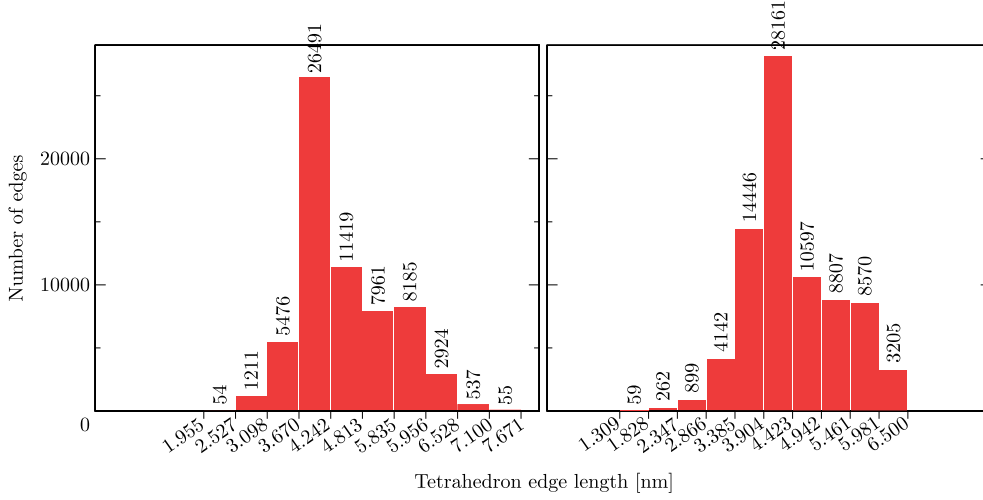


Figure D.1.: The distribution of the edge lengths within the mesh of a pyramidal shell ($a = 120$ nm, $t_{\text{rel}} = 80$ %) is given. The data has been obtained with Nmag's nmeshpp command [93]. It defines certain intervals (x -axis) and computes the number of edges, whose length lies within this interval. The meshes have been created with Fluent Gambit 2.4.6. Left: this mesh has been created by setting the Gambit meshing parameter to 4.0 nm. Right: this mesh has also been created with a Gambit meshing parameter of 4.0 nm. Afterwards an h-type refinement has been used in order to ensure that only edges with a length below or equal 6.5 nm occur, i.e. every edge initially greater than 6.5 nm is evenly split.

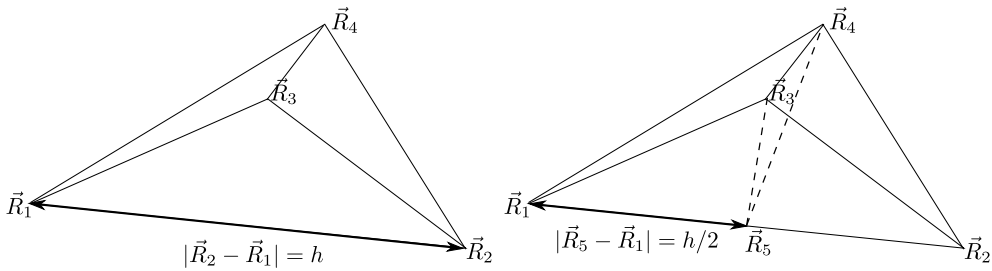


Figure D.2.: Illustration of the splitting of a tetrahedron due to an h-type refinement [110, 136]. The edge (length h) is split in the middle so that two edges with the length $h/2$ are created. Accordingly, two smaller tetrahedrons are created from the initial tetrahedron. Every tetrahedron, of which the initial edge is part of, has to be split in this way.

D.1. Tests on the accuracy of micromagnetic simulations on pyramidal shells.

meshing parameter	With refinement		No refinement	
	$\langle r \rangle$	r_{\max}	$\langle r \rangle$	r_{\max}
4.0	4.411	6.500	4.489	7.671
3.5	3.834	5.600	3.938	6.669
3.0	3.314	4.900	3.357	5.736
2.5	2.870	4.300	2.922	5.102
2.0	2.307	3.500	2.325	3.934
1.5	1.697	2.500	1.731	3.010
1.0	1.178	1.750	1.199	2.115

Table D.1.: The average and the maximal edge length within different tetrahedral meshes is given. The meshes describe a pyramidal shell ($a = 120$ nm, $t_{\text{rel}} = 80\%$) and have been created with different values for the Gambit meshing parameter. Furthermore, an h-type refinement has been applied in order to trim the longest edges within the distribution. The data of meshes, which have been created with and without such an a posteriori refinement, is shown.

average edge length $\langle r \rangle$	maximal edge length r_{\max}	number of layers
0.5474	0.9592	4
0.7618	1.394	3
1.166	2.000	2
1.791	2.500	1
2.052	2.943	1
2.442	3.487	1
2.796	3.984	1

Table D.2.: Table giving the average and maximal edge length of tetrahedral meshes with a varying mesh resolution. The geometry parameters of the modelled pyramidal shell are $a = 50$ nm and $t_{\text{rel}} = 10\%$. The third column of the table states the number of tetrahedron layers, which are counted with respect to the normal direction of the side faces.

D. Accuracy of the finite element discretisation

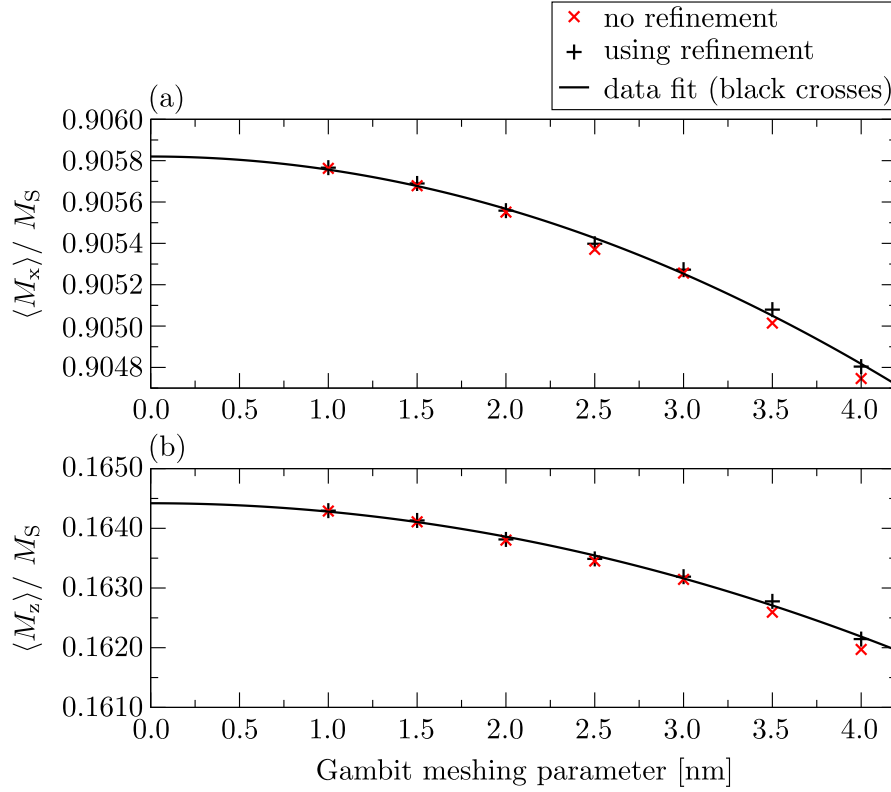


Figure D.3.: The magnetisation is relaxed within a pyramidal shell ($a = 120$ nm, $t_{\text{rel}} = 80$ %) for different mesh resolutions (see also table D.1), which are tagged by the used Gambit meshing parameter. (a) The magnetisation is homogeneously aligned in x -direction and then relaxed. The resulting configuration is a flower state (see Section 4.3.1 in Chapter 4) for all investigated mesh resolutions. The graph shows the x component of the spatially averaged magnetisation $\langle M_x \rangle$ as a function of the used Gambit meshing parameter. The fitted data curve is a third-order polynomial with the coefficients (equation (D.1)) $a_1 = 0.90582$, $a_2 = -6.3876 \cdot 10^{-5}$ and $a_3 = 2.9693 \cdot 10^{-7}$. The y and z component of the spatially averaged magnetisation are zero (not shown in graph). (b) The magnetisation is homogeneously aligned in z -direction and then relaxed. The resulting configuration is a vortex state (see Section 4.3.1 in Chapter 4) for all investigated mesh resolutions. The graph shows the z -component of the spatially averaged magnetisation $\langle M_z \rangle$ as a function of the used Gambit meshing parameter. The fitted data curve is a third-order polynomial with the coefficients (equation (D.1)) $a_1 = 0.16442$, $a_2 = -1.4074 \cdot 10^{-4}$ and $a_3 = 2.7328 \cdot 10^{-7}$. The x and y -component of the spatially averaged magnetisation are zero (not shown in graph).

D.1. Tests on the accuracy of micromagnetic simulations on pyramidal shells.

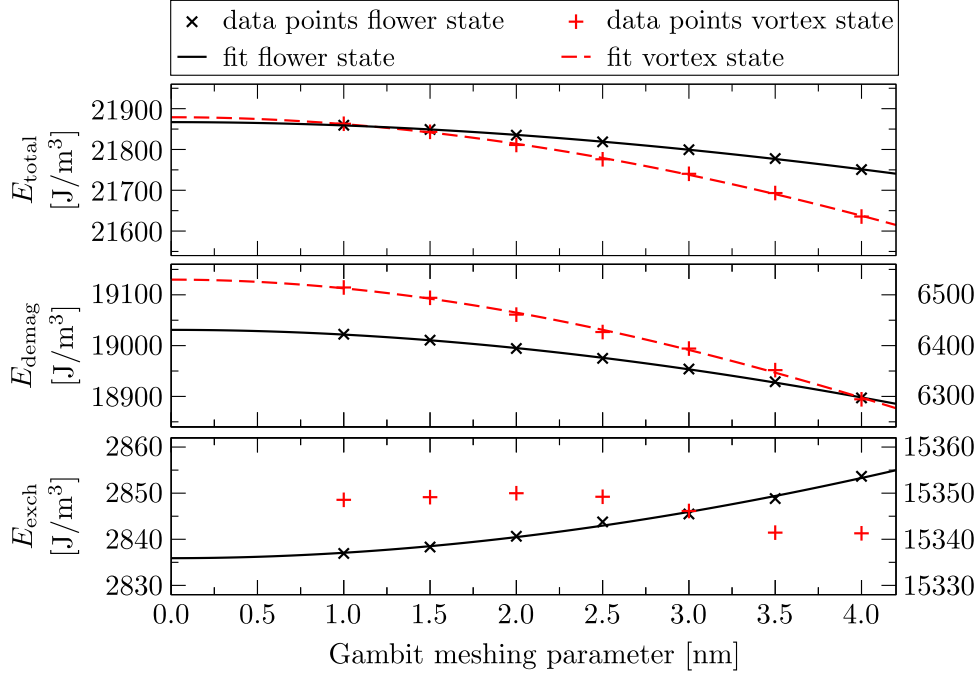


Figure D.4.: The magnetisation within a pyramidal shell with $a = 120$ nm and $t_{\text{rel}} = 80\%$ is relaxed to a flower state and a symmetric vortex state and the corresponding micromagnetic energy densities of the relaxed configurations E_{demag} , E_{exch} and E_{tot} are computed. This is done for different mesh resolutions (with and without an h-type refinement). The labels of the y-axis on the left refer to the energy densities of the flower state and the labels on the right to those of the vortex configuration. The data points have been fitted by a third-order polynomial (see equation D.1). The coefficients are $a_1 = 21867 \text{ Jm}^{-3}$, $a_2 = -8.3957 \text{ Jm}^{-3}\text{nm}^{-2}$ and $a_3 = 0.29196 \text{ Jm}^{-3}\text{nm}^{-3}$ for E_{tot} and the flower state, $a_1 = 21879 \text{ Jm}^{-3}$, $a_2 = -17.477 \text{ Jm}^{-3}\text{nm}^{-2}$ and $a_3 = 0.59664 \text{ Jm}^{-3}\text{nm}^{-3}$ for E_{tot} and the vortex state, $a_1 = 19031 \text{ Jm}^{-3}$, $a_2 = -9.5949 \text{ Jm}^{-3}\text{nm}^{-2}$ and $a_3 = 0.32002 \text{ Jm}^{-3}\text{nm}^{-3}$ for E_{demag} and the flower state, $a_1 = 6529.9 \text{ Jm}^{-3}$, $a_2 = -17.958 \text{ Jm}^{-3}\text{nm}^{-2}$ and $a_3 = 0.85900 \text{ Jm}^{-3}\text{nm}^{-3}$ for E_{demag} and the vortex state and $a_1 = 2835.6 \text{ Jm}^{-3}$, $a_2 = 1.1992 \text{ Jm}^{-3}\text{nm}^{-2}$ and $a_3 = -0.02806 \text{ Jm}^{-3}\text{nm}^{-3}$ for E_{exch} and the flower state. We have not performed a fit of the exchange energy of the vortex state as the data points do not suggest a certain functional dependence.

D. Accuracy of the finite element discretisation

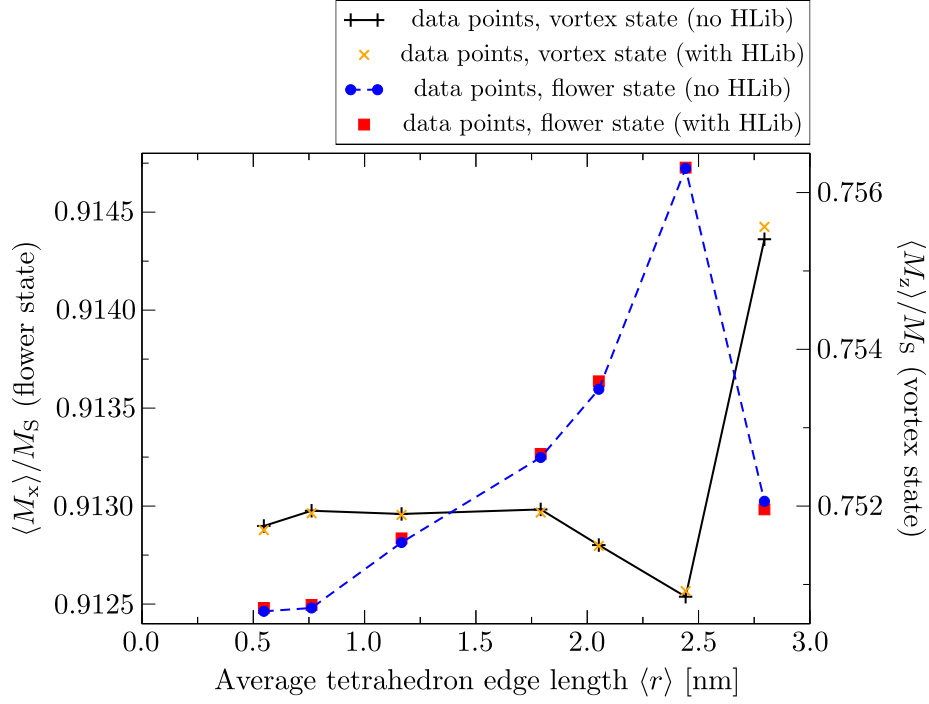


Figure D.5.: The major component of the spatially averaged magnetisation as a function of the used mesh resolution is given for the flower and the vortex state in a pyramidal shell with $a = 50$ nm and $t_{\text{rel}} = 10\%$. These states have been obtained by relaxing the magnetisation from an initial configuration aligned along the x and the z -direction, respectively. The quantity $\langle M_x \rangle / M_S$ on the left-hand y -axis corresponds to the flower state, $\langle M_z \rangle / M_S$ on the right-hand y -axis to the vortex state. Details on the used mesh resolutions are given in table D.2.

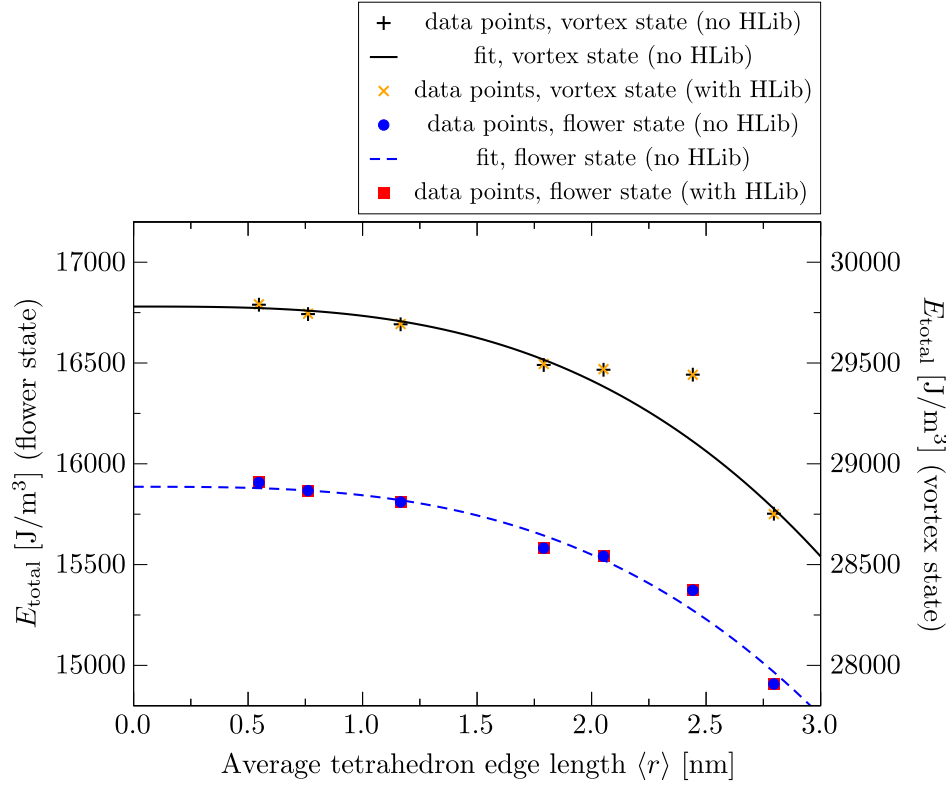


Figure D.6.: The total micromagnetic energy density of the flower and the vortex state within a pyramidal shell with $a = 50$ nm and $t_{\text{rel}} = 10\%$ is given as a function of the mesh resolution. As indicated, the energy scale of the y -axis on the left refers to the energy of the flower state and the one on the right to the vortex state. The fits have been made with respect to the data points which have been obtained without the use of HLib. The fit parameters are as follows: $a_1 = 15886 \text{ J m}^{-3}$, $a_2 = -2.9902 \cdot 10^{-3} \text{ J nm}^{-2} \text{ m}^{-3}$, $a_3 = -42.057 \text{ J nm}^{-3} \text{ m}^{-3}$ for the flower state and $a_1 = 29780 \text{ J m}^{-3}$, $a_2 = -1.1140 \cdot 10^{-3} \text{ J nm}^{-2} \text{ m}^{-3}$, $a_3 = -45.894 \text{ J nm}^{-3} \text{ m}^{-3}$ for the vortex state.

D. Accuracy of the finite element discretisation

200000 surface nodes) it seems pertinent to split no more than the 2 % of the total number of edges.

For our first numerical test we consider a pyramidal shell with $a = 120$ nm and $t_{\text{rel}} = 80$ %. Table D.1 shows the average and maximal edge length of meshes (for a pyramidal shell with $a = 120$ nm and $t_{\text{rel}} = 80$ %), which have been created with different values for the Gambit meshing parameter. Each mesh is created with and without an a posteriori h-type refinement and satisfies the condition (see for example [46, 45, 99]) that for each edge length h $h \lesssim l_{\text{exch}}$ should hold. We choose two homogeneous initial configurations, namely $\vec{M}(\vec{r}) = (M_S, 0, 0)$ and $\vec{M}(\vec{r}) = (0, 0, M_S)$ (see Figure 4.2 in Section 4.2.1 for the definition of the cartesian directions), in order to relax (Gilbert damping constant $\alpha = 1$) the magnetic system to a stable state. This is done for all meshes of table D.1. We find that for each mesh we obtain the same final state, i.e. a flower state from the initial state aligned along the x -direction and a vortex state from the initial state aligned along the z -direction. Figure D.3 shows the spatially averaged magnetisation $\langle \vec{M} \rangle$ obtained for the flower and the vortex state as a function of the used Gambit meshing parameter. We only show the x -component $\langle M_x \rangle$ for the flower state and the z -component $\langle M_z \rangle$ for the vortex state. The other two cartesian components are 0 due to the symmetry of these states. Both depicted magnetisation components increase with an increasing mesh resolution (decreasing meshing parameter). Furthermore, we find that the refinement procedure only has a significant impact on the accuracy of the computation for a relatively coarse resolution (Gambit meshing parameter $\gtrsim 3.0$), i.e. when the maximal edge length is in the range of the exchange length and higher. To estimate the error we have extrapolated the illustrated magnetisation components using a polynome of the form:

$$f(x) = a_1 \pm |a_2| x^2 + a_3 x^3. \quad (\text{D.1})$$

The sign of the coefficient $|a_2|$ is chosen such that it corresponds to the sign of the coefficient a_3 . Thus, we avoid the occurrence of a minimum/maximum for small values of x , which is not suggested by the data sets. Extrapolating the Gambit meshing parameter to zero we obtain $\langle M_x \rangle = 0.90582$ for the flower state and $\langle M_z \rangle = 0.16442$ for the vortex state. The simulations on the pyramidal structures of Chapter 4 have been performed with such mesh resolutions that all edge lengths are smaller than $0.035 \cdot a = 4.2$ nm, which, for the given example, corresponds to a meshing parameter between 2.0 and 2.5. When using a mesh parameter of 2.0 we find $\langle M_x \rangle = 0.90555$ and $\langle M_z \rangle = 0.16380$, corresponding to a deviation from the extrapolated value of -0.030 % and -0.064 %, respectively. Figure D.4 shows the micromagnetic energy densities of these states as a function of the Gambit mesh parameter. We find that the

D.1. Tests on the accuracy of micromagnetic simulations on pyramidal shells.

demagnetisation energy density shows a significant dependence on the used mesh resolution, which, in its extent, is also different for the flower and the vortex state. As a result, the vortex state has a lower total energy density than the flower state for a Gambit mesh parameter $\gtrsim 1.3$, but a higher total energy density for a Gambit mesh parameter below 1.3. Thus, with a Gambit mesh parameter between 2.0 and 2.5 we do not get the correct result and the computed critical edge length $a_{\text{trans}} = 119.862 \text{ nm}$ for the phase transition between the flower and the vortex state is slightly underestimated. To estimate the error, we have calculated the total micromagnetic energy density of the flower state and the vortex state in a pyramidal shell with $a = 121 \text{ nm}$ and $t_{\text{rel}} = 80 \%$ as a function of the Gambit mesh parameter and extrapolated the obtained data curves to a mesh parameter of 0 using equation (D.1). Analogously to Figure D.4 we then obtain $E_{\text{tot,flower}} = a_1 = 21818 \text{ J/m}$ for the flower state and $E_{\text{tot,vortex}} = a_1 = 21625 \text{ J/m}$ for the vortex state, i.e. the vortex state has a lower micromagnetic energy. Linearly interpolating between the energies at $a = 120 \text{ nm}$ and 121 nm , we find $a_{\text{trans}} = 120.059$. Thus, the estimated error of our initial result is $\Delta a < 0.2 \text{ nm}$. Such a small numerical error appears to be acceptable, since the alternative approach, i.e. to compute the energies at different mesh resolutions and extrapolate to a infinitely fine resolution, leads to a significant increase in the work load, especially with respect to the computation of the phase diagramme of figure 4.9 (see Section 4.3.1). The relatively poor convergence of the demagnetisation energy density seems to be due to the occurrence of diverging demagnetisation fields in the vicinity of sharp edges and corners. This effect is discussed in Chapter 3 and Appendix C for cuboidal geometries and may well be the reason for quantitative differences in the results obtained with finite-difference and finite-element based micromagnetic simulations (see Standard Problem No. 3, [104]). In Figure D.5 we investigate the dependence of the major magnetisation component of the flower and the vortex state on the mesh resolution for a pyramidal shell with $a = 50 \text{ nm}$ and $t_{\text{rel}} = 10 \%$. Here, the mesh resolution is expressed in terms of the average edge length. The corresponding maximal edge length and the number of tetrahedron layers, which are counted with respect to the normal direction of the side faces, are given in table D.2. Furthermore, we run simulations with and without the approximation of a dense boundary element matrix in order to assess the corresponding error. We find that the error introduced by the use of a hierarchical matrix is negligible compared to the error due to the finite element discretisation on an unstructured mesh. The latter error shows fluctuations, which, in the regime of the tested mesh resolutions, do not exceed 0.5% . In Figure D.6 the corresponding micromagnetic total energy density is illustrated as a function of the average tetrahedron edge length $\langle r \rangle$. We see that the micromagnetic energy density exhibits a very strong dependence on

D. Accuracy of the finite element discretisation

the mesh resolution, indicated by the variation of $\sim 1000 \text{ [J/m}^3\text{]}$ within the investigated range. In order to get a decent accuracy, we use a discretisation, which corresponds to three tetrahedron layers over the shell thickness. In Figure D.6 this is equivalent to the data points at $\langle r \rangle = 0.7618 \text{ nm}$ (see also table D.2), i.e. $\langle r \rangle$ is smaller than half the shell thickness.

D.2. Numerical tests on the computation of the superconducting volume

In Sub-section 5.2.1 we compute the superconducting fraction within the core of a triangular platelet-shaped Ni/Pb core-shell structure. This is done by relaxing the micromagnetic configuration of the Nickel shell at a certain pinning field (e.g. 1000 Oe), which is applied parallel to the normal of the structure's triangular base. For these micromagnetic simulations the saturation magnetisation is set to $M_S = 510000 \text{ A/m}$, the exchange constant to $A = 7.2 \cdot 10^{-12} \text{ J/m}$ and no cubic anisotropy is assumed. The stray field calculation is optimised using hierarchical matrices. Pinning the magnetisation and, thus, the resulting stray field, the externally applied field is systematically varied (also along the normal of the structure's base) in order to compute that volume within the core, where $|\vec{H}_{\text{ext}} + \vec{H}_{\text{demag}}| < H_{\text{crit}}^{\text{Pb}}(T = 4.2 \text{ K}) = 530 \text{ Oe}$ applies. As a result one obtains a data curve showing the superconducting fraction within the core as a function of the external field strength. These computations are performed numerically on a tetrahedral mesh within the core region. For details on this approach the reader is referred to Sub-section 5.2.1. Here we want to investigate, how its accuracy depends on the mesh resolution of the mesh within the core region. Furthermore, although the core region is not ferromagnetic, one has to define a small saturation magnetisation M_S^{Vac} at the nodes of the core mesh in order to avoid zero divisions. Therefore, the second aim is to investigate how small M_S^{Vac} has to be chosen, so that it does not influence the stray field computation.

Figure D.7 shows the superconducting fraction within the Pb core as a function of the external field for different mesh resolutions. We find that the computed data curve is relatively insensitive with respect to the mesh resolution, especially for a Gambit mesh parameters $\leq 10 \text{ nm}$. As the investigated structures of Section 5.1 are about a factor 2 larger than that of Figure D.7, we use a Gambit mesh parameter of 20 nm in Sub-section 5.2.1. The reasoning behind this choice is as follows: like in Sub-section 5.2.1 (see Figure 5.6 and 5.7) the pinned micromagnetic configuration of Figure D.7 is a vortex state. Due to its scale-invariance, the stray field will approximately be the same in both

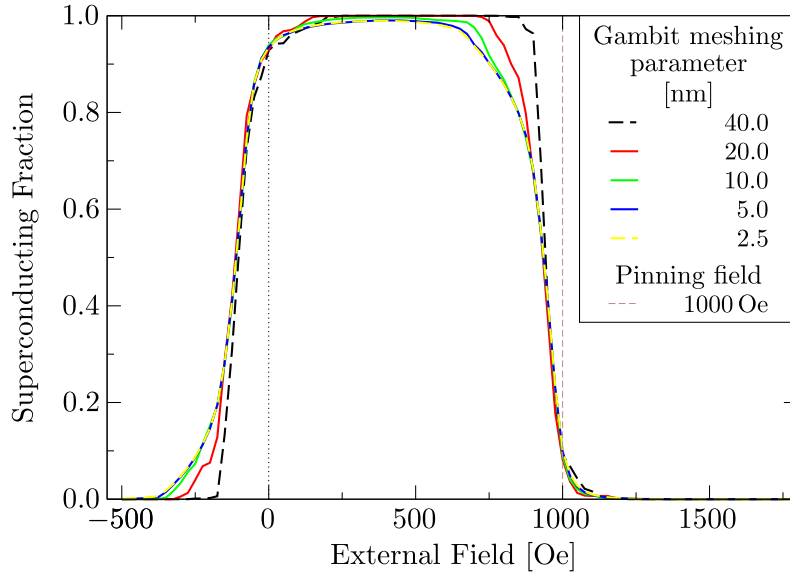


Figure D.7.: Test of the impact of the core mesh resolution on the computation of the superconducting fraction within the core of a triangular platelet-shaped Pb/Ni core-shell structure. The external field has been applied parallel to normal of the triangular base. The magnetisation has been pinned at a field strength of 1000 Oe. The triangular core-shell structure has a side length of 252 nm, a height of 115 nm and a shell thickness of 10 nm (see Figure 5.5(b) of Section 5.2) The presented data corresponds to a temperature of $T = 4.2$ K and therefore to a critical field $H_{\text{crit}}^{\text{Pb}} = 530$ Oe.

D. Accuracy of the finite element discretisation

systems. As we only want to resolve the stray field with our core mesh, we can just scale the mesh resolution in the same way as the system is scaled. Thus, choosing a Gambit mesh parameter of 10 nm for our test system results in a Gambit mesh parameter of 20 nm for the systems of Section 5.2.1.

We now want to investigate how M_S^{Vac} has to be chosen so that its influence on the stray field calculation within the core region is negligible. Our test system is a triangular platelet-shaped Pb/Ni core-shell structure with a side length of $a = 252$ nm, a height of 115 nm and a shell thickness of $t = 10$ nm. We relax the system from a homogeneous alignment of the magnetisation along the z -direction (parallel to the normal of the structure's triangular base) at $\vec{H}_{\text{ext}} = 0$ Oe. This simulation is repeated, varying M_S^{Vac} by powers of ten between 1000 A/m and 10^{-5} A/m. Each time, the rms error of the resulting stray field within the core region is computed with respect to the result obtained with $M_S^{\text{Vac}} = 10^{-7}$ A/m:

$$\delta_{\text{rms}} = \sqrt{\frac{\sum_{i=1}^N \sum_{j=1}^3 (H_{\text{demag},j}^i(M_S) - H_{\text{demag},j}^i(10^{-7} \text{ A/m}))^2}{\left(\sum_{i=1}^N \sum_{j=1}^3 H_{\text{demag},j}^i(10^{-7} \text{ A/m})^2 \right)}}.$$

Here, the index i runs of all N nodes of the mesh within the core region and the index j over the three cartesian coordinates. The results are given in table D.3. We find that a saturation magnetisation of $M_S^{\text{Vac}} < 10$ A/m virtually does not have an effect on the stray field computation within the core.

D.2. Numerical tests on the computation of the superconducting volume

M_S^{Vac}	rms deviation [%]
1000	3.11
100	0.320
10	0.0320
1	0.00339
0.1	0.000731
0.01	0.000706
0.001	0.000731
0.0001	0.000684
0.00001	0.000347

Table D.3.: Table showing the rms error of the stray field computation within the core region of a triangular-shaped Pb/Ni core-shell structure, which has been computed from a vortex state at $|\vec{H}_{\text{ext}}| = 0$ (see also Figure 5.6 in Sub-section 5.2.1) using different values of M_S^{Vac} . As a reference, simulation results, which have been obtained with $M_S^{\text{Vac}} = 10^{-7}$ A/m, are used. The test system is a triangular platelet-shaped Ni/Pb core-shell structure with a side length of $a = 252$ nm, a height of $h = 120$ nm and a thickness of $t = 10$ nm.

Bibliography

- [1] A. Müller, S. E. C. Dale, M. A. Engbarth, S. J. Bending, L. M. Peter, A. Knittel, and H. Fangohr. Field-tuneable diamagnetism in ferromagnetic-superconducting core-shell structures. *Advanced Functional Materials*, 21(10):1874–1880, 2011.
- [2] G. E. Moore. Cramming more components onto Integrated circuits, reprinted from electronics, volume 38, number 8, april 19, 1965, pp.114 ff. *Solid-State Circuits Newsletter, IEEE*, 20(3):33 –35, sept. 2006.
- [3] R. R. Schaller. Moore’s law: past, present and future. *Spectrum, IEEE*, 34(6):52 –59, jun 1997.
- [4] R. M. Penner. Mesoscopic metal particles and wires by electrodeposition. *The Journal of Physical Chemistry B*, 106(13):3339–3353, 2002.
- [5] S. Ripka and P. Ripka. *Modern Sensors Handbook, chapter 10: magnetic sensors*. Iste Publishing Company, 2007.
- [6] M. N. Baibich, J. M. Broto, A. Fert, F. Nguyen van Dau, F. Petroff, P. Etienne, G. Creuzet, A. Friederich, and J. Chazelas. Giant magnetoresistance of (001)Fe/(001)Cr magnetic superlattices. *Phys. Rev. Lett.*, 61:2472–2475, 1988.
- [7] G. Binash, P. Grünberg, F. Saurenbach, and W. Zinn. Enhanced magnetoresistance in layered magnetic structures with antiferromagnetic interlayer exchange. *Phys. Rev. B*, 39:4828, 1989.
- [8] P. Grünberg. From spinwaves to giant magnetoresistance (GMR) and beyond. http://nobelprize.org/nobel_prizes/physics/laureates/2007/grunberg-lecture.html, 2007. Nobel lecture.
- [9] S. Tehrani, B. Engel, J.M. Slaughter, E. Chen, M. DeHerrera, M. Durlam, P. Naji, R. Whig, J. Janesky, and J. Calder. Recent developments in magnetic tunnel junction MRAM. *Magnetics, IEEE Transactions on*, 36(5):2752 –2757, sep 2000.
- [10] S. S. P. Parkin, M. Hayashi, and L. Thomas. Magnetic domain-wall racetrack memory. *Science*, 320(5873):190–194, 2008.

Bibliography

- [11] S. Bohlens, B. Krüger, A. Drews, M. Bolte, G. Meier, and D. Pfannkuche. Current controlled random-access memory based on magnetic vortex handedness. *Applied Physics Lett.*, 93(14):142508, 2008.
- [12] S. D. Bader. Colloquium: Opportunities in nanomagnetism. *Rev. Mod. Phys.*, 78(1):1–15, Jan 2006.
- [13] R. P. Cowburn and M. E. Welland. Room temperature magnetic quantum cellular automata. *Science*, 287(5457):1466–1468, 2000.
- [14] R. P. Cowburn. Where have all the transistors gone? *Science*, 311(5758):183–184, 2006.
- [15] C. A. Ross. Patterned magnetic recording media. *Annual Review of Materials Research*, 31:203–235, 2001.
- [16] R. P. Cowburn. Property variation with shape in magnetic nanoelements. *Journal of Physics D: Applied Physics*, 33:R1–R16, 2000.
- [17] J. Fassbender and J. McCord. Magnetic patterning by means of ion irradiation and implantation. *Journal of Magnetism and Magnetic Materials*, 320(3-4):579 – 596, 2008.
- [18] J. L. Martín, J. Nogués, K. Liu, J. L. Vicent, and I. K. Schuller. Ordered magnetic nanostructures: fabrication and properties. *Journal of Magnetism and Magnetic Materials*, 256(1-3):449–501, 2003.
- [19] V. F. Puentes, K. M. Krishnan, and A. P. Alivisatos. Colloidal nanocrystal shape and size control: The case of cobalt. *Science*, 291(5511):2115–2117, 2001.
- [20] N. Shukla, C. Liu, and A. G. Roy. Oriented self-assembly of cubic FePt nanoparticles. *Materials Letters*, 60(8):995 – 998, 2006.
- [21] D. Ung, L. D. Tung, G. Caruntu, D. Delaportas, I. Alexandrou, I. A. Prior, and N. T. K. Thanh. Variant shape growth of nanoparticles of metallic Fe-Pt, Fe-Pd and Fe-Pt-Pd alloys. *CrystEngComm*, 11:1309–1316, March 2009.
- [22] Z.-L. Xiao, C. Y. Han, W.-K. Kwok, H.-H. Wang, U. Welp, J. Wang, and G. W. Crabtree. Tuning the architecture of mesostructures by electrodeposition. *Journal of the American Chemical Society*, 126(8):2316–2317, 2004.
- [23] A. Müller, S. E. C. Dale, M. A. Engbarth, S. J. Bending, and L. M. Peter. Shape-controlled electrodeposition of tin crystals from Sn(ii)-fluoroborate solutions. *CrystEngComm*, 12:2135–2138, 2010.

- [24] W. F. Brown, Jr. *Micromagnetics*. Wiley Interscience, New York, 1963.
- [25] J. Fidler and T. Schrefl. Micromagnetic modelling - the current state of the art. *Journal of Physics D: Applied Physics*, 33:R135–R156, 2000.
- [26] M. J. Donahue and D. G. Porter. *OOMMF User's Guide, Version 1.0*. National Institute of Standards and Technology, Gaithersburg, MD, September 1999. Interagency Report NISTIR 6376.
- [27] C. J. García-Cervera, Z. Gimbutas, and Weinan E. Accurate numerical methods for micromagnetics simulations with general geometries. *Journal of Computational Physics*, 184(1):37 – 52, 2003.
- [28] M. J. Donahue and R. D. McMichael. Micromagnetics on curved geometries using rectangular cells: Error correction and analysis. *IEEE Transactions on Magnetics*, 43(6):2878–2880, JUN 2007. 10th Joint Magnetism and Magnetic Materials Conference/International Magnetism Conference, Baltimore, MD, JAN 07-11, 2007.
- [29] A. Witt, K. Fabian, and U. Bleil. Three-dimensional micromagnetic calculations for naturally shaped magnetite: Octahedra and magnetosomes. *Earth and Planetary Science Letters*, 233(3-4):311 – 324, 2005.
- [30] T. Fischbacher, M. Franchin, G. Bordignon, and H. Fangohr. A systematic approach to multiphysics extensions of finite-element based micromagnetic simulations: Nmag. *IEEE Transactions on Magnetics*, 43(6):2896–2898, 2007. <http://nmag.soton.ac.uk>.
- [31] L. Grasedyck and S. Börm. HLib - hierarchical matrices. <http://www.hlib.org>.
- [32] R. P. Cowburn and M. E. Welland. Micromagnetics of the single-domain state of square ferromagnetic nanostructures. *Phys. Rev. B*, 58(14):9217–9226, 1998.
- [33] D. Goll, G. Schütz, and H. Kronmüller. Critical thickness for high-remanent single-domain configurations in square ferromagnetic thin platelets. *Phys. Rev. B*, 67(9):0944141–0944148, 2003.
- [34] H. Kronmüller, D. Goll, R. Hertel, and G. Schütz. Critical thicknesses of domain formations in cubic particles and thin films. *Physica B: Condensed Matter*, 343(1-4):229 – 235, 2004. Proceedings of the Fourth Intional Conference on Hysteresis and Micromagnetic Modeling.
- [35] M.-F. Lai and C.-N. Liao. Size dependence of c and s states in circular and square permalloy dots. *Journal of Applied Physics*, 103(7):07E737, 2008.

Bibliography

- [36] R. P. Cowburn, D. K. Koltsov, A. O. Adeyeye, M. E. Welland, and D. M. Tricker. Single-domain circular nanomagnets. *Phys. Rev. Lett*, 83(5):1042–1045, August 1999.
- [37] J. K. Ha, R. Hertel, and J. Kirschner. Configurational stability and magnetization processes in submicron permalloy disks. *Phys. Rev. B*, 67:064418, 2003.
- [38] M. E. Schabes and H. N. Bertram. Magnetisation processes in ferromagnetic cubes. *Journal of Applied Physics*, 64(3):1347–1357, 1988.
- [39] W. Rave, K. Fabian, and A. Hubert. Magnetic states of small cubic particles with uniaxial anisotropy. *Journal of Magnetism and Magnetic Materials*, 190(3):332 – 348, 1998.
- [40] C. A. Ross, M. Farhoud, M. Hwang, H. I. Smith, M. Redjda, and F. B. Humphrey. Micromagnetic behaviour of conical ferromagnetic particles. *Journal of Applied Physics*, 89(2):1310–1319, 2001.
- [41] Richard P. Boardman, Hans Fangohr, Matthew J. Fairman, Jrgen Zimmermann, Simon J. Cox, Alexander A. Zhukov, and Peter A.J. de Groot. Micromagnetic modelling of ferromagnetic cones. *Journal of Magnetism and Magnetic Materials*, 312(1):234 – 238, 2007.
- [42] R. P. Boardman, H. Fangohr, A. V. Goncharov, A. A. Zhukov, P. A. J. de Groot, and S. J. Cox. Micromagnetic simulation of ferromagnetic part-spherical particles. *Journal of Applied Physics*, 95(11):7037–7039, 2004.
- [43] R. P. Boardman, J. Zimmermann, H. Fangohr, A. A. Zhukov, and P. A. J. de Groot. Micromagnetic simulation studies of ferromagnetic part-spheres. *Journal of Applied Physics*, 97(10):10E305, 2005.
- [44] D. R. Fredkin and T. R. Koehler. Numerical micromagnetics: prolate spheroids. *Magnetics, IEEE Transactions on*, 25(5):3473 –3475, sep 1989.
- [45] W. Williams, A. R. Muxworthy, and G. A. Paterson. Configurational anisotropy in single-domain and pseudosingle-domain grains of magnetite. *J. Geophys. Res.*, 111(B12S13), 2006.
- [46] R. Hertel, O. Fruchart, S. Cherifi, P.-O. Jubert, S. Heun, A. Locatelli, and J. Kirschner. Three-dimensional magnetic-flux-closure patterns in mesoscopic Fe islands. *Phys. Rev. B*, 72(21):214409, Dec 2005.
- [47] D. Goll, A. E. Berkowitz, and H. N. Bertram. Critical sizes for ferro-

- magnetic spherical hollow nanoparticles. *Phys. Rev. B*, 70(18):184432, Nov 2004.
- [48] C. J. García-Cervera and A. M. Roma. Adaptive mesh refinement for micromagnetics simulations. *Magnetics, IEEE Transactions on*, 42(6):1648–1654, june 2006.
- [49] R. C. O’Handley. *Modern Magnetic Materials: Principles and Applications*. John Wiley and Sons, Inc., 1999.
- [50] H. Kronmüller and M. Fähnle. *Micromagnetism and the Microstructure of Ferromagnetic Solids*. Cambridge University Press, 1st edition, 2003.
- [51] W. Scholz, J. Fidler, T. Schrefl, D. Süß, R. Dittrich, H. Forster, and V. Tsiantos. Scalable parallel micromagnetic solvers for magnetic nanostructures. *Computational Materials Science*, 28:366–383, 2003.
- [52] L. D. Landau and E. M. Lifshitz. On the theory of the dispersion of magnetic permeability in ferromagnetic bodies. *Physikalische Zeitschrift der Sowjetunion*, 8(2):153–169, 1935.
- [53] M. D. Stiles, S. V. Halilov, R. A. Hyman, and A. Zangwill. Spin-orbit-orbit interaction and magnetocrystalline anisotropy. *Phys. Rev. B*, 64(10):104430, Aug 2001.
- [54] T. Burkert, O. Eriksson, P. James, S. I. Simak, B. Johansson, and L. Nordström. Calculation of uniaxial magnetic anisotropy energy of tetragonal and trigonal Fe, Co, and Ni. *Phys. Rev. B*, 69(10):104426, Mar 2004.
- [55] J. D. Jackson. *Classical Electrodynamics*. Wiley, 3 edition, 1999.
- [56] M. d’Aquino. *Nonlinear magnetization dynamics in thin-films and nanoparticles*. PhD thesis, Facoltà di Ingegneria, Università degli studi di Napoli ”Federico II”, 2004.
- [57] T. L. Gilbert. A phenomenological theory of damping in ferromagnetic materials. *Magnetics, IEEE Transactions on*, 40(6):3443 – 3449, nov. 2004.
- [58] J. Mallinson. On damped gyromagnetic precession. *Magnetics, IEEE Transactions on*, 23(4):2003 – 2004, jul 1987.
- [59] A. W. Spargo. *Finite element analysis of magnetisation reversal in granular thin films*. PhD thesis, School of Informatics, University of Wales, Bangor, 2002.

- [60] W. Williams and D.J. Dunlop. Three-dimensional micromagnetic modelling of ferromagnetic domain structure. *Nature*, 337:634–637, 1989.
- [61] P. H. W. Ridley. *Finite element simulation of the micromagnetic behaviour of nanoelements*. PhD thesis, School of Informatics, University of Wales, Bangor, 2000.
- [62] W. Scholz. *Scalable parallel micromagnetic solvers for magnetic nanostructures*. PhD thesis, Fakultät für Naturwissenschaften und Informatik, Technische Universität Wien, 2003.
- [63] D. Suess, V. Tsiantos, T. Schrefl, J. Fidler, W. Scholz, H. Forster, R. Dittrich, and J. J. Miles. Time resolved micromagnetics using a preconditioned time integration method. *Journal of Magnetism and Magnetic Materials*, 248(2):298 – 311, 2002.
- [64] Bo Yang and D. R. Fredkin. Dynamical micromagnetics by the finite element method. *Magnetics, IEEE Transactions on*, 34(6):3842 –3852, November 1998.
- [65] Qiushi Chen and A. Konrad. A review of finite element open boundary techniques for static and quasi-static electromagnetic field problems. *Magnetics, IEEE Transactions on*, 33(1):663 –676, jan 1997.
- [66] D. R. Fredkin and T. R. Koehler. Hybrid method for computing demagnetizing fields. *IEEE Trans. Magn.*, 26:415–417, 1990.
- [67] A. van Herk. *Three-dimensional analysis of magnetic fields in recording head configurations*. PhD thesis, Tech. Hogeschool, Delft, October 1980.
- [68] D. A. Lindholm. Three-dimensional magnetostatic fields from point-matched integral equations with linearly varying scalar sources. *IEEE Trans. Magn.*, 20:2025–2032, 1984.
- [69] A. Van Oosterom and J. Strackee. The solid angle of a plane triangle. *Biomedical Engineering, IEEE Transactions on*, BME-30(2):125 –126, 1983.
- [70] H. Forster, T. Schrefl, R. Dittrich, W. Scholz, and J. Fidler. Fast boundary methods for magnetostatic interactions in micromagnetics. *Magnetics, IEEE Transactions on*, 39(5):2513 – 2515, sept. 2003.
- [71] T. Schrefl, G. Hrkac, S. Bance, D. Suess, O. Ertl, and J. Fidler. Numerical methods in micromagnetics (Finite Element Method). *Handbook of magnetism and advanced magnetic materials*, 2007.
- [72] S. Börm, L. Grasedyck, and W. Hackbusch. Hierarchical matrices. Technical report, Max-Planck-Institut fuer Math-

- ematik in den Naturwissenschaften, Leipzig, June 2006.
<http://www.mis.mpg.de/publications/other-series/ln/lecturenote-2103.html>.
- [73] S. Börm, L. Grasedyck, and W. Hackbusch. Introduction to hierarchical matrices with applications. *Engineering Analysis with Boundary Elements*, 27(5):405 – 422, 2003. Large scale problems using BEM.
 - [74] W. Hackbusch. A sparse matrix arithmetic based on \mathcal{H} -matrices. Part I: Introduction to \mathcal{H} -matrices. *Computing*, 62(2):89–108, 1999.
 - [75] W. Hackbusch and B. N. Khoromskij. A sparse \mathcal{H} -matrix arithmetic. Part II: Application to multi-dimensional problems. *Computing*, 64:21–47, 2000.
 - [76] I. Benedetti, M.H. Aliabadi, and G. Davì. A fast 3D dual boundary element method based on hierarchical matrices. *International Journal of Solids and Structures*, 45(7-8):2355 – 2376, 2008.
 - [77] S. Kurz, O. Rain, and S. Rjasanow. The adaptive cross-approximation technique for the 3D boundary-element method. *Magnetics, IEEE Transactions on*, 38(2):421 –424, mar 2002.
 - [78] J. Ostrowski, Z. Andjelic, M. Bebendorf, B. Cranganu-Cretu, and J. Smajic. Fast BEM-solution of Laplace problems with \mathcal{H} -matrices and aca. *Magnetics, IEEE Transactions on*, 42(4):627 –630, april 2006.
 - [79] Kezhong Zhao, M.N. Vouvakis, and Jin-Fa Lee. The adaptive cross approximation algorithm for accelerated method of moments computations of EMC problems. *Electromagnetic Compatibility, IEEE Transactions on*, 47(4):763 – 773, nov. 2005.
 - [80] T. Schrefl, M.E. Schabes, D. Suess, O. Ertl, M. Kirschner, F. Dorfbauer, G. Hrkac, and J. Fidler. Partitioning of the perpendicular write field into head and SUL contributions. *Magnetics, IEEE Transactions on*, 41(10):3064 – 3066, oct. 2005.
 - [81] N. Popovic and D. Praetorius. Applications of \mathcal{H} -matrix techniques in micromagnetics. *Computing*, 74(3):177–204, 2005.
 - [82] M. Najafi, B. Krüger, S. Bohlens, M. Franchin, H. Fangohr, A. Vanhaverbeke, R. Allenspach, M. Bolte, U. Merkt, D. Pfannkuche, D. P. D. Möller, and G. Meier. Proposal for a standard problem for micro-magnetic simulations including spin-transfer torque. *Journal of Applied Physics*, 105:113914, 2009.

Bibliography

- [83] L. Grasedyck and W. Hackbusch. Construction and arithmetics of \mathcal{H} -matrices. *Computing*, 70(4):295 – 334, August 2003.
- [84] M. Bebendorf. Approximation of boundary element matrices. *Numerische Mathematik*, 86:565–589, 2000.
- [85] M. Bebendorf and R. Grzibovski. Accelerating Galerkin BEM for linear elasticity using adaptive cross approximation. *Mathematical Methods in the Applied Sciences*, 29(14):1721–1747, 2006.
- [86] M. Bebendorf and S. Rjasanow. Adaptive low-rank approximation of collocation matrices. *Computing*, 70:1–24, 2003.
- [87] S. Börm and L. Grasedyck. Hybrid cross approximation of integral operators. *Numerische Mathematik*, 101:221 – 249, 2005.
- [88] L. Grasedyck. Adaptive recompression of \mathcal{H} -matrices for BEM. *Computing*, 74(205-223), 2005.
- [89] S. Börm and L. Grasedyck. Low-rank approximation of integral operators by interpolation. *Computing*, 72:325–332, 2004.
- [90] W. Hackbusch and S. Börm. Data-sparse approximation by adaptive \mathcal{H}^2 -matrices. *Computing*, 69:1–35, 2002.
- [91] J. Fidler, T. Schrefl, W. Scholz, D. Suess, and V.D. Tsiantos. Micromagnetic simulation of magnetization reversal in rotational magnetic fields. *Physica B: Condensed Matter*, 306(1-4):112 – 116, 2001. Proceedings of the Third International Symposium on Hysteresis and Micromagnetics Modeling.
- [92] A. Knittel, M. Franchin, G. Bordignon, T. Fischbacher, S. Bending, and H. Fangohr. Compression of boundary element matrix in micromagnetic simulations. *Journal of Applied Physics*, 105:07D542, 2009.
- [93] *Nmag — a micromagnetic simulation environment*, 2007. <http://nmag.soton.ac.uk/>.
- [94] A. Aharoni. Demagnetizing factors for rectangular ferromagnetic prisms. *Journal of Applied Physics*, 83(6):3432–3434, 1998.
- [95] S. W. Yuan and H. N. Bertram. Fast adaptive algorithms for micromagnetics. *Magnetics, IEEE Transactions on*, 28(5):2031 –2036, September 1992.
- [96] H. H. Long, E. T. Ong, Z. J. Liu, and E. P. Li. Fast fourier transform on multipoles for rapid calculation of magnetostatic fields. *Magnetics, IEEE Transactions on*, 42(2):295 – 300, feb. 2006.

- [97] H. Liu and D. Jiao. Existence of \mathcal{H} -matrix representations of the inverse finite-element matrix of electrodynamic problems and \mathcal{H} -based fast direct finite-element solvers. *Microwave Theory and Techniques, IEEE Transactions on*, 58(12):3697–3709, 2010.
- [98] T. Wan, X.Q. Hu, and R.S. Chen. An \mathcal{H} -matrix direct method with improved solution for finite element analysis of scattering problems. In *Microwave and Millimeter Wave Technology (ICMMT), 2010 International Conference on*, pages 244–247, May 2010.
- [99] W. Rave, K. Ramstck, and A. Hubert. Corners and nucleation in micromagnetics. *Journal of Magnetism and Magnetic Materials*, 183(3):329–333, 1998.
- [100] D. V. Berkov, K. Ramstöck, and A. Hubert. Solving micromagnetic problems. Towards an optimal numerical method. *physica status solidi (a)*, 137(1):207–225, 1993.
- [101] J. Schöberl. Netgen website. <http://www.hpfem.jku.at/netgen>.
- [102] M. J. Donahue and D. G. Porter. *OOMMF User's Guide*. National Institute of Standards and Technology, Gaithersburg, MD, 1999. Interagency Report NISTIR 6376, <http://math.nist.gov/oommf/>.
- [103] R. Hertel and H. Kronmüller. Micromagnetic simulation of the domain structure of a flat rectangular permalloy prism. *Journal of Applied Physics*, 85:6190–6192, 1999.
- [104] R. Hertel and H. Kronmüller. Finite element calculations on the single-domain limit of a ferromagnetic cube – a solution to μ MAG Standard Problem No. 3. *Journal of Magnetism and Magnetic Materials*, 238(2-3):185–199, 2002.
- [105] R. P. Cowburn and M. E. Welland. Phase transitions in planar magnetic nanostructures. *Applied Physics Letters*, 72(16):2041–2043, 1998.
- [106] C. J. Dedman, K. G. H. Baldwin, and M. Colla. Fast switching of magnetic fields in a magneto-optic trap. *Review of Scientific Instruments*, 72(11):4055–4058, 2001.
- [107] D. Goll, G. Schütz, and H. Kronmüller. Analysis of switching times of inhomogeneous magnetization processes in thin platelets. *Physica B: Condensed Matter*, 372(1-2):273–276, 2006. Proceedings of the Fifth International Symposium on Hysteresis and Micromagnetic Modeling.
- [108] A. Knittel, M. Franchin, T. Fischbacher, F. Nasirpour, S. J. Bending,

- and H. Fangohr. Micromagnetic studies of three-dimensional pyramidal shell structures. *New Journal of Physics*, 12(11):113048, 2010.
- [109] F. Nasirpouri, M. A. Engbarth, S. J. Bending, L. M. Peter, A. Knittel, H. Fangohr, and M. V. Milosevic. Three-dimensional ferromagnetic architectures with multiple metastable states. *Applied Physics Letters*, 98(22):222506, 2011.
- [110] A. Raizer, S. R. H. Hoole, G. Meunier, and J.-L. Coulomb. p- and h-type adaptive mesh generation. *Journal of Applied Physics*, 67(9):5803–5805, 1990.
- [111] M. J. Donahue. A variational approach to exchange energy calculations in micromagnetics. *Journal of Applied Physics*, 83(11):6491–6493, 1998.
- [112] A. C. Hindmarsh, Peter N. Brown, Keith E. Grant, Steven L. Lee, Radu Serban, Dan E. Shumaker, and Carol S. Woodward. Sundials: Suite of nonlinear and differential/algebraic equation solvers. *ACM Trans. Math. Softw.*, 31(3):363–396, 2005.
- [113] A. R. Muxworthy and W. Williams. Critical single-domain/multidomain grain sizes in noninteracting and interacting elongated magnetite particles: Implications for magnetosomes. *J. Geophys. Res.*, 111(B12S12), 2006.
- [114] J. Miltat and A. Thiaville. FERROMAGNETISM: Vortex Cores-Smaller Than Small. *Science*, 298(5593):555–, 2002.
- [115] U. Hartmann. Magnetic force microscopy. *Annual Review of Materials Science*, 29:53–87, 1999.
- [116] A. Wachowiak, J. Wiebe, M. Bode, O. Pietzsch, M. Morgenstern, and R. Wiesendanger. Direct observation of internal spin structure of magnetic vortex cores. *Science*, 298:577–580, October 2002.
- [117] H. Kronmüller and R. Hertel. Computational micromagnetism of magnetic structures and magnetisation processes in small particles. *Journal of Magnetism and Magnetic Materials*, 215-216:11 – 17, 2000.
- [118] A. Hirohata, H.T. Leung, Y.B. Xu, C.C. Yao, W.Y. Lee, J.A.C. Bland, and S.N. Holmes. Magnetic domain evolution in permalloy mesoscopic dots. *Magnetics, IEEE Transactions on*, 35(5):3886 –3888, sep 1999.
- [119] L. Thevenard, H. T. Zeng, D. Petit, and R. P. Cowburn. Six-fold configurational anisotropy and magnetic reversal in nanoscale permalloy triangles. *Journal of Applied Physics*, 106(6):063902 –063902–4, sep 2009.

- [120] H.N. Bertram and M. Williams. SNR and density limit estimates: a comparison of longitudinal and perpendicular recording. *Magnetics, IEEE Transactions on*, 36(1):4–9, 2000.
- [121] R. P. Cowburn. Superparamagnetism and the future of magnetic random access memory. *Journal of Applied Physics*, 93(11):9310–9315, 2003.
- [122] R. Dittrich, T. Schrefl, D. Süß, W. Scholz, H. Forster, and J. Fidler. A path method for finding energy barriers and minimum energy paths in complex micromagnetic systems. *Journal of Magnetism and Magnetic Materials*, 250:L12–L19, 2002.
- [123] J.-G. Zhu and C. Park. Magnetic tunnel junctions. *Materials Today*, 9(11):36–45, 2006.
- [124] H. J. Richter, A. Y. Dobin, R. T. Lynch, D. Weller, R. M. Brockie, O. Heinonen, K. Z. Gao, J. Xue, R. J. M. v. d. Veerdonk, P. Asselin, and M. F. Erden. Recording potential of bit-patterned media. *Applied Physics Letters*, 88(22):222512, 2006.
- [125] D. Ralph. A new twist for magnets. *Science*, 291(5506):999–1000, 2001.
- [126] D. L. Decker, D. E. Mapother, and R. W. Shaw. Critical field measurements on superconducting lead isotopes. *Phys. Rev.*, 112(6):1888–1898, Dec 1958.
- [127] André Müller. Private communication, 2010.
- [128] S. J. Bending. Private communication, 2010.
- [129] M. J. Donahue. Parallelizing a micromagnetic program for use on multiprocessor shared memory computers. *Magnetics, IEEE Transactions on*, 45(10):3923–3925, oct. 2009.
- [130] R. P. Boardman. *Computer simulation studies of magnetic nanostructures*. PhD thesis, School of Engineering Sciences, University of Southampton, 2005.
- [131] M. J. Donahue and D. G. Porter. *OOMMF User’s Guide*. National Institute of Standards and Technology, Gaithersburg, MD, 2002. Documentation of OOMMF release 1.2a3.
- [132] M. H. Aliabadi. *The Boundary Element Method: Applications in Solids and Structures*, volume 2. John Wiley and Sons, 2002.
- [133] A. J. Newell, W. Williams, and D. J. Dunlop. A generalization of the demagnetizing tensor for nonuniform magnetization. *J. Geophys. Res.*, 98:9551–9555, 1993.

Bibliography

- [134] P. Rhodes and G. Rowlands. Demagnetizing energies of uniformly magnetized rectangular blocks. *Proc. Leeds Philos. Lit. Soc. Sci. Sect.*, 6:191–210, 1954.
- [135] K. Fabian, A. Kirchner, W. Williams, F. Heider, T. Leibl, and A. Huber. Three-dimensional micromagnetic calculations for magnetite using FFT. *Geophysical Journal International*, 124:89–104, 1996.
- [136] R. Hertel and H. Kronmüller. Adaptive finite element mesh refinement techniques in three-dimensional micromagnetic modeling. *Magnetics, IEEE Transactions on*, 34(6):3922–3930, nov 1998.